HAL
open science

Simple techniques for piezoelectric energy harvesting optimization

Yang Li

To cite this version:

Yang Li. Simple techniques for piezoelectric energy harvesting optimization. Electronics. INSA de Lyon, 2014. English. NNT : 2014ISAL0077 . tel-01135309

HAL Id: tel-01135309

https://theses.hal.science/tel-01135309v1

Submitted on 25 Mar 2015

HAL is a multi-disciplinary open access archive for the deposit and dissemination of scientific research documents, whether they are published or not. The documents may come from teaching and research institutions in France or abroad, or from public or private research centers.

L'archive ouverte pluridisciplinaire **HAL**, est destinée au dépôt et à la diffusion de documents scientifiques de niveau recherche, publiés ou non, émanant des établissements d'enseignement et de recherche français ou étrangers, des laboratoires publics ou privés.

N° d'ordre 2014ISAL0077
Année 2014

Thèse

Approches simplifiées pour l'optimisation de systèmes piézoélectriques de récupération d'énergie
-
Simple techniques for piezoelectric energy harvesting optimization

Présentée devant
L'institut national des sciences appliquées de Lyon

Pour obtenir
Le grade de docteur

École doctorale
Électronique , Électrotechnique, Automatique de Lyon

Par
LI, Yang
(Master)

Soutenue le *03 Septembre 2014* devant la Commission d'examen

Jury MM.

AUDIGIER, David	Maitre de conférences (INSA-Lyon)	Examinateur
COMBETTE, Philippe	Professeur (Université Montpellier 2)	Rapporteur
COMPEAU, Jean-Louis	Docteur (CALOR SAS)	Examinateur
LEFEUVRE, Elie	Professeur (Université Paris-Sud)	Rapporteur
MURALT, Paul	Professeur (EPFL)	Examinateur
PETIT, Lionel	Professeur (INSA de Lyon)	Examinateur
RICHARD, Claude	Professeur (INSA de Lyon)	Co-directeur

Laboratoire de Génie Électrique et Ferroélectricité (LGEF) de l'INSA de Lyon

Cette thèse est accessible à l'adresse : http://theses.insa-lyon.fr/publication/2014ISAL0077/these.pdf
© [Y. Li], [2014], INSA de Lyon, tous droits réservés

Cette thèse est accessible à l'adresse : http://theses.insa-lyon.fr/publication/2014ISAL0077/these.pdf
© [Y. Li], [2014], INSA de Lyon, tous droits réservés

INSA Direction de la Recherche - Ecoles Doctorales – Quinquennal 2011-2015

SIGLE	ECOLE DOCTORALE	NOM ET COORDONNEES DU RESPONSABLE
CHIMIE	**CHIMIE DE LYON** **http://www.edchimie-lyon.fr** Sec : Renée EL MELHEM Bat Blaise Pascal 3e etage 04 72 43 80 46 Insa : R. GOURDON	M. Jean Marc LANCELIN Université de Lyon – Collège Doctoral Bât ESCPE 43 bd du 11 novembre 1918 69622 VILLEURBANNE Cedex Tél : 04.72.43 13 95 directeur@edchimie-lyon.fr
E.E.A.	**ELECTRONIQUE, ELECTROTECHNIQUE, AUTOMATIQUE** **http://edeea.ec-lyon.fr** Sec : M.C. HAVGOUDOUKIAN eea@ec-lyon.fr	M. Gérard SCORLETTI Ecole Centrale de Lyon 36 avenue Guy de Collongue 69134 ECULLY Tél : 04.72.18 60.97 Fax : 04 78 43 37 17 Gerard.scorletti@ec-lyon.fr
E2M2	**EVOLUTION, ECOSYSTEME, MICROBIOLOGIE, MODELISATION** **http://e2m2.universite-lyon.fr** Sec : Safia AIT CHALAL Bat Darwin - UCB Lyon 1 04.72.43.28.91 Insa : H. CHARLES	Mme Gudrun BORNETTE CNRS UMR 5023 LEHNA Université Claude Bernard Lyon 1 Bât Forel 43 bd du 11 novembre 1918 69622 VILLEURBANNE Cédex Tél : 06.07.53.89.13 e2m2@ univ-lyon1.fr
EDISS	**INTERDISCIPLINAIRE SCIENCES-SANTE** **http://www.ediss-lyon.fr** Sec : Safia AIT CHALAL Hôpital Louis Pradel - Bron 04 72 68 49 09 Insa : M. LAGARDE Safia.ait-chalal@univ-lyon1.fr	Mme Emmanuelle CANET-SOULAS INSERM U1060, CarMeN lab, Univ. Lyon 1 Bâtiment IMBL 11 avenue Jean Capelle INSA de Lyon 696621 Villeurbanne Tél : 04.72.68.49.09 Fax :04 72 68 49 16 Emmanuelle.canet@univ-lyon1.fr
INFOMATHS	**INFORMATIQUE ET MATHEMATIQUES** **http://infomaths.univ-lyon1.fr** Sec :Renée EL MELHEM Bat Blaise Pascal 3e etage infomaths@univ-lyon1.fr	Mme Sylvie CALABRETTO LIRIS – INSA de Lyon Bat Blaise Pascal 7 avenue Jean Capelle 69622 VILLEURBANNE Cedex Tél : 04.72. 43. 80. 46 Fax 04 72 43 16 87 Sylvie.calabretto@insa-lyon.fr
Matériaux	**MATERIAUX DE LYON** **http://ed34.universite-lyon.fr** Sec : M. LABOUNE PM : 71.70 –Fax : 87.12 Bat. Saint Exupéry Ed.materiaux@insa-lyon.fr	M. Jean-Yves BUFFIERE INSA de Lyon MATEIS Bâtiment Saint Exupéry 7 avenue Jean Capelle 69621 VILLEURBANNE Cedex Tél : 04.72.43 83 18 Fax 04 72 43 85 28 Jean-yves.buffiere@insa-lyon.fr
MEGA	**MECANIQUE, ENERGETIQUE, GENIE CIVIL, ACOUSTIQUE** **http://mega.universite-lyon.fr** Sec : M. LABOUNE PM : 71.70 –Fax : 87.12 Bat. Saint Exupéry mega@insa-lyon.fr	M. Philippe BOISSE INSA de Lyon Laboratoire LAMCOS Bâtiment Jacquard 25 bis avenue Jean Capelle 69621 VILLEURBANNE Cedex Tél :04.72 .43.71.70 Fax : 04 72 43 72 37 Philippe.boisse@insa-lyon.fr
ScSo	**ScSo*** **http://recherche.univ-lyon2.fr/scso/** Sec : Viviane POLSINELLI Brigitte DUBOIS Insa : J.Y. TOUSSAINT	Mme Isabelle VON BUELTZINGLOEWEN Université Lyon 2 86 rue Pasteur 69365 LYON Cedex 07 Tél : 04.78.77.23.86 Fax : 04.37.28.04.48 viviane.polsinelli@univ-lyon2.fr

*ScSo : Histoire, Géographie, Aménagement, Urbanisme, Archéologie, Science politique, Sociologie, Anthropologie

Cette thèse est accessible à l'adresse : http://theses.insa-lyon.fr/publication/2014ISAL0077/these.pdf
© [Y. Li], [2014], INSA de Lyon, tous droits réservés

(this page intentionally left blank)

Cette thèse est accessible à l'adresse : http://theses.insa-lyon.fr/publication/2014ISAL0077/these.pdf
© [Y. Li], [2014], INSA de Lyon, tous droits réservés

Abstract

Piezoelectric energy harvesting is a promising technique for battery-less miniature electronic devices. The object of this work is to evaluate simple and robust approaches to optimize the extracted power.

First, a lightweight equivalent circuit derived from the Mason equivalent circuit is proposed. It's a comprehensive circuit, which is suitable for piezoelectric seismic energy harvester investigation and power optimization. The optimal charge impedance for both the resistive load and complex load are given and analyzed. When complex load type can be implemented, the power output is constant at any excitation frequency with constant acceleration excitation. This power output is exactly the maximum power that can be extracted with matched resistive load without losses. However, this wide bandwidth optimization is not practical due to the high sensitivity the reactive component mismatch.

Another approach to improve power extraction is the capability to implement a network of piezoelectric generators harvesting on various frequency nodes and different locations on a host structure. Simulations are conducted in the case of direct harvesting on a planar structure excited by a force pulse. These distributed harvesters, equipped with nonlinear technique SSHI (Synchronized Switching Harvesting on Inductor) devices, were connected in parallel, series, independently and other complex forms. The comparison results showed that the energy output didn't depend on the storage capacitor connection method. However, only one set of SSHI circuit for a whole distributed harvesters system degrades the energy scavenging capability due to switching conflict.

Finally a novel non-linear approach is proposed to allow optimization of the extracted energy while keeping simplicity and standalone capability. This circuit named S3H for "Synchronized Serial Switch Harvesting" does not rely on any inductor and is constructed with a simple switch. The power harvested is more than twice the conventional technique one on a wide band of resistive load.

Keywords: *Energy harvesting; Piezoelectricity; Equivalent circuit modeling; Mason equivalent circuit; Non-linear techniques; Piezoelectric Harvester Network*

Cette thèse est accessible à l'adresse : http://theses.insa-lyon.fr/publication/2014ISAL0077/these.pdf
© [Y. Li], [2014], INSA de Lyon, tous droits réservés

(this page intentionally left blank)

Cette thèse est accessible à l'adresse : http://theses.insa-lyon.fr/publication/2014ISAL0077/these.pdf
© [Y. Li], [2014], INSA de Lyon, tous droits réservés

Résumé

La récupération d'énergie par élément piézoélectrique est une technique prometteuse pour les futurs systèmes électroniques nomades autoalimentés. L'objet de ce travail est d'analyser des approches simples et agiles d'optimisation de la puissance produite par un générateur piézoélectrique.

D'abord le problème de l'optimisation de l'impédance de charge d'un générateur piézoélectrique sismique est posé. Une analyse du schéma équivalent global de ce générateur a été menée sur la base du schéma de Mason. Il est démontré que la puissance extraite avec une charge complexe adaptée puisse être constante quelle que soit la fréquence et que de plus elle est égale à la puissance extraite avec la charge résistive adaptée du même système sans pertes. Il est montré toutefois que la sensibilité de cette adaptation à la valeur de la réactance de la charge la rend difficilement réaliste pour une application pratique.

Une autre solution pour améliorer l'énergie extraite est de considérer un réseau de générateurs positionnés en différents endroits d'une structure. Des simulations sont proposées dans une configuration de récupération d'énergie de type directe sur une plaque encastrée. Les générateurs piézoélectriques, associés à la technique SSHI, ont été reliés selon différentes configurations. Les résultats attestent que l'énergie produite ne dépend pas de façon critique de la manière dont sont connectés les éléments. Toutefois l'utilisation d'un seul circuit SSHI pour l'ensemble du réseau dégrade l'énergie extraite du fait des interactions entre les trop nombreuses commutations.

Enfin une nouvelle approche non-linéaire est étudiée qui permet l'optimisation de l'énergie extraite tout en gardant une grande simplicité et des possibilités d'auto alimentation. Cette technique appelée S3H pour « Synchronized Serial Switch Harvesting » n'utilise pas d'inductance et consiste en un simple interrupteur en série avec l'élément piézoélectrique. La puissance récupérée est le double de celle extraite par les méthodes conventionnelles et reste totalement invariante sur une large gamme de résistances de charge.

Mots-clés: *Récupération d'énergie ; Piézoélectricité ; Schéma équivalent de Mason ; Traitement non-linéaire ; Réseau de générateurs piézoélectrique*

Cette thèse est accessible à l'adresse : http://theses.insa-lyon.fr/publication/2014ISAL0077/these.pdf
© [Y. Li], [2014], INSA de Lyon, tous droits réservés

(this page intentionally left blank)

Cette thèse est accessible à l'adresse : http://theses.insa-lyon.fr/publication/2014ISAL0077/these.pdf
© [Y. Li], [2014], INSA de Lyon, tous droits réservés

Acknowledgement

Foremost, thanks all my friends who helped me in the past several years.

I would like to thanks Prof. Daniel Guyomar and Prof. Claude Richard, the supervisors of my thesis. Prof. Guyomar has inspired me to find new solution for smart materials. Prof. Richard taught me a lot. His meticulous work attitude and his unique analytical approach have shaped my research style. His passion and patient give me enough faith to fix the tricky problem one by one.

I also would like to express my gratitude to the committee members, for their corrections and suggestions.

I also would like express my gratitude to Dr. Pierre-Jean Cottinet, Dr. Jean-Fabien Capsal and Dr. Jeremy Galineau for their guidance on natural rubber and polymer making, although these work are not included in this thesis.

I would like to acknowledge Dr. Laurence Seveyrat, Ms. Véronique Perin for their kindly help on experiments. I will not forget Mr. Frederic Defromerie's help on experiments and the joyful daily lunch time. Ms. Evelyne Dorieux, the secretary of laboratory LGEF, is a warm lady who helps me a lot (from accommodation to conference travel).

I would like to acknowledge the China Scholarship Council (CSC) for the financial support.

I would like to acknowledge Dr. Dan Wu, Dr. Yi-Chieh Wu, Bin Zhang for the wonderful office time. And the other colleges (Dr. Linjuan Yan, Dr. Kaixiang LI, Dr. Qin LIU, Xunqian, Zhongjian, Yuki, Alex, …) are also appreciated for the research discussion and joyful memories.

My parents and brother receive my deepest gratitude and love for their endless support and encouragement.

A very special acknowledgement goes to my fiancée Miss Zhijun ZHANG, who gives me warm and lovely support during these days.

Yang LI

Cette thèse est accessible à l'adresse : http://theses.insa-lyon.fr/publication/2014ISAL0077/these.pdf
© [Y. Li], [2014], INSA de Lyon, tous droits réservés

(this page intentionally left blank)

Cette thèse est accessible à l'adresse : http://theses.insa-lyon.fr/publication/2014ISAL0077/these.pdf
© [Y. Li], [2014], INSA de Lyon, tous droits réservés

TABLE OF CONTENTS

Abstract i

Résumé iii

Acknowledgement v

NOTATIONS 1

ABBREVIATIONS 3

Introduction 5

C H A P T E R 1 Piezoelectric energy harvesting 9

1.1 Motivation 9

1.2 Energy harvesting techniques 10

1.2.1 Solar radiation 10

1.2.2 Thermal energy 12

1.2.3 Mechanical motion 14

1.3 Fundamental of piezoelectric energy harvesting 18

1.3.1 Piezoelectric effect 18

1.3.2 Piezoelectric energy harvester modeling 19

1.3.3 Circuit topology for piezoelectric energy harvesting optimization 24

1.3.4 Wide bandwidth consideration 31

1.4 Outline of the thesis 33

C H A P T E R 2 The power optimization by impedance matching 35

2.1 Introduction 35

2.2 Piezoelectric harvester equivalent circuit modelling 36

Cette thèse est accessible à l'adresse : http://theses.insa-lyon.fr/publication/2014ISAL0077/these.pdf
© [Y. Li], [2014], INSA de Lyon, tous droits réservés

2.2.1 Derivation of the generator equivalent circuit using Mason approach 37
2.2.2 Piezoelectric generator equivalent circuit..... 40
2.3 Optimal impedance matching..... 43
2.3.1 Impedance matching theory 43
2.3.2 Case study: purely resistive load 44
(A) Power optimization 44
(B) Discussion on the viscous factor 47
2.3.3 Case study: complex load 49
2.3.4 Comparison with other power optimization approach..... 56
2.4 Experimental validation 58
2.4.1 Set-up 59
2.4.2 Equivalent circuit identification by LCR meter 60
2.4.3 Measurement process..... 61
(A) Purely resistance load 61
(B) Optimal impedance matching with a parallel L-R load 62
2.4.4 Results and discussion..... 63
(A) Purely resistance load 63
(B) Optimal impedance matching with a parallel L-R load 63
(C) High sensitivity of the impedance matching process to the passive component dispersion 65
2.5 Conclusion and future work 67
C H A P T E R 3 Power optimization for SSHI network.....69
3.1 Introduction..... 69
3.2 Piezoelectric harvester modeling 71
3.3 Network topology design 74
3.3.1 Circuit basic 74

Cette thèse est accessible à l'adresse : http://theses.insa-lyon.fr/publication/2014ISAL0077/these.pdf
© [Y. Li], [2014], INSA de Lyon, tous droits réservés

3.3.2 Network topology design 78
(A) Standard 78
(B) Independent SSHI 78
(C) SSHI in parallel..... 79
(D) Mono SSHI..... 80
(E) SSHI in series..... 80
3.4 Power performance comparison 80
3.4.1 Decay time (Energy harvesting process) 80
3.4.2 Power performance 83
3.4.3 Energy balance 84
3.4.4 Influence of the coupling coefficients 85
3.5 Improvement for pulse operation 86
3.6 Bonding effect 88
3.7 Conclusion 92
C H A P T E R 4 Synchronized serial switch for piezoelectric energy harvesting 95
4.1 Motivation 95
4.2 Energy harvesting modelling 97
4.2.1 Piezogenerator electro-mechanical model 97
4.2.2 Analytical model development: Constant displacement 98
(A) Standard circuit 99
(B) S3H circuit..... 100
4.2.3 Analytical model development: Constant force104
(A) Standard circuit 105
(B) S3H circuit..... 106
4.3 Circuit performance discussion..... 107
4.3.1 Duty cycle..... 107
(A) Constant displacement 107

Cette thèse est accessible à l'adresse : http://theses.insa-lyon.fr/publication/2014ISAL0077/these.pdf
© [Y. Li], [2014], INSA de Lyon, tous droits réservés

(B) Constant Force 110
4.3.2 Electromechanical coupling effect 111
4.4 Experimental validation 115
4.4.1 Set-up 115
4.4.2 Mono-mode case study 116
4.4.3 Multi-mode case study 120
4.5 S3H working in pulsed mode 122
4.6 Combination with Buck-boost circuit 123
4.7 Conclusion 124
C H A P T E R 5 Conclusion 127
5.1 Designing the harvesting circuit for piezoelectric energy harvester 127
5.2 Employing distributed harvesters 128
5.3 Obtaining a robust harvester 129
5.4 Revisit the energy harvesting system architecture 129
BIBLIOGRAPHY 131
LIST OF FIGURES 141
LIST OF TABLES 149
Appendix. A. Piezoelectric generator modeling by Mason Equivalent circuit 151
A.1 Piezoelectric constants relationship 151
A.1.1 Permittivity 151
A.1.2 Elastic stiffness coefficient 151
A.1.3 Stiffness and others 152
A.2 The simplification of Mason equivalent circuit: Preparation . 153
A.2.1 Propagation speed 153
A.2.2 Impedance in mechanical side 154
A.2.3 Turn ratio (Coupling) 155
A.3 The simplification of Mason equivalent circuit 156
A.3.1 Mechanical side 156

Cette thèse est accessible à l'adresse : http://theses.insa-lyon.fr/publication/2014ISAL0077/these.pdf
© [Y. Li], [2014], INSA de Lyon, tous droits réservés

A.3.2 The combination with electrical side 157
A.3.3 The impedance of generator 160
Appendix. B. The power optimization for piezoelectric energy harveste 162
B.1 Purely resistive case 162
B.1.1 Low loss (low coupling) condition..... 164
(A) Stationary points..... 164
(B) When Ω=1 166
(C) When $\Omega=\sqrt{1+\kappa^2}$ 167
B.1.2 General case 168
B.2 Complex load case 171
Appendix. C. Simulink Simscape model for network SSHI harvester 174
C.1 Method 174
C.2 Simulation environment 174
C.3 An example: SSHI circuit..... 175
Appendix. D. Simulink Simscape model for peak-detecting switch 177
D.1 Peak detecting 177
D.2 Generate the switch on pulse 177
D.3 Generate the dead zone pulse 177
D.4 Control signal (output)..... 177
Appendix. E. The optimization for STD 180
Appendix. F. The optimization for S3H 184
F.1 Power of S3H at constant displacement condition 184
F.2 S3H for constant force 186
PUBLICATIONS 189

Cette thèse est accessible à l'adresse : http://theses.insa-lyon.fr/publication/2014ISAL0077/these.pdf
© [Y. Li], [2014], INSA de Lyon, tous droits réservés

(this page intentionally left blank)

Cette thèse est accessible à l'adresse : http://theses.insa-lyon.fr/publication/2014ISAL0077/these.pdf
© [Y. Li], [2014], INSA de Lyon, tous droits réservés

NOTATIONS

Piezoelectric related parameters

T	mechanical stress
D	electrical displacement
S	mechanical strain
E	electrical field
d	piezoelectric charge constant
g	piezoelectric voltage constant
e	piezoelectric constant
h	piezoelectric stiffness constant
s	piezoelectric elastic compliance
β	piezoelectric dielectric constants
c	piezoelectric elastic stiffness constant
k or k^2	piezoelectric coupling factor, i.e. k_{33}
f	frequency
ω	angular frequency
ω_D (corresponding to f_{oc})	open circuit angular frequency
ω_E (corresponding to f_{cc})	short circuit angular frequency
ε_0	absolute permittivity
ε	relative permittivity
C_0	blocked capacitance of piezoelectric element

Electrical parameters

C	capacitor
L	inductor
R	resistor
Z	impedance
X	reactance
Y	admittance
G	conductance
B	susceptance
P	harvested power
N	turn ratio
E	energy
I or i	current
V	voltage

Cette thèse est accessible à l'adresse : http://theses.insa-lyon.fr/publication/2014ISAL0077/these.pdf
© [Y. Li], [2014], INSA de Lyon, tous droits réservés

Other modelling parameters

ρ	density
K	lumped stiffness
C	lumped viscous loss
Q_E	electrical quality factor
Q_M	mechanical quality factor
$tan\delta$	the (mechanical) loss
ζ	system damping ratio
κ	curvature
G	shear modulus
Y	Young's modulus
t	thickness
m or M	the lumped mass
U	displacement
t_0 or Δt	switch on time

Superscripts

T	mechanical stress is constant
D	electrical displacement is constant
S	mechanical strain is constant
E	electrical field is constant

Subscripts

S	source
p , P or PZ	piezoelectric element

Cette thèse est accessible à l'adresse : http://theses.insa-lyon.fr/publication/2014ISAL0077/these.pdf
© [Y. Li], [2014], INSA de Lyon, tous droits réservés

ABBREVIATIONS

General

IoT	Internet of Things
ICT	Internet Communication Technology
LCD	Liquid Crystal Display
MPPT	Maximum Power Point Tracking
PVDF	Polyvinylidene fluoride
PZT	Lead zirconate titanate
SHM	Structure Health Monitoring
WSNs	Wireless Sensor Nodes

Electrical related

AC	Alternating Current
DC	Direct Current
RLC	Resistor, inductor and capacitor
RMS	Root Mean Square

Modelling related

BVD	Butterworth-Van Dyke equivalent circuit
KLM	Krimholtz Leedom Matthaei equivalent circuit
KKT	Karush-Kuhn-Tucker condition
MEC	Mason Equivalent Circuit
SDOF	Single Degree of Freedom

Energy harvesting circuits

STD	Standard technique
SSDI	Synchronized Switch Damping on Inductor
SSDS	Synchronized Switch Damping on Short
p-SSHI	Synchronized Switch Harvesting on Inductor (placed in parallel)
s-SSHI	Synchronized Switch Harvesting on Inductor (placed in series)
SECE	Synchronous Electric Charge Extraction
DSSH	Double Synchronized Switch Harvesting
OSECE	Optimized SECE
S3H	Synchronized Serial Switch Harvesting

Cette thèse est accessible à l'adresse : http://theses.insa-lyon.fr/publication/2014ISAL0077/these.pdf
© [Y. Li], [2014], INSA de Lyon, tous droits réservés

(this page intentionally left blank)

Cette thèse est accessible à l'adresse : http://theses.insa-lyon.fr/publication/2014ISAL0077/these.pdf
© [Y. Li], [2014], INSA de Lyon, tous droits réservés

Introduction

The incredible development of lithography technique is pushing the boundary of chip density. This achievement in the semiconductor industry brings to reality the low-cost, compact, low-power, multi-function integrated chips (ICs). It stimulates the development of miniature electronics devices, such as portable mobile, compact tablet computer, handheld GPS, pressure sensor, temperature sensor. Furthermore, specific applications such as Wireless Sensor Nodes (WSNs), Structural Health Monitoring (SHM), Non-Destructive Evaluation (NDE) and wearable computing benefited from it. For mobility and practical considerations, they shall work independently without electrical power grid. In other words, they need a standalone power supply which nowadays consists essentially of a battery. Unfortunately, the development of the battery industry is quite slow. For instance, the most popular Li-ion batteries today, was introduced to the mass market nearly 30 years ago. Moreover, the lifespan of battery steers the miniature electronics devices' application and innovation. The solutions that are considered are increasing the charging speed, restraining the power need, charging wirelessly or developing battery-less products.

A battery-less device, would extract the required energy from ambient environment. Harvesting energy from ambient sources is a promising way to provide continuous ubiquitous energy supply. The energy source could be solar radiation, thermal gradient and mechanical motion. Many researches focus on mechanical motion, especially vibration, on account of the widely distributed vibration of objects. Piezoelectricity is one of the physical effects allowing conversion of the mechanical energy to electrical energy.

When applying piezoelectricity to electric harvesting, the most common way is connecting a vibrating or mechanically actuated piezoelectric elements with the load or storage devices directly. Mostly, an AC-DC converter is required to regulate the output voltage. The power output is affected by vibration amplitude, vibration frequency, mechanical configuration, harvesting circuit and the storage device. However, for a given application case, the only way to improve the power efficiency is to optimize the output voltage of the piezoelectric element by a specific electric circuit.

As mentioned before, the basic energy harvesting circuit is the so-called standard circuit which connects the load directly. This type of energy circuit has a low efficiency and must be tuned to match the maximum power

Cette thèse est accessible à l'adresse : http://theses.insa-lyon.fr/publication/2014ISAL0077/these.pdf
© [Y. Li], [2014], INSA de Lyon, tous droits réservés

output. In real application, the multi harvester could be applied to have the distributed strain harvesting or multi-frequency harvesting, how to manage the harvester power is one practical problem, the connection topology should be considered. Moreover, a tuning-free harvesting circuit will be an ideal replacement for the standard technique.

Another way to improve the available energy is the multiplication of energy sources. It could be exploiting in the same time, radiation, temperature and vibration. But if only vibration is considered, it could be exploiting a full network of piezogenerators. Indeed in most of the development this last decade, an energy harvesting system is an add-on localized device optimized in terms of energy conversion. It is known as *indirect energy harvesting* or seismic harvesting devices. Now the energy is usually spread everywhere within a given structure, and therefore the structure itself could be entirely the energy harvesting device. This is known as *direct energy harvesting*. This has not been extensively studied due to the low useful piezoelectric coupling available but mostly due to practical deployment consideration. But direct distributed energy harvesting could be considered and a network of piezoelectric harvester piezoelement could be integrated at the design stage of a given mechanical part. In this case, the challenge is setting up and controlling such a network exploiting only weakly coupled piezoelement to harvest a large quantity of energy, with a robust and as simple as possible electric circuit.

It is the object of this work to revisit this type of harvesting architecture by considering simple tools to deal with the electric generator, by considering the association of piezoelement spread on a given structure and associated as a network, and finally, by considering the possible simplification of the energy harvesting circuit while maintaining optimization of the extracted power.

Firstly, the power transferring ability of the piezoelectric energy harvester is investigated. With linear motion assumption, the harvester is treated as a Single Degree of Freedom (SDOF) system. Such a SDOF piezoelectric harvester is modelled by Mason equivalent circuit. By using electrical mechanical analogies, an equivalent circuit of such a SDOF harvester is derived. After complete circuit analysis, it is simplified to a voltage source with inherent impedance in series or a current source with inherent impedance in parallel. The voltage/current source is related to the vibration frequency and amplitude. The parameters of this model are comprehensively defined. Next, using impedance matching method, the

Cette thèse est accessible à l'adresse : http://theses.insa-lyon.fr/publication/2014ISAL0077/these.pdf
© [Y. Li], [2014], INSA de Lyon, tous droits réservés

optimal load for purely resistive case and complex case will be discussed. The results will show the outline of piezoelectric energy harvesting optimization. The feasibility of these matching impedances will also be discussed.

Next, the distributed energy harvester case is considered: 3 piezoelectric patches are bonded on a plate. There are plenty of ways to connect them to charge a storage capacitor. The three piezoelectric patches will be arranged in series, parallel or other complex form. The comparison among these different network topologies will give simple guidelines for application cases. The harvesting approach considered here, is the direct mode, which means the piezoelectric patches are bonded directly on the plate. SSHI technique is used in this network topology design to increase the power extraction, especially for weak coupling conditions. For this direct mode energy harvesting configuration, the effect of the bonding layer between the structure and the piezo patches is considered in the power analysis because corresponding parasitic capacitance could interfere with the correct operation of the network.

It is worth emphasizing that there are two critical problems for piezoelectric energy harvesting, the working frequency and the load. Distributed harvester and direct energy harvesting provides a solution for multi frequencies application. A simple way is expected to overcome the matching load limitation to obtain a load-independent power optimization method. Instead of using impedance matching method, a novel non-linear harvesting technique, named as Synchronized Serial Switch Harvesting (S3H) will be proposed to optimize the harvesting process. The power output of this technique is load-independent when the load impedance is low. The analysis of this technique is based on the electrical differential equations and first harmonic analysis. For sake of comparison, the traditional standard circuit is also considered. Both the constant displacement excitation and constant force excitation cases will be discussed. Other key parameters consideration, such as duty cycle and electromechanical coupling effect are also included. This technique will be validated by experiment and compared to the SECE technique, which is another load-independent energy harvesting circuit. Experimental validations are given with mono-mode and multi-mode sinusoidal force.

The manuscript is organized as follows:

Chapter 1 is a review of recent the energy harvesting research progress. Vibration based piezoelectric energy harvester is considered. Starting from basic linear piezoelectric equations, the modeling method for a

Cette thèse est accessible à l'adresse : http://theses.insa-lyon.fr/publication/2014ISAL0077/these.pdf
© [Y. Li], [2014], INSA de Lyon, tous droits réservés

general piezoelectric energy harvester will be exposed. The comparison with published works will be showed to demonstrate their advantages and limitations. This chapter is expected to illustrate the fundamental scope of piezoelectric energy harvesting technique.

Chapter 2 starts from the Mason equivalent circuit, describes the whole derivation process for a lightweight equivalent circuit for assessing the piezoelectric generator and power optimization.

Chapter 3 investigates a distributed harvester. Such kind of harvester is composed of multiple piezoelectric energy harvesters. The connection method, or network topology, will be discussed in order to derive simple implementation guidelines.

Chapter 4 introduces a novel load-independent power conditioning circuit, named S3H. S3H only adds one simple switch on the standard technique. Thanks to the well-designed switch strategy, the S3H power output is dramatically different from standard technique. Both the constant displacement and constant force cases will be discussed. The duty cycle, referring to the switch on-time, and the coupling conditions will be used as evaluation parameters to examine the performance of such technique. Both the sinusoidal excitation and pulse excitation will be taken in consideration. This chapter will provide fundamental information on the advantages and limitations of this new technique.

Cette thèse est accessible à l'adresse : http://theses.insa-lyon.fr/publication/2014ISAL0077/these.pdf
© [Y. Li], [2014], INSA de Lyon, tous droits réservés

C H A P T E R 1 Piezoelectric energy harvesting

1.1 Motivation

1.2 Energy harvesting techniques

1.2.1 Solar radiation

1.2.2 Thermal energy

1.2.3 Mechanical motion

1.3 Fundamental of piezoelectric energy harvesting

1.3.1 Piezoelectric effect

1.3.2 Piezoelectric energy harvester modeling

1.3.3 Circuit topology for piezoelectric energy harvesting optimization

1.3.4 Wide bandwidth consideration

1.4 Outline of the thesis

1.1 Motivation

The fast development of semiconducting industry dramatically improved the computing capability and reduced the power consumption in the past decade. It stimulates the use of electric devices not only for the multi-functionality mobile, portable video player but also for Wireless Sensor Nodes (WSNs), Structural Health Monitoring (SHM) and wearable computing. Most of them should work independently, without electrical grid, which means that an energy storage device such as a battery is required. Unfortunately the lifespan of a battery is limited. The energy source or the battery capacity steers the product innovation: the battery should be replaced/charged easily and periodically. In this way, the extension for tiny electrical devices is limited. Besides, the large amount of discarded batteries leads to a chemical waste problem.

In recent years, another new concept “Internet of Things (IoT)” spread widely in electronics, house construction, internet communication technology (ICT), automatic controlling and logistics community. The IoT actually is the cluster of modern technology based on miniature electronics devices. In the world of IoT, each object has its unique identity and the ability to transfer data. They are supposed to appear everywhere. As a conventional power grid is impossible and the costly battery replacing/charging should be avoided to cut down the cost, a ubiquitous energy source should be considered.

The concept of “ubiquitous energy” refers to the electrical energy harvested from surrounding environment. The energy doesn’t come from the conventional electrical grid or

Cette thèse est accessible à l'adresse : http://theses.insa-lyon.fr/publication/2014ISAL0077/these.pdf
© [Y. Li], [2014], INSA de Lyon, tous droits réservés

commercial batteries. Compared with the short-life battery, potential ambient energy is inexhaustible energy. Ubiquitous energy expands the global capabilities of tiny devices.

All these advantages motivate the research on transferring ambient energy into electrical form.

1.2 Energy harvesting techniques

The human beings depend largely on energy harvesting from the surrounding environment. We harvest the energy constantly and ubiquitously. Specifically, the term "Energy harvesting" here refers to the technique that scavenge ambient energy, such as solar, temperature gradient and mechanical motion, to drive the target device (small scale electronic device) synchronously (using right away) or asynchronously (storing in battery or supercapacitor for future using). The surrounding energy (Table 1-1) could be radiation form like solar, be field difference like temperature, and be mechanical motion like biological energy or vibration. Additional intermediate materials are required to transform these kinds of energy source into electrical energy.

Although several authors have already well documented the energy harvesting techniques [1-4], the state-of-art progress (laboratory progress and commercial products) among them will be summarized here for a clear understanding and comparison.

1.2.1 Solar radiation

Solar is the source of all plants thanks to the photosynthesis. Human beings have benefit from solar from their birth. It's a history of about 2000 years long, if we consider Archimedes destroying enemy's battleship with the reflection of solar rays by polished bronze mirror as the human beings first intentionally technical use of solar radiation. But it isn't a long story since we combine solar and electricity together. The first photovoltaic phenomenon was reported by a French experimental physicist named Edmond Becquerel in 1839 [5]. The so-called photovoltaic effect can convert solar energy into electricity via materials such as monocrystalline silicon, multicrystalline silicon and cadmimum telluride [6]. When sunlight is

Table 1-1. Summary of energy sources in residential and commercial buildings[1]

Harvester type	Typical range of ambient energy levels	Estimated electrical dc power	Calculated power density
Photovoltaic	Light intensity: 100 to 3700 lx	25 to 1149 µW	9 to 399 µWcm^{-3}
Thermal	Thermal gradient: 10 to 40 °C	1 to 10 mW	0.7 to 7.1 mWcm^{-3}
Periodic kinetic	Acceleration: 2.45 × 10^{-2} to 2.82 ms^{-2} Frequency: 43.1 to 162.3 Hz	0.008 to 68.97 µW	0.05 to 459.8 µWcm^{-3}
EM wave	EM wave strength: -74 to -29 dBm	0.028 to 944 nW	1.69 × 10^{-3} to 57.37 nWcm^{-3}
Airflow	Airflow speed 1 to 10 ms^{-1}	0.9 to 324 mW	1.7 × 10^{-2} to 6.0 mWcm^{-3}

Cette thèse est accessible à l'adresse : http://theses.insa-lyon.fr/publication/2014ISAL0077/these.pdf
© [Y. Li], [2014], INSA de Lyon, tous droits réservés

absorbed by these materials, the solar energy knocks electrons loose from their atoms, allowing the electrons to flow through the material to produce electricity [7]. The key parameter in photovoltaic is the solar cell efficiency. In mass market, the value is around 17%, while it could reach 44% in laboratory (Figure 1-1). Apart from the material research to increase the efficiency, the strategy to extract energy from solar cell is also widely studied.

To have the maximum power transfer of photovoltaic cells, many different Maximum Power Point Tracking (MPPT) methods are studied[9]. In general, the so-called MPPT technique is to automatically find the output voltage or current at which a PV cell reaches its maximum power point. The MPPT method could be Hill Climbing [10, 11], Incremental Conductance [12], Neural Network [13]. Taking Hill Climbing method as an example, Qiu *et al.* [11] proposed an inductive boost convertor for photovoltaic energy harvesting. The MPPT algorithm was divided into two sessions, *Search* and *Long-wait*. In search session, three consecutive operation points (N_{Less}, N_0, N_{More}) were used to compare the output current. The three output currents were used to charge the corresponding three capacitors. By using voltage comparator, the optimal operation point was found and set as the new middle point N_0. The process was repeated for several times. Then the final optimal point N_0 was found. It is like hill climbing to find the peak step by step. The *Search* session then ended and the *Long-wait* session started. In the later session, the harvesting circuit was working on the optimal point

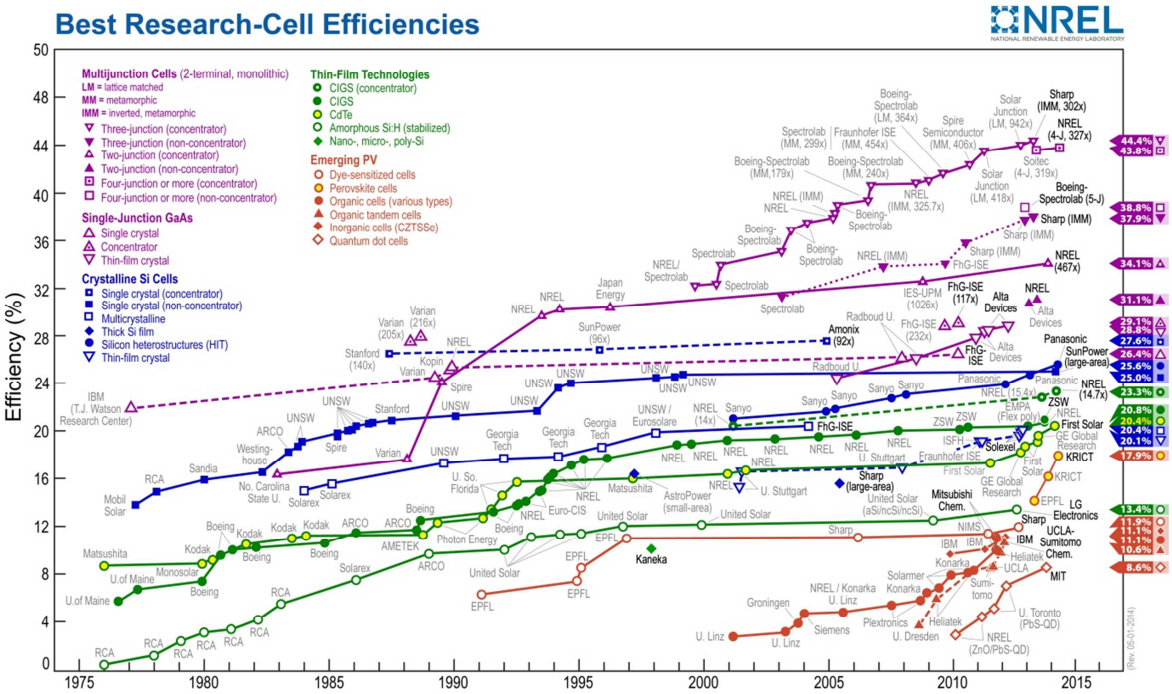

Figure 1-1. Research cell efficiency records of photovoltaic by NREL [8]

Yang LI
École doctorale EEA de Lyon / 2014
Institut national des sciences appliquées de Lyon

Cette thèse est accessible à l'adresse : http://theses.insa-lyon.fr/publication/2014ISAL0077/these.pdf
© [Y. Li], [2014], INSA de Lyon, tous droits réservés

obtained from Search session.

1.2.2 Thermal energy

Generally speaking, thermal energy can be converted to electricity by thermoelectric effect and pyroelectric effect. The former relies on a thermal gradient while the latter one relies on the temperature changes. The most common use of energy generation from thermal gradient is with Seebeck effect type devices. The Seebeck effect consists of the generation of an electrical potential difference with two conducting materials junctions, either metal or semiconductors, which are subjected to different temperatures. The generated voltage and power consumption are an increasing function of the temperature difference [14].

Samson *et al.* [15] proposed an interesting application of thermoelectric generator (TEG). In their study, the fuselage temperature varying between +20.4°C and -21.8°C of an aircraft (i.e. from taking-off to climbing) is used to drive a TEG. The experiments showed that with optimal load, the output energy is around 26.5J for a 3000 s operation time.

The application of thermal gradient energy harvester is not reality suitable for mass market at present. For instance, a device based on BiTe/SbTe having a footprint of 10.3 mm^2 generates 130 mW at a temperature difference of 70 K, while the power will drop to only 1.5mW for a 10K temperature difference[16]. Now obtaining large thermal gradient from hot surfaces usually relies on large and voluminous heat sinks, limiting the integrability of these devices. To use such TEG for daily life, the challenge is to decrease the required temperature difference. Lu *et al.* [17] proposed a TEG prototype which could generate 150mW with a temperature difference as low as 34°C with the cold side at room temperature. Kim *et al.* developed a wearable thermoelectric generator fabricated on a glass fabric [18]. This device is about 500 µm thin, lightweight and flexible. The power density can reach 28 mWg^{-1} with a 50 °C temperature difference. For instance, placing this device on the human skin in a surrounding temperature of 15 °C, a 3 mV voltage output is generated.

The main problem of the application in domestic application is that only limited temperature difference can be exploited.

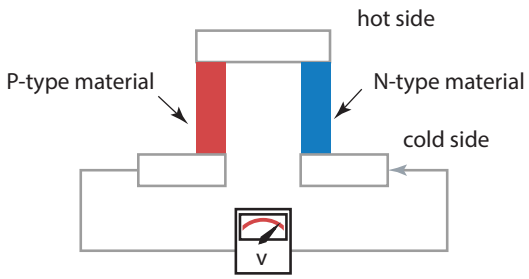

Figure 1-2. The operation principle of a thermal energy generator using Seebeck effect

Cette thèse est accessible à l'adresse : http://theses.insa-lyon.fr/publication/2014ISAL0077/these.pdf
© [Y. Li], [2014], INSA de Lyon, tous droits réservés

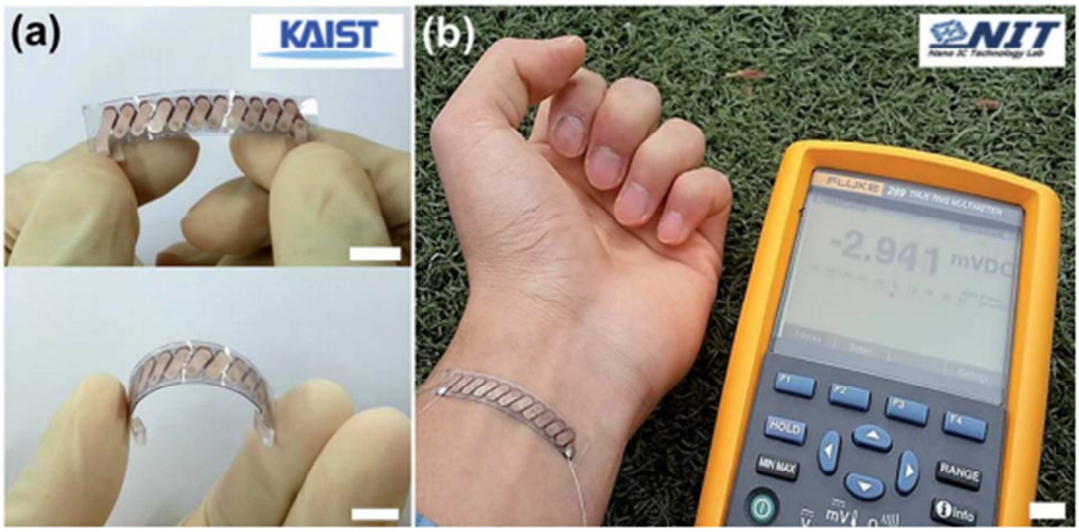

Figure 1-3. A werable energy harvseting demonstation.[18]

With pyroelectric materials, which are in form of thin-film, an energy harvesting textile is possible. Pyroelecticity consists of the variation of the polarization of ferroelectric materials with the temperature change. Elastic changes and electric field variations can be exploited for energy harvesting from thermal variation cycles [19]. Actually, pyroelectricity has been used for sensor application for a long time in thermal imaging cameras. Cuadras *et al.* [20] investigated the possibility of pyroelectric type energy harvesting using screen-printed PZT cell or commercial PVDF. With a 60 K temperature variation (from 300 K to 360 K), by connecting two PZT cells in parallel, a 0.5 mJ available energy is obtained, which is enough to power an autonomous sensor node. However, the energy harvested by PVDF is smaller. With pyroelectricity, currents in the order of 0.1 mA and charges in the order of 10 µC have been achieved.

Waste heat is the common end form of energy consuming. In fact, all power plants and heavy industries, release tremendous thermal energy to ambient temperature. Very recently, to harvest such wasted heat, Lee *et al.* [21] proposed a novel waste heat harness mechanism for charging battery by applying thermogalvanic effect. The thermogalvanic effect means the output voltage of battery increased as the temperature decreases. As Figure 1-4 shows, the charging process is divided into 4 steps: firstly, the battery is heated by waste thermal energy; Then the hot battery is charged at low voltage; Once the charging operation finishes, the battery is allowed to cool. At the end, at low temperature environment, the battery discharges and outputs more electricity than the convention case. In their report, a copper hexacyanoferrate cathode and a Cu/Cu^{2+} anode is used to convert heat into electricity. When

Cette thèse est accessible à l'adresse : http://theses.insa-lyon.fr/publication/2014ISAL0077/these.pdf
© [Y. Li], [2014], INSA de Lyon, tous droits réservés

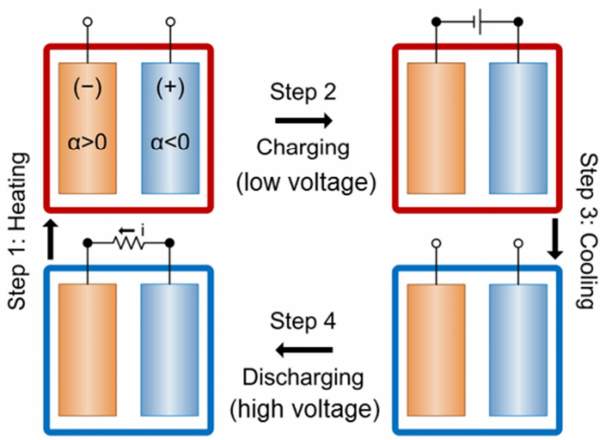

Figure 1-4. The battery charging process with thermogalvanic effect[21]

such electrochemical system is cycled in a temperature gradient range between 274K and 333K, a 5.7% energy conversion efficiency is reached.

1.2.3 Mechanical motion

Most of the kinetic energy harvesters use electromagnetic, piezoelectric and electrostatic principles to convert the mechanical (periodic or intermittent motion) energy into electric form.

Enocean is the pioneer of the Smart House. They developed and deployed a complete autonomous system for domestic applications. The basic idea is to develop an entirely autonomous self-powered node to send information or communicate within a domestic wireless network. The most commonly used power unit is the motion energy harvester ECO-200. It uses electromagnetic conversion to transform a tiny push action of the finger into a wireless control signal [22]. More recently, Enerbee a company from Grenoble developed a piezomagnetic harvesting system combining the movement of a magnet (rotation movement) and a piezomagnetic element to generate electrical energy [23]. The advantage of such a harvester is

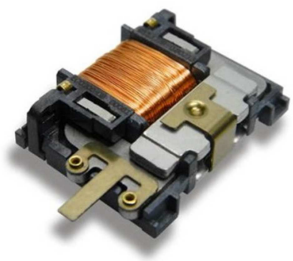

Figure 1-5. EnOcean Motion Harvester[22]

Cette thèse est accessible à l'adresse : http://theses.insa-lyon.fr/publication/2014ISAL0077/these.pdf
© [Y. Li], [2014], INSA de Lyon, tous droits réservés

its independence to the speed leading to potential use of this technique on slow motion systems such as gas meter or the wireless light buttons.

Wang and Song proposed a piezogenerator based on ZnO nanowire [24] in 2006. This generator is able to achieve an enhanced output voltage of 0.243 V with current density of 18 nA cm^{-2} [25]. This flexible nanowire piezoelectric material expands the potential usage of piezoelectric generator. For instance, Hu *et al.* [26] placed this nanogenerator inside a tire as a sensor element. A 1.5 V and 25 nA signal was generated during the deformation of the tire. Moreover, LCD screen was lit directly by the power transferred from this nanogenerator. Later on, this ZnO nanowire device was excited with sound pressure [27]. It generate a AC output voltage of 50mV from a sound field with an intensity of approximately 100dB. Due to the flexibility of nanowire, this piezoelectric generator is also feasible to harvest energy from waving flag or to detect the winkling of a human face [28] (Figure 1-6). Other similar works can be found in Refs[29-31].

In nanoscale, there are more opportunities for energy harvesting [32], even for the biomedical engineering. Lee *et al.* [33] proposed a virus-based piezoelectric energy generating method. Considering that M13 aligned protein coat structure over phage (*a virus that infects and replicates within the bacteria*) lacks inversion symmetry (Figure 1-7.a), the phage is expected to present intrinsic piezoelectric character. Then they fabricated a self-assembled thin films of phage which can exhibit a piezoelectric strengths of up to 7.8 pm V^{-1}. Next, they developed a phage-based piezoelectric generator with 6 nA of current made a 400 mV potential voltage output(Figure 1-7.b), and claimed it can drive a liquid-crystal display[34].

Biomechanical energy harvesting is the technique which transfers biological motional energy to electrical energy with the mechanical movements of active materials. Potential energy sources could be knee motion[35], foot pressure changes, blood pressure variations[36],

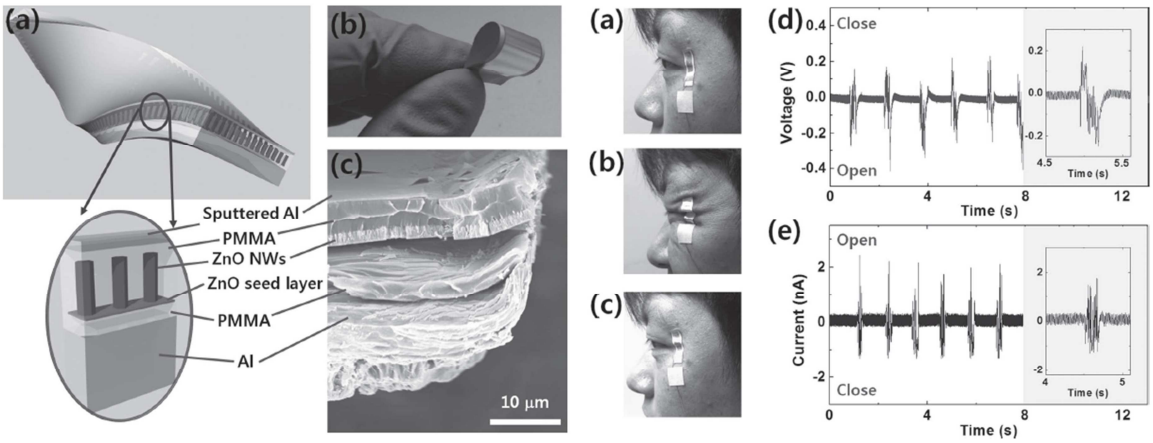

(a) (b)

Figure 1-6. The piezoelectric nanowire generator(a) and the voltage and curent(b) generated from the movements of winkling [28].

Cette thèse est accessible à l'adresse : http://theses.insa-lyon.fr/publication/2014ISAL0077/these.pdf
© [Y. Li], [2014], INSA de Lyon, tous droits réservés

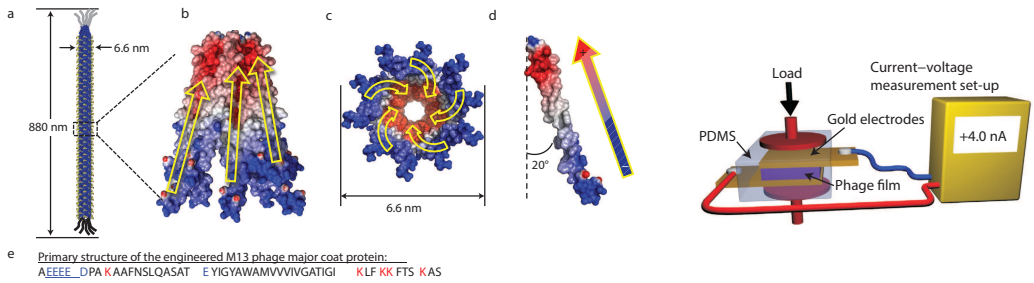

(a) (b)

Figure 1-7. Schematic of piezoelectric M13 phage structure (a) and schematic of piezoelectirc electrical energy generation measurement set-up(b)[33]

nose breathing, even the cardiac motion [37].

Bionic Power's product PowerWalk M-Series is mounted on the knee and can output an average 12 W electric power with a comfortable speed walking [38]. The main principle is illustrated in Figure 1-8. The Pavegen tile is a product designed for converting energy from footsteps into electricity. By deploying the Pavegen tiles on a temporary footbridge connecting one subway station to the Olympic park, 12 million footballs were received and an 21 kWh energy were harvested in total [1]. All the energy was generated by the passengers walk.

Lefeuvre *et al.* [36, 39] used the blood pressure to achieve a piezoelectric based energy harvester. Experimental results showed energy densities up to 30µJ/cm^3, while their target is to produce 10 µJ per heartbeat [39]. The group of John Rogers proposed a flexible polymer (Figure 1-9) based energy harvester scavenging the energy from the motion of the heart, lung and diaphragm [37]. A prototype was tested a the mechanical bending stage then placed on bovine and ovine hearts. During the heart expansion and relaxation at 80-120 beats per min heart rates, the voltage output reached 4 V for a bovine and 2 V for an ovine heart.

On another scale, a helicopter blade is a key component, whose failure will no doubt cause the aircraft accident. Therefore the lifespan of helicopter blades is calculated using a worst-case operation scenario [40] , which means that a potential ten thousand hours life span blade will be discarded after only a three thousand hours service. Arms *et al.* [41] proposed energy harvesting for wireless sensors for helicopter blade damage tracking. The main challenge is making sure all the system can be powered by the energy harvesting unit. To increase the power efficiency, de Jong *et al.* [42] proposed the piezoelectric energy harvester with SECE enhanced energy harvesting circuit (*This circuit will be discussed later*). With the simulation, de Jong *et al.* claimed that the output power can be larger than 5 W. However, this power value is heavily depending on the helicopter operation condition and the deployment quality of the harvester. In view of the complexity of such kind harvester modelling [43] and the power output level of piezoelectric energy harvester, it is believed that the real power won't exceed 1 W. In this sense, the challenge for structure health monitoring of helicopter blade is the design of and the improvement of the energy harvesting device.

Cette thèse est accessible à l'adresse : http://theses.insa-lyon.fr/publication/2014ISAL0077/these.pdf
© [Y. Li], [2014], INSA de Lyon, tous droits réservés

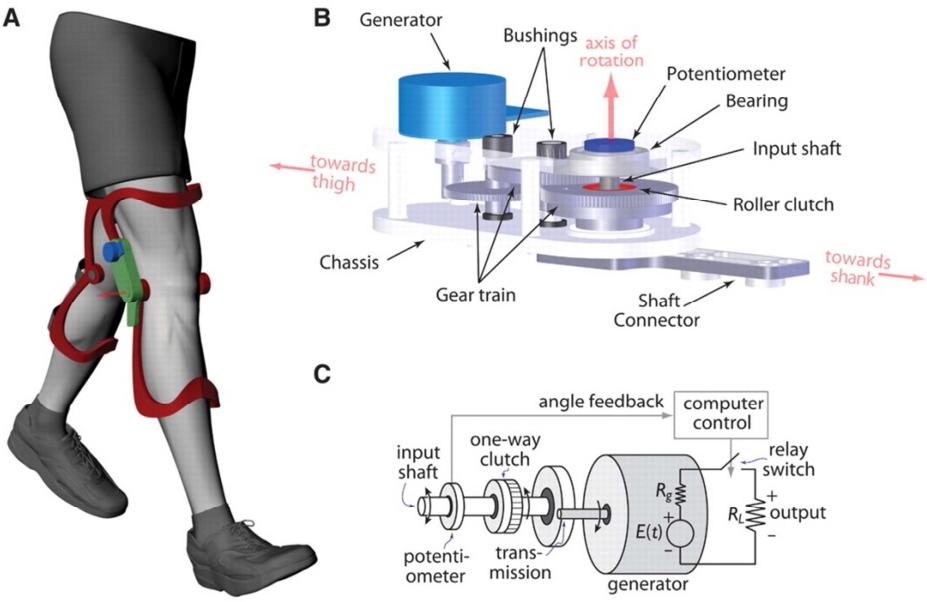

Figure 1-8. Biomechanical energy harvester by the movements of knee [35]

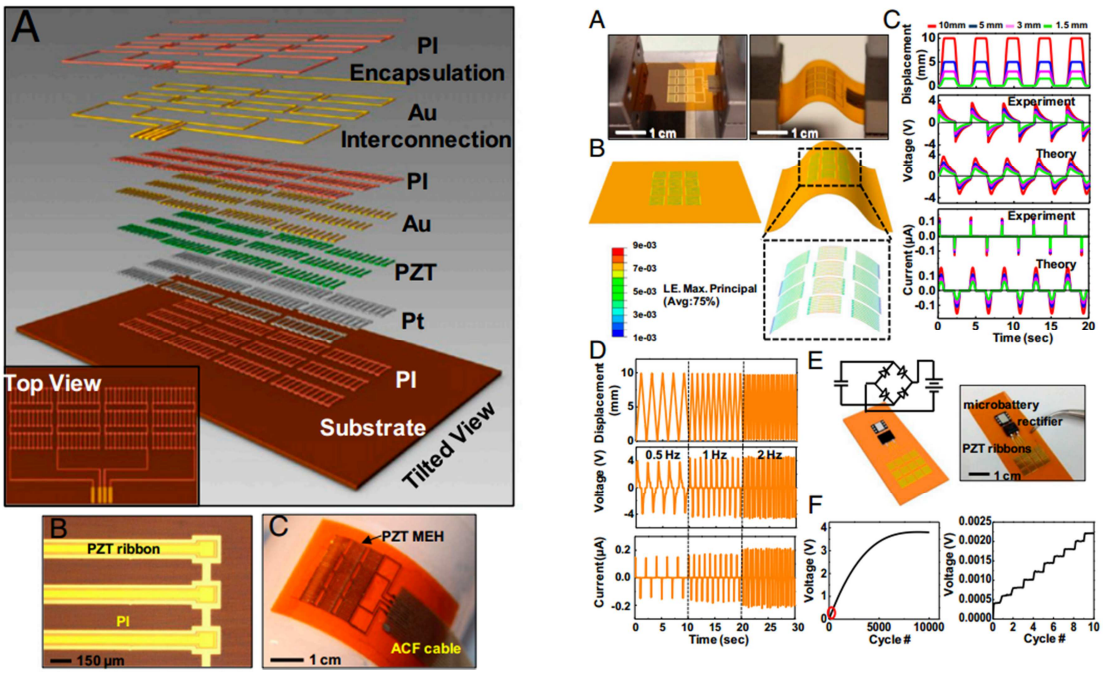

(a) MEH demonstration (b) Experimental process

Figure 1-9. The flexible MEH and the experiments comparison [37]

Cette thèse est accessible à l'adresse : http://theses.insa-lyon.fr/publication/2014ISAL0077/these.pdf
© [Y. Li], [2014], INSA de Lyon, tous droits réservés

Finally, apart from these implementation examples, energy harvesting could benefit from coupled method to improve the global performance. Shape memory effect coupled with direct piezoelectric effect [44], thermal/solar coupled with piezoelectric effect [45], magnetic effect coupled with piezoelectric effect [46], and biochemical [47] appears to be the most promising researches.

1.3 Fundamental of piezoelectric energy harvesting

1.3.1 Piezoelectric effect

Piezoelectric effect couples the mechanical movements and electrical energies within specific materials. Once the piezoelectric material is applied with pressure, it produces electricity. Conversely, when the piezoelectric material is applied with electric field, it changes shape producing variation of stress/strain (Figure 1-10). Starting from the first law of thermodynamics, the piezoelectric constitutive equations for linear piezoelectricity is given as,

$$\begin{cases}[T]=\left[c^{E}\right][S]-[e][E],\\ [D]=[e][S]+\left[\varepsilon^{S}\right][E].\end{cases} \tag{1.1}$$

All the other equivalent system of state equations with different boundary conditions are expressed as follows [48, 49],

$$\begin{cases}[S]=\left[s^{E}\right][T]+[d][E],\\ [D]=[d][T]+\left[\varepsilon^{T}\right][E].\end{cases} \tag{1.2}$$

$$\begin{cases}[S]=\left[s^{D}\right][T]+[g][D],\\ [E]=-[g][T]+\left[\beta^{T}\right][D].\end{cases} \tag{1.3}$$

$$\begin{cases}[T]=\left[c^{D}\right][S]-[h][D],\\ [E]=-[h][S]+\left[\beta^{S}\right][D].\end{cases} \tag{1.4}$$

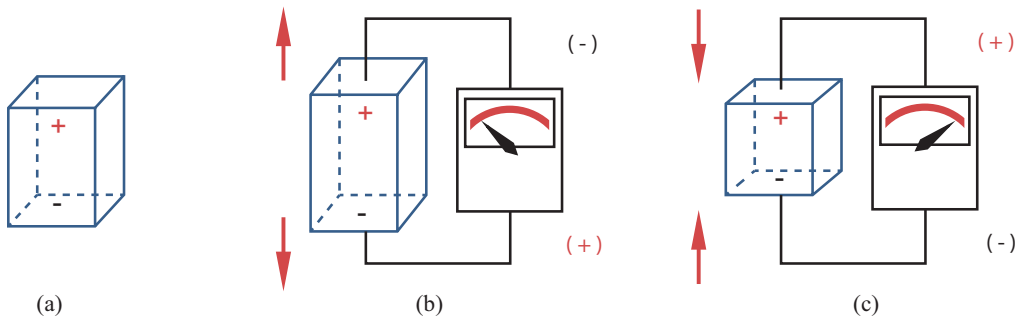

Figure 1-10. Piezoelectric effects

Cette thèse est accessible à l'adresse : http://theses.insa-lyon.fr/publication/2014ISAL0077/these.pdf
© [Y. Li], [2014], INSA de Lyon, tous droits réservés

Depending on the specific boundary conditions one of these systems could be preferable for sake of simplification. Variables *T*, *D*, *S* and *E* represent the mechanical stress, electrical displacement, mechanical strain and electrical field, respectively. All the piezoelectric constant matrices are interrelated as follows(derived from [48])

$$\begin{aligned}
&[d]=\left[\varepsilon^{T}\right][g]=[e]\left[s^{E}\right],\\
&[g]=\left[\beta^{T}\right][d]=[h]\left[s^{D}\right],\\
&[e]=\left[\varepsilon^{S}\right][h]=[d]\left[c^{E}\right],\\
&[h]=\left[\beta^{S}\right][e]=[g]\left[c^{D}\right].
\end{aligned} \tag{1.5}$$

1.3.2 Piezoelectric energy harvester modeling

The core part for a piezoelectric energy harvester is the piezoelectric element (ceramic or polymer). Considering a piezoelectric plate working on thickness mode (Figure 1-11.a),

$$Q = \text{charge of eletrode } = D \cdot A \tag{1.6}$$

$$V = \text{Voltage accross electrode} = E \cdot L \tag{1.7}$$

$$F_P = \text{force over the area} = T \cdot A \tag{1.8}$$

The strain S_3 is defined as,

$$S_3 = \frac{U}{L} \tag{1.9}$$

It can be assumed that,

$$S_1 = S_2 = 0 \tag{1.10}$$

In this case, Equation(1.1) is used as,

$$\begin{cases} A \cdot T_3 = A \cdot c_{33}^{E} S - A \cdot e_{33} E \\ A \cdot D_3 = A \cdot e_{33} S + A \cdot \varepsilon_{33}^{S} E \end{cases} \tag{1.11}$$

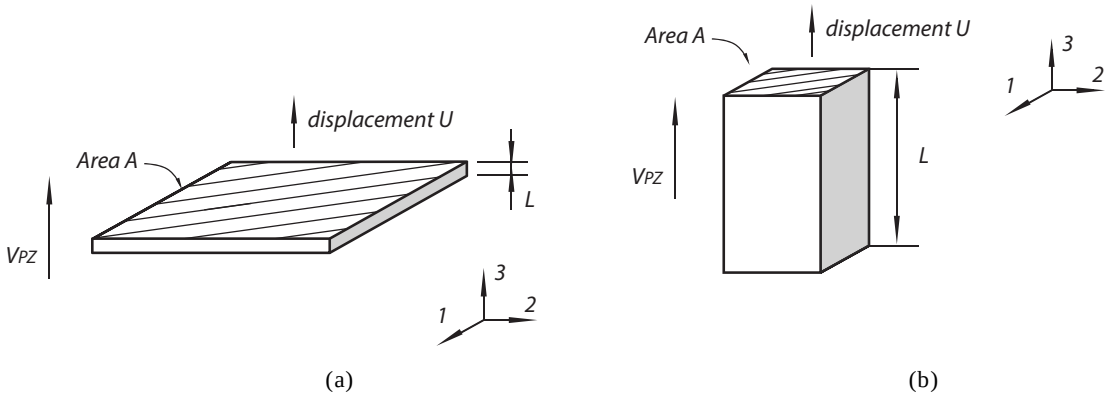

Figure 1-11. The piezoelectric element (a) plate in thickness mode (b) rod in 3-3 mode

Cette thèse est accessible à l'adresse : http://theses.insa-lyon.fr/publication/2014ISAL0077/these.pdf
© [Y. Li], [2014], INSA de Lyon, tous droits réservés

Substituting Equations (1.7)(1.9) into (1.11), obtain,

$$\begin{cases} A \cdot T = A \cdot c_{33}^{E} \dfrac{U}{L} - A \cdot e_{33} \dfrac{V}{L} \\ A \cdot D = A \cdot e_{33} \dfrac{U}{L} + A \cdot \varepsilon_{33}^{S} \dfrac{V}{L} \end{cases} \tag{1.12}$$

Considering (1.6)(1.8), that is,

$$\begin{cases} F_P = K_P^E U + \alpha V \\ Q = -\alpha U + C_0 V \end{cases} \tag{1.13}$$

Differentiate Q with respect to time t, we have,

$$I = -\alpha \dot{U} + C_0 \dot{V} \tag{1.14}$$

where,

$$\alpha = -\frac{e_{33} A}{L}, \quad C_0 = \frac{\varepsilon_{33}^{S} A}{L}, \quad K_P^E = \frac{c_{33}^{E} A}{L} \tag{1.15}$$

With the consideration of current direction, obtain,

$$\begin{cases} F_P = K_P^E U + \alpha V, \\ I = \alpha \dot{U} - C_0 \dot{V}. \end{cases} \tag{1.16}$$

Moreover, if a rod shape piezoelectric element is considered (Figure 1-11.b), the lateral stress is very small,

$$T_1 = T_2 = 0, \tag{1.17}$$

therefore the lateral stress can be neglected. In these conditions usually known as longitudinal 3-3 mode, the previous Equation (1.2) is used. Following the same derivation process as above, the Equation (1.16) holds with another set of definitions,

$$\alpha = \frac{d_{33}}{s_{33}^{E}} \frac{A}{L}, \quad C_0 = \left(\varepsilon_{33}^{T} + \frac{d_{33}^2}{s_{33}^{E}} \right) \frac{A}{L}, \quad K_p^E = \frac{1}{s_{33}^{E}} \frac{A}{L} \tag{1.18}$$

Compared with Equations(1.15)(1.18), it is obvious that the piezoelectric equations can be described by different piezoelectric constants depending on the boundary condition. In addition, these simplified and approximate relationships are obtained,

$$e_{33} = \frac{d_{33}}{s_{33}^{E}}, \quad \varepsilon_{33}^{S} = \varepsilon_{33}^{T} + \frac{d_{33}^2}{s_{33}^{E}}, \quad c_{33}^{E} = \frac{1}{s_{33}^{E}}. \tag{1.19}$$

They are based on the ideal uniaxial assumption. These definitions will be used in Chapter 2 for various piezoelectric constants derivation.

In Equation(1.16), the outgoing current of piezoelectric element I contains two items. The former $\alpha \dot{U}$ represents the mechanical movement and relates to the speed of mechanical strain, the latter $-C_0 \dot{V}$ denotes the current of an equivalent capacitance C_0 charged with voltage V. The minus symbol in front of the equivalent capacitor points out that the current directions of the two items are different. Therefore, the 2nd equation of (1.16) is equivalent to a

Cette thèse est accessible à l'adresse : http://theses.insa-lyon.fr/publication/2014ISAL0077/these.pdf
© [Y. Li], [2014], INSA de Lyon, tous droits réservés

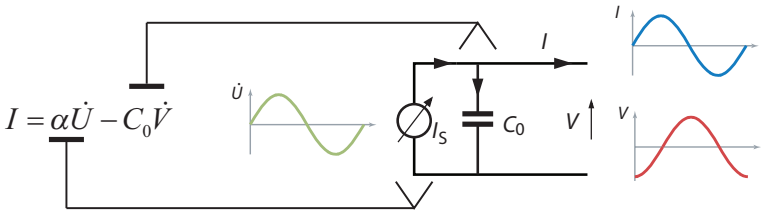

Figure 1-12. The equivalent circuit for piezoelectric element(electrical view)

circuit, which contains one controlled current source and a capacitor in parallel (Figure 1-12). This capacitor is also known as the blocked capacitance C_0 of piezoelement.

Note that, if damping effect by the load is neglected, this equivalent circuit is self-sufficient to model the complete harvester. Equation (1.16) is the macro scale expression of the linear piezoelectric equations. The next step is to integrate it into a piezoelectric energy harvester, such as cantilever beam or seismic device. For simplification, single degree of freedom (SDOF) is considered here. Near its resonance frequency, this electromechanical system can be represented by Figure 1-13. This model is slightly different from the conventional mechanical mass-spring-damper modeling approach. The piezoelectric coupling effect is included in term of the additional piezoelectric force. In this way, the electromechanical system based on mechanical mass-spring-damper system is governed by,

$$M\ddot{U} = F - K^E U - \alpha V - C\dot{U} \tag{1.20}$$

It is worth to point out that, the global stiffness of system K^E depends on the harvester configuration. For a cantilever beam case, the global stiffness is equal to two springs in parallel, leads to global stiffness expression as,

$$K^E = K_P^E + K \tag{1.21}$$

If the beam is very flexible, the global stiffness is determined by the piezoelectric element.

For a seismic piezoelectric energy harvester, the global stiffness is expressed as,

$$\frac{1}{K^E} = \frac{1}{K_P^E} + \frac{1}{K} \tag{1.22}$$

If the structure is very stiff, then the global stiffness is determined by the piezoelectric element.

Once the governing equations are established, the harvester can be modelled using state-space equations (Chapter 3), analytical approach (Chapter 4) or numerical approach [50]. Of course, it is not the only modeling method for piezoelectric energy harvester. A lightweight equivalent circuit approach derived from Mason equivalent circuit will be discussed in Chapter 2.

Another consideration is the coupling coefficient. The ***coupling coefficient*** k^2, which qualifies how effective is the mechanical to electrical energy conversion. In general, it is defined as,

Cette thèse est accessible à l'adresse : http://theses.insa-lyon.fr/publication/2014ISAL0077/these.pdf
© [Y. Li], [2014], INSA de Lyon, tous droits réservés

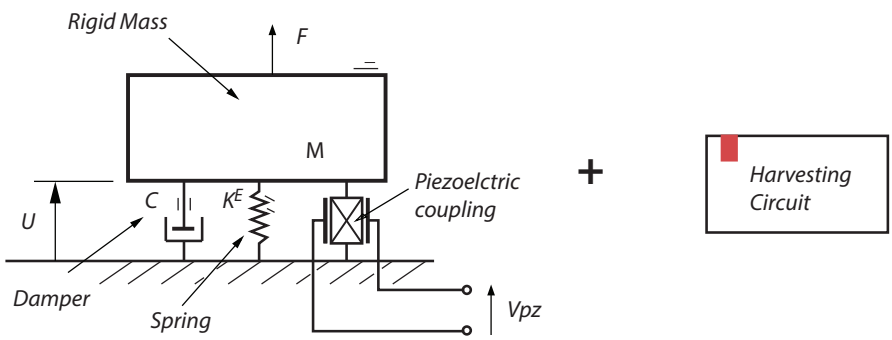

Figure 1-13. The 1-DOF modeling of piezoelectric energy harvester

$$k^2 = \frac{\text{stored mechanical energy}}{\text{supplied electrical energy}} \tag{1.23}$$

More precisely, it is defined as,

$$k^2 = \frac{U_m^2}{U_{elas} U_{elec}} \tag{1.24}$$

where U_{elas}, U_{elec} and U_m represents the elastic energy, electrostatic energy and mutual energy, respectively.

Considering a mixed type of coupling coefficient, we can also have [51],

$$k_e^2 = \frac{k^2}{1-k^2} \tag{1.25}$$

Within this alternative coupling factor, we can find the piezoelectric constant relationship in a clear way (Figure 1-14).

Dimensionless parameter ***Quality factor*** Q is used to measure the stored energy ratio per radian, thus the mechanical quality factor Q_M is expressed as,

$$Q_M = \frac{\text{Energy Stored}}{\text{Energy Dissipated}} \tag{1.26}$$

At low loss damping, Q_M is the ratio of the amplitude of resonance to the amplitude in static mode, yielding,

$$Q_M = \frac{1}{2\zeta} \tag{1.27}$$

Where, ζ is the damping ratio defined as,

$$\zeta = \frac{C}{2m\omega_n} \tag{1.28}$$

We should notice that, Q_M here also denotes the resonance sharpness.

Cette thèse est accessible à l'adresse : http://theses.insa-lyon.fr/publication/2014ISAL0077/these.pdf
© [Y. Li], [2014], INSA de Lyon, tous droits réservés

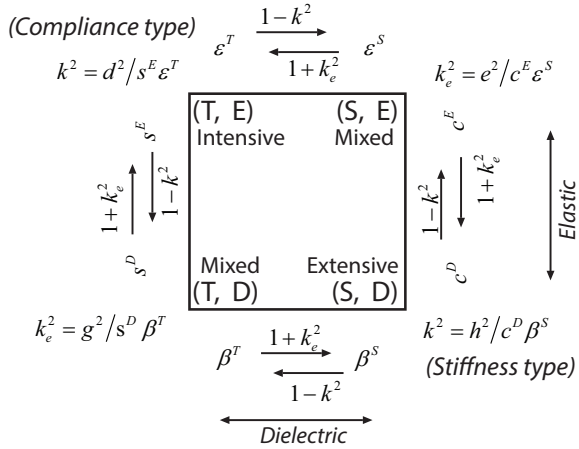

Figure 1-14. Fundamental piezoelectric relation type and electromechanical coupling coefficient corresponding to the choice of independent variable set (from [51])

In piezo-mechanical coupled system, the term k^2Q_M expresses the global electromechanical coupling ability or figure of merit. Therefore, it plays an important role in harvested power. For instance, assuming the external force and velocity are in phase, for a standard technique (connecting the piezoelectric element and the load R directly), the maximum power output is determined by Equation (1.29) when k^2Q_M <2, and only one optimal resistance exists.

$$P_{\max} = \frac{k^2Q_m}{\left(2+k^2Q_m\right)^2}\frac{F_M^2}{C} \tag{1.29}$$

However, this in phase analysis is not precise [52], a more general solution will be discussed in Chapter 4. Moreover, an alternative global coupling coefficient $k_e^2Q_M$ will be used as figure of merit for an ideal seismic energy harvester in Chapter 2. However, generally speaking, the efficiency of the power is increasing with this global coupling coefficient.

Table 1-2. Direct electromechanical analogies for lumped translational systems[53]

Mechanical quantity	Electrical quantity
Force F	Voltage V
Velocity $\dot{U}$	Current $i = \dot{q}$
Displacement U	Charge q
Momentum p	Magnetic flux linkage λ
Mass m	Inductance L
Compliance 1/K	Capacitance C
Viscous resistance C	Resistance R

Cette thèse est accessible à l'adresse : http://theses.insa-lyon.fr/publication/2014ISAL0077/these.pdf
© [Y. Li], [2014], INSA de Lyon, tous droits réservés

For such a piezoelectric energy transducer, the SDOF method is based on lumped parameter considerations. The lumped parameter analysis method cast the target system as the combination of mass, spring and/or dashpot. It is limited to the modelling of one or a few independent modes. Thanks to the formal similarities of the integro-differential equations governing the behavior of electric and mechanical systems, we can find the analogy relationships between electric and mechanical phenomena (Table 1-2). Based on this assumption, a series of equivalent circuits for piezoelectric resonator were proposed, such as Mason equivalent circuit[48], KLM(Krimholtz, Leedom, & Matthaei) equivalent circuit[54, 55], BVD(Butterworth-Van Dyke) equivalent circuit[55-57]. However, to simplify the analysis, the piezoelectric energy harvester is usually modelled by a current source shunted with blocked capacitor (for low damping consideration) or the series RLC circuit with a voltage source. Both modeling method cannot show the details of a piezoelectric energy harvester. The mechanical lumped model is better appropriate to emphasize mechanical motion while electrical lumped models are better suited for electrical consideration such as load matching as it will be discussed in Chapter 2.

Yet such popular SDOF method meets challenges. Erturk and Inman [58] claimed that, for a cantilever beam, the classical resonator SDOF modelling method is only suitable for low damping condition. They suggested that the rigid body motion of the beam was also the contributor of inertia of the system, while SDOF only considered vibratory motion of the beam. Based on this consideration, they corrected the SDOF model by a distributed parameter modeling method [59]. This distributed parameter modeling method is based on Euler-Bernoulli beam assumptions. In a further discussion [60], they claimed that the inaccuracy of SDOF modeling method were, the inaccurate estimation of the harvester mass, the backward coupling effect of piezoelectric energy harvesting in the mechanical domain was not necessarily proportional to velocity only.

The SDOF modelling method was used widely in piezoelectric energy harvesting research community. For the small displacement around resonance application, SDOF method is simple and fully validated by numerous experiments [61-63]. In other words, SDOF method is still a high fidelity model for linear motion applications.

1.3.3 Circuit topology for piezoelectric energy harvesting optimization

A energy harvesting electric or electronic circuit is usually implemented on the output of piezoelectric element in order to optimize the electric output power. In circuit analysis, the load can be represented by its input impedance Z. However, it is usually replaced by a resistive load impedance $\boldsymbol{R}$ for simplification. Moreover, a battery charging or power management device can be considered as equivalent to a resistive load R with several interface circuits [64-66]. In this subsection, the state of art circuit topologies for piezoelectric energy harvesting will be

Cette thèse est accessible à l'adresse : http://theses.insa-lyon.fr/publication/2014ISAL0077/these.pdf
© [Y. Li], [2014], INSA de Lyon, tous droits réservés

compared. The advantage and drawback of these topologies will also be discussed and compared.

The most elementary circuit topology is the Standard technique (STD-AC), which connects the piezoelectric element with load R directly. A regulated output voltage V_c is obtained in Standard technique DC mode (STD DC) by a full-wave diode bridge. The capacitor C_r is used to filter the output voltage V_c. Power output is related to the load impedance R. Thus impedance matching is used to optimize the output power. Ottman *et al.* proposed a DC-DC converter to optimize the power output of a piezoelectric harvesting device [64]. The use of a step-down converter in discontinuous conduction mode optimizes the piezoelectric energy harvesting [65], by tuning the optimal duty cycle, the power improvement can reach by approximately 325%. Lefeuvre *et al.* deployed a buck-boost converter to simulate the optimal resistive load for piezoelectric energy harvester [66]. Their experimental results showed that, in discontinuous conduction mode, this kind of converter can hit a 84% efficiency for input voltages between 1.6 and 5.5 V. The working frequency of the vibration harvester may differ from the resonance frequency. Therefore the impedance should match the harvester in different frequency condition. Kong *et al.* [67] used the impedance matching method to optimize the power output. They used a two-stage power conditioning circuit consisting of an AC-DC converter followed by a DC-DC converter to simulate the resistive load. Similar to the previous case, the optimal load is obtained by tuning the duty cycle of the power conditioning stage. The experimental results showed that their technique can harvest 58% to 72% of the available power around the fundamental resonance of the harvester. However, normally the electromechanical model is built base the linear and near-resonance assumption. If multi-mode vibration happens, the improved model is required [68, 69].

As a piezoelectric energy harvester is capacitive in most cases, perfect impedance matching is impossible with a resistive load. Moreover, the inductance required for perfect matching is usually unrealistic. To solve this problem, Guyomar *et al.* proposed an innovative non-linear circuit named as “Synchronized Switch Harvesting on Inductor”(SSHI) [61]. SSHI is an extension of “Synchronized Switch Damping on Inductor” (SSDI) [70, 71]. The latter

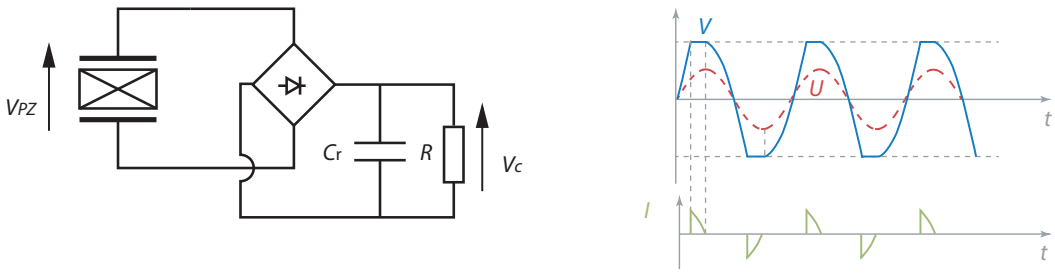

(a) (b)

Figure 1-15. Stanard energy harvseting circuit

Cette thèse est accessible à l'adresse : http://theses.insa-lyon.fr/publication/2014ISAL0077/these.pdf
© [Y. Li], [2014], INSA de Lyon, tous droits réservés

technique is used to control the vibration using a piezoelectric damping element and by inducing a phase shift between the voltage and the strain by a simple switching process synchronized with the vibration. The process is very simple. It consists of inverting the voltage each time it reaches an extremum. The inversion is obtained by a brief oscillation triggered by an electronic switch. It can also be considered as a periodic change of the system's stiffness due to a continuous change of the boundary conditions [72]. The vibration energy is converted into electric energy stored on the piezoelectric element and dissipated into heat during each switching. The energy stored on the piezoelectric element is used to power the switch device. But it can be transfered to an external load, thus resulting in SSHI technique.

The so-called p-SSHI technique modifies the Standard technique (STD AC or STD DC) by adding in parallel with the piezoelectric element a branch composing an inductor *L* in series with a switch *SW* (Figure 1-16). The switch operation will not occur until the displacement of the harvester or the voltage of piezoelectric element reaches its extremum. Once the voltage resulting from this switching process is in phase with the strain speed, the optimizing principle is "pulling up" the piezoelectric voltage as high as possible to encourage more energy to flow out from piezoelectric element. Analytical and experimental comparison of standard technique and SSHI showed that, this "pulling up" design could lead to a 400% power improvement. However, the harvested power gain is depending on the global coupling factor. The electrical harvested power may be increased by more than 400% at low coupling conditions.

A similar topology design is the s-SSHI [73, 74], which places the inductor in series with piezoelectric element. A switch is also connected with the inductor in series following the same control strategy as previous SSHI. It means that, most of the time, the circuit is in open circuit state, and the piezoelectric voltage is determined by the displacement. Once the inverse action occurs, the load is driven with the piezoelectric voltage.

The analytical and experimental results showed that both the p-SSHI and s-SSHI have similar power output level however with different matching resistor. It is interesting to point out that, the optimal resistor for s-SSHI is smaller than p-SSHI while standard technique is in the middle range (Figure 1-21). The high power transfer performance due to these advanced

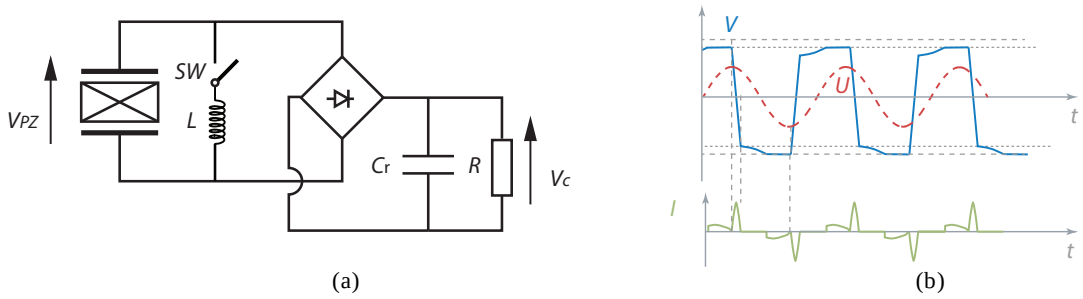

Figure 1-16. p-SSHI energy harvsting circuit

Cette thèse est accessible à l'adresse : http://theses.insa-lyon.fr/publication/2014ISAL0077/these.pdf
© [Y. Li], [2014], INSA de Lyon, tous droits réservés

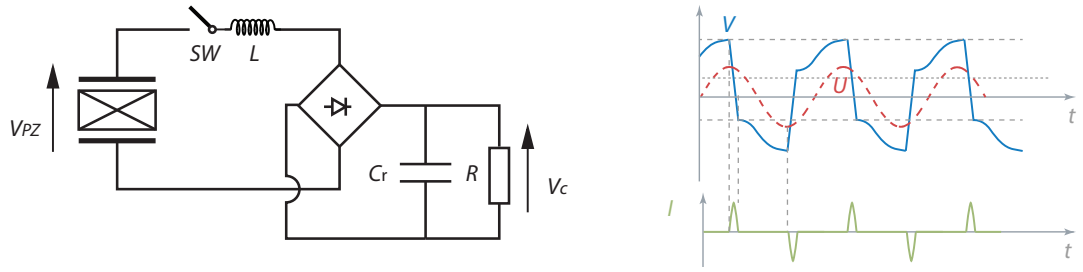

(a) (b)

Figure 1-17. s-SSHI energy harvesting circuit

circuits increase the power density of the whole harvester thus giving the opportunity to reduce the piezoelectric element volume and material cost. It is however important to notice that these adaptive techniques do require impedance matching to reach optimal power. It is noticeable that these techniques and their derivations are the only techniques allowing optimization of the energy harvesting in the case of low coupling and high damping harvesters, thus making them essential for direct harvesting configurations.

Shu *et al.* [75] compared s-SSHI circuit, p-SSHI circuit and Standard circuit (STD DC) in various operation frequency conditions. At middle coupling condition ($k^2Q_M=1$), the optimal resonance frequency for p-SSHI is around short-circuit frequency, the optimal resonance for s-SSHI is around at open-circuit frequency. However, with the same configuration, the standard AC circuit exhibits two maximums at short-circuit frequency and open-circuit frequency. It can be explained as follows. Both the p-SSHI and s-SSHI increase the efficiency of power. At high coupling condition, the inherent property of piezoelectric harvester is possessing two power peaks in frequency domain. For s-SSHI, the piezoelement is nearly always in open circuit state (Figure 1-17.b) thus resulting in optimal frequency around the open circuit frequency. Inversely for p-SSHI circuit, the piezoelement circuit is flowing to the load for a much longer time (Figure 1-16.b) thus reaching its maximum power around the short-circuit frequency.

In long-term operation, the harvester's property (i.e. the capacitance or the resonance frequency) may be changed resulting from variation of temperature or humidity, which leads to the degradation of the optimal impedance of frequency matching. A load-independent processing circuit such as SECE can avoid these problems. SECE (Figure 1-18) is the abbreviation of "Synchronous Electric Charge Extraction". It separates the extraction operation and transfer operation [76]. It uses a DC-DC converter topology to scavenge the mechanical energy via piezoelectric element, but with a particular duty cycle strategy. The MOSFET switch closes synchronously with the displacement of harvester. In addition, the switch closes at the maximum of displacement and opens again when the piezoelectric voltage vanishes and the inductor current is maximum (Figure 1-18.b). At this time, all the available energy is stored in the inductor. Once the switch opens, the diodes switches on to ensure inductor current continuity and therefore the energy stored in the inductor will be transferred to the load. In this

Cette thèse est accessible à l'adresse : http://theses.insa-lyon.fr/publication/2014ISAL0077/these.pdf
© [Y. Li], [2014], INSA de Lyon, tous droits réservés

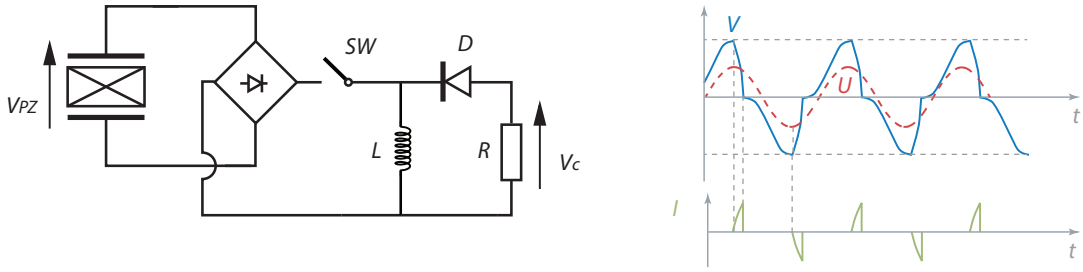

(a) (b)

Figure 1-18. SECE energy harvsting circuit

way, the load (any value) will received all the available energy generated by the mechanical vibration and accumulated on the piezoelement blocked capacitance during two switching sequences. In general, the harvested power harvested with SECE is 4 times larger than standard technique and is fully load independent. Considering the noise at low resistor condition and circuit inherent oscillation in high resistor, the experimental power output is load-independent exists in limited region.

The main problem of SECE is the switch on-time tuning for perfect voltage cancellation. This time may change with the piezoelectric capacitance (temperature, stress or stain amplitude). An optimized version of SECE, called OSECE (Figure 1-19), was proposed by Wu *et al.* [77]. The diode bridge is replaced by a flyback-transformer with two primary windings connected to the piezoelement with two opposite unidirectional switching cells triggered respectively on the maximum and minimum voltage. In this configuration, precise time tuning is no longer required. Moreover, for high load impedance during the primary energy transfer, a small amount of energy is restituted to the piezoelement resulting in higher voltage and consequently better energy extraction. OSECE can therefore be seen as a hybrid between SECE (for low load impedance) and SSHI (for high load impedance).

SSHI-like circuit can reach a 900% power efficiency improvement but with the need of impedance matching; SECE-like circuit is not sensitive to the load but lack the huge power improvement. Thus DSSH "Double Synchronized Switch Harvesting" was proposed [78] to combine the advantages of both adaptive circuits. In DSSH, the energy is transferred to the first storage capacitor C_{int} as series-SSHI does. Then the second switch *SW2* is closed to transfer the

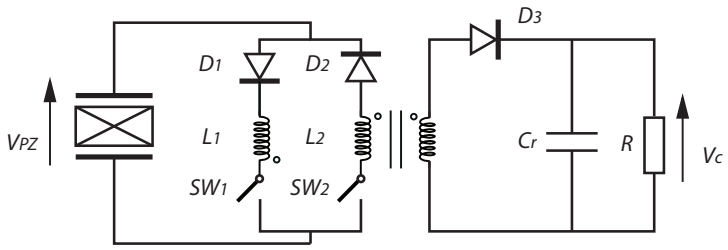

Figure 1-19. The OSECE energy harvesting circuit

Cette thèse est accessible à l'adresse : http://theses.insa-lyon.fr/publication/2014ISAL0077/these.pdf
© [Y. Li], [2014], INSA de Lyon, tous droits réservés

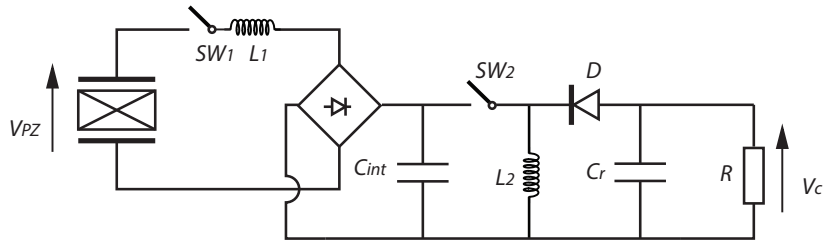

Figure 1-20. DSSH energy harvesting circuit

energy from the intermediate capacitor C_{int} to the inductance load. This second process is similar to the SECE stage. In this whole process, the load is totally independent from the energy extraction by piezoelectric element. The intermediate capacitor C_{int} is used as a temporary energy storage. Therefore, DSSH can improve the power output level while ensuring load-independent property. However, due to a more complex configuration, the energy loss is larger than for s-SSHI.

Table 1-3 summarizes the performances of these techniques in terms of harvested power, advantages and drawbacks [74, 78, 79]. Figure 1-21 illustrates the power versus the load impedance for a given piezoelectric energy harvester excited in forced displacement mode. Both SSHI techniques have significant power harvesting ability. To harvest a given level power, p-SSHI and s-SSHI have a wider load range compared with STD technique. The SECE and DSSH techniques exhibit better harvesting ability with a load-independent behaviour. The harvesting ability of DSSH is determined by $\gamma_{C,}$ the intermediate inversion factor mainly determined by C_{int} and L_2. The OSECE preserves the wide bandwidth property of SECE, but with load sensitive SSHI performance for high load impedance operation. All of these non-linear circuit topologies show improvement harvested power compared to STD technique. The gain is around 800% percent for p-SSHI, 700%for s-SSHI, 600% for DSSH and 400% for SECE. Many problems arise when deploying these non-linear energy harvesting topologies. They rely on signal detection, switch operation, inductors, complex circuitry, and optimal load. Even the load-independent DSSH and SECE have optimal load region due to the oscillation and losses in circuitry. On one hand, the tradeoff between feasibility and high harvested power should be considered. On the other hand, it is worthy to find an energy harvesting circuit with simple topology and strong power harvesting capability.

Cette thèse est accessible à l'adresse : http://theses.insa-lyon.fr/publication/2014ISAL0077/these.pdf
© [Y. Li], [2014], INSA de Lyon, tous droits réservés

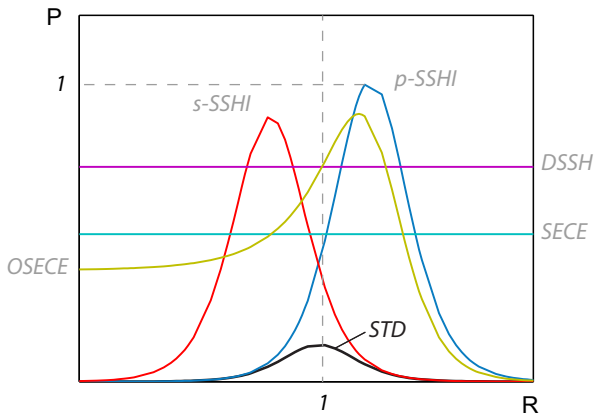

Figure 1-21. Comparison of harveted power(f_{oc}=56.72Hz, α=0.0045 N/V, K^E=10272Nm^{-1},M=0.0818g, C_0=170nF, k^2=0.0113, Q_M=54. Q_I=5.6. γ_c=0.5,γ_0=0.74)

Table 1-3. Comparison of the principle energy harvesting circuits (the various constants are defined in the text)

	Harvested Power (with constant displacement)	Advantage	Drawback
STD	$P=\dfrac{4R\alpha^2}{(2RC_0\omega+\pi)^2}\omega^2U_M^2$	simple	load matching, power output is low
p-SSHI	$P=\dfrac{4R\alpha^2\omega^2}{\left(RC_0\omega\left(1-e^{-\pi/2Q_i}\right)+\pi\right)^2}U_M^2$	high power output switch strategy	load matching, inductor, switch device
s-SSHI	$P=\dfrac{4R\alpha^2\omega^2\left(1+e^{-\pi/2Q_i}\right)^2}{\left(2RC_0\omega\left(1+e^{-\pi/2Q_i}\right)+\pi\left(1-e^{-\pi/2Q_i}\right)\right)^2}U_M^2$	high power output switch strategy	load matching, inductor, switch device
SECE	$P=2\dfrac{\alpha^2\omega}{\pi C_0}U_M^2$	load independents	inductor, switch device, switch strategy
DSSH	$P=\gamma_C\dfrac{(1+\gamma_0)^2}{1-\gamma_0}\dfrac{\alpha^2}{C_0}\dfrac{\omega}{4\pi}U_M^2$	load independent	complex circuitry, complex switch strategy
OSECE	$\begin{cases} P=\dfrac{2\alpha^2\omega}{\pi C_0}\dfrac{\sin^2(\omega_I t_m)e^{-\omega_I t_m/Q_I}}{\left(1+\cos(\omega_I t_m)e^{-\omega_I t_m/2Q_I}\right)^2}U_M^2, \\ \omega_I t_m=\arctan\left(-m\sqrt{\dfrac{2\pi}{RC_0\omega}}\right)+\pi \end{cases}$	wide bandwidth switch strategy	3-port transformer, complex circuitry

Cette thèse est accessible à l'adresse : http://theses.insa-lyon.fr/publication/2014ISAL0077/these.pdf
© [Y. Li], [2014], INSA de Lyon, tous droits réservés

1.3.4 Wide bandwidth consideration

As a resonating device, the piezoelectric energy harvesting device heavily relies upon its resonance frequency. For instance, considering the mechanical quality factor Q_M measuring the sharpness of resonance, a small excitation frequency shift will lead to a dramatically drop of the power output of a high-Q_M harvester. There are several solutions to widen the harvester working frequency range, such as bi-stable harvester, harvester array and active or adaptive frequency-tuning method.

Through a snap-through action, bistable harvester transition from one stable state to the other, appear to be effective across a broad-frequency bandwidth [80]. Such non-linear harvesting device(Figure 1-22) is believed to have power gain between 400% to 600% compared to the standard oscillators [81]. Liu *et al.* [82] proposed a buckled type bistable harvester (Figure 1-23). They found that this device is a high power density harvester (0.33 mW cm^{-3}) which generated 16 mW for a 0.3 g chirp excitation. Then they combine such bistable harvester with non-linear circuit OSECE [83]. The theoretical and experimental investigations showed that, at high k^2 condition, the OSECE circuit induced more damping on such a bistable harvester than it improved energy extraction thus resulting in weaker harvesting efficiency.

Harvester array consists of multiple converters with different frequency responses due to different dimensions and mass. Ferrari *et al.* [84] designed a multi frequency converter array (Figure 1-24) in order to increase the bandwidth of the harvesting device. It contains multiple resonators with different frequency responses, which are connected in parallel. Xue *et al.* [85] proposed a wide bandwidth harvester with a piezoelectric bimorph array. In this case, the bandwidth can be tailored by choosing both the array distribution and the connection topology (Figure 1-25).

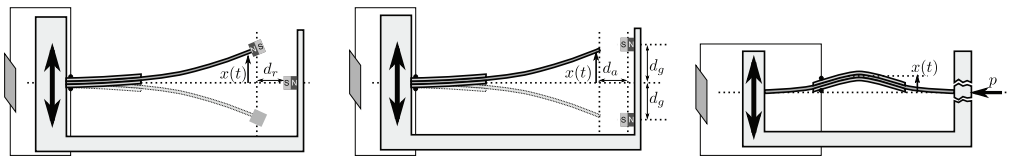

(a) (b) (c)

Figure 1-22.Three different bistable harvester.(a) Magnetic repulsion type (b) Magnetic attraction type(c) Buckled beam type [80]

Cette thèse est accessible à l'adresse : http://theses.insa-lyon.fr/publication/2014ISAL0077/these.pdf
© [Y. Li], [2014], INSA de Lyon, tous droits réservés

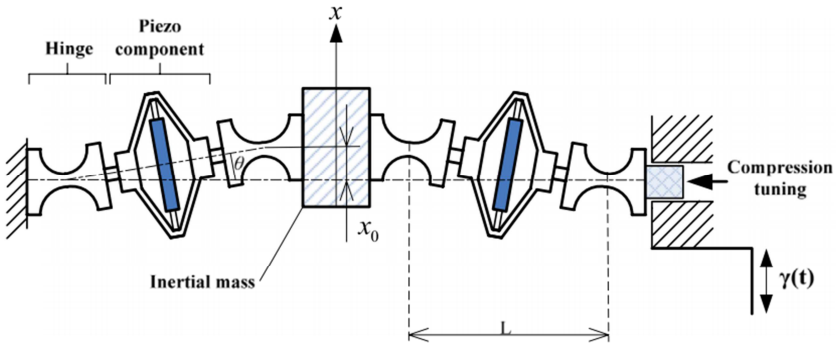

Figure 1-23. A buckled-spring-mass bistable piezoeelctric enegy harvester [82]

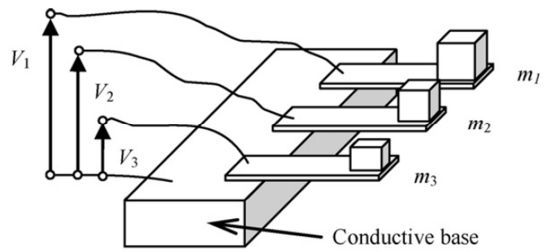

Figure 1-24. The structure of piezoelectric energy harvester array [84]

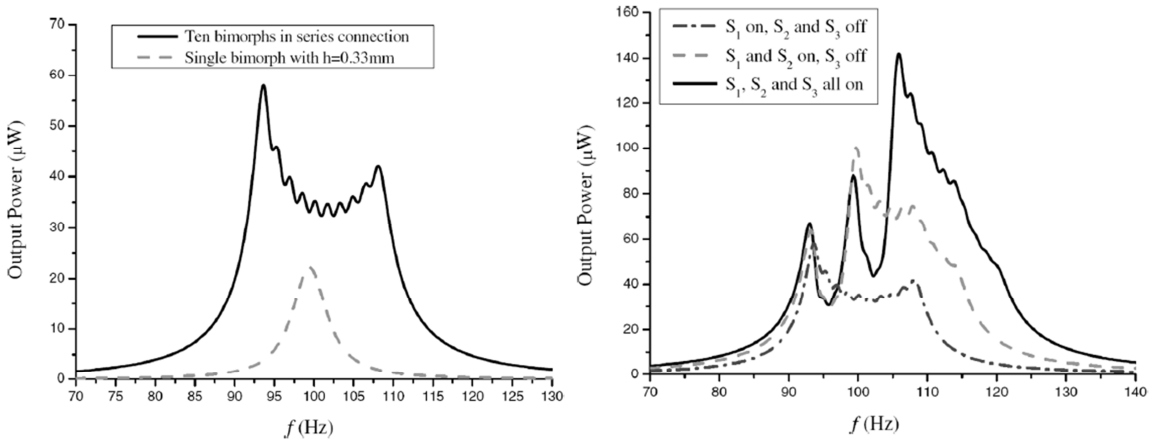

(a) (b)

Figure 1-25. Power response of harvseter array with different connection topology (a) parallel connection (b) mixed connection [85]

Using equivalent impedance approach, Lien et al. [86] analyzed another harvester array for broadband energy harvesting which contains multi piezoelectric patches but one set of processing circuit. The processing circuits were standard technique, p-SSHI technique and s-SSHI technique. They claimed that the p-SSHI technique exhibited more significant bandwidth

Cette thèse est accessible à l'adresse : http://theses.insa-lyon.fr/publication/2014ISAL0077/these.pdf
© [Y. Li], [2014], INSA de Lyon, tous droits réservés

improvement than the other two circuits. The piezovoltage is complex when the harvester is excited in wide bandwidth or comprises multi converters. In fact, the losses introduced by switch action should be considered when non-linear energy harvesting technique (i.e. SSHI) is used. Lallart *et al.* [87] proposed a closed-form model for piezoelectric harvester with a switching interface that closes periodically at any chosen frequency. They claimed that for a random force input, the optimal switch frequency should be slightly less than twice the first resonance of the harvester. Consequently, Wu *et al.* [88] investigated the harvester's performance with SSHI type switching interface. Their work provided a stochastic modeling method in the frequency domain. Their approach can be used for wide bandwidth and random excitation analysis for SSHI type harvesting circuit.

Adaptive frequency-tuning method can also be used for wide bandwidth. The basic principle of electrical tuning method referred here is the impedance matching method. It is not a new idea to widen the working range. When the piezoelectric was used to damp vibration, the shunt ***LC*** circuit was deployed thanks to the capacitive property of a piezoelectric element [89, 90]. Since damping results from energy extraction and dissipation, the similar shunt circuit can be used for harvesting. Wu *et al.* [91] proposed a ***RC*** shunt circuit to tune the harvester. The optimal capacitor load was chosen by a low-power microcontroller from a capacitor load array. With this self-tuning technique, the output power increase reaches almost 30% under random excitation. Renno *et al.* [92] investigated such shunt circuit and claimed that wide bandwidth piezoelectric energy harvesting power optimization was possible. Similar work can be found in Ref [93].

1.4 Outline of the thesis

The widely distributed mechanical movements, especially the vibrations and the impacts, give the piezoelectric energy harvesting a promising future. Power optimization and piezoelectric generator have to be considered simultaneously when designing a piezoelectric energy harvester. On the electrical side, the optimization could be impedance matching or power conditioning circuit topology. The motivation of this thesis is therefore to cover the modeling of the piezoelement and circuit topology consideration.

Chapter 2 focuses on the electromechanical modeling method for piezoelectric energy harvesting and its optimization. An equivalent circuit derived from Mason Equivalent Circuit is proposed. The piezoelectric energy harvesting optimization is considered following this equivalent circuit. The guideline for optimization is proposed for resistive and complex loads cases emphasizing the importance of the electrical side of a piezoelectric device such as a piezoelectric generator.

Chapter 3 focuses on the piezoelectric energy harvesting network. The simulation of a piezoelectric energy harvesting network operating in direct mode is proposed. Different circuit topologies are considered, such as multi-piezoelectric patches in series, in parallel, with and

Cette thèse est accessible à l'adresse : http://theses.insa-lyon.fr/publication/2014ISAL0077/these.pdf
© [Y. Li], [2014], INSA de Lyon, tous droits réservés

without SSHI technique. The solutions give the guideline for choosing a topology in direct energy harvesting. Ground problem is considered, in the case of a fully conductive host structure.

Chapter 4 presents a simple and reliable novel conditioning circuit exhibiting load-independent power output. This technique, named as Synchronous Series Switch, places a switch in series between alternative current signal source and load. The switch will only close for a short time at each extremum of source voltage.

Chapter 5 is the conclusion, and gives the roadmap of future work.

Cette thèse est accessible à l'adresse : http://theses.insa-lyon.fr/publication/2014ISAL0077/these.pdf
© [Y. Li], [2014], INSA de Lyon, tous droits réservés

C H A P T E R 2 The power optimization by impedance matching

2.1 Introduction

2.2 Piezoelectric harvester equivalent circuit modelling

2.2.1 Derivation of the generator equivalent circuit using Mason approach

2.2.2 Piezoelectric generator equivalent circuit

2.3 Optimal impedance matching

2.3.1 Impedance matching theory

2.3.2 Case study: purely resistive load

(A) Power optimization

(B) Discussion on the viscous factor

2.3.3 Case study: complex load

2.3.4 Comparison with other power optimization approach

2.4 Experimental validation

2.4.1 Set-up

2.4.2 Equivalent circuit identification by LCR meter

2.4.3 Measurement process

(A) Purely resistance load

(B) Optimal impedance matching with a parallel L-R load

2.4.4 Results and discussion

(A) Purely resistance load

(B) Optimal impedance matching with a parallel L-R load

(C) High sensitivity of the impedance matching process to the passive component dispersion

2.5 Conclusion and future work

2.1 Introduction

The impedance of the device is a function of the frequency and without precaution the output power is strongly varying with the frequency. In fact the impedance of the generator is either capacitive or inductive, depending on the frequency relatively to the harvesting transducer

Cette thèse est accessible à l'adresse : http://theses.insa-lyon.fr/publication/2014ISAL0077/these.pdf
© [Y. Li], [2014], INSA de Lyon, tous droits réservés

resonance frequency. For a pure resistance load case, the classical solution is tuning the impedance at the working frequency to obtain the maximum output power. In this chapter, a global equivalent circuit method is proposed. It is used to find the optimal load for piezoelectric energy harvester for various excitation frequencies. This chapter is organized in three different parts. In Section 2.2, the equivalent electrical generator circuit of a seismic piezoelectric energy harvester is introduced. In Section 2.3, the optimal load and optimal power are then derived and the results are compared to the results obtained and characterized according to the proposed equivalent circuit. Matched load and optimal output power results are given, showing that at constant acceleration, the output power can be constant with the excitation frequency as long as the matched load is practically feasible. Section 2.4 is an experimental validation of the proposed approach.

2.2 Piezoelectric harvester equivalent circuit modelling

The piezoelectric harvester considered here is a seismic resonant device. It is an electromechanical transducer converting mechanical energy into electrical energy. In most of the cases, for such a transducer working around resonance, the vibration wavelength is greater than the dimensions of the system. Therefore a lumped-parameter modelling method is suitable for system behavior analysis [53]. As usual, and for sake of simplicity, the analysis described below is based on single degree of freedom (SDOF) mechanical system. For a lumped parameter SDOF system with resonant property, an equivalent circuit modeling (ECM) is a powerful analysis approach, such as Mason equivalent circuit [48] and KLM (*Krimholtz, Leedom, & Matthaei*) circuit. Here, the MEC (Mason equivalent circuit) is used to model the piezoelectric harvester. However, readers can find the KLM method and its comparison with MEC in [54, 55].

Mason equivalent circuit is fundamentally an electric circuit and is therefore very

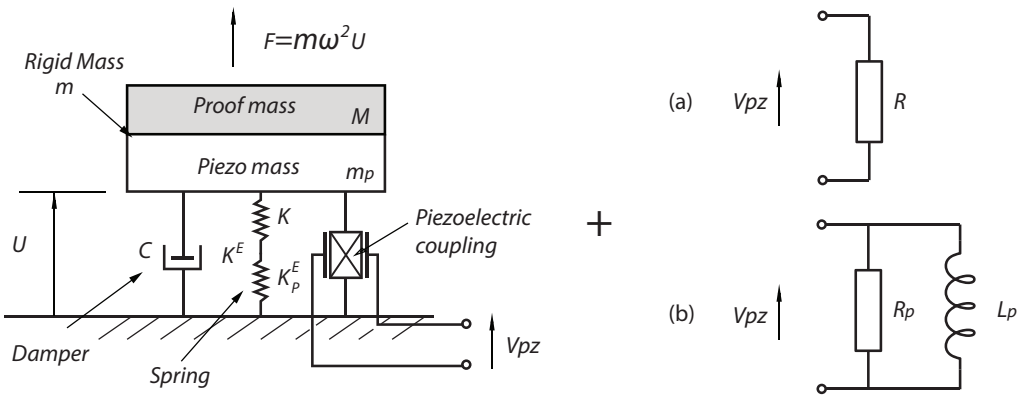

Figure 2-1. Mass-spring-damper model of a seismic piezoelectric generator with (a)purely resistive load or (b)inductive load

Cette thèse est accessible à l'adresse : http://theses.insa-lyon.fr/publication/2014ISAL0077/these.pdf
© [Y. Li], [2014], INSA de Lyon, tous droits réservés

Table 2-1. Numerical data for seismic piezogenerator [92]

M	0.01kg	
t_p	0.01 m	
A_p	0.0001 m²	
m_p	0.0075kg	
Permittivityε_{33}^S	1.137×10^{-8} Fm^{-1}	
Resonance frequencyω_n	2.1520×10^5 rad/s*	*not given in reference[92]

practical to derive an electric equivalent circuit of any piezoelectric generator. The type or generator considered here is a seismic generator, and for sake of comparison with an alternative load optimization theory proposed by Renno *et al.* [92], the device considered here is perfectly analogous to the seismic device described in [92]. The numerical data of this harvester is listed in Table 2-1. This device consists of a ceramic disk (cross-section area A_p, thickness t_p and mass m_p) mounted between a rigid holder, vibrating at constant acceleration, and a proof mass (seismic mass M). It can be modeled as the resonator shown on Figure 2-1.

The whole harvester is usually modeled as a "Mass-Spring-Damper" characterized by a spring K related to the stiffness of the whole device, a damper with a viscous coefficient C and a rigid mass m taking into account the proof mass M and the piezoelement one m_p. The input impedances of the load considered here are (a) purely resistive type and (b) complex type (i.e. resistor paralleled with inductor). Assuming a proof mass with high stiffness, the global stiffness K^E is approximated by the piezoelement stiffness K_P^E. The other parameters of this lumped model are usually defined as,

$$m = M + \frac{1}{2}m_p, \qquad C = m\omega_n \tan\delta, \qquad \omega_n = \sqrt{\frac{K^E}{m}}. \tag{2.1}$$

where, ω_n is the short circuit resonance angular frequency, $tan\delta$ is the system loss angle. For simplification, viscous loss C is assumed as constant within the considered frequency band.

2.2.1 Derivation of the generator equivalent circuit using Mason approach

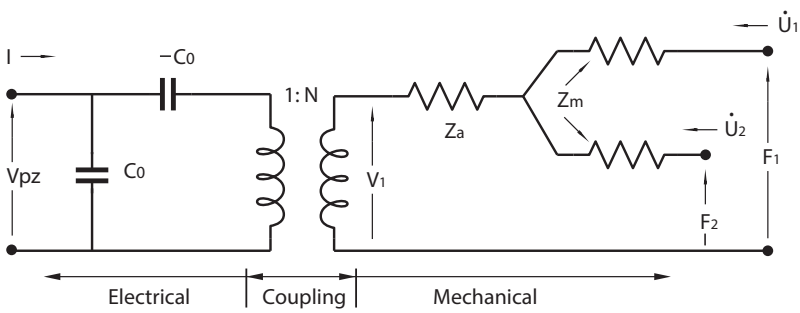

Figure 2-2. Mason Equivalent Circuit for the piezoelectric disk

Cette thèse est accessible à l'adresse : http://theses.insa-lyon.fr/publication/2014ISAL0077/these.pdf
© [Y. Li], [2014], INSA de Lyon, tous droits réservés

With linear wave propagation assumption, the piezoelectric disk of the harvester device can be represented by a three port equivalent circuit (Figure 2-2) proposed by Mason [48]. C_0 is the blocked capacitance (equivalent capacitance of piezoelectric element), N represents the electromechanical coupling, and the impedances (Z_a, Z_m) stand for the mechanical properties. The two ports in right portion of Mason equivalent circuit denote the mechanical input. $\dot{U}_1$ and F_1 (respectively $\dot{U}_2$ and F_2) represent the vibration speed and the total mechanical force acting on the upper face (respectively the lower face).

Assuming it works in *thickness* mode, the various parameters are defined as:

$$Z_a = \frac{Z_0}{j\sin\frac{\omega l}{v_b^D}}, \qquad Z_m = jZ_0\tan\frac{\omega l}{2v_b^D}, \qquad C_0 = \frac{wt}{l}\varepsilon_{33}^T\left(1-k_{33}^2\right),$$
$$v_b^D = \left(\frac{c_{33}^D}{\rho}\right)^{\frac{1}{2}}, \qquad Z_0 = \rho w t v_t^D, \qquad N = \frac{wt}{l}\frac{g_{33}}{s_{33}^E\beta_{33}^T} = \frac{wt}{l}\frac{d_{33}}{s_{33}^E} = \frac{wt}{l}\left(\frac{\varepsilon_{33}^T}{s_{33}^E}\right)^{1/2} k_{33}. \tag{2.2}$$

On the mechanical side (Figure 2-3), considering F_1 as the proof mass M inertia force and $\dot{U}_1$ its vibrating speed, the mass can therefore be represented by an inductance M attached to the upper face terminal. As the lower face speed is forced by the vibration speed of the base, a current generator $\dot{U}$ is attached to the lower face terminal as shown on Figure 2-3.a. According to the relationships given by Equation (2.2), the mechanical side impedances of Figure 2-3.a are defined by [see Appendix A for details]:

$$Z_a = \tan\delta_p\left[\frac{\omega(1-k_{33}^2)}{\omega_n^2 m}\right]^{-1} + \left[j\omega\frac{(1-k_{33}^2)}{\omega_n^2 m}\right]^{-1}$$
$$Z_m = j\frac{\rho A_p t_p}{2}\omega = j\frac{m_p}{2}\omega \tag{2.3}$$

With $tan\delta_p$ the mechanical loss angle of the piezoelectric material. Now, using Kirchhoff's laws, the voltage on the secondary of the electromechanical transformer (Figure 2-3.a) is:

$$V_1 = R_a i_a + \frac{1}{j\omega C_a} i_a + j\omega L_b i_a + V_0 \tag{2.4}$$

with,

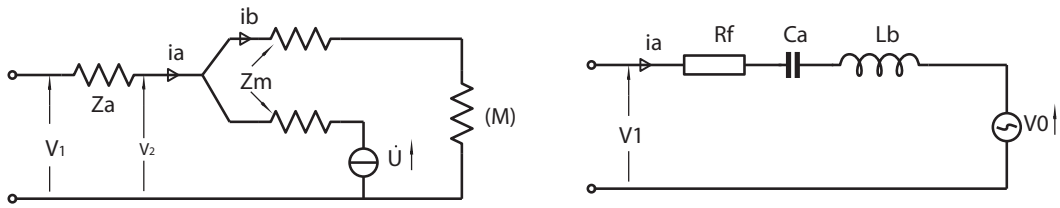

(a) (b)

Figure 2-3. Equivalent circuit on the mechanical side of the electromechanical transformer (a)Initial Mason circuit - (b) Simplified electrical equivalent circuit

Cette thèse est accessible à l'adresse : http://theses.insa-lyon.fr/publication/2014ISAL0077/these.pdf
© [Y. Li], [2014], INSA de Lyon, tous droits réservés

$$R_a = \frac{\tan\delta_p}{\omega}\frac{\omega_n{}^2 m}{\left(1-k_{33}^2\right)}, \quad C_a = \frac{\left(1-k_{33}^2\right)}{\omega_n{}^2 m},$$
$$L_b = \frac{m_p}{2} + M, \qquad V_0 = \omega^2 L_b U. \tag{2.5}$$

The equivalent generator voltage V_0 is directly related to the vibrating base motion RMS value U, in other words, it represents the external excitation force RMS value F. This equation can therefore be represented by the simplified equivalent circuit represented on Figure 2-3.b.

Note that these expressions are slightly different from the usual definitions. Indeed, in order to be consistent with the incomplete parameter set and the assumptions given in reference [92], lateral stresses and strains are not considered and only the longitudinal (poling axis 3) state terms are considered here. With these assumptions corresponding to 33 mode used in Ref [92], the following relationships can be established, with a good consistency with the previously mentioned expressions.

$$c_{33}^E = c_{33}^D - \frac{e_{33}^2}{\varepsilon_{33}^S}, \qquad \varepsilon_{33}^T = \varepsilon_{33}^S + \frac{e_{33}^2}{c_{33}^E}, \qquad k_{33}^2 = \frac{e_{33}^2}{\varepsilon_{33}^T c_{33}^E} = \frac{d_{33}^2}{\varepsilon_{33}^T s_{33}^E}, \qquad K_p^E = \frac{A_p}{t_p} c_{33}^E. \tag{2.6}$$

In Mason equivalent circuit, only the piezoelectric element part is considered. To model the whole piezoelectric harvester, the harvester mechanical loss should also be included in the analysis. Therefore an additional resistance R_f , which is much larger than R_a , representing the mechanical loss is added in the circuit. This resistance is related to the harvester equivalent mass m, resonance frequency ω_n and global damping coefficient ζ by Equation (2.7). R_f is then defined as.

$$R_f = m\omega_n \tan\delta = 2m\omega_n\zeta \tag{2.7}$$

In this way, the final expression of the output voltage of mechanical side V_1 becomes:

$$V_1 = R_f i_a + \frac{1}{j\omega C_a} i_a + j\omega L_b i_a + V_0 \tag{2.8}$$

It should be pointed out that, the current i_a is an important parameter which represent the strain velocity of the piezoelectric element. At the resonance it principally represent the velocity of

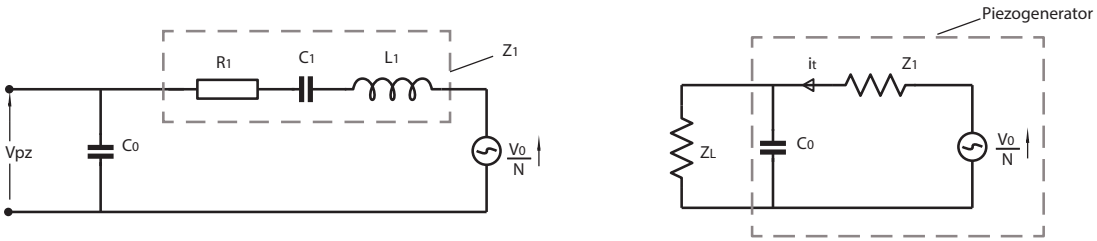

(a) (b)

Figure 2-4. Piezogenerator equivalent circuit: (a) open-circuit and (b) with load Z_L

Cette thèse est accessible à l'adresse : http://theses.insa-lyon.fr/publication/2014ISAL0077/these.pdf
© [Y. Li], [2014], INSA de Lyon, tous droits réservés

the upper face and of the proof mass.

Next, using the transformer turn ratio N, this equivalent mechanical circuit can be transposed to the primary of the transformer. Taking into account the negative capacitance C_0 on the electrical side, the original equivalent circuit (Figure 2-2) finally reduces to the circuits depicted on Figure 2-4 with [see Appendix A.3.2 for details]:

$$Z_1 = R_1 + j\left(\omega L_1 - \frac{1}{\omega C_1}\right) \tag{2.9}$$

$$R_1 = \frac{R_f}{N^2} \quad , \quad L_1 = \frac{L_b}{N^2} \quad , \quad C_1 = \frac{C_0 C_a N^2}{C_0 - C_a N^2} \tag{2.10}$$

$$C_0 = \frac{A_p \varepsilon_{33}^S}{t_p} \quad , \quad N = \omega_n \sqrt{\frac{k_{33}^2}{1-k_{33}^2}\frac{A_p m}{t_p}\varepsilon_{33}^S} \tag{2.11}$$

In order to be consistent with the notations used in reference [92], Equation (2.9) is expressed as follows:

$$Z_1 = \frac{1}{\omega_n C_0}\frac{1}{\Omega}\alpha + j\frac{1}{\omega_n C_0}\frac{1}{\Omega}\beta \tag{2.12}$$

Where,

$$\Omega = \frac{\omega}{\omega_n}, \qquad k_e{}^2 = \frac{k_{33}^2}{1-k_{33}^2}, \qquad \zeta = \frac{\tan\delta}{2}, \qquad \alpha = \Omega\frac{2\zeta}{k_e{}^2}, \qquad \beta = \frac{\Omega^2 - 1}{k_e{}^2}. \tag{2.13}$$

Ω is the normalized frequency to simplify the expression. $k_e{}^2$ is the alternative electromechanical coupling factor of this piezoelectric harvester, this coupling factor was explained in Chapter 1. ζ is the *damping ratio*, representing the system's viscous losses. We should notice that $2\zeta/k_e{}^2$ in α item is related to the global electromechanical coupling ability ($k_{33}^2 Q_M$) which will be discussed later. In addition, it is easy to find that, short circuit angular frequency ω_E corresponds to Ω=1, open circuit angular frequency ω_D corresponds to $\Omega=\sqrt{k_e^2+1}$.

2.2.2 Piezoelectric generator equivalent circuit

(a) (b)

Figure 2-5. Piezoelectric harvester equivalent circuit (Piezoelectric generator with load)using Norton (a) or Thevenin (b) representations

Cette thèse est accessible à l'adresse : http://theses.insa-lyon.fr/publication/2014ISAL0077/these.pdf
© [Y. Li], [2014], INSA de Lyon, tous droits réservés

The energy conversion portion of a piezoelectric energy harvester is the piezoelectric generator. Taking into account the blocked capacitance C_0, this equivalent circuit (Figure 2-4) can also be represented using Norton/Thevenin notations as a current source I_s in parallel with the impedance Z_G or by a voltage source V_S in series with the impedance Z_G. They are illustrated in Figure 2-5, and the corresponding components are given by:

$$V_S = \frac{V_0}{N}\frac{\frac{1}{jC_0\omega}}{Z_1 + \frac{1}{jC_0\omega}} = \frac{V_0}{N}\frac{1}{1+jC_0\omega Z_1} = \frac{V_0}{N}\frac{1-\beta-j\alpha}{1+A} \tag{2.14}$$

$$I_S = \frac{V_0}{N}\frac{1}{Z_1} \tag{2.15}$$

$$Z_G = Z_1 // C_0 = \frac{1}{C_0\omega_n}\frac{1}{\Omega}\left(\frac{\alpha}{1+A} - j\frac{A+\beta}{1+A}\right) \quad with \quad A = \alpha^2 + \beta^2 - 2\beta \tag{2.16}$$

In this way, the sophisticated Mason equation circuit of a piezoelectric generator (Figure 2-2) is transformed into a lightweight circuit which only contains one energy source (voltage source/ current source) with its impedance. Both the mechanical and piezoelectric characters are considered in this analytical model. The piezoelectric generator with load is shown in Figure 2-5 for different applications. All the parameters of this lightweight circuit are derived from Mason equivalent circuit.

Using this circuit, it is possible to analysis the piezoelectric generator's impedance, which is mainly determined by piezoelectric element in this system. A clear view of the piezoelectric generator inherent property will help us to understand the generator's behavior and find the proper way to optimize the power output. The admittance behavior of this equivalent circuit is shown as a function of normalized frequency in Figure 2-6. The amplitude and phase of admittance of piezoelectric generator is plotted against normalized frequency with various viscous losses in Figure 2-7. The amplitude of admittance increases with the normalized frequency and turns direction around the short circuit frequency. Then a local minimum is reached when the normalized frequency is around open circuit frequency ($\Omega = \sqrt{k_e^2+1} = 1.16$, $k_e = 0.6$). The amplitude is higher at low losses condition (i.e. $\zeta = 0.02$). Figure 2-7.b demonstrates that the piezoelectric generator is fully capacitive as long as the viscous losses are large enough (i.e. $\zeta = 1$). For low losses case, piezoelectric generator is inductive between short circuit frequency and open circuit frequency. In fact, this watershed is determined not only by the viscous loss ζ but also by the electromechanical coupling coefficient k_e^2, which will be discussed later. But the results can be listed here in advance:

The piezoelectric generator is fully capacitive when

$$\zeta > \frac{1}{2}\left(\sqrt{1+k_e^2} - 1\right)$$

Cette thèse est accessible à l'adresse : http://theses.insa-lyon.fr/publication/2014ISAL0077/these.pdf
© [Y. Li], [2014], INSA de Lyon, tous droits réservés

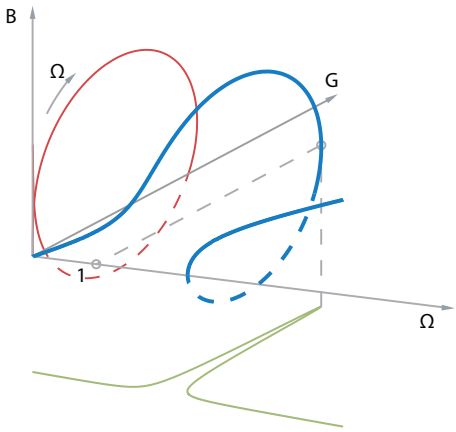

Figure 2-6. Admittance behaviour of the piezoelectric generator as a function of normalized frequency (ζ=0.04, k_e=0.6).

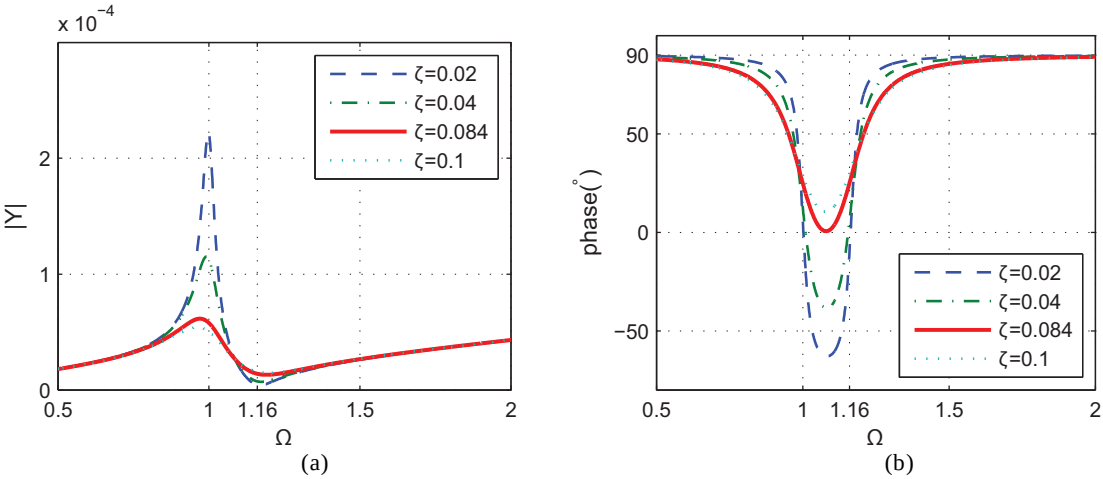

Figure 2-7. The amplitdue and phase of the impedance of piezoelectric generator(k_e=0.6)

When the piezoelectric generator is connected with the load, the voltage V_L over load and current I_L through load can be easily obtained for any load impedance Z_L and for any equivalent circuit from Figure 2-5:

$$V_L = I_S \frac{1}{Z_L^{-1} + Z_T^{-1}} \tag{2.17}$$

$$I_L = V_S \frac{1}{Z_T + Z_L} \tag{2.18}$$

And finally, the power dissipated in the load is obtained easily by using the power definition in Equation (2.19),

$$P = \mathrm{Re}(V_L I_L^*) \tag{2.19}$$

Cette thèse est accessible à l'adresse : http://theses.insa-lyon.fr/publication/2014ISAL0077/these.pdf
© [Y. Li], [2014], INSA de Lyon, tous droits réservés

Since current i_a in mechanical side represents the piezoelectric load strain velocity (i.e. the velocity of proof mass) as we mentioned in Section 2.2.1, the displacement X of the proof mass can be obtained using *Fourier* notation for harmonic motion:

$$X = \frac{i_a}{j\omega} = \frac{1}{j\omega_n \Omega} \frac{1}{N} (I_L + j\omega_n \Omega C_0 V_L) \tag{2.20}$$

2.3 Optimal impedance matching

A piezoelectric energy harvester is composed of a piezoelectric generator and an equivalent load. The task here is *how to transfer the maximal power from piezoelectric side to load side*. As a lightweight circuit (Figure 2-5) has already been derived from Mason equivalent circuit, we can find the optimal load and harvested power immediately and easily by impedance matching method. The obtained results will be compared with the results of the global optimizing technique based on the Karush-Kuhn-Tucker (KKT) approach that is described in [92]. As previously mentioned, and for sake of comparison, the proposed development is illustrated with the same piezoelectric generator data presented in [92].

2.3.1 Impedance matching theory

Firstly, revisit the so-called *impedance matching theory* as considered in the electrical engineering community. Considering the circuit represented in Figure 2-5.b, the voltage source is V_S, the corresponding impedance is $Z_G = R_G + jX_G$. To get the maximum power transfer from the voltage source V_S to load Z_L, two cases of the load impedance are discussed: (a) Impedance angle is constant and modulus is variable, and (b) Resistance and reactance are variable independently.

For the first case, we can set the load impedance as,

$$Z_L = |Z| \angle \varphi = |Z| \cos\varphi + j|Z| \sin\varphi \tag{2.21}$$

Then the power received by the load is expressed as,

$$P_L = \frac{V_G^2 |Z| \cos\varphi}{\left(R_G + |Z| \cos\varphi\right)^2 + j\left(X_G + |Z| \sin\varphi\right)^2} \tag{2.22}$$

Differentiate P_L with respect to |Z| and let the result equal to zero, to get the maximal power output. We obtain the optimal value for load,

$$|Z| = \sqrt{R_G^2 + X_G^2} \tag{2.23}$$

Notice that when the load is purely resistive R, the optimal load for maximal power is the modulus of impedance of generator, $R_{opt} = \sqrt{R_G^2 + X_G^2}$

Then for the second case, we can set the load impedance as,

$$Z_L = R_L + jX_L \tag{2.24}$$

The power on the load is expressed as,

Cette thèse est accessible à l'adresse : http://theses.insa-lyon.fr/publication/2014ISAL0077/these.pdf
© [Y. Li], [2014], INSA de Lyon, tous droits réservés

$$P_L = \frac{V_G^2}{\left(R_G + R_L\right)^2 + \left(X_G + X_L\right)^2} R_L \tag{2.25}$$

To get the maximum power transferring, we shall have the relation $X_L = -X_G$, then differentiate P_L with respect to R_L and let the result equal to zero to get the maximal power output. We obtain the optimal value for load,

$$R_L = R_G \tag{2.26}$$

Thus the optimal load is $Z_L = R_G - jX_G$, which is the conjugate of impedance of source Z_G. The corresponding optimal power is,

$$P_L = \frac{V_G^2}{4R_G} \tag{2.27}$$

It is obvious that the optimal power of load is only related to voltage source and generator's resistive impedance. They are represented by the excitation force and losses in the piezoelectric generator.

2.3.2 Case study: purely resistive load

In this case, the load type which can be represented by resistance is studied [see Appendix B.1 for detail]. In fact, for the real applications, the load is more sophisticated. However, it can be treated as a resistive load using converter circuits, such as step-down converter[94] or Buck-boost converter[66, 67].

(A) Power optimization

With the impedance matching theory, for a purely resistive load, the optimal load R_{opt} is the modulus of impedance of generator Z_G,

$$R_{opt} = \left|Z_G\right| = \frac{1}{\omega_n C_0} \frac{1}{\Omega} \sqrt{\frac{\alpha^2 + \beta^2}{1 + A}} \tag{2.28}$$

Considering the Norton equivalent circuit (Figure 2-5.a), the voltage over load V_L is obtained from Equation (2.17), then the expression of current through load I_L is obtained,

$$V_L = \frac{V_0}{N} \frac{1}{\left(\frac{\alpha}{B} + 1 - \beta\right) + j\left(\frac{\beta}{B} + \alpha\right)} \tag{2.29}$$

$$I_L = \frac{V_0}{N} \frac{1}{\left[\left(\frac{\alpha}{B} + 1 - \beta\right) + j\left(\frac{\beta}{B} + \alpha\right)\right]} \frac{C_0 \omega_n}{B \frac{1}{\Omega}}, \qquad \text{with,} \quad B = \sqrt{\frac{\alpha^2 + \beta^2}{1 + A}} \tag{2.30}$$

By substituting the Equations (2.29) (2.30) into (2.19), the power harvested by optimal load R_{opt} is then expressed as:

Cette thèse est accessible à l'adresse : http://theses.insa-lyon.fr/publication/2014ISAL0077/these.pdf
© [Y. Li], [2014], INSA de Lyon, tous droits réservés

$$P = V_L I_L^* = \left(\frac{V_0}{N}\right)^2 \frac{C_0 \omega_n}{\left[\left(\frac{\alpha}{B}+1-\beta\right)^2 + \left(\frac{\beta}{B}+\alpha\right)^2\right] B \frac{1}{\Omega}} \tag{2.31}$$

This optimal resistive load is plotted as a function of the relative frequency Ω and for various loss coefficients ζ on Figure 2-8. It is clearly seen that the natural damping of the harvester governs strongly the matched impedance. The optimal value is decreasing when the frequency is increasing toward short circuit angular frequency (Ω=1). Then optimal load reaches its maximum around open circuit angular frequency (Ω=1.16). For the optimal value of load, there is one order of magnitude difference between short circuit frequency spot and open circuit spot. This difference is shrinking with the increase of damping ratio ζ. If only consider the optimization of the harvester between short circuit frequency and open circuit frequency region, the window for choosing optimal resistive load is very large.

The corresponding output power P_{opt} and proof mass amplitude X_{opt} are plotted on Figure 2-9. Not the same as optimal load curve, at low loss condition, the power has two symmetric peaks value close to short circuit frequency and open circuit frequency, and one valley point (local minimum) between them (Figure 2-9.a). However, with the increasing of losses, the two peaks are decreasing, merging and vanishing while the valley point becomes the only existing peak point (i.e., ζ=0.084). Similar situation happens on proof mass displacement case. Two local maximum values appear around both short circuit frequency and open circuit frequency (Figure 2-9.b). The displacement around short circuit frequency is higher than open circuit frequency corresponding the minimum value in optimal load. It can be explained that, the damping effect around short circuit frequency is weak. The strong displacement around short/open circuit frequency demonstrated that it is not possible to maintain the maximal power transferring while minimizing the structure damping.

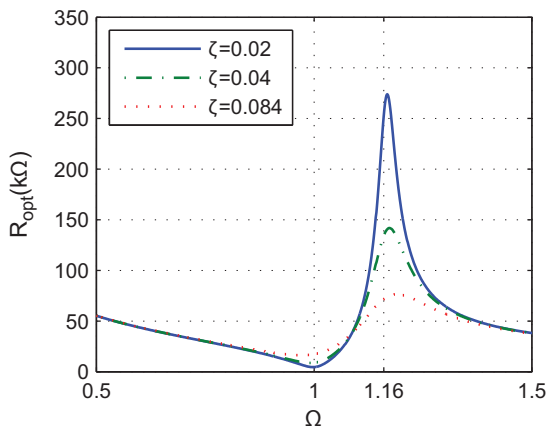

Figure 2-8. Optimal load R_{opt} for pure resistive load matching with various damping coefficients ζ (k_e=0.6).

Cette thèse est accessible à l'adresse : http://theses.insa-lyon.fr/publication/2014ISAL0077/these.pdf
© [Y. Li], [2014], INSA de Lyon, tous droits réservés

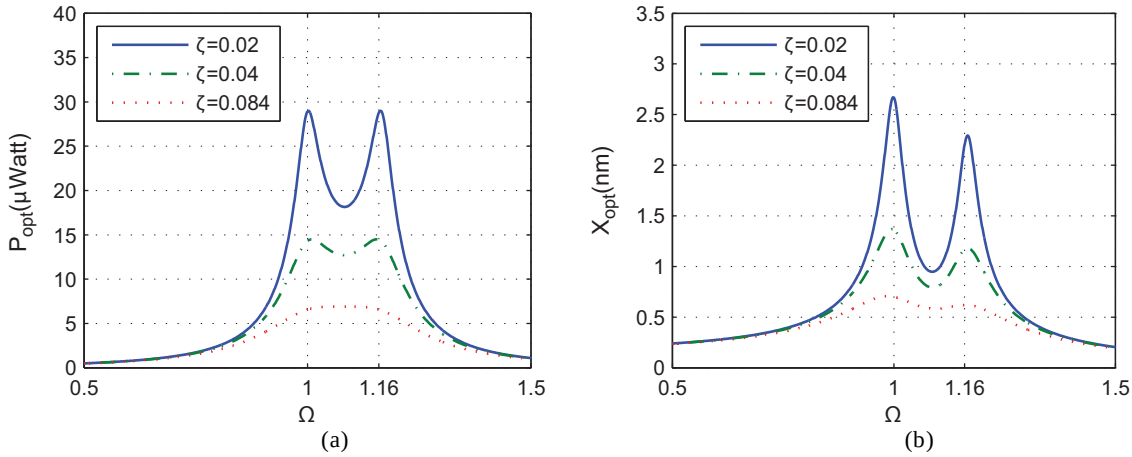

Figure 2-9. Optimal ouptut power (a) and corresponding proof mass motion amplitude (b) as a function of the normalized frequency obtained for the optimal load resistance depicted in Figure 2-8. Calculation is done for various loss coefficient ζ, for k_e=0.6 and for a 1g base acceleration.

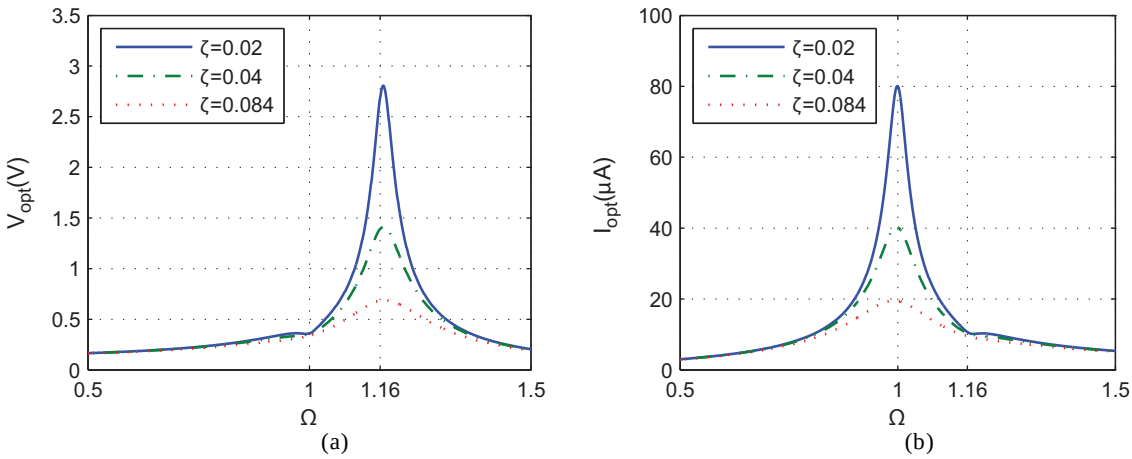

Figure 2-10. Circuit property with optimal load (a) voltage (b) current. k_e=0.6

The corresponding output voltage V_{opt} and current I_{opt} through optimal load are plotted in Figure 2-10. As the voltage increases with frequency, a tiny transient point appears around the short circuit frequency, and then the voltage reaches its maximum value around open circuit frequency (Figure 2-10.a). It is well known that, the voltage response is proportional to load value. Moreover, the voltage response is strong around resonance frequency. The competition between the two factors yields the tiny transient point around short circuit frequency. Similar with optimal load plot (Figure 2-8), the amplitude difference between the local minimum (transient point) and the maximum is about one order of magnitude. Naturally, the current curve is reversed (Figure 2-10.b). In piezoelectric energy harvesting application, the energy is

Cette thèse est accessible à l'adresse : http://theses.insa-lyon.fr/publication/2014ISAL0077/these.pdf
© [Y. Li], [2014], INSA de Lyon, tous droits réservés

stored in supercapacitor/chargeable batteries for use-on-demand, or used to drive the load directly. Charging operation prefers high current, while DC-DC converter prefers higher voltage. Taking both the voltage and current plot as reference, we can find the trade-off working frequency for different requirements.

In resistive load case, the amplitude differences (power, displacement, voltage, etc.) between low losses (i.e. δ=0.02) and high losses (i.e. δ=0.084) conditions are huge. It denotes that for a high losses, the power efficiency is quite low. Therefore, optimizing piezoelectric energy harvester with only a resistive load is not a wise choice. However, this basic optimization method provides a simple way to investigate harvester deeply, for instance, by considering the viscous losses as an important parameter.

(B) Discussion on the viscous factor

In the previous discussion, it is known that the natural damping of the harvester governs very strongly the optimal results. It is also clear that, the lower are the viscous losses the more critical are the short circuit frequency and open circuit frequency on the optimal result. In this section, we will give the critical value of frequency under different natural damping conditions and the power harvested limitation for resistive load case.

In the case of small natural damping ($\zeta \approx 0$), the α item is approaching zero, and then the power function versus the resistive load (2.31) is simplified to,

$$P = \left| \left(\frac{V_0}{N}\right)^2 \frac{C_0 \omega_n}{2(\beta - 1)\beta \frac{1}{\Omega}} \right| \tag{2.32}$$

Taking derivation of power P with respect to relative frequency Ω, three stationary points are found. These stationary points correspond to two identical maximum values and one local minimum value appearing on the power vs. relative frequency plot (Figure 2-9.a). These corresponding critical frequencies are defined as follows:

$$\begin{cases} \Omega_{\max 1} = 1 \\ \Omega_{\max 2} = \sqrt{k_e^2 + 1} \\ \Omega_{\min} = \frac{1}{\sqrt{6}} \sqrt{k_e^2 + 2 + \sqrt{k_e^4 + 16k_e^2 + 16}} \end{cases} \tag{2.33}$$

Notice that here Ω_{max1} and Ω_{max2} represent the short circuit and open circuit frequencies, respectively. This results show that, at low loss condition, maximum power transferring is operated by short circuit frequency and open circuit frequency which is observable from Figure 2-9. With the decreasing of loss, the maximal power output points are shifting toward short circuit frequency and open circuit frequency separately.

Cette thèse est accessible à l'adresse : http://theses.insa-lyon.fr/publication/2014ISAL0077/these.pdf
© [Y. Li], [2014], INSA de Lyon, tous droits réservés

Since these two frequencies are in such import place, let's substitute the critical frequency ($\Omega_{\max 1}=1$ or $\Omega_{\max 2}=\sqrt{k_e^2+1}$) from Equation (2.33) into the original power expression (2.31), then maximum power can be derived as:

$$P=\left(\frac{V_0}{N}\right)^2\frac{C_0\omega_n}{2\alpha\left(1+\sqrt{1+\alpha^2}\right)\frac{1}{\Omega}} \tag{2.34}$$

We can simplify the power expression to,

$$P=\frac{U_0{}^2}{4\zeta\omega_n m}\frac{1}{1+\sqrt{1+\left(\frac{2\zeta}{k_e^2}\right)^2}} \tag{2.35}$$

For very low damping coefficient and strong coupling condition, if it can be assumed that $\zeta \ll k_e^2$, the power expression (2.34) can be simplified to:

$$P_{opt}=(\omega^2 U)^2\frac{K_E}{8\zeta\omega_n^3}=\frac{F^2}{4C} \tag{2.36}$$

$$or \qquad P_{norm}=\frac{P_{opt}}{(\omega^2 U\ )^2}=\frac{K^E}{8\zeta\omega_n^3} \tag{2.37}$$

With F_m the total force acting on the piezoelement. Equation (2.36) shows that, for ideal condition ($\zeta\approx 0, \zeta \ll k_e^2$), the harvested power is only the function of the input force (or acceleration) and of the viscous loss C of the harvester.

In addition, we should notice that the item $2\zeta/k_e^2$ is the reciprocal of the usual term $k_e^2 Q_m$,

$$\frac{2\zeta}{k_e^2}=\frac{1}{Q_M}\frac{1}{k_e^2}=\left(k_e^2 Q_M\right)^{-1} \tag{2.38}$$

Whatever it is at low loss condition ($\zeta \approx 0$), or weak mechanical loss condition $\zeta \ll k_e^2$, they all can be represented by coupling coefficient condition $k_e^2 Q_M \gg 1$. In other words, the conclusion on maximum power output is also suitable for high $k_e^2 Q_M$ condition. That is,

> At strong coupling condition ($k_e^2 Q_M \gg 1$), the piezoelectric harvester approaches maximum power transfer at short circuit frequency and open circuit frequency.

However, in most of the applications, the damping coefficient is not negligible. In this case, from Equation (2.31), the three stationary points of the power versus frequency plot are obtained:

Cette thèse est accessible à l'adresse : http://theses.insa-lyon.fr/publication/2014ISAL0077/these.pdf
© [Y. Li], [2014], INSA de Lyon, tous droits réservés

$$\begin{cases} \Omega_1 = \frac{1}{\sqrt{2}}\sqrt{k_e^2 - 4\zeta^2 + 2 - \sqrt{\left(4\zeta^2 - k_e^2\right)^2 - 16\zeta^2}} \\ \Omega_2 = \frac{1}{\sqrt{2}}\sqrt{k_e^2 - 4\zeta^2 + 2 + \sqrt{\left(4\zeta^2 - k_e^2\right)^2 - 16\zeta^2}} \\ \Omega_3 = \frac{1}{\sqrt{6}}\sqrt{k_e^2 - 4\zeta^2 + 2 + \sqrt{\left(4\zeta^2 - k_e^2\right)^2 - 16\zeta^2 + 16(1+k_e^2)}} \end{cases} \tag{2.39}$$

Figure 2-9 has illustrated these 3 points and shows that the optimal output power is a decreasing function of the loss coefficient ζ. Considering the 3 normalized frequencies given in expression (2.39), it can be stated that when $\left(4\zeta^2 - k_e^2\right)^2 - 16\zeta^2 < 0$, the real roots for Ω_1 and Ω_2 don't exist anymore. In this case the optimal power has only one extremum remaining at the normalized frequency Ω_3, which means the previous local minimum becomes the only existent maximum value. Therefore, a critical damping ratio ζ_c arises.

When $\zeta < \zeta_c$, the maximum power output operated at Ω_3, when $\zeta > \zeta_c$, the maximum power transferring operated at Ω_1 or Ω_2 .The corresponding critical loss ζ_c is expressed as:

$$\zeta_c = \frac{1}{2}\left(\sqrt{1+k_e^2} - 1\right) \tag{2.40}$$

That is,

> With various excitation frequency, the harvester has two identical maximum power points when,
>
> $$\zeta > \frac{1}{2}\left(\sqrt{1+k_e^2} - 1\right)$$

It is interesting to note that these results are *simply* obtained from the expression (2.28) which is the trivial matched resistor for a generator such as defined by the equivalent circuit shown on Figure 2-4 or Figure 2-5. It is remarkable that these results are in perfect agreement with the optimal resistive load and harvested power derived from the KKT optimizing algorithm described in [67, 92], here obtained using a much more physical and comprehensive approach.

2.3.3 Case study: complex load

In practice, most of the loads of piezoelectric harvester aren't the resistive type. They always contain resistive and reactive components. As the previous purely resistive load optimization shows, perfect electrical impedance matching is *impossible* because the impedance of the electrical generator is complex (Figure 2-6, Figure 2-7). If the load was equal to a complex load, for instance, made with an inductive (or a capacitive) load in parallel (or in series) with a resistive load, perfect matching is achievable, and consequently optimal power can be extracted

Cette thèse est accessible à l'adresse : http://theses.insa-lyon.fr/publication/2014ISAL0077/these.pdf
© [Y. Li], [2014], INSA de Lyon, tous droits réservés

for any frequency. Only the significant results are listed here, for details, please refer to Appendix B.2.

Firstly, let's consider a general case. The optimal load impedance Z_{opt} is the conjugate of the source impedance Z_G, which is defined as:

$$Z_{opt} = Z_G^{\ *} = \frac{1}{C_0 \omega_n \Omega}\left(\frac{\alpha}{1+A} + j\frac{A+\beta}{1+A}\right) \tag{2.41}$$

The corresponding matched impedance spectrums are illustrated in Figure 2-11.

In view of the equivalent circuit shown in Figure 2-5.b and Equation(2.18), the load current and voltage can be derived. By substituting the results into Equation(2.19), the power harvested by optimal load Z_{opt} is obtained,

$$P_{opt} = (\omega^2 U\ )^2 \frac{K_E}{8\zeta\omega_n^3} = \frac{F^2}{4C} \tag{2.42}$$

The optimal power is only the function of excitation force F_m and viscous loss C. In other words, for a given structure, the power output is constant (in frequency domain) when optimal complex load is applied. It should be pointed out that applying complex load to match the piezoelectric harvester; we can transfer the same power as for the resistive load without any damping (see Equation(2.36)). This energy quantity is considered as the maximum limitation power of the piezoelectric energy harvester. In fact, this power limitation is observed or calculated by many researchers with different SDOF modeling method [61, 62, 67, 95, 96]. In other words, the equivalent circuit derived from Mason equivalent circuit to model a SDOF piezoelectric energy harvester appears as a very good approach. Here, it can be concluded that,

Maximum power transfer for a piezoelectric energy harvester is,

$$P_{opt} = (\omega^2 U\ )^2 \frac{K_E}{8\zeta\omega_n^3} = \frac{F^2}{4C}$$

Besides, it is interesting to notice that there is no link between harvested power and working frequency, which means the same constant power can be observed at any given frequency. Power harvested is plotted against normalized frequency in Figure 2-12.a. Unlike the as resistive load case, the short circuit frequency and open circuit frequency have no special meaning with this type of load. Similar situation happens in proof mass displacement plot as Figure 2-12.b shows. However, same as the purely resistive load case, the displacement is decreasing with the increment of working frequency.

Although the power is totally the same at any given working frequency, the complex load may still need different operation conditions. The corresponding output voltage V_{opt} and current I_{opt} through optimal load Z_{opt} are plotted on Figure 2-13, which can be referred as the load design guide. Voltage has the minimum value around short circuit frequency while current

Cette thèse est accessible à l'adresse : http://theses.insa-lyon.fr/publication/2014ISAL0077/these.pdf
© [Y. Li], [2014], INSA de Lyon, tous droits réservés

has the minimum value around open circuit frequency. For instance, if the harvester is used to charge supercapacitor or battery, the working frequency should avoid open circuit frequency.

Next, the normal cases are considered. Such complex load can be represented by inductor and resistor in series or in parallel combination. In this configuration, the resistor R denotes the energy consuming part (harvesting energy), and inductor L denotes the additional circuit component to match the generator physical property.

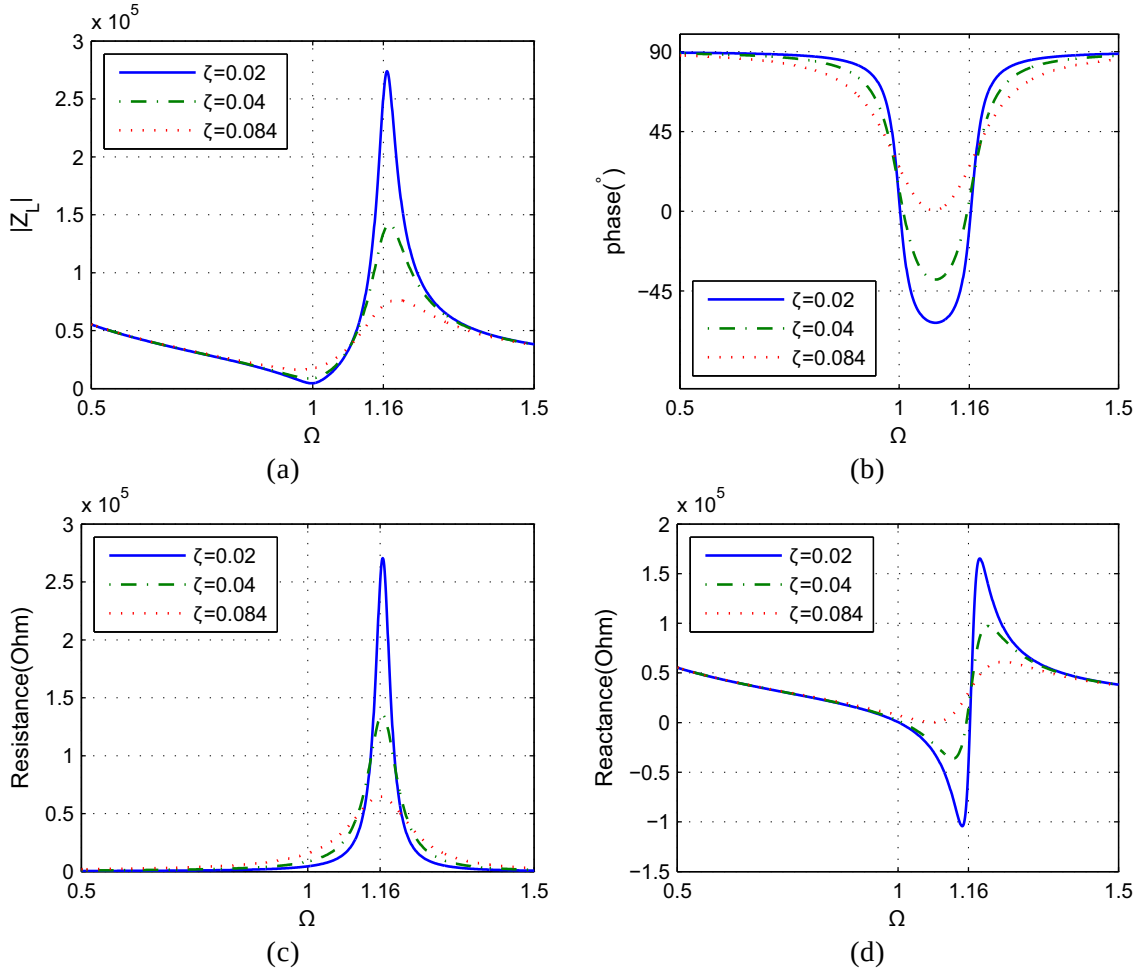

Figure 2-11. The impedance of complex load (a) modulous (b) phase (c) resistance (d) reactance

Cette thèse est accessible à l'adresse : http://theses.insa-lyon.fr/publication/2014ISAL0077/these.pdf
© [Y. Li], [2014], INSA de Lyon, tous droits réservés

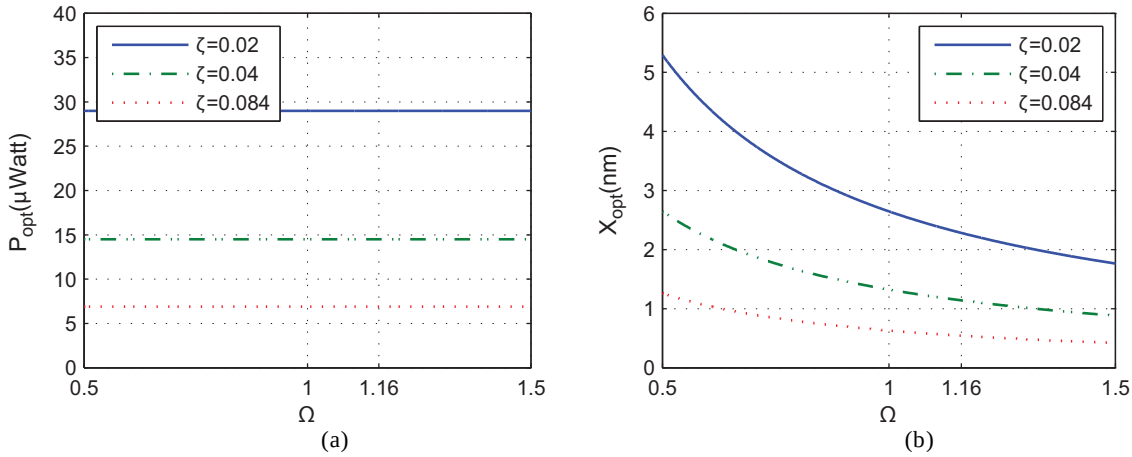

Figure 2-12. Optimal power harvested (a) and corresponding proof mass motion amplitude (b) as a function of the relative frequency.

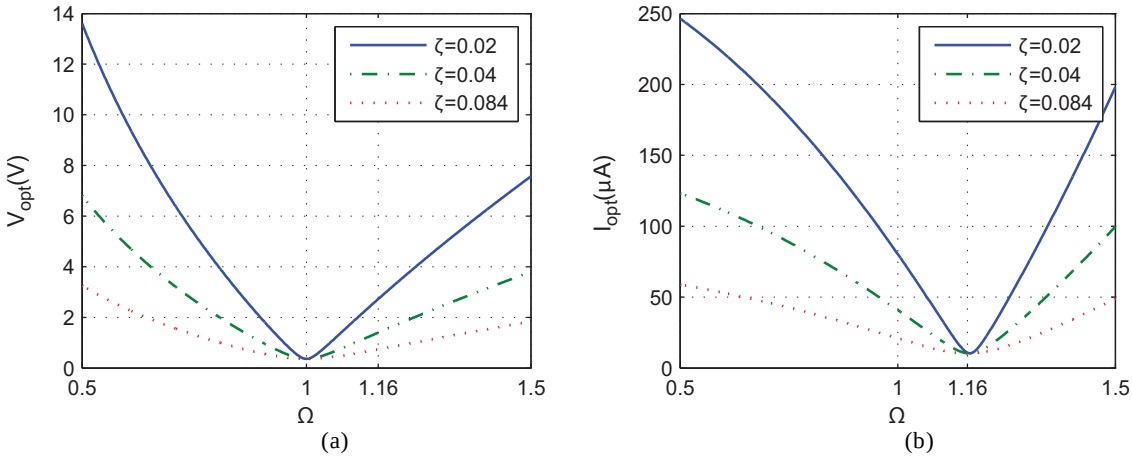

Figure 2-13. Circuit parameter for complex load case. (a) Voltage (b) Current

Cette thèse est accessible à l'adresse : http://theses.insa-lyon.fr/publication/2014ISAL0077/these.pdf
© [Y. Li], [2014], INSA de Lyon, tous droits réservés

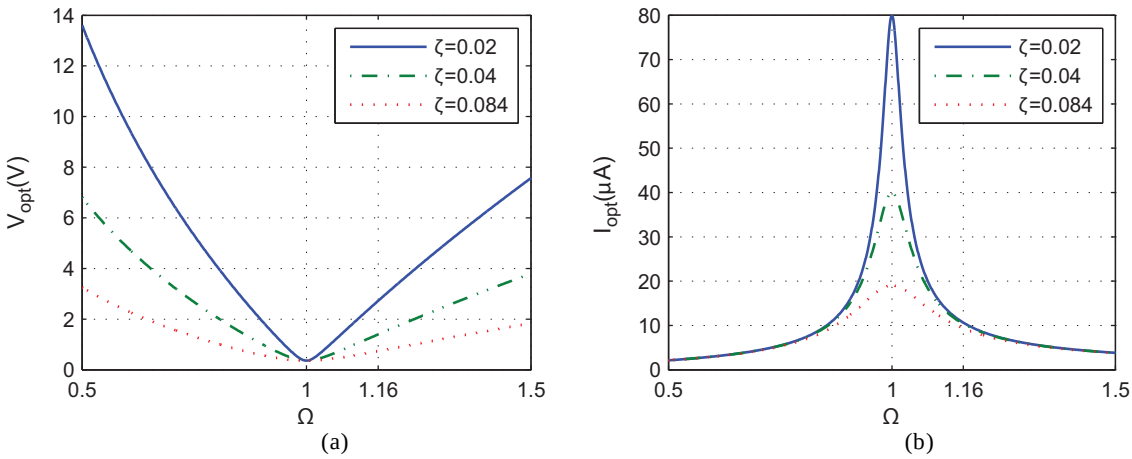

Figure 2-14. Circuit property for RL parallel case. (a) Voltage (b) Current

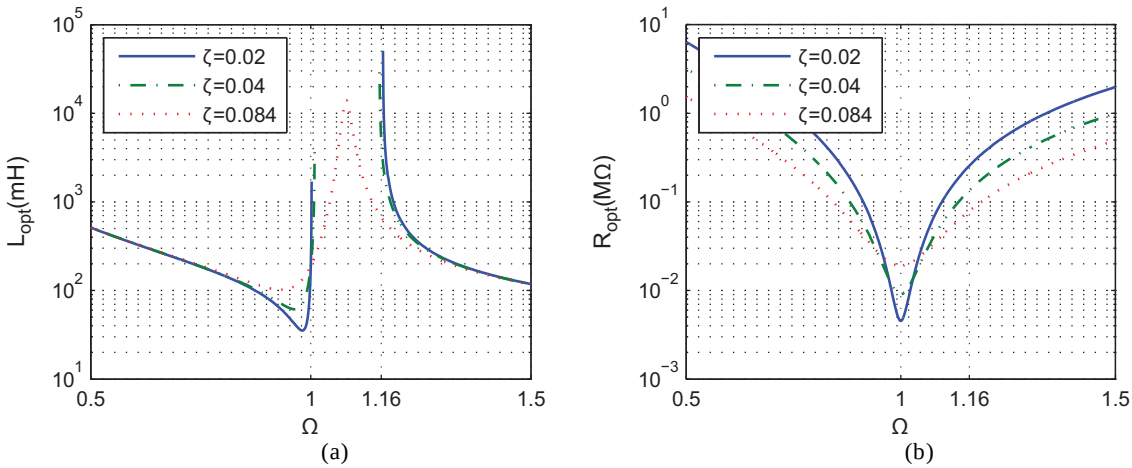

Figure 2-15. RL parallel case : optimal inductor and resistor with various of viscous loss

For R_{opt} in parallel with L_{opt} , this corresponds to $Z_{opt} = 1\Big/\left(\left(R_{opt}\right)^{-1} + \left(j\omega L_{opt}\right)^{-1}\right)$, yield,

$$\begin{cases} R_{opt} = \dfrac{1}{C_0\omega_n}\dfrac{1}{\Omega}\left(\dfrac{\beta^2}{\alpha} + \alpha\right) \\ L_{opt} = \dfrac{1}{C_0\omega_n{}^2}\dfrac{1}{\Omega^2}\dfrac{\alpha^2+\beta^2}{A+\beta} \end{cases} \tag{2.43}$$

Starting from Equation (2.17), the voltage over resistor is found, and then the current through resistor can be found by $I_L = V_L \big/ R_{opt}$.

For R_{opt} in series with L_{opt} , this corresponds to $Z_{opt} = R_{opt} + j\omega L_{opt}$, yields,

Cette thèse est accessible à l'adresse : http://theses.insa-lyon.fr/publication/2014ISAL0077/these.pdf
© [Y. Li], [2014], INSA de Lyon, tous droits réservés

$$\begin{cases} R_{opt} = \dfrac{1}{C_0\omega_n}\dfrac{1}{\Omega}\dfrac{\alpha}{1+A} \\ L_{opt} = \dfrac{1}{C_0\omega_n^{\ 2}}\dfrac{1}{\Omega^2}\dfrac{\beta+A}{1+A} \end{cases} \tag{2.44}$$

Starting from Equation(2.18), the current through resistor is found, and then the voltage over resistor can be found by $V_L = I_L R_{opt}$.

For resistor in parallel with inductor case (Figure 2-14, Figure 2-15), the current rises to maximum close to the short circuit frequency. In this frequency region, the requirement for inductance value and resistor value is minimal. It makes possible to select proper value for inductance. Unfortunately, the voltage here is minimal. If a diode recfier circuit is needed, it would be necessary to shift another proper working frequency. The problem for inductor is that, between resonance and anti-resonance the required optimal inductance value is negative in low loss conditions. If viscous loss is increased (i.e., ζ=0.084), this inconsistency problem vanishes due to the full capacitive character of the piezogenerator at this condition (Figure 2-7.b).

Once negative inductance value is required, we have three options:

- Using passive component, a capacitor to fill the gap
- Using active component, a gyrator to simulate negative inductor to fill the gap
- Removing this reactance component, leave resistive component only

For the first option, according to Equation (2.43) (2.44) and $j\omega L = (j\omega C)^{-1}$, the optimal value for the replacement capacitor is obtained. For the second option, a gyrator or a NIC (negative impedance converter) is possible to use to simulate a negative inductor (Figure 2-18). For the last option, it is the easiest solution. Once the inductor value is not positive, use the optimal resistor value obtained from resistive case to replace the *L-R* combination (Figure 2-16, Figure 2-17) such as recommended by Renno *et al.* [92].

Another problem is the unpractical value of inductor. It can be observed from Equation(2.43)(2.44) that, the optimal inductor value is increasing with the resonance frequency decrease. In fact, it is also affected by the competition between damping ratio ζ and electromechancial coupling coefficient k_e^2(see Equation(2.40) and Figure 2-15).

The case for resistor in series with inductor is similar. The corresponding results can be found by Equation(2.44).

Figure 2-16 and Figure 2-17 illustrate this process for the previously described seismic piezoelectric generator. Figure 2-16 shows the optimal resistance and inductance defined by Equation (2.43), while Figure 2-17 shows the optimal power and corresponding proof mass motion as a function of the normalized frequency for a 1*g* base acceleration. In fact this type of impedance matching is feasible as long as the transducer impedance is capacitive. Between the short circuit frequency an open circuit frequency and for a weekly damped transducer, the impedance becomes inductive (Figure 2-7.b), therefore no L-R matched load can be defined thus explaining the gap observed on Figure 2-16.b. As the optimal inductance

Cette thèse est accessible à l'adresse : http://theses.insa-lyon.fr/publication/2014ISAL0077/these.pdf
© [Y. Li], [2014], INSA de Lyon, tous droits réservés

cannot be defined, the optimal load is only defined by the optimal resistance and therefore the extracted power is lower than the optimal value defined by Equation (2.42) that can be obtained uniformly elsewhere.

It is interesting to remark that the optimal power is the same as the pure resistance case with low loss condition(2.36). Piezoelectric generator mechanical losses appear to be, along with the coupling coefficient, the central parameter allowing the definition of the optimal load as well as of the optimal power that can be extracted for a given excitation. Again the agreement with the results obtained with a numerical optimization approach (KKT) is excellent. Moreover, the proposed impedance matching method is simple, universal and very close to the physics of the piezoelectric generator.

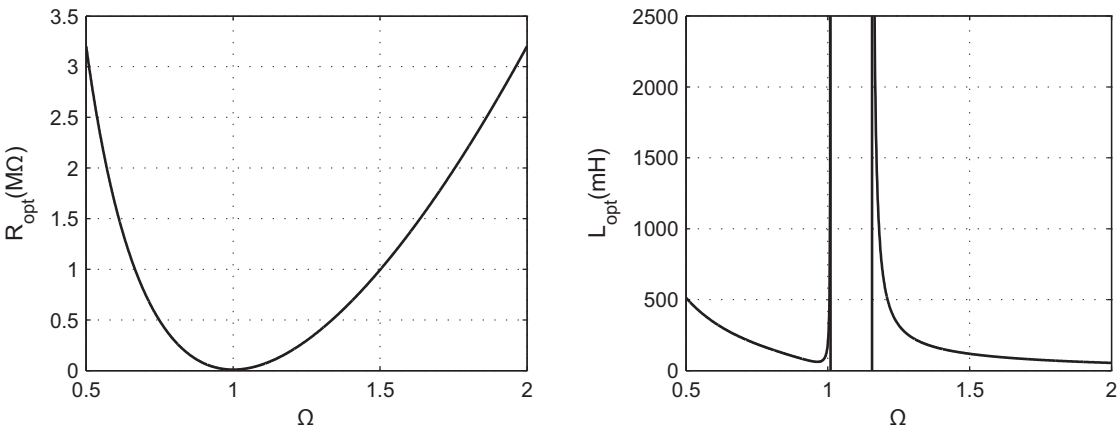

(a) (b)

Figure 2-16. Optimal resistor (a) and optimal inductor (b) as a function of the normalized frequency for optimal impedance matching with a resistance in parralel with an inductance (k_e=0.6 and ζ=0.04)

Cette thèse est accessible à l'adresse : http://theses.insa-lyon.fr/publication/2014ISAL0077/these.pdf
© [Y. Li], [2014], INSA de Lyon, tous droits réservés

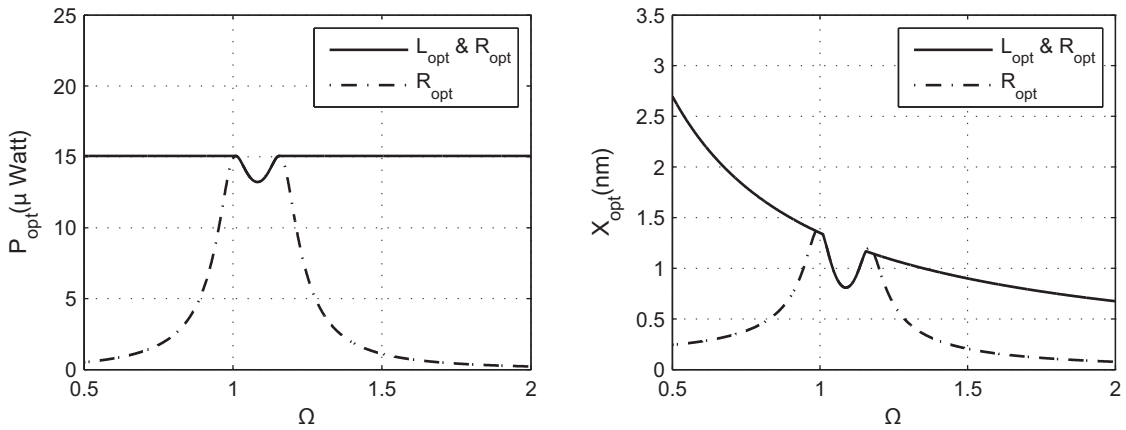

(a) (b)

Figure 2-17. Optimal ouptut power (b) and corresponding proof mass motion amplitude (a) as a function of the normalized frequency obtained for the optimal impedance defined in Figure 8. Calculation is done for k_e=0.6, for ζ=0.04 and for a 10 m/s² base acceleration.

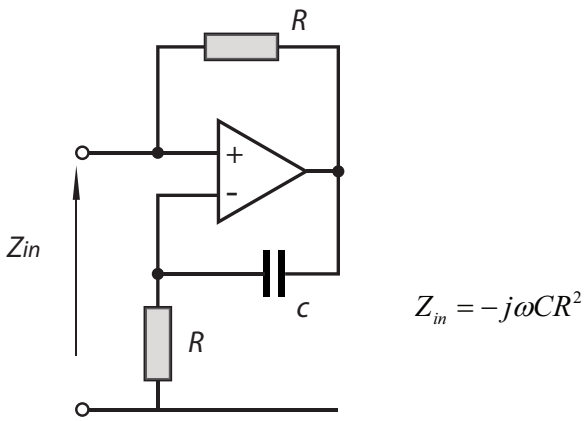

Figure 2-18. The negative inductor by gyrator

2.3.4 Comparison with other power optimization approach

Renno *et al.* [92] proposed another approach to optimize the power output of a piezoelectric vibration-based energy harvester. For a resistor parallel with inductor case, they established the governing equation for such SDOF system firstly, then obtained the power expression as,

Cette thèse est accessible à l'adresse : http://theses.insa-lyon.fr/publication/2014ISAL0077/these.pdf
© [Y. Li], [2014], INSA de Lyon, tous droits réservés

$$\mathcal{P}(\alpha_{KKT},\beta_{KKT})=\frac{1}{\omega_n^3}\frac{K\alpha_{KKT}\beta_{KKT}^2k_e^2\Omega^4}{\mathcal{B}} \tag{2.45}$$

where,

$$\alpha_{KKT}=R\omega_nC_0,\qquad \beta_{KKT}=\omega_n^2LC_0. \tag{2.46}$$

$$\mathcal{B}=\left(\left(\beta_{KKT}+2\alpha_{KKT}\zeta\right)\Omega-\beta_{KKT}\left(1+2\alpha_{KKT}\zeta\right)\Omega^3\right)^2+\left(\alpha_{KKT}-\left(2\beta_{KKT}\zeta+\alpha_{KKT}\left(1+\beta+\beta k_e^2\right)\right)\Omega^2+\alpha_{KKT}\beta_{KKT}\Omega^4\right)^2 \tag{2.47}$$

The α_{KKT} and β_{KKT} are related to resistive load and inductive load, respectively. It is clear that, the power is the function of quantities α_{KKT} and $\beta_{KKT.}$ By using Karush-Kuhn-Tucker (KKT) method[92, 97], they found the optimal α_{KKT} and β_{KKT} for optimal load. Following their expression, the optimal results are,

$$\begin{aligned}(\alpha_{KKT})_{opt}&=\frac{\Omega^4+\left(4\zeta^2-2\right)\Omega^2+1}{2\zeta k_e^2\Omega^2}\\(\beta_{KKT})_{opt}&=\frac{\Omega^4+\left(4\zeta^2-2\right)\Omega^2+1}{\Omega^2\left(\Omega^4-\left(2+k_e^2-4\zeta^2\right)\Omega^2+k_e^2+1\right)}\end{aligned} \tag{2.48}$$

Substituting Equation (2.48) into (2.46), the optimal load for R-L parallel case are obtained,

$$\begin{aligned}R_{opt}&=\frac{1}{C_0\omega_n}\frac{\Omega^4+\left(4\zeta^2-2\right)\Omega^2+1}{2\zeta k_e^2\Omega^2}\\L_{opt}&=\frac{1}{C_0\omega_n^2}\frac{\Omega^4+\left(4\zeta^2-2\right)\Omega^2+1}{\Omega^2\left(\Omega^4-\left(2+k_e^2-4\zeta^2\right)\Omega^2+k_e^2+1\right)}\end{aligned} \tag{2.49}$$

Compared with the optimal expression obtained by equivalent circuit method(2.43), the similarity exists. In fact, the optimal results obtained by KKT method and by equivalent circuit method are same (Figure 2-19).

It is worth to note that, optimal purely resistive load can also be found when applying KKT on Equation(2.45). Unfortunately, due to the complexity of optimal factor, obtaining the precise expression for purely resistive load is impossible. Not as the previous expression derived by equivalent circuit method(2.33)(2.39), using KKT method cannot find the analytical solution for these critical frequencies. Moreover, another governing equations system can be built for RL in series, and this complex process has to be repeated to optimize an RL series load by the KKT approach.

Comparing with the KKT optimization method, it can be concluded that, the equivalent circuit and the impedance matching method proposed in this chapter has strong physical sense and much more simple expression. Naturally, both the two optimization method are identically in terms of final optimal result.

Cette thèse est accessible à l'adresse : http://theses.insa-lyon.fr/publication/2014ISAL0077/these.pdf
© [Y. Li], [2014], INSA de Lyon, tous droits réservés

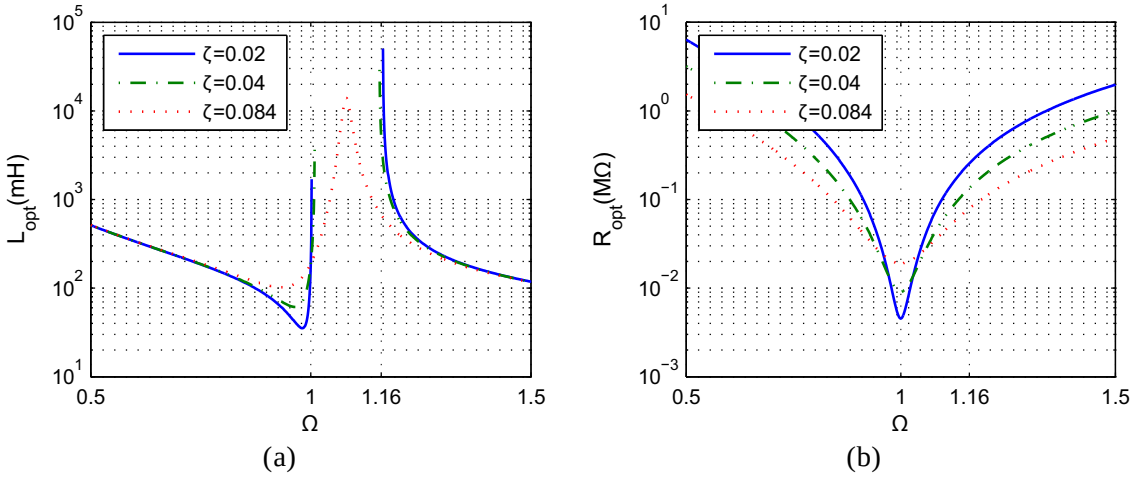

Figure 2-19. The optimal load for LR parallel case obtained KKT method (a) Optimal inductor with various losses (b) Optimal resistor with various losses

2.4 Experimental validation

In the previous sections, the optimal load of a piezoelectric generator has been fully derived and justified on the basis of an electrical equivalent circuit derived from the Mason equivalent circuit shown on Figure 2-4.a. The full impedance matching process and power optimization have been implemented on an experimental seismic piezoelectric generator. In order to have a tuning inductance that can be implemented with practical passive components and a device easy to excite, a simple seismic harvester made with a vibrating buzzer is considered experimentally.

Table 2-2. The comparison between KKT approach and equivalent circuit approach

	Electromechanical equations + KKT method	Equivalent circuit + Impedance matching
Solving technique	Mathematical	Physical
Difficulty	Complex	Straightforward
Final expression	Long and complicated	Simple and clear
Optimal purely resistance	Numerical solution	Analytical solution
Optimal RL in parallel	Analytical solution	Analytical solution
Optimal RL in series*	Analytical solution * (need specific equation for each type of load)	Analytical solution

Cette thèse est accessible à l'adresse : http://theses.insa-lyon.fr/publication/2014ISAL0077/these.pdf
© [Y. Li], [2014], INSA de Lyon, tous droits réservés

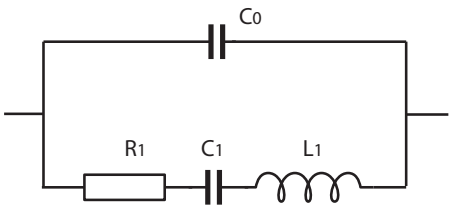

Figure 2-20. Piezoelectric generator equivalent impedance near its resonance.

A resonator such as a piezoelectric harvester can be represented by the Butterworth-Van Dyke (BVD) equivalent circuit[56, 57] recommended by IEEE standard 1987[49]. This BVD equivalent circuit is depicted in Figure 2-20. It corresponds precisely to the circuit derived from Mason (Figure 2-4), and can be identified easily with an impedance analyzer. Once the identification is done, the optimal loads are calculated and compared to the experimental ones for both resistance and resistance in parallel with inductance loads. Finally, the influence of the accuracy of the impedance on the extracted power will be discussed showing that achieving practically such a power optimization process is totally unrealistic.

2.4.1 Set-up

The experimental seismic harvester structure is depicted on Figure 2-21. It is made with a circular piezoelectric buzzer, whose dimensions are given in Figure 2-21.b, clamped on its external circular edge with an aluminum fringe. No proof mass is added in the center of the buzzer in order to keep a rather high resonance frequency ensuring practical fairly low optimal inductances. Figure 2-21.a shows the device mounted on a shaker (LDS V201) used to excite it at a given acceleration in the 2 kHz to 5 kHz frequency range. The motion of the harvester is monitored using a Laser Doppler Vibrometer (Polytech OFV 5000) aiming at the rigid aluminum fringe, thus measuring the “base” vibration speed. The shaker is driven with an audio amplifier. The whole measurement process is controlled with an HP4194A used as a network analyzer, generating the drive signal and monitoring both the base speed and the harvester voltage, in open circuit or with a given load. Harvested power is derived from the measured voltage and the considered load.

Cette thèse est accessible à l'adresse : http://theses.insa-lyon.fr/publication/2014ISAL0077/these.pdf
© [Y. Li], [2014], INSA de Lyon, tous droits réservés

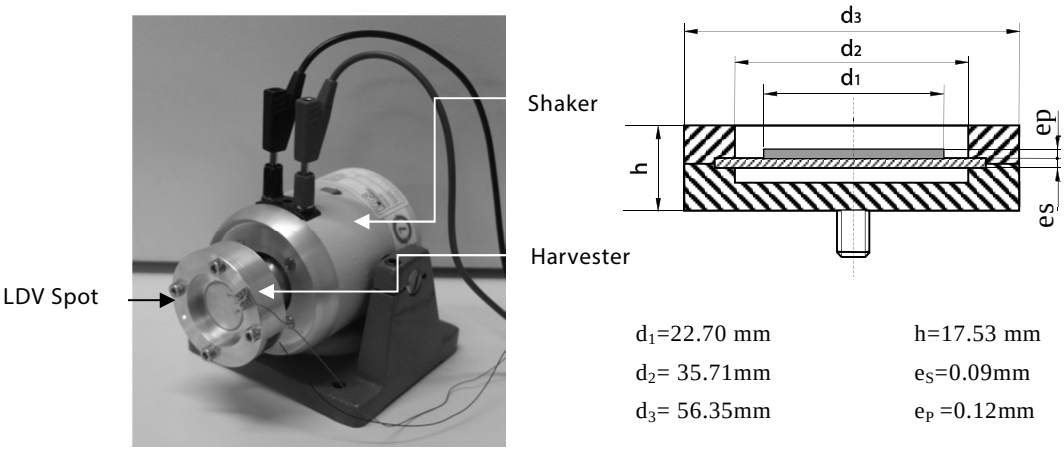

d_1=22.70 mm h=17.53 mm

d_2= 35.71mm e_S=0.09mm

d_3= 56.35mm e_P =0.12mm

(a) (b)

Figure 2-21. Experimental device: a) seismic piezoelectric-harvester mounted on the shaker. b) Cross-section of the piezoelectric-harvester made with a commercial piezoelectric buzzer.

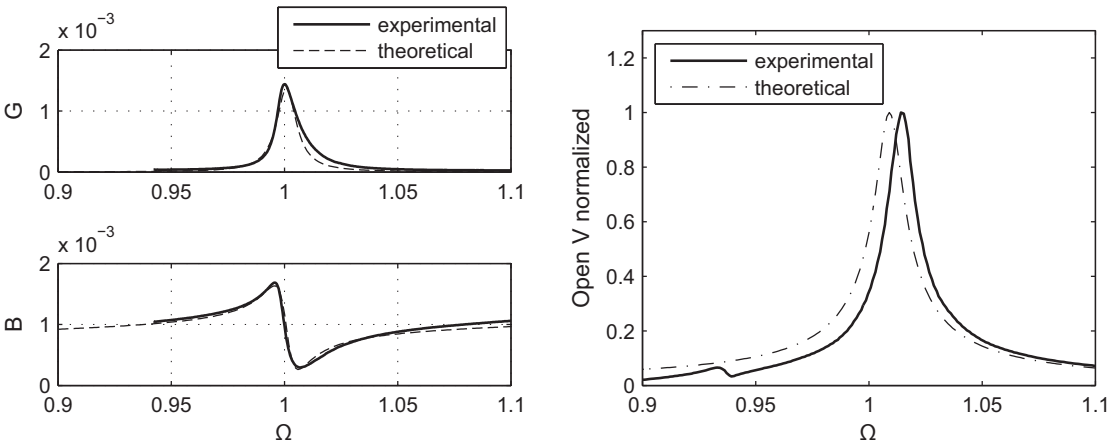

(a) (b)

Figure 2-22. Equivalent circuit identification process: a) Real and imaginary parts of the identified piezoelectric harvester admittance. Central frequency is 2335Hz; b) open circuit voltage response comparison.

Experiments were operated around the resonance frequency of the harvester. For each load, slow frequency sweeps (20 seconds long) are implemented to record the output voltage response in the frequency domain.

2.4.2 Equivalent circuit identification by LCR meter

The impedance of the piezoelectric energy harvester device is simply measured with the HP4194A used in impedance analyzer mode. The admittance spectrum is measured close to the

Cette thèse est accessible à l'adresse : http://theses.insa-lyon.fr/publication/2014ISAL0077/these.pdf
© [Y. Li], [2014], INSA de Lyon, tous droits réservés

transducer resonance frequency, and the equivalent circuit shown on Figure 2-20 is identified using the built-in equivalent circuit identification function (Usually it is circuit type E). In this way, the harvester's equivalent circuit can be obtained at any workable resonance frequency. For instance according to Figure 2-22 plot, around the considered resonance frequency at 2335Hz, the equivalent circuit parameters are L_1=4.69H, C_1=0.988nF, R_1=724Ω, C_0=64.6nF.

Figure 2-22.a shows a comparison of the experimental admittance ($Y=G+jB$) with the admittance derived from the identified equivalent circuit. Figure 2-22.b shows a comparison of the experimental open circuit voltage with the theoretical open-circuit voltage obtained using the Figure 2-4.a equivalent circuit. Note that these plots are normalized and that this measure allows, for a known base acceleration, to identify the electromechanical response according to Equation (2.5) V_0 definition. These results prove that the equivalent circuit of any given piezoelectric harvester can be easily represented and identified according to the circuit considered in Figure 2-4.a and Figure 2-20. Note that, the proposed theory is essentially linear theory. Now depending on the excitation level, light non-liner behavior can be observed. This explains the shift between the experimental and identified theoretical plots shown on Figure 2-22.

2.4.3 Measurement process

As mentioned before, two cases are considered here. Use the resistor to validate the resistive load optimization, and use the resistor in parallel with inductor to validate one case of the complex load optimization. For each load value, a sweep function is operated to record the voltage response of harvester.

(A) Purely resistance load

A rheostat, ranging from 100 Ohm to 10K Ohm, is used to as the variable resistive load. For a given target frequency, i.e., 2335Hz, sweep function will start at 2100 Hz and end at 2600 Hz to record the voltage response over load. The experimental optimal load is evaluated for each frequency by measuring the output power as a function of the load resistance for a given base acceleration. By selecting the maximum power value and the corresponding resistance load, the optimal power and load curve are obtained. Briefly, process as follows,

1. Take the system identification value to plot the theoretical optimal load curve (like Figure 2-8) as rheostat value choosing reference.
2. Extend the rheostat value range to 150% of theoretical prediction.
3. Start the sweep and record the voltage response curve V for each load R.
4. Calculate the power output at each frequency by $P=V^2/R$
5. Pick up the maximum power P at each frequency and record the corresponding load R by a Python program.

Cette thèse est accessible à l'adresse : http://theses.insa-lyon.fr/publication/2014ISAL0077/these.pdf
© [Y. Li], [2014], INSA de Lyon, tous droits réservés

6. Draw the optimal load curve.

(B) *Optimal impedance matching with a parallel L-R load*

For a resistor in parallel with an inductor load, the derivation of the optimal conditions is slightly more complex. A rheostat and a series of fixed value inductor were used in parallel L-R load case. To achieve a precise validation, the inductor was modelled as an ideal inductor shunted by an ideal resistor (Figure 2-23). We should notice that, although the theoretical prediction will give the optimal value for resistor and inductor, the value don't correspond to rheostat value and inductor value directly. The relationship is depicted in Figure 2-23.

For each inductance, a set of resistance is considered (with logarithmic step) and for each resistance the output power is plotted as a function of the frequency. The maximum power obtained thus defines for which frequency and which resistance the considered inductance is optimal. This procedure is conducted for a constant base acceleration. Nevertheless, the process is similar as previous operation:

1. Take the system identification value to plot the theoretical optimal load curve (like Figure 2-15) as rheostat value and inductor value choosing reference.
2. Extend the range to 150% of theoretical prediction.
3. Measure each of the fixed value inductor to obtain the R_i and L_i
4. Referring the theoretical prediction and the parasitic resistance R_i of inductor, choose a proper range for rheostat.
5. For each inductor L, repeat the step3 in Purely resistance load case.
6. Calculate the power output at each frequency, each R and each L by $P = V^2/R$
7. Pick up the maximum power P at each frequency and record the corresponding load L and R by a Python program.
8. Considering the L_i and parasitic resistance R_i to calculate the ideal R value and ideal L value.
9. Draw the optimal load curve.

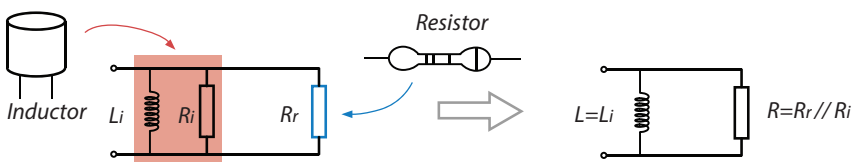

Figure 2-23. The model for LR load

Cette thèse est accessible à l'adresse : http://theses.insa-lyon.fr/publication/2014ISAL0077/these.pdf
© [Y. Li], [2014], INSA de Lyon, tous droits réservés

2.4.4 Results and discussion

(A) Purely resistance load

According to the process described in Section 2.3.2, the optimal resistance load can be derived using Equation (2.28) as the modulus of the transducer impedance defined by Figure 2-4 and identified previously. The optimal resistance and output power can finally be obtained (Figure 2-24).

The experimental results and theoretical prediction are compared on Figure 2-24. Experimental and theoretical optimal load and output power are in overall very good agreement. Note that due to the high level of mechanical losses of the device (flexion mode), only one peak is observable on the output power plot.

(B) Optimal impedance matching with a parallel L-R load

Following the process described in Section 2.3.3, the optimal resistance and inductance load can be derived using Equation (2.41) from the transducer impedance ZT* such as defined by Figure 2-4 and identified previously. From the optimal load, the optimal power can finally be derived. This result is shown on Figure 2-25. Note that again, due to the high level of mechanical losses of the considered experimental device the harvester impedance is always capacitive (showed on Figure 2-22.a) and thus the optimal inductance L_{opt} can always be obtained.

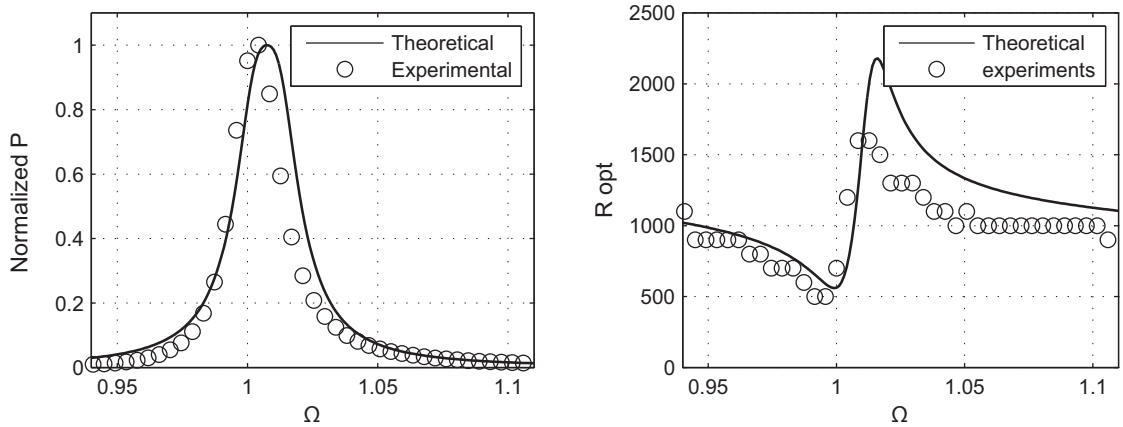

(a) (b)

Figure 2-24. Impedance matching of the experimental harvester structure with a pure resistive load. a) Experimental and theoretical normalized out power, b) Theoretical and experimental optimal resistance.

Cette thèse est accessible à l'adresse : http://theses.insa-lyon.fr/publication/2014ISAL0077/these.pdf
© [Y. Li], [2014], INSA de Lyon, tous droits réservés

The results are plot on Figure 2-25 showing an overall good agreement with the theoretical predictions. It is interesting to note that as expected, Figure 2-25.a shows that for the optimal load, the output power appears to be constant as a function of the frequency for a given acceleration. The experimental impedance matching was chosen to be entirely done with passive components. However these components are not perfect and for example a strong limitation was due to the fact that the inductances present a parasitic resistance. Hence the frequency band of the experimental results presented in Figure 2-25 is limited to low R_{opt} resistors in order to avoid that the high parasitic resistance of the experimental inductors would distort to much the effective load.

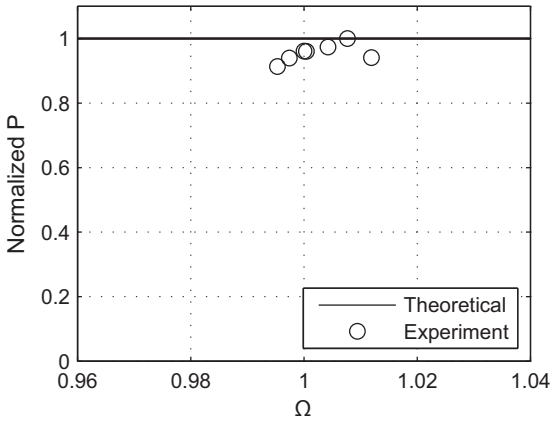

(a)

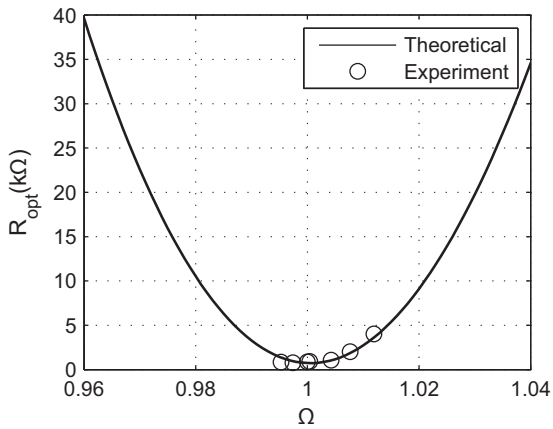

(b)

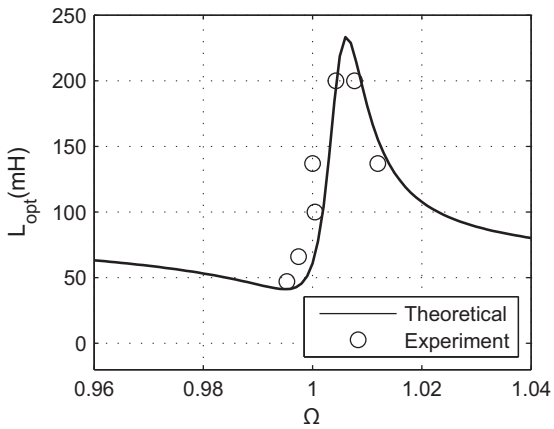

(c)

Figure 2-25. Impedance matching of the experimental harvester structure with a R-L load. a) Experimental and theoretical normalized out power, b) Theoretical and experimental optimal inductance, c) Theoretical and experimental optimal resistance.

Cette thèse est accessible à l'adresse : http://theses.insa-lyon.fr/publication/2014ISAL0077/these.pdf
© [Y. Li], [2014], INSA de Lyon, tous droits réservés

(C) High sensitivity of the impedance matching process to the passive component dispersion

Passive impedance matching appears to be very difficult due to dispersion in the components and to the large inaccuracy of these components due for example to the variations of the apparent resistance or inductance with the frequency. This is particularly true for large inductances wounded on a ferrite core. As expected parallel L-R matching is much sensitive than pure resistance matching. Another situation is that the system parameters may varying with temperature. If the parameters are changed, it seems however that no dramatic effects are observed for pure resistive load.

In practice, it is impossible to make each of the value of load falls on the optimal curve. The difference between real active value and the theoretical requiring value depends on the circuit property, circuit limitation, available components for choosing, operation temperature. Suppose the real value in circuit and the theoretical value has the difference represents by a normal distribution, then we have,

$$X = \mathcal{N}(\mu, \sigma) \tag{2.50}$$

Here X represents the real active value in circuit, μ represents the theoretical value and σ is the standard deviation. The error ratio is used for standard deviation. For instance, the 30% error between theoretical value and the real value will lead,

$$X = \mathcal{N}(\mu, 30\% \cdot \mu) \tag{2.51}$$

Figure 2-26 illustrates the sensitivity for resistance matching. It shows the normalized output power as a function of the frequency (Figure 2-26.b) for a 30% standard deviation of the optimal resistance load (Figure 2-26.a). Small variations are visible according to the nice and

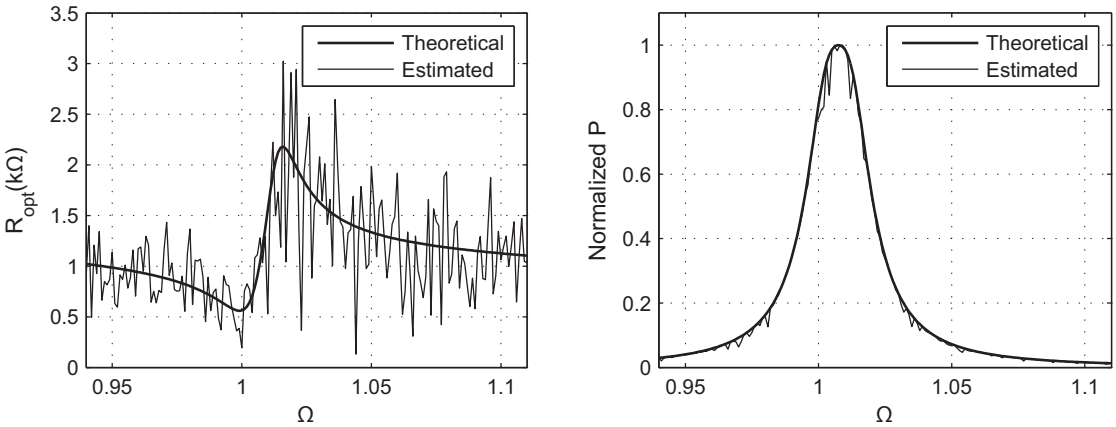

(a) (b)

Figure 2-26. Sensitivity of the impedance matching to the optimal load for resistive optimal load: a) 30% standard deviation of the optimal resistance load, b) corresponding optimal output power.

Cette thèse est accessible à l'adresse : http://theses.insa-lyon.fr/publication/2014ISAL0077/these.pdf
© [Y. Li], [2014], INSA de Lyon, tous droits réservés

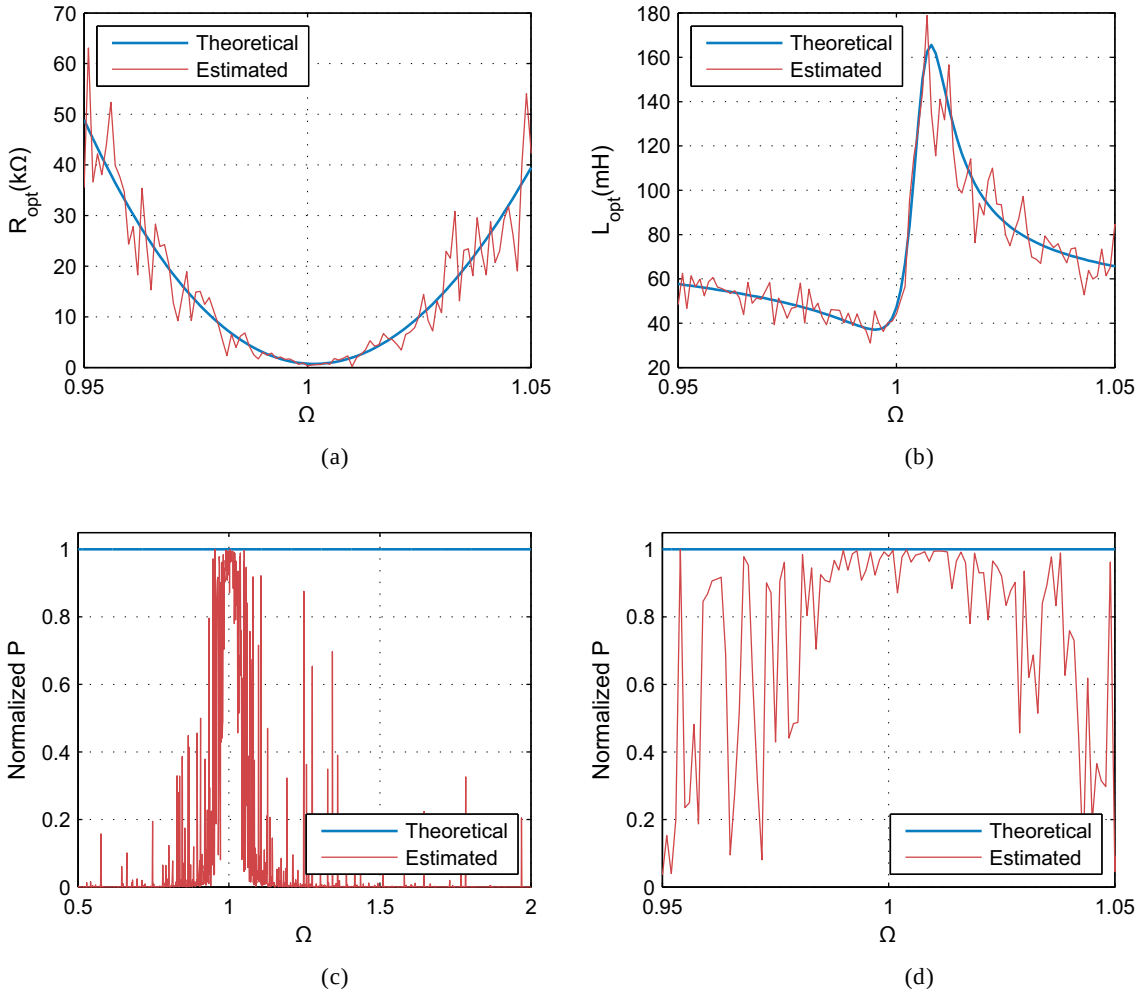

Figure 2-27. Sensitivity of the impedance matching to the optimal load for parralel R-L load: a) 30% standard deviation of the optimal resistance load, b) 10% standard deviation of the optimal inductance load, c) corresponding output power dispersion and d) zoomed version of the plot shown in c)

smooth curves obtained for this case on Figure 2-24.

The low sensitivity to the resistance is still true in LR case, which means optimal load (even with error of the resistance component) won't affect the power performance much. However, the inductance does, even a small difference will cause obviously optimization failure.

Figure 2-27 illustrates this problem for LR optimal load. In this case Figure 2-27.c and Figure 2-27.d represent the output power variation with the frequency for a 30% standard deviation of the optimal resistance and only a 10% standard deviation of the inductance shown on Figure 2-27.a and Figure 2-27.b respectively. The corresponding variations are huge,

Cette thèse est accessible à l'adresse : http://theses.insa-lyon.fr/publication/2014ISAL0077/these.pdf
© [Y. Li], [2014], INSA de Lyon, tous droits réservés

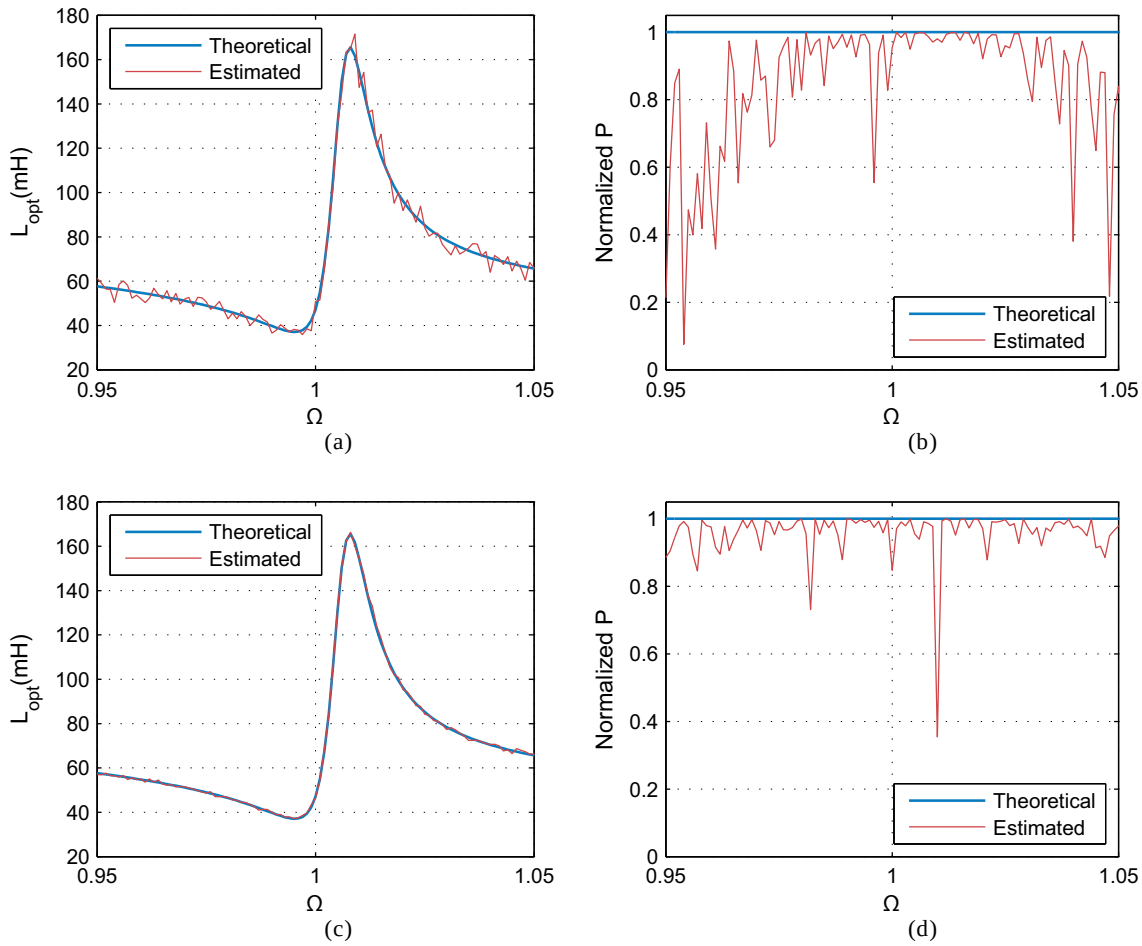

Figure 2-28. Power sensitivity with 30% error of resistive load. (a) 5% error of inductor and (b)the corresponding power output (c) 1% error of inductor and (d) the corresponding power output.

showing that the output power can be practically made constant only in a very narrow frequency band.

Moreover, decreasing this error of inductor to 5% (Figure 2-28) cannot improve the power performance dramatically. Only when the deployed inductor is matched with the theoretical prediction perfectly (i.e. 1% error in Figure 2-28), the harvested power can be held for a limited wide bandwidth (0.95 to 1.05). The sensitivity of inductor (reactive component) is the obstacle to achieve perfect power.

2.5 Conclusion and future work

A lumped parameter model for a SDOF piezoelectric energy harvester is derived from the Mason equivalent circuit. This model is represented by an equivalent circuit (Figure 2-20) same

Cette thèse est accessible à l'adresse : http://theses.insa-lyon.fr/publication/2014ISAL0077/these.pdf
© [Y. Li], [2014], INSA de Lyon, tous droits réservés

as BVD equivalent circuit, but all parameter are defined clearly. By using this model, the impedance property of such electromechanical resonator can be assessed. Besides, the power transferring process can be optimized by impedance matching theory. This power optimization process is simple and easy to handle. The optimization results show that, short circuit frequency and open circuit frequency play important role. For purely resistive load case, the power can reach its maximum around the short circuit frequency and open circuit frequency. When complex type load is used, the power transferring is only the function of input force and viscous load. With the impedance matching analysis, the maximum power transferring is obtained. The perfect impedance matching demonstrates that, for any kinds of energy harvesting circuit, it cannot over the power limit achieved by optimal complex load. The performance of the proposed approach was compared to a very sophisticated optimization technique derived from the Karush-Kuhn-Tucker procedure.

The very good agreement with the results of this technique associated with the great simplicity of the equivalent circuit approach makes the later an excellent choice for the power optimization of any piezoelectric generator. This technique was then experimentally implemented for a seismic harvester made with a piezoelectric buzzer. A simple technique of identification of the equivalent circuit of the harvester was demonstrated. It was shown that resistive optimal matching is very easy to implement with good precision and stability. Optimal L-R impedance matching appeared to be much more difficult to implement. It was shown that for the optimal load the output power can be made independent of the frequency for a given input acceleration. Further investigation showed that the global performance is very sensitive to the implemented load inductance.

Although applying complex optimal load to ensure the maximum and frequency-independent power transferring is a tough task, it is still worthy to face this challenge due to its promising power output level. One of the possible solutions is using the DC-DC converter to equal the load to a resistor, meanwhile employing a self-tuned gyrator to simulate the required reactance value (inductive or capacitive). Since the theoretical prediction by LCR system identification is possible, a special circuit can be developed to predict the required optimal value for such self-tuned gyrator. The difficulty is that such sophisticated technique need power to be implemented and this power is usually lacking when consider energy harvesting. These works have a long way to go. A similar tuning circuit based microcontroller has already been proposed [91].

However, such difficulties in achieving optimization of the output power of any piezoelectric generators justify therefore perfectly the development of alternative non-linear techniques such as SSHI, S3H or SECE developed these last years that replace the needed phase shift implemented by the inductance by a specific switching process of the harvester voltage.

Cette thèse est accessible à l'adresse : http://theses.insa-lyon.fr/publication/2014ISAL0077/these.pdf
© [Y. Li], [2014], INSA de Lyon, tous droits réservés

C H A P T E R 3 Power optimization for SSHI network

3.1 Introduction

3.2 Piezoelectric harvester modeling

3.3 Network topology design

3.3.1 Circuit basic

3.3.2 Network topology design

(A) Standard

(B) Independent SSHI

(C) SSHI in parallel

(D) Mono SSHI

(E) SSHI in series

3.4 Power performance comparison

3.4.1 Decay time (Energy harvesting process)

3.4.2 Power performance

3.4.3 Energy balance

3.4.4 Influence of the coupling coefficients

3.5 Improvement for pulse operation

3.6 Bonding effect

3.7 Conclusion

3.1 Introduction

In general, piezoelectric energy harvester relies on the tuned excitation frequency. To extend the bandwidth and increase the harvested power, the distributed piezoelectric energy harvester is considered in this chapter. The distributed piezoelectric energy harvester is composed of several independent harvesters who have their own resonance frequencies. The harvested power is limited by the piezoelectric material's size and the working frequency. By using such distributed harvesters, each harvester unit can be placed in the regions of maximal strain of the host structure. Moreover, the energy stored in different frequencies can be extracted due to the multi-frequency character of distributed harvester. In this way, the global power harvesting efficiency is augmented.

Cette thèse est accessible à l'adresse : http://theses.insa-lyon.fr/publication/2014ISAL0077/these.pdf
© [Y. Li], [2014], INSA de Lyon, tous droits réservés

(a) (b)

Figure 3-1. The direct energy harvesting (a) and indirect energy harveting (b)

In terms of energy harvesting circuit, the critical task for distributed harvester is the connection approach. *How to connect these distributed units and the corresponding energy harvesting circuits to achieve maximum power output?*

Another problem considered in this chapter is the direct energy harvesting, which is more suitable for distributed strain energy harvesting. Many of the piezoelectric energy harvesters are indirect harvester, in the sense that the harvesting piezoelectric element is bonded to an optimized resonator (usually a cantilever beam) that is attached on the vibrating mechanical structure. The motion of the host structure then excites the resonator resulting in energy harvesting. In direct energy harvesting, there is no additional resonator structure, the piezoelectric element is directly attached to the host structure and is strained by and at the structure vibration frequency [98]. A simple illustration of these two harvesting types is given in Figure 3-1. On one hand, unlike indirect harvesting, there is no need for resonator tuning or adapted bandwidth requirement, since the energy is directly extracted at the structure vibration frequency. On the other hand, it is difficult to get high piezoelectric coupling coefficients due to size requirements and the natural damping of the structure is usually high. Therefore, in this case, non-linear technique (such as SSHI) which has high power efficiency in weak coupling condition is suitable for direct piezoelectric energy harvesting.

Therefore the SSHI network energy harvesting circuit is used to investigate the distributed harvester. The distributed harvester will be placed on a multi modes structure. All these research works are arranged as follows, Section 3.2 will describe the state-space modeling method for multi piezoelectric patches with multi modes. Section 3.3 will discuss the basic circuits used for such distributed harvester firstly. Then the design principle and schematic for five different network energy harvesting topologies will be provided. With Matlab/Simulink environment and Simscape toolbox, all the proposed circuit topologies will be assessed thoroughly in Section 3.4. In the next section, a possible solution for wasted energy in pulse excitation will be proposed and discussed. In Section 3.6, the short circuit issue and bonding layer parasitic capacitance, which exist uniquely in direct harvesting mode, will be analyzed carefully. The recommend bonding layer thickness will also be provided. The conclusion and outlook will be made in the final Section 3.7.

Cette thèse est accessible à l'adresse : http://theses.insa-lyon.fr/publication/2014ISAL0077/these.pdf
© [Y. Li], [2014], INSA de Lyon, tous droits réservés

3.2 Piezoelectric harvester modeling

The structure which has been used in this work as a matter of benchmark is a large steel plate, 60 *cm* wide, 40 *cm* high and 1 *mm* thick described in previous work [99] . This plate is clamped on its four edges on a metallic frame. This plate is equipped with four piezoelectric elements bonded along the clamped edges as depicted on Figure 3-2.

The structure motion will be considered in the low frequency band corresponding essentially to flexure modes. These flexure modes are reasonably coupled with the four piezoelectric elements. The piezoelectric elements are 600 μm thick, made with a Navy III PZT (P189 from Saint-Gobain Quartz). The overall size of each patch is 12 *cm* per 4 *cm*. As such a large area is difficult to make in only one piece, it is segmented into 8 pieces, each 3 *cm* long and 2 *cm* wide.

A multimodal 'Mass-Spring-Damper' model, based on the SDOF model proposed in Chapter 1, is used to describe the whole structure (Figure 3-3).Only the first four modes are considered. These modes have been selected because of their high coupling coefficient. Considering an *m* mode system with *n* piezoelectric patches, the mechanical equations can be written for each mode.

The governing equation of mth mode and n^{th} piezoelectric patch are given in Equations (3.1)(3.2). In this model, u_m is the structure modal displacement of the modal mass M_m which is motioned by the external excitation force F. C_m and K_m^E are the viscous coefficient and the short circuit stiffness of the structure respectively. α_{mn} is the force factor for piezoelectric patch n on mode m. The β_m term is related to the location of the application of force F. If applied in the center of the plate, this term equals unity for each mode. The piezoelectric element n generates an outgoing current I_n and a voltage V_n across its blocked capacitance C_{0n}.

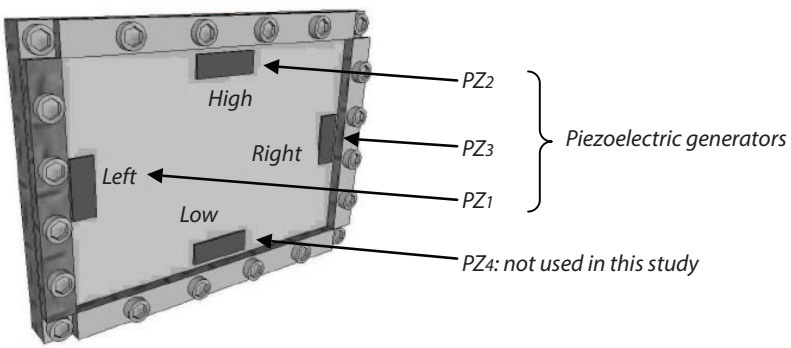

Figure 3-2. The metallic plate structure equipped with piezoelectric generators used in this study

Cette thèse est accessible à l'adresse : http://theses.insa-lyon.fr/publication/2014ISAL0077/these.pdf
© [Y. Li], [2014], INSA de Lyon, tous droits réservés

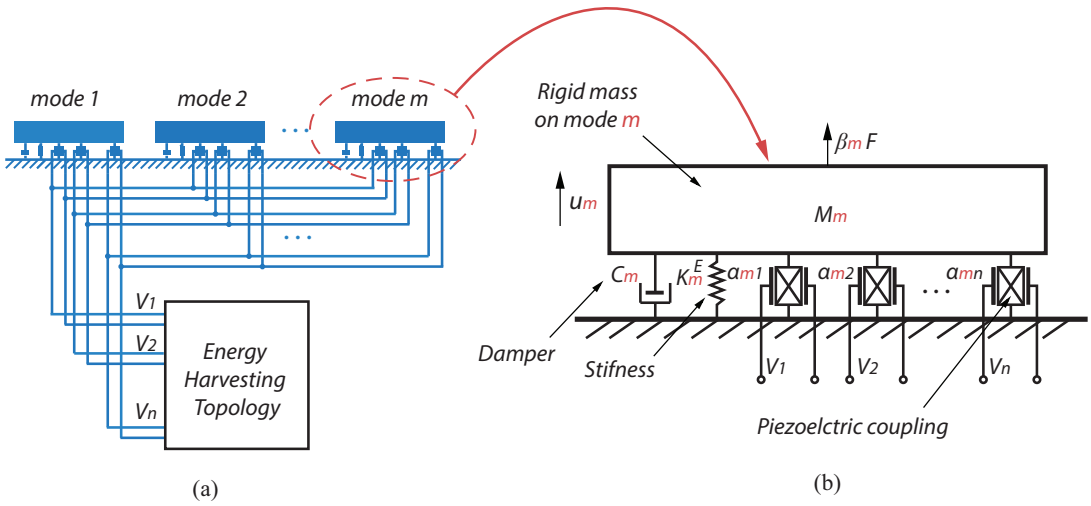

Figure 3-3. Multimodal mass-spring-damper model of the smart structure with *n* piezoelectric elements

$$M_m\ddot{u}_m + C_m\dot{u}_m + K_m^E u_m = -\sum_{j=1}^{n}\alpha_{mj}V_j + \beta_m F \tag{3.1}$$

$$I_n = \sum_{k=1}^{m}\alpha_{kn}\dot{u}_k - C_{0n}\dot{V}_n \tag{3.2}$$

Using the governing equation above, building the system dynamic equilibrium equation is possible. Considering a 4 modes structure with 4 piezoelectric patches, Equation (3.3) gives the dynamic equations of this system.

$$\begin{cases} M_1\ddot{u}_1 + C_1\dot{u}_1 + K_1^E u_1 = -\sum_{j=1}^{4}\alpha_{1j}V_j + \beta_1 F \\ M_2\ddot{u}_2 + C_2\dot{u}_2 + K_2^E u_2 = -\sum_{j=1}^{4}\alpha_{2j}V_j + \beta_2 F \\ M_3\ddot{u}_3 + C_3\dot{u}_3 + K_3^E u_3 = -\sum_{j=1}^{4}\alpha_{3j}V_j + \beta_3 F \\ M_4\ddot{u}_4 + C_4\dot{u}_4 + K_4^E u_4 = -\sum_{j=1}^{4}\alpha_{4j}V_j + \beta_4 F \end{cases} \tag{3.3}$$

State-space method is introduced to solve the above equations. Considering it is a linear 4th order system in continuous time, an input variable (one force and four voltages) and a state variable (four modal displacements and four modal velocities) are chosen. The output variable consists of the modal displacements and velocities. The state-space system summarized by Equation (3.4) describes the whole structure vibration,

$$\begin{cases} dX = A_{ss}X + B_{ss}U \\ Y = C_{ss}X + D_{ss}U \end{cases} \tag{3.4}$$

Cette thèse est accessible à l'adresse : http://theses.insa-lyon.fr/publication/2014ISAL0077/these.pdf
© [Y. Li], [2014], INSA de Lyon, tous droits réservés

Where,

$$A_{ss} = \begin{bmatrix} I_4 & 0_{4,4} \\ 0_{4,4} & inv(M) \end{bmatrix} \cdot \begin{bmatrix} 0_{4,4} & I_4 \\ -K^E & -C \end{bmatrix}, \quad B_{ss} = \begin{bmatrix} I_4 & 0_{4,4} \\ 0_{4,4} & inv(M) \end{bmatrix} \cdot \begin{bmatrix} 0_{4,4} & 0_{4,4} \\ \beta & -\alpha \end{bmatrix},$$
$$C_{ss} = I_8, \qquad D_{ss} = 0_{8,5}. \tag{3.5}$$

$$X = [u_1 \quad u_2 \quad u_3 \quad u_4 \quad \dot{u}_1 \quad \dot{u}_2 \quad \dot{u}_3 \quad \dot{u}_4]^T, \quad U = [F \quad V_1 \quad V_2 \quad V_3 \quad V_4]^T,$$
$$Y = [u_1 \quad u_2 \quad u_3 \quad u_4 \quad \dot{u}_1 \quad \dot{u}_2 \quad \dot{u}_3 \quad \dot{u}_4]^T$$

M, C, and K^E are the positive diagonal 4x4 matrices. I_4 and I_8 are the 4x4 and 8x8 identity matrix respectively. $0_{4.4}$ and $0_{8,5}$ are zero matrices with a 4x4 and 8x5 size respectively.

Table 3-1 lists the various parameters used in the simulations. They have been identified by a proper set of measurements on the structure[99]. The dynamic mass is taken as unity. The short-circuit stiffness K^E is derived from the measurement of the short-circuit resonance frequencies. The viscous coefficient is derived from the mechanical quality factor Q_M of each resonance obtained with the 3 dB method. The piezoelectric force factor α_{mn} are related to the electromechanical coupling coefficients k_{mn} according to Equation (3.6). In this equation that has to be considered for each mode, K^D is the modal open circuit stiffness of the structure. The coupling coefficient k is also related to the mechanical resonance frequencies in short circuit ω_E and in open-circuit ω_D respectively.

$$k^2 = \frac{\omega_D^2 - \omega_E^2}{\omega_D^2} = \frac{K^D - K^E}{K^D} = \frac{\alpha^2}{K^D C_0} \tag{3.6}$$

Equation (3.6) is considered for each mode and each piezoelectric element. The mode m short circuit resonance frequency ω_{Emn} is obtained when all the elements are short-circuited; the corresponding open circuit resonance frequency ω_{Dmn} is measured with all the elements in short-circuit except the nth piezoelectric element. The blocked capacitance C_{0n} is measured with a network analyzer, out of resonance, usually in high frequency (@. 10KHz)

In the simulation only the first three piezoelectric elements will be considered as part of the network. The fourth one will be used for voltage monitoring and is always considered in open-circuit condition. The simulations considered in this work are done with a pulse type excitation. The input force used is a 20 μs, 0.88 mJ pulse signal which applied in the geometric center of the plate.

The simulations are made in the Matlab/Simulink environment. The piezoelements, the network and SSHI interfaces are modelled by the Simscape toolbox (see Appendix C & D for detail). With the Simscape toolbox, a piezoelectric patch is modeled by a controlled current source in parallel with the blocked capacitance C_0 (as discussed in Chapter 1).

Cette thèse est accessible à l'adresse : http://theses.insa-lyon.fr/publication/2014ISAL0077/these.pdf
© [Y. Li], [2014], INSA de Lyon, tous droits réservés

Table 3-1. Smart structure numerical data used in the simulation

	Mode 1	Mode 2	Mode 3	Mode 4
Frequency(Hz)	96	175	204	228
Dynamic mass(kg)	1	1	1	1
Stiffness K_m^E (10^6 N/m)	0.3609	1.1832	1.6075	2.0257
Force factor α_{mn}	α_{11}=0.0079	α_{21}=0	α_{31}=0.0314	α_{41}=0.0079
	α_{12}=0.0101	α_{22}=0	α_{32}=0.0292	α_{42}=0.0079
	α_{13}=0	α_{23}=0.0372	α_{33}=0	α_{43}=0.0079
	α_{14}=0	α_{24}=0.0276	α_{34}=0	α_{44}=0.0079
Mechanical quality factor Q_M	90	90	170	250
Electromechanical coupling coefficients k(%)	k_{11}=6.43	k_{21}=0	k_{31}=11.96	k_{41}=7.64
	k_{12}=6.29	k_{22}=0	k_{32}=8.54	k_{42}=3.82
	k_{13}=0	k_{23}=11.42	k_{33}=0	k_{43}=6.38
	k_{14}=0	k_{24}=9.1	k_{34}=0	k_{44}=3.95
Viscous coefficients C_m (N s/m)	6.7021	12.2173	7.5398	5.7303
	PZ 1	PZ 2	PZ 3	PZ 4
Blocked capacitance C_{0n}(nF)	42	71	88	76

According to Equation (3.2), the current source intensity I_{sn} is related to the modal velocities by,

$$I_{sn} = \sum_{k=1}^{m} \alpha_{kn} \dot{u}_k \tag{3.7}$$

3.3 Network topology design

The network contains multiple harvesting interfaces. These basic harvesting interfaces will be explained firstly. The network topology designing principle will be illustrated subsequently.

3.3.1 Circuit basic

The basic interface circuits used here are Standard circuit and SSHI circuit (Figure 3-4). Both of them are built by a full-wave diode bridge. The rectified voltage is used to charge the storage capacitor *Cr* directly. The standard circuit here is used for the comparison baseline. In SSHI circuit interface, the piezoelectric element is shunted with a switchable inductor. By operating the series switch on each piezoelectric voltage extremum, the inductor will be connected to circuit for a short time Δt, results in an oscillation discharge of the blocked capacitance of the piezoelectric element which leads to a brief inversion of the capacitance

Cette thèse est accessible à l'adresse : http://theses.insa-lyon.fr/publication/2014ISAL0077/these.pdf
© [Y. Li], [2014], INSA de Lyon, tous droits réservés

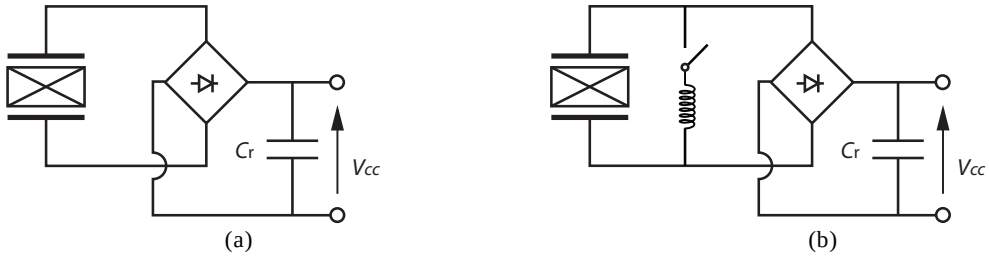

Figure 3-4. Basic energy harvesting circuit (a) Standard circuit (b) SSHI circuit

voltage. Repetition of this process will obtain a magnified voltage in phase with vibration speed thus generating improved electromechanical conversion and energy harvesting power efficiency.

The ”SSHI Technique” used in this work is actually the p-SSHI consisting in adding a switching network in parallel with the piezoelectric element and comprising a 1 *mH* inductance in series with an ideal switch. The switch is driven in such a way to be switched-on at each voltage extremum. This initiates an oscillating discharge of the blocked capacitance in the inverting inductor. The switch on-time Δt corresponds exactly to half an oscillation period ($\Delta t = \pi\sqrt{LC_0}$), thus resulting in an inversion of the voltage. This can be obtained by either controlling precisely this inversion time, or more practically by adding a diode in series with the switch in order to stop the oscillation when the current changes sign. In this case, two switching networks in parallel are necessary, one for positive voltage, the other for negative voltage. Finally the voltage inversion is not perfect since there are losses in the inverting network. These losses are modelled by a non-perfect voltage inversion defined by a coefficient γ set in our case to 0.75.

The secret of high electromechanical conversion ratio is the inversion process. In fact, SSHI circuit is a RLC oscillation circuit when the switch closes. To give insight of SSHI circuit, especially the voltage response V_C in inversion process, several simplification and hypothesis are given. The piezoelectric element is modelled as a controlled current source *Is* shunted with the blocked capacitor C_0. The successor circuit is modelled as the purely resistive load *Rc*. The switchable inductor here is modelled as an ideal switch, an inductor *Li* and a purely resistive *Ri* (represents the losses of inductor) in series. Assume that the current source is de-coupled with load (aka *Constant Displacement*). Based on this preparation work, the target SSHI circuit is illustrated in Figure 3-5.

Assuming the displacement *U* is given as,

$$U = U_m \cos\omega_0 t \tag{3.8}$$

Then the current source I_S is,

$$I_S = \alpha\dot{U} = -\alpha U_m \omega_0 \sin\omega_0 t \tag{3.9}$$

With Kirchhoff’s circuit laws, when the switch is closed, we have,

Cette thèse est accessible à l'adresse : http://theses.insa-lyon.fr/publication/2014ISAL0077/these.pdf
© [Y. Li], [2014], INSA de Lyon, tous droits réservés

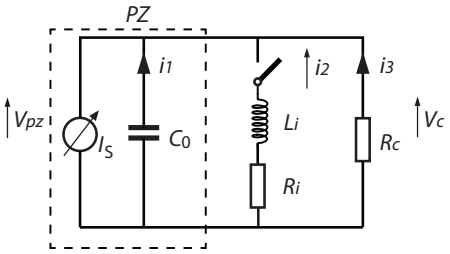

Figure 3-5. The SSHI circuit topology in detail

$$\begin{cases} I_S = C_0 \dfrac{dV_C}{dt} + i_2 + \dfrac{V_C}{R_C} \\ V_C = L_i \dfrac{di_2}{dt} + R_i i_2 \end{cases} \tag{3.10}$$

Obtain,

$$V_C = L_i \frac{dI_S}{dt} - L_i C_0 \frac{d^2 V_C}{dt^2} - \frac{L_i}{R_C} dV_C + R_i I_S - R_i C_0 dV_C - \frac{R_i}{R_C} V_C \tag{3.11}$$

That is,

$$L_i C_0 \frac{d^2 V_C}{dt^2} + \left(\frac{L_i}{R_C} + R_i C_0 \right) dV_C + \left(1 + \frac{R_i}{R_C} \right) V_C = L_i \frac{dI_S}{dt} + R_i I_S \tag{3.12}$$

Equation (3.12) is a classical second order linear nonhomogeneous differential equation; the solution is given as,

$$\begin{aligned} V_C &= e^{-\left(\frac{1}{2R_C C_0} + \frac{\pi}{TQ_E}\right)t} \left(C_1 \cos \beta t + C_2 \sin \beta t \right) \\ &+ \left(-\frac{\alpha U_M \omega_0}{\mathcal{A}^2 + \mathcal{B}^2} \right) \left[\left(\omega_0 L_i \mathcal{B} - R_i \mathcal{A} \right) \cos \omega_0 t + \left(\omega_0 L_i \mathcal{A} + R_i \mathcal{B} \right) \sin \omega_0 t \right] \end{aligned} \tag{3.13}$$

Where,

$$\begin{aligned} \beta &= \sqrt{\frac{4C_0 L_i \left(1 + \frac{R_i}{R_C} \right) - \left(\frac{L_i}{R_C} + C_0 R_i \right)^2}{4C_0^2 L_i^2}}, \\ \mathcal{A} &= \left(\frac{L_i}{R_C} + C_0 R_i \right) \omega_0, \\ \mathcal{B} &= \frac{R_i}{R_C} + 1 - C_0 L_i \omega_0^2. \end{aligned} \tag{3.14}$$

Cette thèse est accessible à l'adresse : http://theses.insa-lyon.fr/publication/2014ISAL0077/these.pdf
© [Y. Li], [2014], INSA de Lyon, tous droits réservés

C_1 and C_2 are the constant determined by boundary conditions. Q_E here is the RLC circuit electrical quality factor. As we discussed in Chapter1, quality factor Q is the ratio of stored energy (represented by inductor L_i) to dissipated energy (represented by resistor R_i),

$$Q_E = \omega_0 \frac{L_i}{R_i} \tag{3.15}$$

From Equation (3.13) we can find that, the voltage response has three different states.

- When $4C_0L_i\left(1+\frac{R_i}{R_C}\right) < \left(\frac{L_i}{R_C}+C_0R_i\right)^2$, the voltage V_C cannot oscillate. It's called nonoscillatory motion state.
- When $4C_0L_i\left(1+\frac{R_i}{R_C}\right) = \left(\frac{L_i}{R_C}+C_0R_i\right)^2$, the voltage V_C just cannot oscillate. It's called critically damped motion state.
- When $4C_0L_i\left(1+\frac{R_i}{R_C}\right) > \left(\frac{L_i}{R_C}+C_0R_i\right)^2$, the voltage V_C can oscillate. It's called oscillatory motion state.

It is obvious that, the SSHI circuit should satisfy the oscillatory motion state. For a given SSHI circuit, the state is only determined by *Rc*. Generally speaking, the *Rc* should be large enough to avoid the nonoscillatory region. On the other hand, the optimal load for SSHI is always larger than $1e^5$ Ohm which makes it in oscillatory motion state. Nevertheless, we should notice that SSHI circuit cannot work with low *Rc* case due to its inversion failure (Figure 3-6).

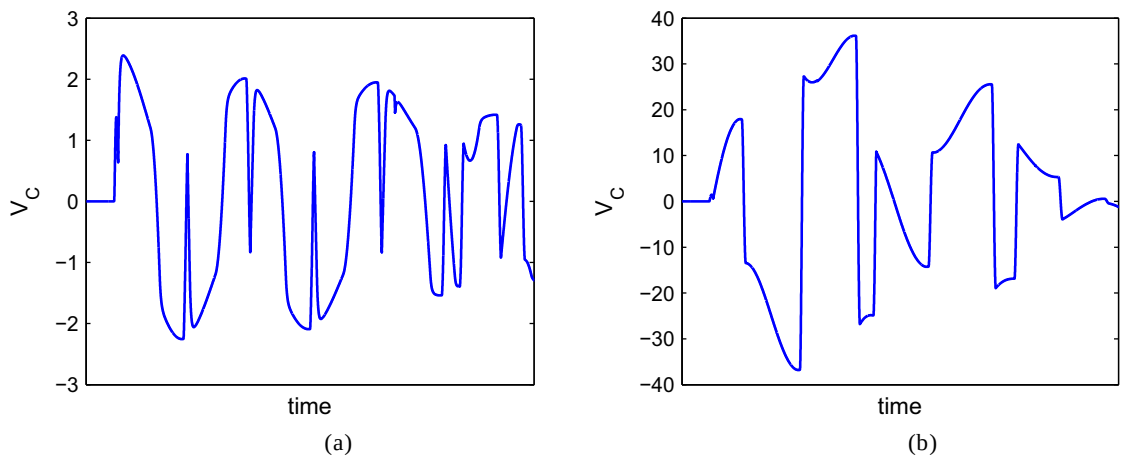

Figure 3-6. The inperfect switch and perfect switch in SSHI. (a) *Rc*=$1e^3$ Ohm. (b) *Rc*=$1e^5$ Ohm

Cette thèse est accessible à l'adresse : http://theses.insa-lyon.fr/publication/2014ISAL0077/these.pdf
© [Y. Li], [2014], INSA de Lyon, tous droits réservés

Equation (3.14) denotes the oscillation angular frequency is,

$$\omega=\sqrt{\frac{4C_0L_i\left(1+\frac{R_i}{R_C}\right)-\left(\frac{L_i}{R_C}+C_0R_i\right)^2}{4C_0^2L_i^2}} \tag{3.16}$$

When *Rc* is large enough, it is simplified to,

$$\omega=\sqrt{\frac{4C_0L_i-\left(C_0R_i\right)^2}{4C_0^2L_i^2}} \tag{3.17}$$

Considering block capacitance is in nF scale, $4C_0L_i \gg \left(C_0R_i\right)^2$,thus,

$$\omega=\sqrt{\frac{1}{C_0L_i}} \tag{3.18}$$

Therefore, the switch on-time is half period,

$$\Delta t=\pi\sqrt{C_0L_i} \tag{3.19}$$

From Equation (3.13), we can find the inversion factor γ, which represents the ratio of voltage after inversion to voltage before inversion(half period),

$$\gamma=e^{-\left(\frac{1}{2R_CC_0}+\frac{\pi}{TQ_E}\right)\frac{T}{2}}=e^{-\left(\frac{T}{4R_CC_0}+\frac{\pi}{2Q_E}\right)} \tag{3.20}$$

It could be simplified to,

$$\gamma=e^{-\left(\frac{\pi}{2Q_E}\right)} \tag{3.21}$$

It is worth to note that, the switch on-time calculation Equation (3.19) is only suitable for large *Rc* case. In other cases, the switch on-time calculation should follow Equation (3.16) to avoid inversion failure (Figure 3-6).

3.3.2 Network topology design

Five different circuit topologies for multiple piezoelectric patches are presented in this subsection. All of them are based either on the Standard Technique (Figure 3-4.a) which includes a rectifier bridge and a storage capacitor, or on the SSHI Technique (Figure 3-4.b).

(A) Standard

The baseline used for comparison is **Standard Network** (topology A, Figure 3-7.a), which is based on standard technique. In this configuration, three harvesters are organized in parallel with a common storage capacitor. The three piezoelectric elements will charge the common storage capacitor simultaneously.

Cette thèse est accessible à l'adresse : http://theses.insa-lyon.fr/publication/2014ISAL0077/these.pdf
© [Y. Li], [2014], INSA de Lyon, tous droits réservés

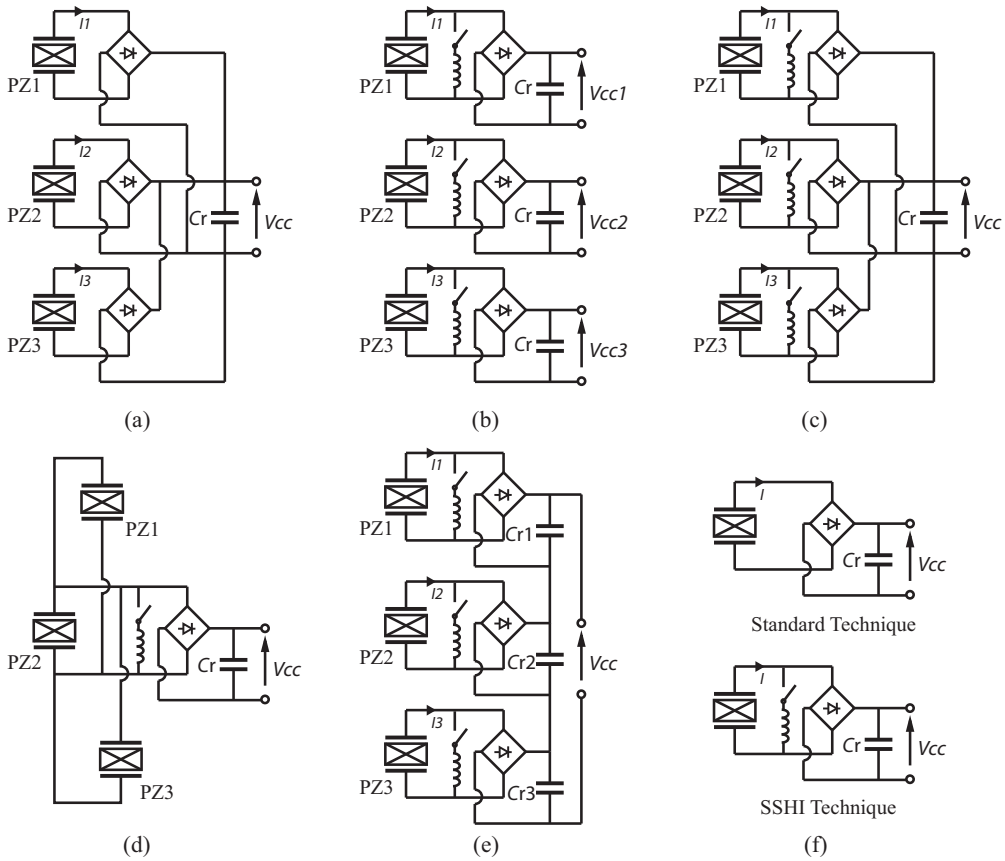

Figure 3-7. Different network topologies for distribtued piezoelectric energy harvester: (a) A. Standard Network (b) B. Independent SSHI Network (c) C. SSHI in Parallel Network (d) D. Mono-SSHI Network (e) E. SSHI in Series Network.

(B) Independent SSHI

The so-called **Independent SSHI Network** (topology B, Figure 3-7.b) is the most straightforward one. It is not really a network since 3 independent harvesters optimized with SSHI circuit are considered. They are totally independent sources. The drawback of this configuration is that the sources are separate. It is the objective of this work to verify that if these independent harvesters can be connected together on a unique harvesting capacitance or load without affecting too much the harvested energy.

(C) SSHI in parallel

An enhanced version of Standard Network is the **SSHI Network in Parallel** (topology C, Figure 3-7.c), with 3 additional non-linear circuits before each diode bridges. Similar to the

Cette thèse est accessible à l'adresse : http://theses.insa-lyon.fr/publication/2014ISAL0077/these.pdf
© [Y. Li], [2014], INSA de Lyon, tous droits réservés

Standard Network, the voltage generated by the bridge cannot charge C_r directly. There is a competition among the three generation patches. The storage capacitor is charged by the harvesters producing an instantaneous output voltage higher than V_{cc}, otherwise the corresponding bridge is blocked. In other words, V_{cc} is mainly determined by the most powerful harvester.

(D) Mono SSHI

Only one SSHI circuit is used in the **Mono-SSHI Network** (topology D, Figure 3-7.d). In this network configuration, all the piezoelectric patches are wired in parallel. This structure is simplified by the using of only one SSHI circuit. However the piezoelectric voltage waveform is more complex due to all the patches and vibration modes contributions.

(E) SSHI in series

Instead of adding the generated currents such as in topology C, it could be interesting to sum up the output voltages in order to generate a higher output voltage. The **SSHI Network in Series** (topology E, Figure 3-7.e) is designed by connecting the output capacitances of the 3 harvesters in series. Each piezoelement energy extraction is optimized with a parallel SSHI network. The total output voltage capacitor consists of the series association of the 3 output capacitances. This topology has the independent character of Topology B, but results in a unique high output voltage source. Moreover, in order to respect the equality of charge of the 3 output capacitances, charge redistribution takes place within the output arrangement resulting in a slight output voltages increase of the less powerful harvesting unit.

3.4 Power performance comparison

3.4.1 Decay time (Energy harvesting process)

In the case of pulse excitation mode, the amplitude of the structure displacement is continuously decreasing due to damping and energy extraction. The typical waveforms of the 4 modal displacements are shown on Figure 3-8.a. It is clearly that the kinetic energy stored in mode 1 is slower (frequency) than higher order mode. For each case, the initial maximum amplitudes of the 4 modes are around 0.046 *mm*, 0.018 *mm*, 0.0016 *mm* and 0.0014 *mm*, respectively. If the displacement decay is quick, a larger part of the initial mechanical energy can be transformed into electrical energy via the piezoelectric harvesters. The reference decay time is defined as the time needed to decrease the displacement down to 10% of the initial amplitude. As the mechanical damping coefficient is the same in all the cases, a comparison of these decay times shown of Figure 3-8.b is a good image of the harvesting capabilities. It can be observed globally that, the mode 1 decay time is the longest while the mode 4 one is shortest,

Cette thèse est accessible à l'adresse : http://theses.insa-lyon.fr/publication/2014ISAL0077/these.pdf
© [Y. Li], [2014], INSA de Lyon, tous droits réservés

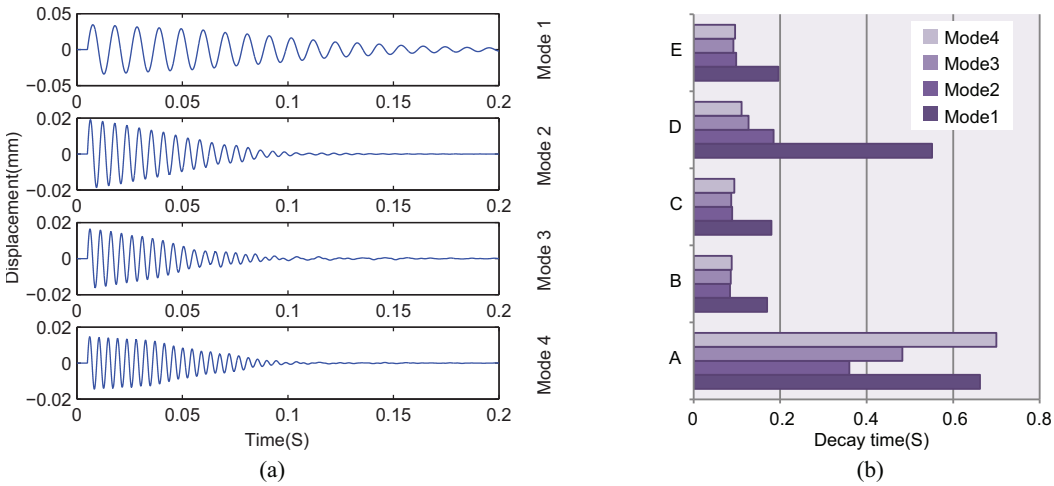

Figure 3-8. Damping of the structure: (a) The 4 modal displacement waveforms for topology C (b) Decay time comparison.

except in topology A. This is mainly a consequence of the SSHI device. Due to the complex nature of the voltage waveform and as the switch is triggered on each voltage extremum, SSHI firstly improves harvesting on the highest frequency modes, then when the amplitude of these modes have decreased significantly, extraction and the corresponding damping affect the lower one. All the SSHI based topologies (B, C, D and E) present better harvesting capabilities with much quicker decay times than the standard based topology A.

A significant difference can also be observed on Figure 3-9. It represents for the various topologies the 3 harvesting piezoelement voltage waveforms, as well as the output voltage V_{cc} (dashed line) as a function of the time. The complexity of the multimodal waveform is clearly seen for the topology A. In the other cases, switching is visible, initially triggered principally on the higher modes extremum, then on the lower modes at the end of the pulse. When a current flows from the bridges, the piezoelectric element voltages are flattened by the voltage V_{cc} imposed by the output capacitance. Due to the diodes threshold (2 x 0.6V), the V_{cc} voltage appears to be a little lower than the piezoelectric voltages. It is clear from the Figure 3-9 switching patterns that in topologies B, C and E, the energy is extracted from all the modes and particularly also from mode 1. It is coherent with the decay times shown on Figure 3-8.b

In the case of topology D, all the patches are connected together, thus resulting in a global voltage common to the 3 piezoelectric elements. This voltage is built with the contributions of the 12 α_{mn} terms given on Table 3-1 and of the four considered vibration modes. The consequence is a lot of local extreme and a resulting complex switching pattern that degrades the benefit of the SSHI network on the global extracted energy. In fact, when only one piezoelement is considered, the voltage generated is an image of its own strain.

Cette thèse est accessible à l'adresse : http://theses.insa-lyon.fr/publication/2014ISAL0077/these.pdf
© [Y. Li], [2014], INSA de Lyon, tous droits réservés

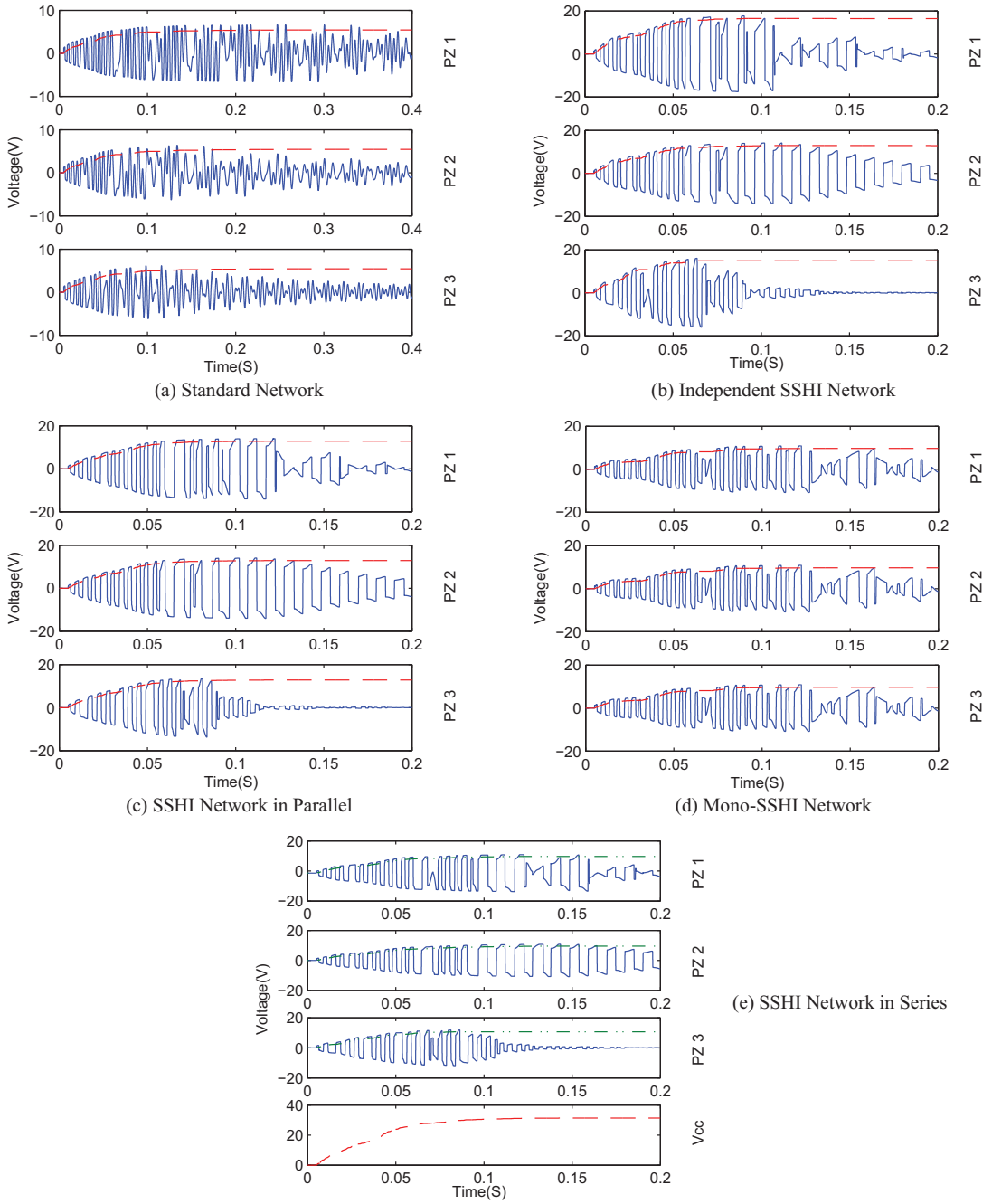

(a) Standard Network
(b) Independent SSHI Network
(c) SSHI Network in Parallel
(d) Mono-SSHI Network
(e) SSHI Network in Series

Figure 3-9. Voltage waveform of the 3 harvesting piezoelectric elements. Solid line represents the piezovoltage, dashed line represents the harvested voltage on storage the capacitor

Cette thèse est accessible à l'adresse : http://theses.insa-lyon.fr/publication/2014ISAL0077/these.pdf
© [Y. Li], [2014], INSA de Lyon, tous droits réservés

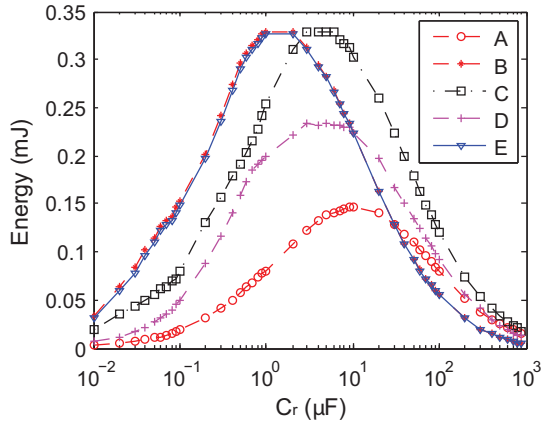

Figure 3-10. Harvested energy versus the capacitance C_r, A. Standard Network. B. Independent SSHI Network. C. SSHI Network in Parallel. D. Mono-SSHI Network. E. SSHI Network in Series.

Therefore, as the switching is synchronized with its own generated voltage, it is properly synchronous with the strain and it results in higher extracted energy. This natural correspondence is lost in the last case. Switching on the highest modes appears to be effective but the system is unable to extract energy on mode 1 as it is visible on Figure 3-8.b.

In the case of topology E, in addition to the V_{cc} voltage waveform plot on the lowest graph, dotted line curves materialize the voltages on the 3 output capacitances that are connected in parallel.

3.4.2 Power performance

The simulations are made essentially in pulse mode. The input energy of the pulse is nearly constant for all the considered and is equal to 0.88 *mJ*. For each topology, the structure modal displacements, piezoelement voltages and output capacitance voltages are calculated. The various topologies are compared in terms of total extracted energy which is the energy on the output capacitance when all the energy in the structure vanished. No load is connected on the output capacitance during this process. It is known that in this mode[50] the output energy is dependent on the output capacitance. Therefore for each topology, this optimal capacitance is defined as shown on Figure 3-10 showing the variation of the final harvested energy versus C_r. The results presented and discussed in the next sections are obtained exclusively with the optimal capacitance.

The various topologies will also be compared in terms of damping (modal displacement decay). Due to the inherent viscous losses that degrade the initial mechanical energy within the structure, the energy extraction process has to be as quick and efficient as

Cette thèse est accessible à l'adresse : http://theses.insa-lyon.fr/publication/2014ISAL0077/these.pdf
© [Y. Li], [2014], INSA de Lyon, tous droits réservés

possible in order to avoid losing the finite initial mechanical energy during the structure ringing.

3.4.3 Energy balance

The total energy in the structure E_R comprises kinetic energy, elastic potential energy and electrostatic energy stored in piezoelectric element blocked capacitances. These energies can be calculated according to the modal model of the structure as,

$$E_R = \frac{1}{2}\sum_{j=1}^{4} K_j^E u_j + \frac{1}{2}\sum_{j=1}^{4} M_j \dot{u}_j^2 + \frac{1}{2}\sum_{k=1}^{4} C_{0k} V_k^2 \tag{3.22}$$

A part of this energy is lost as viscous losses in the structure and the last part is extracted via the energy harvesting process and contributes to the energy stored in the output capacitance C_r. Note that a part of the energy is also lost in the inverting SSHI network according to the inversion coefficient mentioned previously. For topologies A, C and D, the harvested energy E_H is given by:

$$E_H = \frac{1}{2} C_r V_{cc}^2 \tag{3.23}$$

In the case of topology B, as there are multiple output capacitances ($C_{r1} = C_{r2} = C_{r3}$), the harvested energy is expressed as:

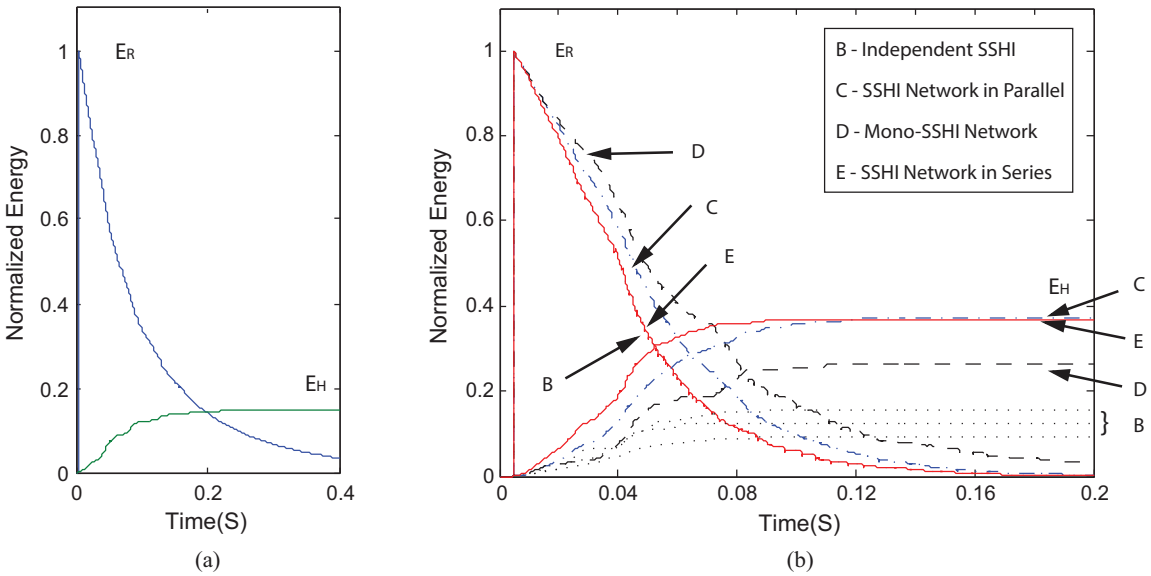

Figure 3-11. Mechanical and harvested energy variations during the pulse (the values are normalized according to the initial pulse energy: 0.88 *mJ*: (a) Standard Network (b) SSHI based networks.

Cette thèse est accessible à l'adresse : http://theses.insa-lyon.fr/publication/2014ISAL0077/these.pdf
© [Y. Li], [2014], INSA de Lyon, tous droits réservés

$$E_H = \frac{1}{2}\sum_{j=1}^{3} C_{rj} V_{ccj}^2 \tag{3.24}$$

In the case of topology E, due to the series connection of 3 identical capacitances ($C_{r1} = C_{r2} = C_{r3} = C_r$), the harvested energy E_H is calculated by,

$$E_H = \frac{1}{2}\left(C_{r1}, C_{r2}, C_{r3}\right)_{series} V_{cc}^2 = \frac{1}{6} C_r V_{cc}^2 \tag{3.25}$$

Figure 3-11 illustrates the energy decay in the structure and the corresponding harvested energy increase for the various considered cases. The energies are normalized according to the pulse energy which is initially converted only into mechanical energy. Due to the competition with the mechanical losses, which represents the difference between the harvested energy upward slope and the mechanical energy downward one, the more effective is the energy extraction performance, the shorter would be the harvesting energy process and the higher would be the total harvested energy. According to this representation, the C and E harvester networks extract the same energy as the 3 harvesters of topology B, while the D configuration extracted energy is 30% lower. The best total energy conversion efficiency is approximately 40%. These results show the feasibility of associating a network of harvester either in series or in parallel while using p-SSHI. Moreover, it shows that it is necessary to have one SSHI network per piezoelectric element.

3.4.4 Influence of the coupling coefficients

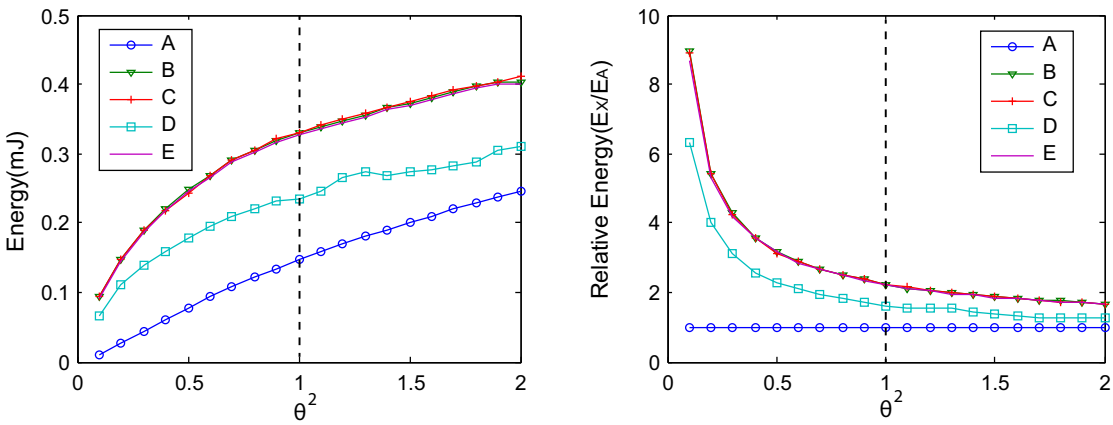

(a) (b)

Figure 3-12. Total harvested electrical energy versus the square of the coupling multiplication factor. Each simulations are obtained with the optimal output capacitance A. Standard Network. B. Independent SSHI Network. C. SSHI Network in Parallel. D. Mono-SSHI Network. E. SSHI Network in Series: (a) Harvested energy (b) Normalized harvested energy.

Cette thèse est accessible à l'adresse : http://theses.insa-lyon.fr/publication/2014ISAL0077/these.pdf
© [Y. Li], [2014], INSA de Lyon, tous droits réservés

The globally low harvesting efficiency obtained is a consequence of the low piezoelectric coupling coefficients of the total structure. Note that, as direct energy harvesting is considered, the efficiency is calculated according to the global vibration energy of the structure. Now, it is known that the total harvested energy and the corresponding global efficiency is directly a function of the k^2Q_M figure of merit, it is therefore interesting to visualize the influence of the coupling coefficients for the various networks considered here. Since a multi-modal vibration model with many piezoelectric elements is considered, the variation of particular coupling coefficients is not trivial. It is therefore chosen to artificially change the entire coefficients simultaneously according to a unique multiplication factor θ^2 lying between 0.3 and 1.4. Then the modified coupling factor is expressed as,

$$k^2_{\mathrm{mod}\,ified} = \theta^2 k^2 \tag{3.26}$$

The corresponding extracted energy simulations are shown on Figure 3-12 as a function of θ^2. Figure 3-12.a shows the extracted energy while Figure 3-12.b shows the energies normalized according to the energy extracted by the baseline topology A.

It is shown that especially for weak coupling conditions, the B, C and E topologies, benefiting from the p-SSHI network, are especially advantageous. For a unique piezoelectric element with parallel SSHI, the extracted energy ratio with the standard case is given for very low coupling coefficient as a function of the inversion coefficient γ by[62]:

$$P_{SSHI} = \frac{2}{1-\gamma} P_{STD} \tag{3.27}$$

Considering that γ=0.75 in the present study, P_{SSHI} is around 8 times larger than P_{STD}. It is interesting to note that, at weak coupling condition, the SSHI based network topologies could also reach 6.5 to 9 times the energy harvested by topology A(Figure 3-12).

3.5 Improvement for pulse operation

During one pulse operation, the energy stored in higher modes is harvested firstly, and then the energy stored in lower modes is scavenged from the vibration plate. The capacitor will only be charged when the charging voltage is higher than the capacitor voltage. Due to this capacitor charging limitation, once the storage capacitor is charged strongly by the high vibration modes, most of the energy stored in lower modes is wasted (Figure 3-9). Although the energy stored in lower modes are scavenged by SSHI technique, the energy transferring is blocked by the full-wave bridge. The charging process is aborted until the energy in storage capacitor is decreased. This are two way to decrease the energy of storage capacitor, driving other devices and use another capacitor as replacement. Here, the latter solution is chosen and the object of this part is to discuss the harvested energy.

Cette thèse est accessible à l'adresse : http://theses.insa-lyon.fr/publication/2014ISAL0077/these.pdf
© [Y. Li], [2014], INSA de Lyon, tous droits réservés

The block action of the bridge will be cancelled when the second empty capacitor is switched. Thus we replace the storage capacitor with a capacitor charging group. This capacitor charging group consists of two capacitors in parallel and one switch. The switch connects with one capacitor firstly, and then after a delay time t, the switch is set to connect with another capacitor. Therefore, once the first capacitor C_{r1} is charged fully, the second capacitor C_{r2} is available for continuous charging. The switch command is driven by a delay unit. The delay unit will be triggered as long as the pulse vibration occurs.

With this new strategy (Figure 3-13), the harvested voltage in storage capacitor increased allowing the increment of harvested energy. This storage capacitor array could be used to enhance these network topologies. For instance, set the delay time as 0.1S, storage capacitor as 10 µF for both C_{r1} and C_{r2}, the harvested energy of enhanced topology C is around 0.45mJ while it is only 0.30 mJ for normal topology C with 10 µF storage capacitor. In other words, this storage capacitor array can improve the harvested energy by 50%. Figure 3-14 provides a global comparison of such storage capacitor array to mono storage capacitor used in normal approach. On the optimal storage capacitor, with the improvement of storage capacitor portion, the enhanced topology C can store 46% more energy than normal topology C dose.

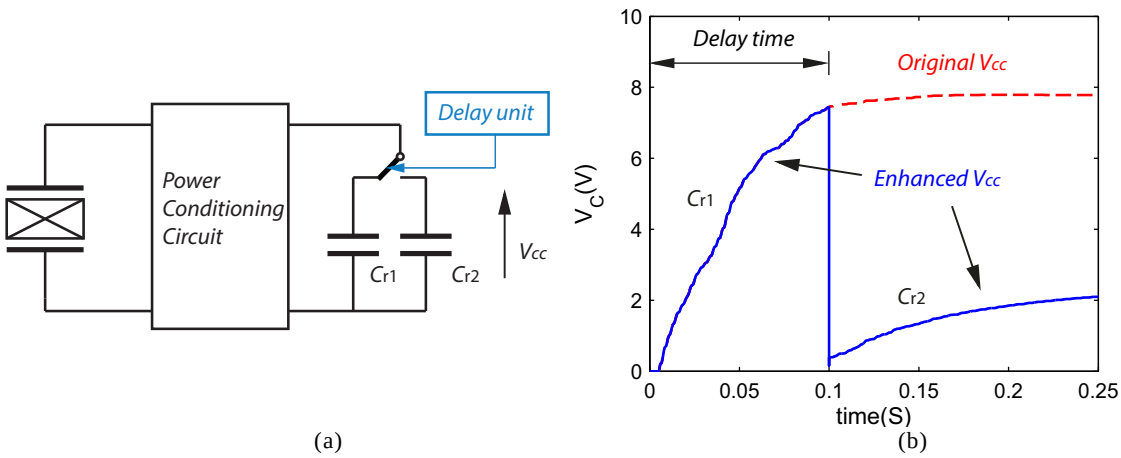

Figure 3-13. The enhanced storage capacitor for pulse operation (a) the circuit (b) the harvested voltage

Cette thèse est accessible à l'adresse : http://theses.insa-lyon.fr/publication/2014ISAL0077/these.pdf
© [Y. Li], [2014], INSA de Lyon, tous droits réservés

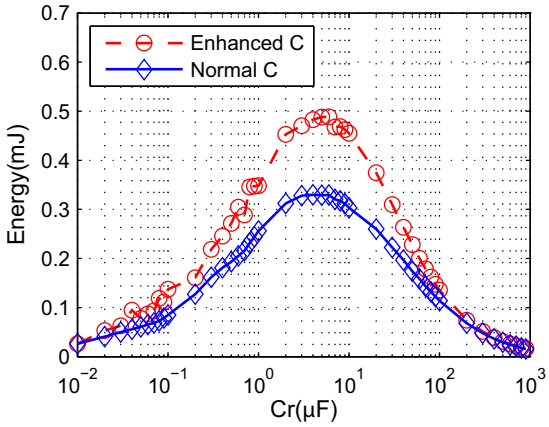

Figure 3-14. Harvested eenrgy compasition of enhanced storage capacitor and normal storage capacitor. Topolocy C is used, pulse excitaiton. The value of capacitors in enhanced version are identical

3.6 Bonding effect

If the considered host structure is made with an insulating material such as GFRP(Glass Fiber Reinforced Polymer) or glass, it is clear that the piezoelectric electrode potentials are totally floating, therefore the various piezoelectric harvesters can be wired without trouble according to the various topologies of Figure 3-7. Inversely, if the structure is made with steel or aluminum as it is often the case, precautions have to be taken.

Indeed, a contact between the piezoelectric element electrodes and the structure would short circuit part of the harvesting rectifier bridges and would modify the global topology of the network resulting in degraded energy harvesting. In this case, it is therefore compulsory to insulate the bottom electrode of each piezoelectric element. This insulation is simply obtained with a thick enough bonding layer usually obtained with epoxy material used for bonding the piezoelectric element to the structure.

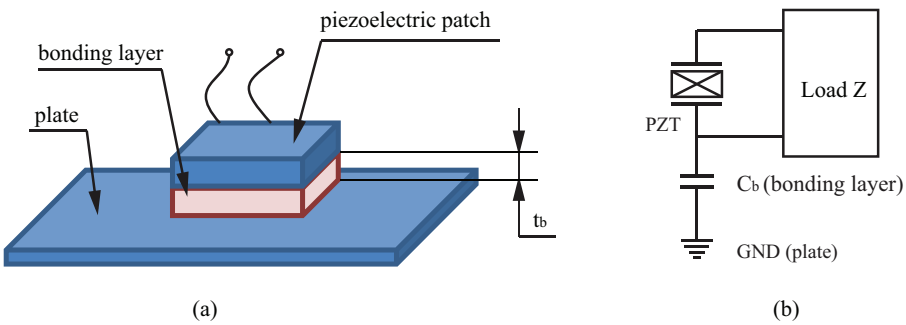

Figure 3-15. Definition of the insulating bonding layer: (a) schematic of the t_b thick bonding layer; (b) Corresponding electric capacitance C_b.

Cette thèse est accessible à l'adresse : http://theses.insa-lyon.fr/publication/2014ISAL0077/these.pdf
© [Y. Li], [2014], INSA de Lyon, tous droits réservés

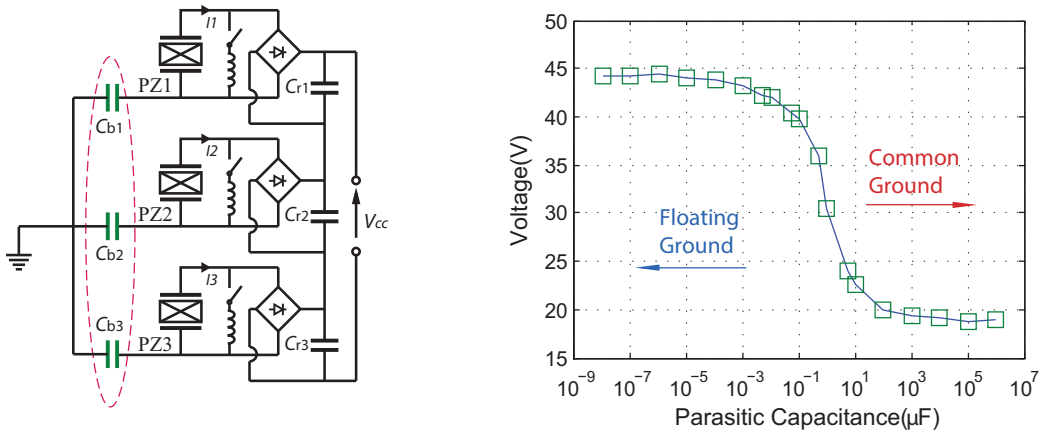

(a) (b)

Figure 3-16. Parasitic capacitance effect on the network harvesting performance with perfect coupling: (a) Location of the bonding parasitic capacitances within the E network. (b) Harvested voltage as a function of C_b.

In order to study the effect of this insulating layer, the parasitic capacitance C_b resulting from the insulating bonding layer between the bottom electrode of the piezoelectric element and the surface of the host structure is considered as illustrated on Figure 3-15. As a general capacitance parameter definition, this parasitic C_b is given by,

$$C_b = \frac{\varepsilon_0 \varepsilon_b A}{t_b}, \tag{3.28}$$

where t_b is the bonding layer thickness, A is the electrode area, ε_0 and ε_b are the vacuum permittivity and relative permittivity, respectively.

Figure 3-16.a illustrates how this capacitance has to be taken in account in the electric network. When t_b is low, the capacitance C_b appears to be very high, thus approaching to short circuit condition, and therefore all the piezoelectric elements bottom electrodes are connected to the metallic structure common ground. Inversely when t_b is large, this capacitance C_b decreases, establishing floating potentials for all the piezoelectric elements. In the case of topology E, the performance of the energy harvesting network has been simulated versus the value of the parasitic capacitance C_b. The simulation results are summarized on Figure 3-16 .b. For low value of C_b, corresponding to floating ground conditions, the harvested energy is similar to what has been presented in previous sections. For high value of C_b, the short-circuited diodes bridges do not work adequately and there is a drastic decrease of the harvested energy. The threshold is approximately 20 nF, corresponding to a 14 μm bonding thickness in the case of a classical epoxy (physical parameters listed on Table 3-2).

From these results, it appears that the higher is the bonding layer thickness, the better the harvesting network performs. Now it is known that a too thick and soft bonding layer would

Cette thèse est accessible à l'adresse : http://theses.insa-lyon.fr/publication/2014ISAL0077/these.pdf
© [Y. Li], [2014], INSA de Lyon, tous droits réservés

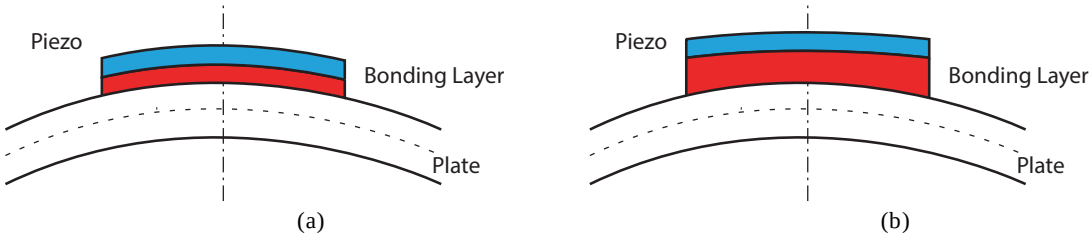

Figure 3-17. The thickness affects the bending of piezoelectric element (a) ideal bending (b) bonding layer is too thick

also result in the degradation of the piezoelectric bending (Figure 3-17). Consequently, there should be an optimal t_b. It would result from a trade-off between a layer thick enough to ensure floating ground conditions and the validity of the considered network topology, and thin enough to do not degrade the fundamental piezoelectric coupling.

In order to approach this trade-off the variation of the coupling with the bonding layer thickness has been considered. As defined previously in the case of a bimorph actuator, when a finite stiffness bonding layer with shear modulus G_b and thickness t_b is included between the structure and actuator, there is imperfect actuation due to shear lag in the bonding layer and the ideal curvature κ_0 that would be obtained for perfect bonding decreases and becomes a function of the bonding layer characteristics[100, 101]. According to reference[101], the curvature κ is related to the shear lag parameter as follows:

$$\kappa = \kappa_0 \left(1 - \frac{1}{\Gamma}\tan(\Gamma)\right) \tag{3.29}$$

Where Γ is a function of the piezoelectric actuator Young modulus E_p, thickness t_p and length l according to:

$$\Gamma^2 = \frac{\left(G_b/E_p\right)\left(t_b/t_p\right)}{\left(t_b/l\right)^2}\left(\frac{\alpha+\psi}{\psi}\right) \tag{3.30}$$

Table 3-2. Direct piezoelectric harvester deploying parameters

Material	Parameter	Symbol(Unit)	Numerical value
Metallic plate(steel)	Thickness	tm(mm)	1.0
	Young modulus	Em(GPa)	210
Piezoelectric layer(PZT P189)	Thickness	tp(mm)	0.6
	Young modulus	Ep	80
	Relative permittivity	ε_p	1250
	Length	l(mm)	20
Bonding layer	Shear modulus	G_b(GPa)	2.4
	Relative permittivity	ε_b	3.5

Cette thèse est accessible à l'adresse : http://theses.insa-lyon.fr/publication/2014ISAL0077/these.pdf
© [Y. Li], [2014], INSA de Lyon, tous droits réservés

The geometric constant α is set to 6 for bending[101]. ψ is the relative stiffness parameter, it is defined as a function of the piezoelectric layer stiffness and thickness as well as a function of the metallic structure stiffness E_m and thickness t_m as:

$$\psi = \frac{E_m t_m}{E_p t_p} \tag{3.31}$$

Finally the piezoelectric force coefficient α_{mn} which are proportional to the flexure induced strain are proportional to the curvature, hence they vary according to Figure 3-18.a showing the variation of the normalized curvature (κ/κ_0) as the function of the bonding layer thickness t_b. The data indicates that κ weakly depends on t_b when t_b is smaller than 100 μm. These calculations have been made according to the data gathered in Table 3-2. The considered bonding layer material is epoxy. The length of the piezoelectric actuator is 20 *mm*, corresponding to the smallest length of the segmented configuration described in Section 3.2.

Exploiting the piezoelectric force coefficient variation shown on Figure 3-18.a and considering that the overall harvested voltage is proportional to the voltage coefficients, it is possible to derive the output harvester network voltage as a function of the bonding layer thickness. This is done on Figure 3-18.b according to the definition of the parasitic capacitance given by Equation(3.28). This last figure shows the variation of the harvested voltage as a function of the bonding layer thickness. This shows that the aforementioned trade-off can be reached for a perfectly feasible and controllable bonding layer thickness leading to a maximal piezoelectric harvesting network output voltage. It shows that for a thickness between 0.001 *mm* ~ 1 *mm*, the harvested voltage drop is still moderate. The optimal bonding ranges between 10 to 40 μm level where a small enough capacitance allows an isolation sufficient for the network and without any strong degradation of the piezoelectric coupling coefficients.

3.7 Conclusion

This chapter investigates the feasibility of the association of distributed piezoelectric energy harvesters in order to form a unique source of energy in the case of a planar structure excited in pulse mode. It is the direct energy harvesting harvester which the piezoelectric elements are bonded directly on the vibration source. The considered harvesting circuits are standard technique and SSHI technique. Then they are arranged with multi piezoelectric elements in various forms to develop five different network topologies. These network topologies are standard network, independent SSHI network, SSHI in parallel network, Mono-SSHI network and SSHI in series network.

Firstly, all the five topologies have been compared in terms of structure damping, harvested voltage and energy. It is shown that associating in parallel or in series different harvesting units, each comprising a piezoelectric element, a parallel SSHI network and a rectifier diode bridge, do not change significantly the harvested power in comparison with usual separate harvesters. It is however compulsory, in the case of a complex vibration pattern,

Cette thèse est accessible à l'adresse : http://theses.insa-lyon.fr/publication/2014ISAL0077/these.pdf
© [Y. Li], [2014], INSA de Lyon, tous droits réservés

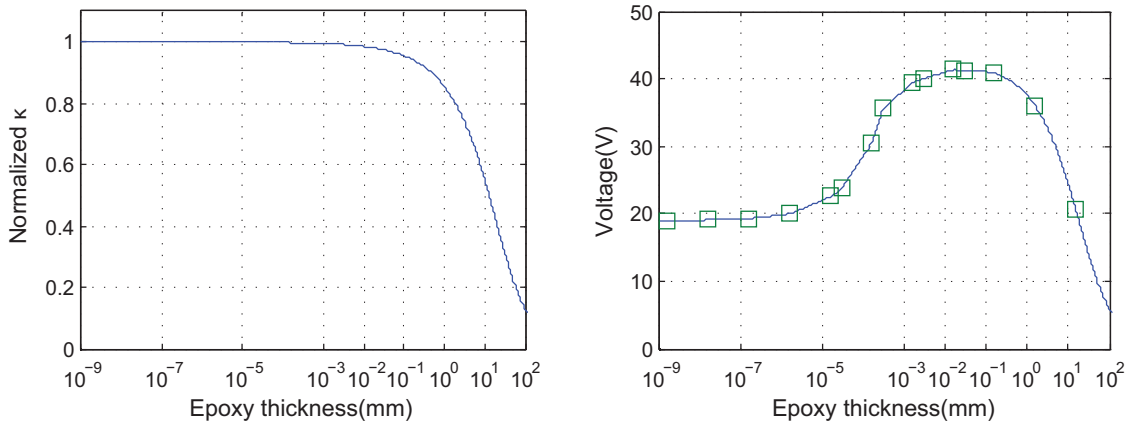

(a) (b)

Figure 3-18. Bonding Layer thickness influence on the harvester performance: (a) The piezoelectric force coefficient vs. the bonding layer thickness (normalized) (b) Overall harvested voltage.

to add as many SSHI network as piezoelectric elements used. Considering the practical applications, when higher output voltage is required, SSHI in series network is a good candidate. If higher current is preferred, SSHI in parallel network is preferable. Despite its simplicity, using a unique SSHI network in parallel with an association of piezoelectric elements will degrade the harvesting capability. Indeed, it is similar to the random vibration case. Low frequency switch operation cannot extract sufficient energy while higher frequency switch operation will degrade the efficiency due to the losses in the switch components (switch and inductor). In this case, the tradeoff of frequency of switch for such non-linear technique should be considered [102].

Then, a storage capacitor array mechanism is proposed to decrease the waste of extracted energy. It's a common issue that the extracted energy will be discarded when the capacitor is charged fully, in pulse excitation case. A storage capacitor array, consisting of two or more capacitors and delayed switch is used to increase the energy harvesting efficiency. Once the first capacitor is fully charged, it will disconnect from the harvesting circuit. At the same time, the second capacitor will be placed in the circuit to have continuously harvesting. The delay time is related to the pulse excitation amplitude and the character of energy harvester. Referring the voltage waveform in this chapter, the delay time could be 0.1 for SSHI network in parallel topology.

Then the problem of the electric insulation of the elements of the network in the case of a metallic conductive structure has been considered, and especially the influence of the thickness of the insulating bonding layer between the planar piezoelectric element and the structure. This layer is compulsory to ensure a proper energy harvesting, but in the same time,

Cette thèse est accessible à l'adresse : http://theses.insa-lyon.fr/publication/2014ISAL0077/these.pdf
© [Y. Li], [2014], INSA de Lyon, tous droits réservés

it degrades the piezoelectric element coupling coefficient. A very realistic 10 to 40 μm thick bonding layer is shown as a good trade-off ensuring both electrical integrity of the network and high energy extraction level.

All results demonstrate the possibility to build direct piezoelectric energy harvesting networks useful in the case of large bodies or shells where the harvesting piezoelectric elements are distributed all over the structure in the regions of maximum strain. Moreover, such distributed energy harvesters can also be used for multi-frequencies energy harvesting. The discussion of topology design provides the reference for energy harvesting toward wide bandwidth.

Cette thèse est accessible à l'adresse : http://theses.insa-lyon.fr/publication/2014ISAL0077/these.pdf
© [Y. Li], [2014], INSA de Lyon, tous droits réservés

(this page intentionally left blank)

Cette thèse est accessible à l'adresse : http://theses.insa-lyon.fr/publication/2014ISAL0077/these.pdf
© [Y. Li], [2014], INSA de Lyon, tous droits réservés

CHAPTER 4 Synchronized Serial switch for piezoelectric energy harvesting

4.1 Motivation

4.2 Energy harvesting modelling

4.2.1 Piezogenerator electro-mechanical model

4.2.2 Analytical model development: Constant displacement

(A) Standard circuit

(B) S3H circuit

4.2.3 Analytical model development: Constant force

(A) Standard circuit

(B) S3H circuit

4.3 Circuit performance discussion

4.3.1 Duty cycle

(A) Constant displacement

(B) Constant Force

4.3.2 Electromechanical coupling effect

4.4 Experimental validation

4.4.1 Set-up

4.4.2 Mono-mode case study

4.4.3 Multi-mode case study

4.5 S3H working in pulsed mode

4.6 Combination with Buck-boost circuit

4.7 Conclusion

4.1 Motivation

The operation condition for a piezoelectric energy harvester is dynamic and complex. The convention of energy harvesting circuit relies on load matching as it was discussed in Chapter 2. The coupling coefficient of such electromechanical system can be improved by fine structure design or adaptive energy harvesting circuit (i.e. SSHI circuit). However, the system sensitivity

Cette thèse est accessible à l'adresse : http://theses.insa-lyon.fr/publication/2014ISAL0077/these.pdf
© [Y. Li], [2014], INSA de Lyon, tous droits réservés

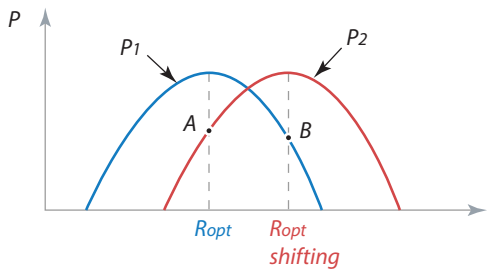

Figure 4-1. The shifting of optimal load

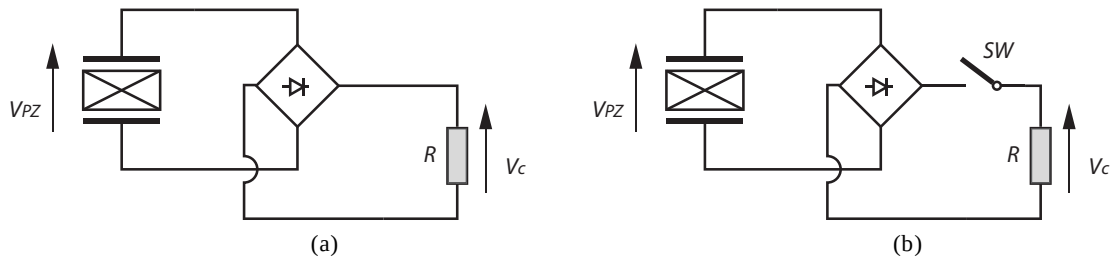

Figure 4-2. Two energy harvsting circuits (a) Standard circuit (b) S3H circuit

to the load is also increased with the increasing of the energy harvesting ability. For any matched load driven system, the load shifting degrades strongly the harvested energy (Figure 4-1).

The advanced circuit (i.e. SSHI) is strongly dependent on the load impedance. In order to improve the load bandwidth (as well as the extraction frequency bandwidth) and to obtain independence to the load, an alternative technique called SECE has been developed. The corresponding topology is very similar to the well-known buck boost chopper as show on Figure 4-3. Following this process, the switch is triggered-on each time the voltage reaches an extremum. According to the voltage imposed by the rectifier, the diode is blocked and the electrostatic energy initially within the blocked capacitance of the piezogenerator is transferred to the inductance by an increase of the ongoing current. When this current is max and that the piezoelectric element is completely discharged, the switch is opened and therefore, in order to ensure continuity of the inductance current, the diode switches on and the magnetic energy in the inductor is finally transferred to the load. Due to a characteristic transfer time much smaller than the vibration period, the resulting voltage on the piezoelement is very similar to the SSDS damping technique voltage. It is amplified and time shifted compared to the standard technique resulting in improved energy extraction. However, the 200% improvement achieved is much smaller than the SSHI performance. The main advantage results from a total independence of the extracted power to the load due to the pulsed character of the oscillating charge period (LC_0 circuit). Now best performance relies on a precise time of the switch on-time to exactly one quarter of the oscillation period. Moreover, as this oscillation frequency is dependent on the

Cette thèse est accessible à l'adresse : http://theses.insa-lyon.fr/publication/2014ISAL0077/these.pdf
© [Y. Li], [2014], INSA de Lyon, tous droits réservés

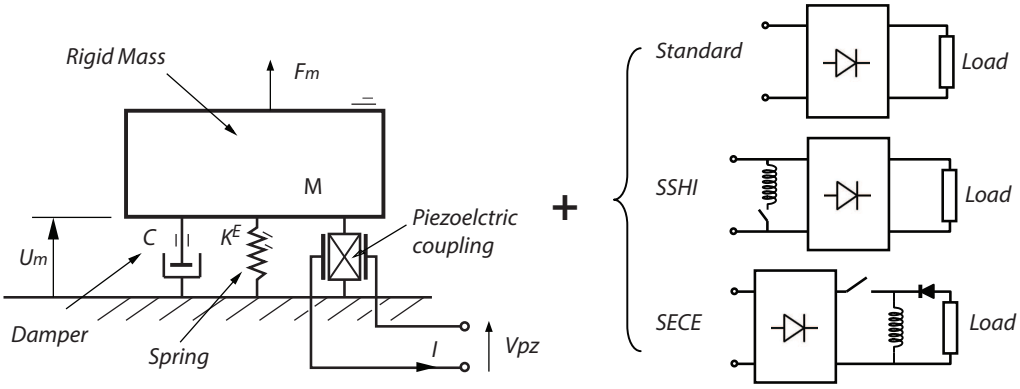

Figure 4-3 The MDS modeling method

piezoelement capacitance which could present variations with the temperature or the stress, adjustable tuning has to be implemented.

The objective of the technique proposed here is to develop a circuit interface with the same power extraction capability as SECE with a comparable independence to the load, but without any need for fine tuning of the switch on-time. The proposed topology schematically depicted on Figure 4-2.b is called Synchronized Serial Switch Harvesting (S3H) because it is simply implemented with a simple switch in series between the bridge rectifier and the load. This switch is triggered-on at each voltage extremum (or displacement extremum) and remains closed for an imposed and arbitrary on-time t_0, no larger than half the oscillation period. As for SECE, the extracted power is pulsed and therefore independent to the vibration frequency and consequently to the load.

This chapter is organized as follows. The analytical development based on electrical differential equations will be given in Section 4.2. Based on this analytical model obtained in previous section, the circuit property will be investigated and compared with STD technique in Section 4.3. Section 4.4 will validate the analysis by a precise set of experiments. Both the mono-mode and multi-mode sinusoidal excitations will be considered. Section 4.5 will validate the feasibility of direct charging capacitor by S3H. A short investigation of buck-boost combination will be discussed in Section 4.6. The conclusion will be made in Section 4.7.

4.2 Energy harvesting modelling

4.2.1 Piezogenerator electro-mechanical model

The considered piezogenerator is a simple vibrating structure, such as a plate of a cantilever beam, equipped with a piezoelectric plate bonded usually close to the attachment. This structure can be either a resonator designed to be excited by the vibration of the host structure (such as indirect harvesting with seismic harvester) or directly the structure equipped with a

Cette thèse est accessible à l'adresse : http://theses.insa-lyon.fr/publication/2014ISAL0077/these.pdf
© [Y. Li], [2014], INSA de Lyon, tous droits réservés

harvesting piezoelement (direct harvesting). In the case considered here the piezogenerator is excited by a mono-modal sinusoidal excitation force $F_m(t)$ with a frequency close to its natural frequency. For low amplitude displacement, for which the motion is assumed to be linear and close to the considered resonance mode, the structures behavior can be reliably and simply modelled as the Spring-mass-damper system illustrated on Figure 4-3. With this assumption, M is the equivalent mass of structure, K^E the stiffness in short-circuit and C the damping coefficient of the considered mode. U represents the motion (displacement) of the structure. These parameters can be easily identified from the real structure as described in Literature[61].

This structure previously described using electric equivalent circuit is represented here by Equations(4.1)(4.2). Equation (4.1) is usually referred as the mechanical equation since it represents the dynamic mechanical equilibrium. Equation (4.2) is the electrical equation representing the relation between the voltage V_{PZ} and the outgoing current I flowing from the piezoelement. In these equations, F is the external force exerted on the structure, α is the piezoelectric force factor representing the electromechanical coupling and C_0 is the blocked capacitance of the piezoelement.

$$M\ddot{U} = F - K^E U - \alpha V_{PZ} - C\dot{U} \tag{4.1}$$

$$I = \alpha\dot{U} - C_0\dot{V}_{PZ} \tag{4.2}$$

In the following, the analytical development of the proposed energy harvesting circuit is given. First, constant displacement excitation case is discussed. Then by relating the damping of the harvesting structure to the first-harmonic component frequency of the voltage, the response under constant force excitation is also derived.

4.2.2 Analytical model development: Constant displacement

Firstly, we consider a special case, the various loads don't damp the harvester. This case results from out of resonance operation, low coupling or high natural damping. In the viewpoint of harvester, the displacement is constant. If the harvester is excited by sinusoidal signal, the displacement U of structure can be expressed as,

$$U = U_m \cos\omega t \tag{4.3}$$

U_m is the harvester vibration amplitude and ω is the corresponding angular frequency. As we discussed in Chapter 1, the piezoelement can be schematically represented as a current source Is in parallel with the capacitance C_0 as shown on Figure 4-4.a. The current source Is is *controlled* by the velocity of harvester,

$$I_s = \alpha\dot{U} = -\alpha U_m \omega \sin\omega t \tag{4.4}$$

In this way, the basic circuit model of the piezoelectric element is built. Starting from this basic equivalent circuit assumption, analytical models for standard circuit (STD) and synchronized series switch harvesting circuit (S3H) are derived respectively in the following subsections. For sake of having full analytical solution and simplification, only the AC mode is

Cette thèse est accessible à l'adresse : http://theses.insa-lyon.fr/publication/2014ISAL0077/these.pdf
© [Y. Li], [2014], INSA de Lyon, tous droits réservés

considered in the following sections. Practically, the piezoelectric energy harvester is connected with an AC-DC converter (a 4-diode full-wave bridge, typically) to drive the secondary circuit (storage capacitor or electric load). However, the analysis results based on AC mode is nearly the same with DC mode. Only slight differences (power degradation) results from the AC-DC converter.

(A) Standard circuit

The standard technique (STD) discussed here is the most straightforward energy harvesting implementation. Same as the purely resistive case we investigated in Chapter 2, the piezoelectric element is connected with the load R directly (Figure 4-4). A resistive load R is placed here to simplify the analysis. In reality, load R is the *input impedance* of the secondary circuit, for instance, LED bulb, Buck-boost converter, energy management circuit, etc. In this configuration, the displacement U and piezoelectric outgoing voltage V_{PZ} are in phase, they are plotted in Figure 4-4.b. Moreover, the harvested voltage V_C is the same as the piezoelectric voltage V_{PZ}.

With Kirchhoff's circuit laws, the quantity of current source I_s is the sum of the current passing through blocked capacitor C_0 and the current passing through the resistive load R, yielding,

$$C_0 \frac{dV_{PZ}}{dt} + \frac{V_{PZ}}{R} = I_S \tag{4.5}$$

The solution is,

$$V_{PZ}(t) = e^{-\frac{t}{RC_0}} \left(V_{PZ}(0) - \frac{\alpha U_m}{C_0} \frac{R^2 C_0^2 \omega^2}{1 + R^2 C_0^2 \omega^2} \right) + \frac{\alpha U_m}{C_0} \frac{R^2 C_0^2 \omega^2}{1 + R^2 C_0^2 \omega^2} \left(\cos \omega t - \frac{1}{RC_0 \omega} \sin \omega t \right) \tag{4.6}$$

$V_{PZ}(0)$ is the boundary condition. Equation (4.6) gives the full response of the piezoelectric voltage under the imposed displacement U_m. This equation can be also used to describe the voltage over load R.

The piezovoltage is entering steady state when transient response becomes null. And therefore the steady state solution is derived as:

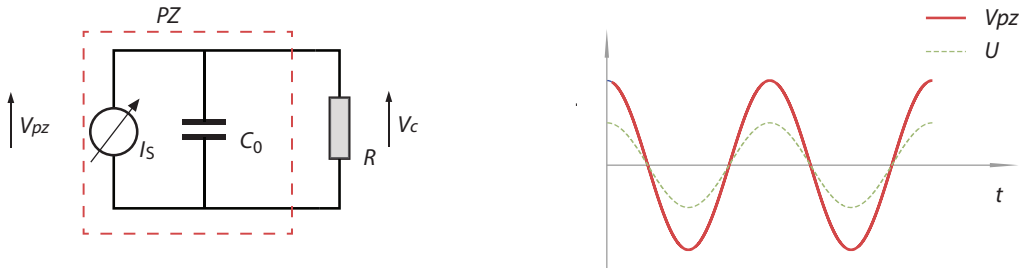

(a) (b)

Figure 4-4. Standard circuit. (a) Circuit principle (b) Piezoelectric voltage V_{PZ} and displacement U

Cette thèse est accessible à l'adresse : http://theses.insa-lyon.fr/publication/2014ISAL0077/these.pdf
© [Y. Li], [2014], INSA de Lyon, tous droits réservés

$$V_{PZ}(t)=\frac{\alpha U_m}{C_0}\frac{R^2C_0^2\omega^2}{1+R^2C_0^2\omega^2}\left(\cos\omega t-\frac{1}{RC_0\omega}\sin\omega t\right) \tag{4.7}$$

Since the voltage over load R is same as piezovoltage, with Equation (4.7), the *average power* dissipated in the load resistance R is calculated as,

$$P=\frac{1}{T}\int P(t)dt=\frac{1}{T}\int\frac{V_{PZ}^2}{R}dt=\frac{\alpha^2U_m^2\omega}{2C_0}\left(\frac{RC_0\omega}{1+R^2C_0^2\omega^2}\right) \tag{4.8}$$

It is clear that, for a given harvester, the dissipated power is the function of imposed displacement U_m and load R. Besides, harvested power is proportional to U_m^2.

$$P=f\left(U_m,R\right) \tag{4.9}$$

By tuning the load resistor according to,

$$\frac{\partial}{\partial R}f\left(U_m,R\right)=0, \tag{4.10}$$

the optimal load resistor is found,

$$R_{opt}=\frac{1}{C_0\omega} \tag{4.11}$$

The corresponding optimal harvested power is,

$$P_{STD}=\frac{1}{4}\frac{\alpha^2U_m^2\omega}{C_0} \tag{4.12}$$

(B) S3H circuit

By adding a controlled switch in the STD circuit, the energy harvesting circuit is transposed to series synchronized switch harvesting (S3H) circuit (Figure 4-5.a).The switch is triggered-on at each voltage extreme and held in on-state for a fixed time t_0, then released back to off-state. The voltages on each side of the switch are showed in Figure 4-5.b. The switch on-time t_0 is no larger than the structure mechanical vibration half-period T/2. In S3H technique, the harvested current flows only when the switch is closed during interval t_0. Most of the time, the piezoelement is simply in open circuit state.

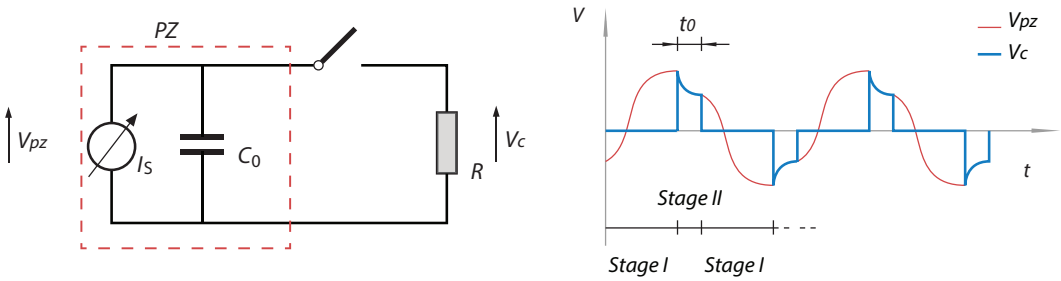

(a) (b)

Figure 4-5. S3H circuit. (a) Circuit principle (b) Piezovoltage and load voltage

Cette thèse est accessible à l'adresse : http://theses.insa-lyon.fr/publication/2014ISAL0077/these.pdf
© [Y. Li], [2014], INSA de Lyon, tous droits réservés

In other words, the whole process is divided into two stages.

- Stage I: Off-state, the switch is open, the current through the load and the load voltage are both null.
- Stage II: On-state, the piezoelement is connected to the load and the discharge occurs.

For stage II, the solution of piezovoltage is a first order exponential discharge forced by the current source resulting from the vibration of the structure. It is a simple exponential discharge if t_0 is small compared to $T/2$. Note that when $t_0=T/2$, only Stage II exists. In this case, S3H is equal to standard technique (STD).

Figure 4-6 shows the piezovoltage waveform and load voltage waveform in steady-state regime. It is clear that the piezovoltage is built with both stages I and II while the load voltage is only defined by stage II. The piezovoltage and load voltage are the same during stage II. In the following the piezovoltage solution will be derived analytically following these two stage arrangement and for sake of clarity the piezoelectric voltage will be noted $V_I(t)$ during off-state operation and $V_{II}(t)$ during on-state operation.

On-state ($0<t\leq t_0$): It starts when the voltage or strain reach an extremum (time origin on Figure 4-6, point a). At that time, the initial value of the piezoelectric voltage is $V_{II}(0)$. As the switch is closed, the circuit is STD-like (Figure 4-4.a). Therefore the voltage is governed by Equation (4.5), whose general solution is given by Equation (4.6). Therefore at the end of this stage (point b), when the switch re-opens at time t_0, the voltage on the piezoelement is $V_{II}(t_0)$, defined by:

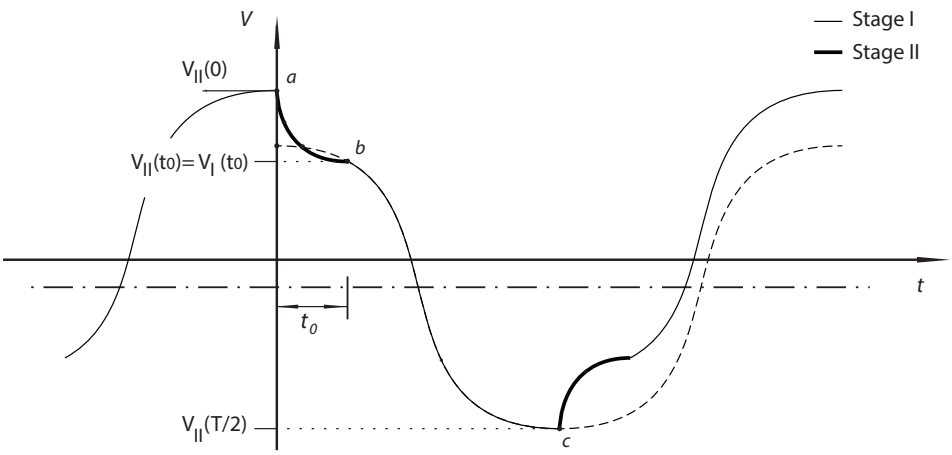

Figure 4-6. Piezoelectric element voltage for S3H – The thin line (b to c) represents the voltage during the off-state position of the switch (Stage I) and the thick line (a to b) the voltage during the on-state (Stage II).

Cette thèse est accessible à l'adresse : http://theses.insa-lyon.fr/publication/2014ISAL0077/these.pdf
© [Y. Li], [2014], INSA de Lyon, tous droits réservés

$$V_{II}(t_0) = e^{-\frac{t_0}{RC_0}} V_{II}(0) + \frac{\alpha U_m}{C_0} A(t_0) \tag{4.13}$$

Where,

$$A(t_0) = \frac{R^2 C_0^2 \omega^2}{1 + R^2 C_0^2 \omega^2} \left(\cos \omega t_0 - \frac{1}{RC_0 \omega} \sin \omega t_0 - e^{-\frac{t_0}{RC_0}} \right) \tag{4.14}$$

Off state (t_0<t<T/2): In this state the switch is open and therefore the piezoelement voltage is governed by the open circuit differential equation,

$$C_0 \frac{dV_{PZ}}{dt} = I_S \tag{4.15}$$

Yields,

$$V_I(t) = V_I(0) + \left[\frac{\alpha U_m}{C_0} \cos \omega t \right]_{t_0}^{t} \tag{4.16}$$

Due to the boundary condition $V_I(0)=V_{II}(t_0)$, we have,

$$V_I(t) = V_{II}(t_0) + \frac{\alpha U_m}{C_0} \left(\cos \omega t - \cos \omega t_0 \right) \tag{4.17}$$

Consequently, at the end of the semi period (t=T/2), the voltage reaches the minimum value (point *c* in Figure 4-6):

$$V_I(\frac{T}{2}) = V_{II}(t_0) - \frac{\alpha U_m}{C_0} \left(1 + \cos \omega t_0 \right) \tag{4.18}$$

Now in steady state regime, the piezoelement voltage is periodic, therefore,

$$V_I(\frac{T}{2}) = -V_{II}(0) \tag{4.19}$$

Which allows to derive the initial value $V_{II}(0)$ solution as :

$$V_{II}(0) = \frac{1}{e^{-t_0/RC_0} + 1} \frac{\alpha U_m}{C_0} \left(1 + \cos \omega t_0 - A(t_0) \right) \tag{4.20}$$

In this way, we can find the full expression for voltage in stage I & II, they are,

$$V_I(t) = \frac{1}{e^{-t_0/RC_0} + 1} \frac{\alpha U_m}{C_0} \left(1 + \cos \omega t_0 - A(t_0) \right) + \frac{\alpha U_m}{C_0} \left(\cos \omega t - \cos \omega t_0 \right) \tag{4.21}$$

$$V_{II}(t) = e^{-\frac{t}{RC_0}} \frac{1}{e^{-t_0/RC_0} + 1} \frac{\alpha U_m}{C_0} \left(1 + \cos \omega t_0 - A(t_0) \right) + \frac{\alpha U_m}{C_0} A(t) \tag{4.22}$$

Due to the sinusoidal and periodical nature of the problem, symmetric behaviour occurs during the following semi-period leading to a completely defined solution for the piezoelectric voltage. The piezovoltage is given as,

Cette thèse est accessible à l'adresse : http://theses.insa-lyon.fr/publication/2014ISAL0077/these.pdf
© [Y. Li], [2014], INSA de Lyon, tous droits réservés

$$V(t)=\begin{cases} V_{II}(t) & , \quad 0<t\le t_0 \\ V_I(t) & , \quad t_0<t\le \frac{T}{2} \\ -V_{II}(t-\frac{T}{2}) & , \quad \frac{T}{2}<t\le \frac{T}{2}+t_0 \\ -V_I(t-\frac{T}{2}) & , \quad \frac{T}{2}+t_0<t\le T \end{cases} \tag{4.23}$$

The voltage over load R is given as,

$$V(t)=\begin{cases} V_{II}(t) & , \quad 0<t\le t_0 \\ 0 & , \quad t_0<t\le \frac{T}{2} \\ -V_{II}(t-\frac{T}{2}) & , \quad \frac{T}{2}<t\le \frac{T}{2}+t_0 \\ 0 & , \quad \frac{T}{2}+t_0<t\le T \end{cases} \tag{4.24}$$

Consequently, with Equation (4.8) and Equation(4.24), the *average power* on load R can be derived from the RMS voltage on the load calculated for example on a semi-period of the strain [see Appendix F.1 for detail].

$$P=\frac{2}{T}\int_0^{T/2}P(t)dt=\frac{V_{RMS}{}^2}{R}=\frac{1}{\pi}\frac{\alpha^2U_m^2\omega}{C_0}\left\{\begin{array}{l} \frac{1}{2}\left(\frac{\cos\omega t_0+1-A(t_0)}{e^{-t_0/\tau}+1}-\frac{\tau^2\omega^2}{1+\tau^2\omega^2}\right)^2\left(1-e^{-2t_0/\tau}\right) \\ +\frac{\tau\omega}{1+\tau^2\omega^2}\left[\frac{1}{4}\left(\tau^2\omega^2-1\right)\sin 2\omega t_0-\tau\omega\sin^2\omega t_0+\frac{\omega t_0}{2}\left(\tau^2\omega^2+1\right)\right] \\ +2e^{-t_0/\tau}\frac{\tau\omega}{1+\tau^2\omega^2}\left(\frac{\cos\omega t_0+1-A(t_0)}{e^{-t_0/\tau}+1}-\frac{\tau^2\omega^2}{1+\tau^2\omega^2}\right)\sin\omega t_0 \end{array}\right\}$$

(4.25)

By Equation (4.25), the power can be expressed as the function of imposed displacement U_m , circuit time constant τ (τ=RC_0) and switch on time t_0,

$$P=\mathcal{G}(U_m,\tau,t_0) \tag{4.26}$$

Similar as STD case, harvested power is proportional to the square of the displacement U_m^2. For a given displacement excitation, the power versus various load R and various switch on time t_0 is able plotted (Figure 4-7) by Equation(4.25).

From Figure 4-7, it is obvious that harvested power becomes maximum when load R and switch on time is small enough. Mathematically, if the switch on time is small enough ($t_0 \approx 0$) and the load $\boldsymbol{R}$ is chosen a relative low value ($\tau << t_0$), the optimal (maximum) power [see detail in Appendix F.1] is found as:

Cette thèse est accessible à l'adresse : http://theses.insa-lyon.fr/publication/2014ISAL0077/these.pdf
© [Y. Li], [2014], INSA de Lyon, tous droits réservés

$$P_{S3H} = \frac{2}{\pi}\frac{\alpha^2 U_m^2 \omega}{C_0} \tag{4.27}$$

which is approximately more than twice of maximum power extracted by the standard technique(Equation (4.12)):

$$P_{S3H}/P_{STD} = \frac{8}{\pi} \approx 2.55 \tag{4.28}$$

4.2.3 Analytical model development: Constant force

In constant force case, the damping effect due to the energy dissipated in to the load is considered. The vibration amplitude U_m is not independent to the load R. Since the power is a function of the displacement U_m (4.9)(4.26) at constant displacement case, the power is possible to be obtained as long as the U_m for a given load R is known. The analysis of constant force is based on the analysis results of constant displacement and processed as following steps:

The analysis method for constant force

- Solving the corresponding $\boldsymbol{U_m}$ for a given load $\boldsymbol{R}$ at given excitation force $\boldsymbol{F_m}$.
- Once $\boldsymbol{U_m}$ and $\boldsymbol{R}$ are known, calculating the power by (4.9) and (4.25) for STD and S3H, respectively.

For constant amplitude, sinusoidal force excitation, the vibration amplitude U_m is variable and depends on the damping resulting from the harvesting process. For harmonic excitation at the angular frequency ω, the displacement U can be expressed in time domain or in complex notation as :

$$\begin{cases} U(t) = U_m \cos \omega t \\ \tilde{U} = U_m \end{cases} \tag{4.29}$$

Observing from Equation(4.1), the desired displacement can be solved as long as the periodic voltage V is sinusoidal-like signal.

Now the voltage resulting from the switching process shown on Figure 4-5.b is not sinusoidal. However, only the fundamental item which is synchronous with the speed can generate damping. The voltage is therefore written in *Fourier series* [103]as:

$$\tilde{V} = \sum_{1}^{\infty} e^{j\omega_n t} \frac{1}{T} \int V(t) e^{-j\omega_n t} dt \tag{4.30}$$

According to the previous statement, only the fundamental frequency is considered,

$$\tilde{V}_1 = e^{j\omega t} \frac{1}{T} \int V(t) e^{-j\omega t} dt \tag{4.31}$$

Cette thèse est accessible à l'adresse : http://theses.insa-lyon.fr/publication/2014ISAL0077/these.pdf
© [Y. Li], [2014], INSA de Lyon, tous droits réservés

Since displacement U_m is sinusoidal,

$$\tilde{U} = U_m \tilde{B} e^{j\omega t} \tag{4.32}$$

Then we can find that,

$$\tilde{V}_1 = \tilde{B}\tilde{U} \tag{4.33}$$

The complex factor $\tilde{B}$ is therefore derived from Equations(4.31)(4.32)(4.33), considering U_m as unity in the evaluation of *V(t)*.

$$\tilde{B} = \frac{1}{T}\int V(t) e^{-j\omega t} dt \tag{4.34}$$

The damping is related to the frequency term of the voltage synchronous with the vibration therefore, only the fundamental frequency of the voltage is responsible for damping and will be considered in the mechanical Equation(4.1). For harmonic excitation condition, this equation can be re-written in complex form as:

$$-\omega^2 M\tilde{U} = \tilde{F} - K_E\tilde{U} - \alpha\tilde{V}_1 - j\omega C\tilde{U} \tag{4.35}$$

Which, considering Equation(4.33), leads to:

$$\tilde{U} = \frac{\tilde{F}}{K^E + \alpha\tilde{B} - M\omega^2 + j\omega C} = \mathcal{F}(\tilde{F}, \tilde{B}) \tag{4.36}$$

For an imposed force amplitude F_m, the displacement amplitude U_m can be obtained and the voltage and harvested power can be finally calculated. This procedure will be applied in the following to both the STD and the S3H techniques. The calculation details are listed in Appendix E for STD case and Appendix F.2 for S3H case.

(A) Standard circuit

Replacing the voltage expression *V(t)* in Equation (4.34) with (4.7) (U_m=1) leads to:

$$\tilde{B} = \frac{\alpha}{C_0}\frac{R^2C_0^2\omega^2}{1+R^2C_0^2\omega^2}\left(1 + j\frac{1}{RC_0\omega}\right) \tag{4.37}$$

The displacement amplitude U_m can be obtained using Equations (4.36) (4.37):

$$U_m = F_m\left[\left(K^E + \frac{\alpha^2}{C_0}\frac{R^2C_0^2\omega^2}{1+R^2C_0^2\omega_r^2} - M\omega^2\right)^2 + \left(\omega C + \frac{\alpha^2}{C_0}\frac{RC_0\omega}{1+R^2C_0^2\omega^2}\right)^2\right]^{-\frac{1}{2}} \tag{4.38}$$

Substituting Equation (4.38) into (4.8) , the power can be derived as:

$$P = F_m^2\frac{\alpha^2\omega}{2C_0}\cdot\frac{\dfrac{RC_0\omega}{1+R^2C_0^2\omega^2}}{\left(K^E + \dfrac{\alpha^2}{C_0}\dfrac{R^2C_0^2\omega^2}{1+R^2C_0^2\omega^2} - M\omega^2\right)^2 + \left(\omega C + \dfrac{\alpha^2}{C_0}\dfrac{RC_0\omega}{1+R^2C_0^2\omega^2}\right)^2} \tag{4.39}$$

The object here is to find the optimal power output. As discussed in Chapter 2, the piezoelectric energy harvester reaches its maximum power output around short circuit frequency ω_E and open circuit frequency ω_D. Therefore it is necessary to excite this harvester

Cette thèse est accessible à l'adresse : http://theses.insa-lyon.fr/publication/2014ISAL0077/these.pdf
© [Y. Li], [2014], INSA de Lyon, tous droits réservés

around its open circuit frequency($\omega = \omega_D$ with $\omega_D = \left(K^D/M\right)^{1/2}$)to have the maximum power output. Note that,

$$K^D - K^E = \alpha^2/C_0 \tag{4.40}$$

Therefore Equation (4.39) is simplified to

$$P = \frac{F_m^2}{2C} \cdot \frac{\frac{\omega_D C C_0}{\alpha^2} R C_0 \omega_d}{\left(\frac{\omega_D C C_0}{\alpha^2} R C_0 \omega_D + 1\right)^2 + \left(\frac{\omega_D C C_0}{\alpha^2}\right)^2} \tag{4.41}$$

At low loss condition ($\omega_D C C_0 / \alpha^2 \ll 1$), the harvested power reaches its maximum,

$$P_{\max} = \frac{F_m^2}{8C} \tag{4.42}$$

Considering the RMS value of sinusoidal force is defined as,

$$F = \frac{\sqrt{2}}{2} F_m, \tag{4.43}$$

the maximum harvested power can also expressed as,

$$P_{\max} = \frac{F^2}{4C} \tag{4.44}$$

In the resistive load case discussion of Chapter 2, the proposed maximum harvested power is $P_{\max} = F^2/4C$. The power limit of a piezoelectric energy harvester is confirmed.

(B) S3H circuit

According to the development of Section 4.2.2(B), for a sinusoidal displacement with a given amplitude U_m, the piezoelement voltage $V(t)$ represented by Figure 4-6 is defined as a piecewise function constructed with the two stages I & II(Equation (4.23)). This periodic voltage can be decomposed into a *Fourier series*; With Equation (4.34), the fundamental term can therefore be derived for a unity amplitude leading to:

$$\begin{aligned}\tilde{B} = {} & \frac{4}{T}\left\{\frac{A_{II}}{\omega}\left(\frac{\omega t_0}{2} + \frac{1}{4}\sin 2\omega t_0\right) + \frac{B_{II}}{2\omega}\sin^2 \omega t_0 + \frac{C_{II}}{\alpha_{II}^2 + \omega^2}\left[e^{\alpha_{II} t_0}\left(\omega \sin \omega t_0 + \alpha_{II} \cos \omega t_0\right) - \alpha_{II}\right]\right\} \\ & - j\frac{4}{T}\left\{\frac{A_{II}}{2\omega}\sin^2 \omega t_0 + \frac{B_{II}}{\omega}\left(\frac{\omega t_0}{2} - \frac{1}{4}\sin 2\omega t_0\right) + \frac{C_{II}}{\alpha_{II}^2 + \omega^2}\left[e^{\alpha_{II} t_0}\left(\alpha_{II} \sin \omega t_0 - \omega \cos \omega t_0\right) + \omega\right]\right\} \\ & + \frac{4}{T}\left\{\frac{A_I}{\omega}\left(\frac{\omega\left(\frac{T}{2} - t_0\right)}{2} - \frac{1}{4}\sin 2\omega t_0\right) - \frac{C_I}{\omega}\sin \omega t_0\right\} - j\frac{4}{T}\left\{-\frac{A_I}{2\omega}\sin^2 \omega t_0 + \frac{C_I}{\omega}\left(1 + \cos \omega t_0\right)\right\}\end{aligned} \tag{4.45}$$

Where,

Cette thèse est accessible à l'adresse : http://theses.insa-lyon.fr/publication/2014ISAL0077/these.pdf
© [Y. Li], [2014], INSA de Lyon, tous droits réservés

$$A_I = \frac{\alpha}{C_0}, \qquad C_I = \frac{\alpha}{C_0}\left(1 - \frac{\cos\omega t_0 + 1 - A(t_0)}{e^{-t_0/\tau} + 1}\right),$$
$$A_{II} = \frac{\alpha}{C_0}\frac{R^2C_0^2\omega_0^2}{1+R^2C_0^2\omega_0^2}, \qquad B_{II} = -\frac{\alpha}{C_0}\frac{1}{RC_0\omega_0}\frac{R^2C_0^2\omega_0^2}{1+R^2C_0^2\omega_0^2}, \tag{4.46}$$
$$C_{II} = \frac{\alpha}{C_0}\left(\frac{\cos\omega t_0 + 1 - A(t_0)}{e^{-t_0/\tau} + 1} - \frac{R^2C_0^2\omega_0^2}{1+R^2C_0^2\omega_0^2}\right), \qquad \alpha_{II} = -\frac{1}{RC_0}.$$

According to the previously described methodology, substituting the expression of B defined by Equation (4.45) into Equation(4.36), allows the calculation of U_m for a constant force amplitude F_m. From U_m, the maximum harvested power is finally obtained using Equation (4.26) at the resonance frequency. The final expression is not listed here on account of its complex form.

4.3 Circuit performance discussion

This section is the discussion based on the analytical model proposed in Section 4.2.2. Power output level will be investigated by duty cycle and coupling factor. The wide bandwidth property of S3H circuit will also be discussed.

4.3.1 Duty cycle

For sake of simplicity the switch on time will be considered relatively to the vibration period T. The duty cycle t_0/T will be used in the following discussion. Note that when this duty cycle is equal to 0.5, the switch is always closed thus corresponding to the standard (STD) technique.

(A) Constant displacement

Figure 4-7 shows the power output comparison between STD technique and S3H technique at various duty cycle t_0/T for constant displacement condition. The standard circuit optimal load R_{opt} which is given in Equation (4.12) is used as the load reference. The simulation data set used which corresponds to the experimental set-up is described in Section 4.4. The considered amplitude displacement is U_m= 77µm. At very low duty cycle, the output power is higher than two times the maximum power extracted with the standard technique. Moreover for nearly two decades on the low resistance side, this power is constant, and corresponds approximately to the performance of the SECE technique. In this case the on-time is fixed and arbitrarily defined. It is clear that even if there are frequency shifts due to environmental changes or variations in the piezoelement capacitance due to non-linearity or stress, the effect on the harvested power is totally negligible due to the wide impedance range on which the harvested power is constant, making S3H a very robust harvesting technique. Notice that like SECE the independence of the extracted power to the load (i.e. to the vibration frequency) is related to its pulsed nature.

Cette thèse est accessible à l'adresse : http://theses.insa-lyon.fr/publication/2014ISAL0077/these.pdf
© [Y. Li], [2014], INSA de Lyon, tous droits réservés

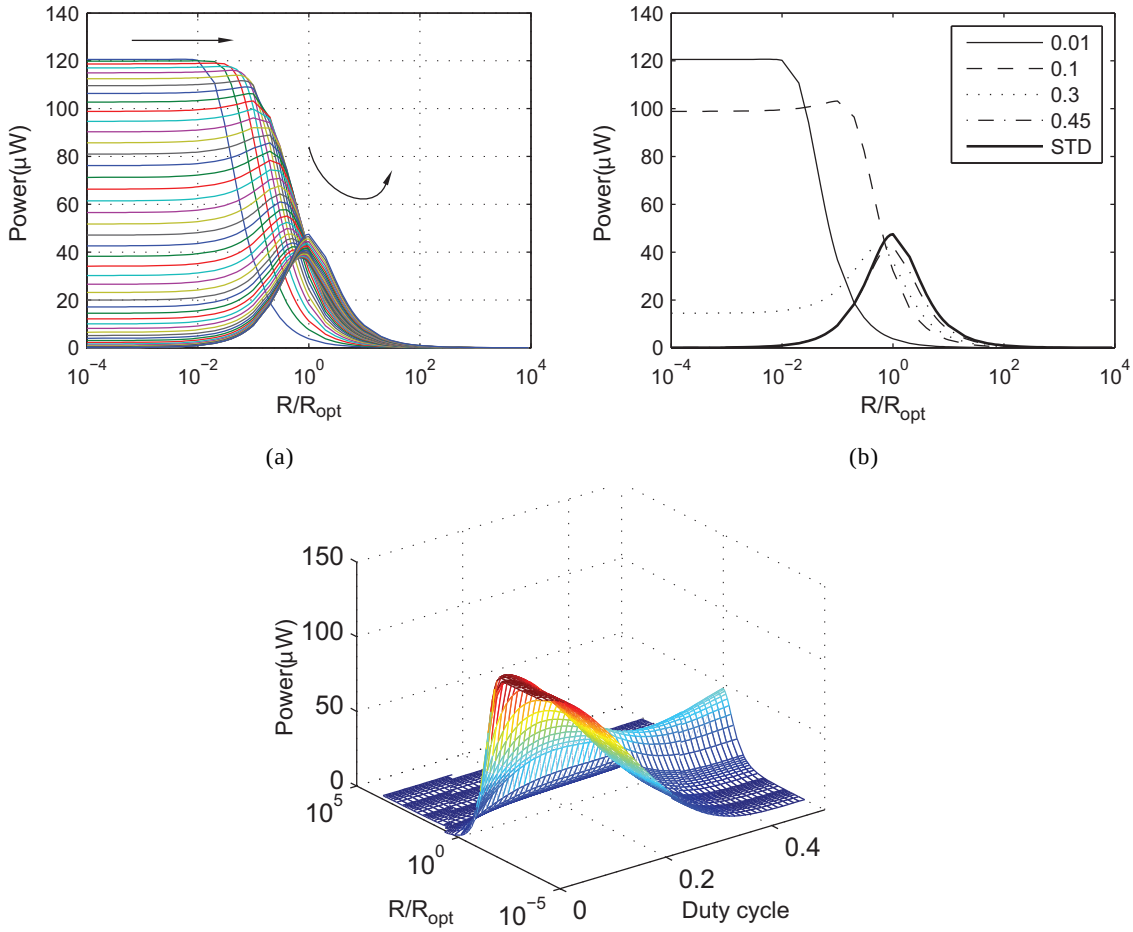

(a) (b)

(c)

Figure 4-7. The harvested power dependence with the load resistance and duty cycle at constant displacement condition. a) Power variation for duty-cycle varying from 0 to 0.5 – b) harvested power for various duty-cycle and comparison to standard technique – c) 3D plot variation(f_{oc}=56.72Hz, α=0.0039 N/V, K^E=9317Nm-1, M=74.1g, C_0=170nF, k^2=0.0094, Q_M=61.1207.)

Consequently, as the duty cycle increases, this independence is less and less clear as shown in Figure 4-7. As the duty cycle increases and approaches 0.5 the characteristic curve progressively merges with the standard technique one defined by Equation(4.8).

From the 3D plot showed in Figure 4-7.c, a trough point exists on the power curve. This valley zone means that the power extracted by S3H is not decreasing monotonously down to Standard technique. In some region the total performance is worse than standard technique. Although at the point where the maximum power output is less than Standard technique, the load bandwidth is still larger than it. (i.e. 0.3 case in Figure 4-7.b).

Cette thèse est accessible à l'adresse : http://theses.insa-lyon.fr/publication/2014ISAL0077/these.pdf
© [Y. Li], [2014], INSA de Lyon, tous droits réservés

The energy cycle plots can be used to visualize the harvesting ability of piezoelectric energy harvester circuit. The area within the cycle in the αV versus U plain in a whole period represents the converted energy (from mechanical to electrical)[50]. The energy cycle of STD case (Figure 4-8.a) is an ellipse and the curve is smooth. For a small load resistance (R/R_{opt} $<10^{-2}$), the energy cycle of S3H is similar to a parallelogram at small duty cycle condition. For S3H (Figure 4-8.b), with the increasing of duty cycle, the area is increasing firstly then shrinking to its minimum (duty cycle is 0.5). The global comparison of these two circuit techniques is given in Figure 4-9.

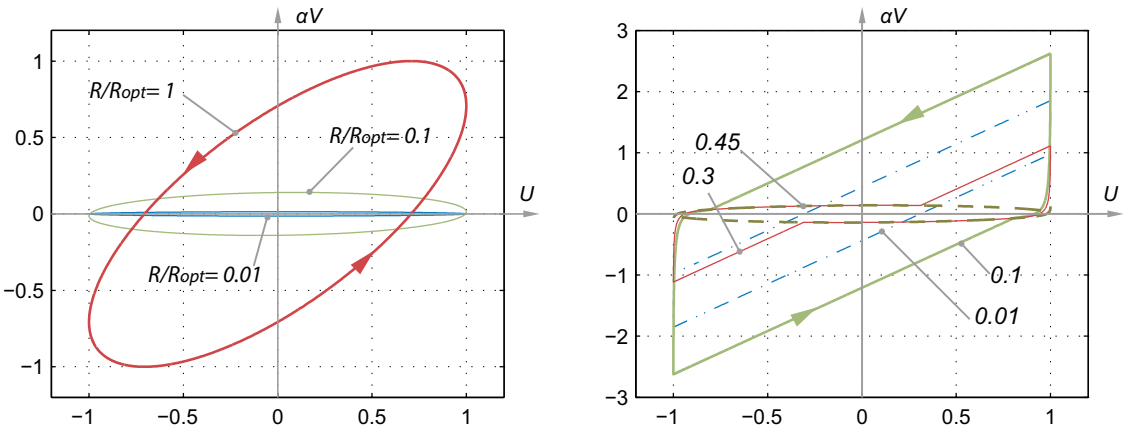

(a) (b)

Figure 4-8. Energy Cycle (a)STD circuit with various loads (b) S3H circuit with various duty cycle with load case R/R_{opt}=0.1

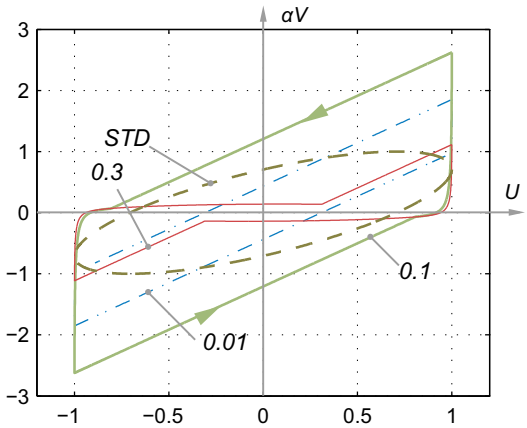

Figure 4-9. Energy Cycle comparison. STD and S3H (with various duty cycle). STD load case R/R_{opt}=1, S3H load case R/R_{opt}=0.1.

Cette thèse est accessible à l'adresse : http://theses.insa-lyon.fr/publication/2014ISAL0077/these.pdf
© [Y. Li], [2014], INSA de Lyon, tous droits réservés

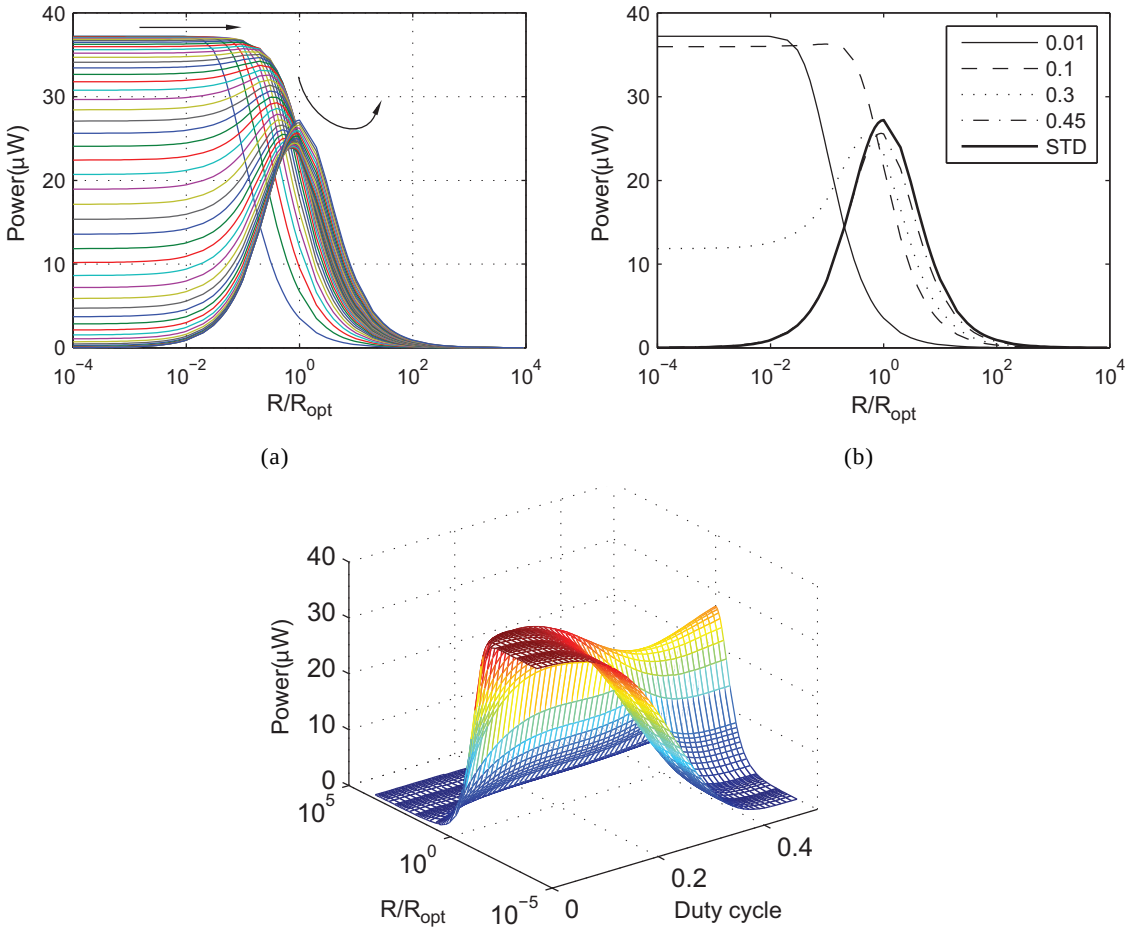

(a) (b)

(c)

Figure 4-10. The harvested power dependence with the load resistance and duty cycle at constant force condition. a) power variation for duty-cycle varying from 0 to 0.5 – b) harvested power for various duty-cycle and comparison to standard technique – c) 3D plot variation. (f_{oc}=56.72Hz, α=0.0045 N/V, K^E=10272Nm^{-1},M=0.0818g, C_0=170nF, k^2=0.0113, Q_M=54.)

(B) Constant Force

Figure 4-10 shows the output power comparison with constant force excitation between the standard and the S3H techniques as a function of the load resistance and for various duty cycle t_0/T ranging between 0 and 0.5. The simulation data set used corresponds to the experimental set-up described is Section 4.4. The considered amplitude force F_m= 0.0127N. Like in the previous case, and for low impedance and low cycle the extracted power is nearly independent to the load. However the damping effect due to the energy harvesting limits the power gain. This damping is directly related to the k^2Q_M figure of merit of the piezogenerator. As this figure

Cette thèse est accessible à l'adresse : http://theses.insa-lyon.fr/publication/2014ISAL0077/these.pdf
© [Y. Li], [2014], INSA de Lyon, tous droits réservés

of merit increases, the maximum power amplitude tends to be equal between the two techniques. However the S3H technique conserves the independence to the load. Figure 4-10 illustrates that as the duty cycles approaches 0.5, both curves representing S3H and standard techniques merge.

Same as constant displacement case, a trough point exists on the power surface Figure 4-10.c. With various duty cycle t_0/T, the power has the comparable trending both on constant displacement case and constant force case. The maximum power gain is achieved on constant displacement case. The advantage of S3H technique in constant force case is limited by the coupling coefficients k^2Q_M. This point is discussed in the next subsection.

4.3.2 Electromechanical coupling effect

It is known that, electromechanical coupling coefficient k^2 is the main parameter allowing to qualify the piezoelement energy conversion capability between electrical and mechanical form. It is usually related to the other relevant terms by Equation(4.47). Besides, for a piezoelectric device, the mechanical quality factor Q_M is used to qualify the natural mechanical losses of the device. It is related to the damping coefficient by Equation(4.48).

$$k^2 = \frac{\alpha^2}{K_D C_0} \tag{4.47}$$

$$Q_M = \frac{m\omega_n}{C} \tag{4.48}$$

In the analytical development of Standard technique at Section 4.2.2(A), it should be pointed out that the maximum harvested power is given by Equation (4.42) when $\omega_d C C_0 / \alpha^2 \ll 1$. Now, rewriting this condition considering k^2 and Q_M leads to,

$$\begin{aligned} &\omega_D C C_0 / \alpha^2 = \frac{\omega_D^2 C C_0 m}{\alpha^2 \omega_d m} = \frac{K^D C_0}{\alpha^2} \bullet \frac{C}{\omega_D m} = \frac{1}{k^2} \bullet \frac{1}{Q_M} = \frac{1}{k^2 Q_M} \ll 1 \\ &\Rightarrow \qquad k^2 Q_M \gg 1 \end{aligned} \tag{4.49}$$

Equation (4.49) demonstrates a universal law that when the efficiency combination term (figure of merit) k^2Q_M increases, the power is reaching its maximum. At strong coupling condition, the harvester power is only the function of input force and the viscous losses(4.42). It is worthy to mention that this conclusion has been validated in Chapter 2.

Due to the variable duty cycle, the coupling coefficient effect on S3H performance is a little more complex. Figure 4-11 shows the coupling effect on S3H technique with variable duty cycle. Standard technique is also considered because it corresponds to S3H with 0.5 the duty cycle. As usual, small k^2Q_M (Figure 4-11.a) is similar to the constant displacement case. It is clear that power of S3H depends on the load R and the duty cycle. As we discussed in Chapter 2, two peaks appears in Standard technique when k^2Q_M increases. At high k^2Q_M condition, the S3H's power and Standard technique power are in same level, but S3H still

Cette thèse est accessible à l'adresse : http://theses.insa-lyon.fr/publication/2014ISAL0077/these.pdf
© [Y. Li], [2014], INSA de Lyon, tous droits réservés

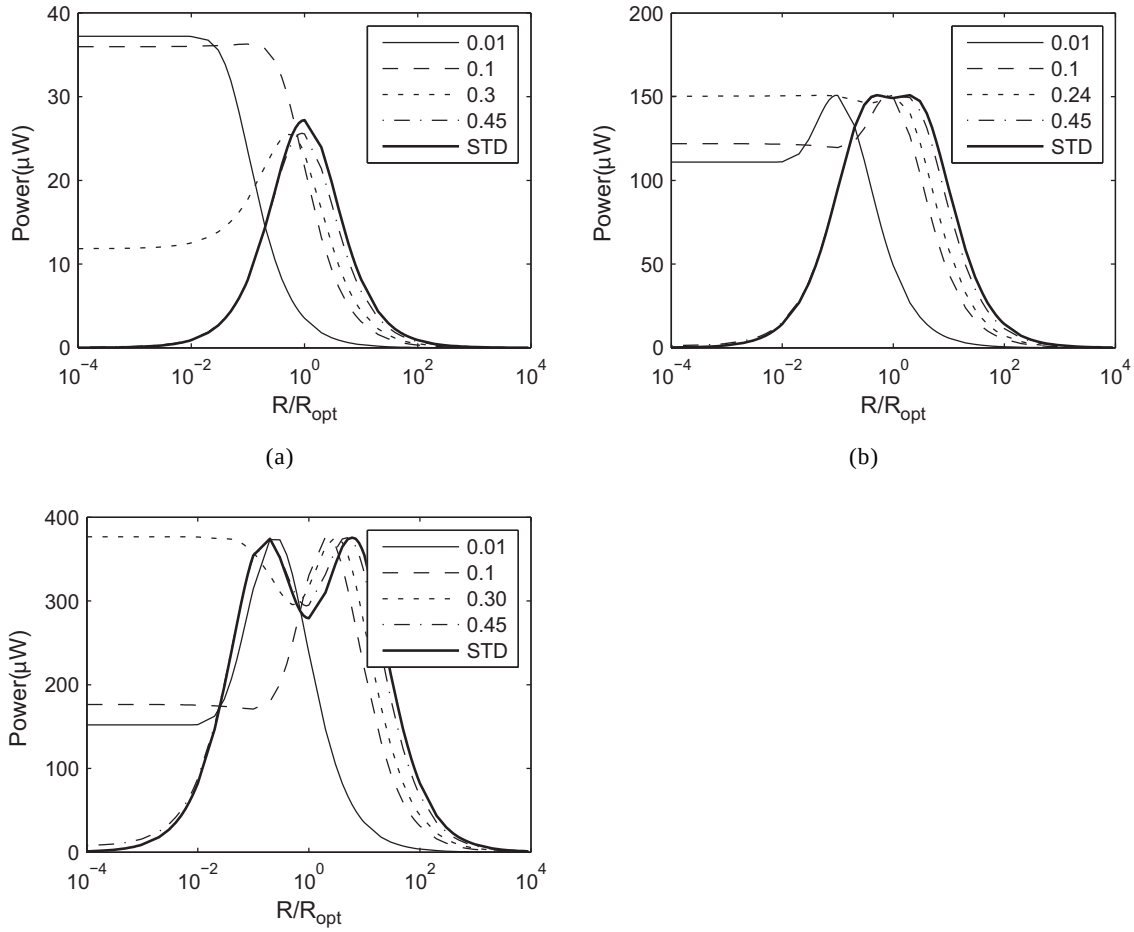

Figure 4-11. Power with various k^2Q_M (a) k^2Q_M= 0.61 (b) k^2Q_M= 6.1 (c) k^2Q_M= 61

keeps the advantage of large bandwidth in the low impedance region. It can be observed from Figure 4-11 that on optimal duty cycle exists and this optimal value is increasing with k^2Q_M.

The main advantage of S3H circuit is to be load-independent in low load impedance region. In the following discussion, such wide bandwidth property will be discussed with various loads and coupling factor k²QM.

Firstly, the comparison is performed for low load impedance. R is chosen such as R/R_{opt}=1e^{-4}, where R_{opt} refers to the optimal load for STD circuit. Figure 4-12 gives the comparison between S3H and STD. It shows the variation of the extracted power versus the k^2Q_M figure of merit for low (0.01) and high (0.3) duty cycle. The power is compared with STD case with corresponding k^2Q_M in Figure 4-12.a and normalized to the maximum extracted power (high k^2Q_M) in Figure 4-12.b. It is interesting to point out that S3H has 2 times

Cette thèse est accessible à l'adresse : http://theses.insa-lyon.fr/publication/2014ISAL0077/these.pdf
© [Y. Li], [2014], INSA de Lyon, tous droits réservés

advantage when k^2Q_M is weak. However, with the increasing of k^2Q_M, the power is decreasing for duty cycle 0.01. When k^2Q_M is larger than 1, the advantage doesn't exist anymore, But the duty cycle can be tuned to maintain the advantage of S3H until S3H and STD reach at the same level at high k^2Q_M condition.(choose duty cycle 0.3 for example). These results show that to maintain a constant extracted power; the tuning of the duty cycle is required in constant load condition.

Next, only the maximum power harvested is concerned. In other words, the load is supposed variable and able to match the optimal power output. Figure 4-13 gives S3H maximum power output compared with STD technique. The power is compared with STD case with corresponding k^2Q_M in Figure 4-13.a and normalized to the maximum extracted power

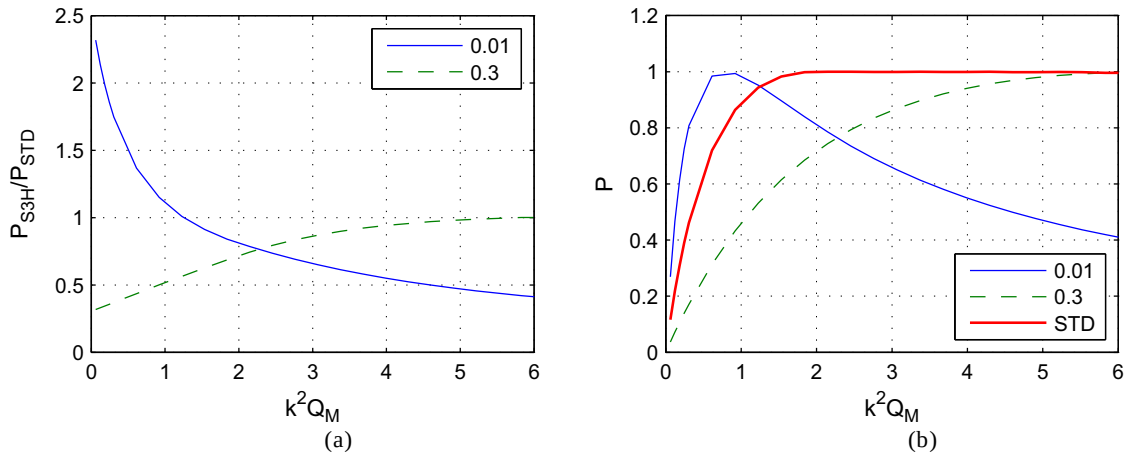

Figure 4-12. Maximum power with various k^2Q_M. The load of S3H is R/R_{opt}=1e^{-4}. The load of STD is R/R_{opt}=1.(a) Relative view (b)Global view

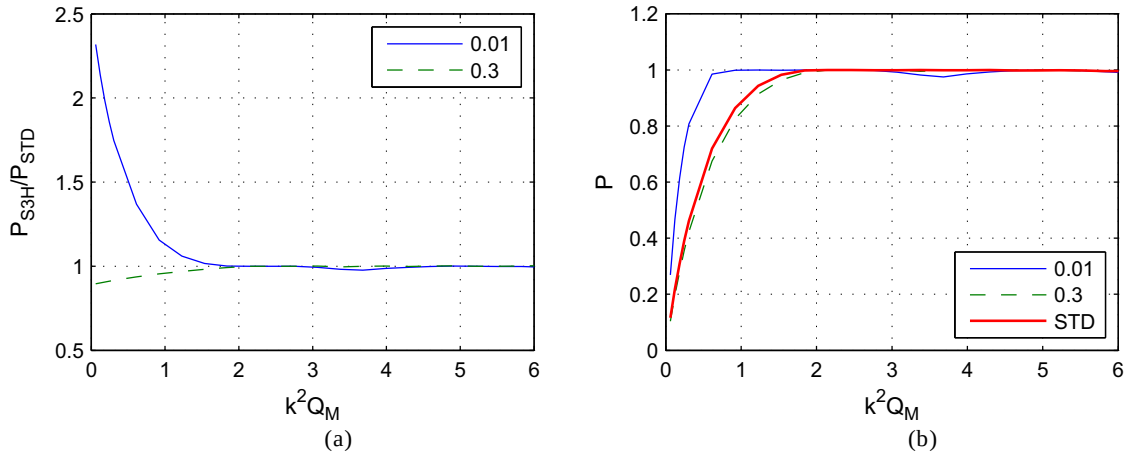

Figure 4-13. Maximum power with various k^2Q_M.

Cette thèse est accessible à l'adresse : http://theses.insa-lyon.fr/publication/2014ISAL0077/these.pdf
© [Y. Li], [2014], INSA de Lyon, tous droits réservés

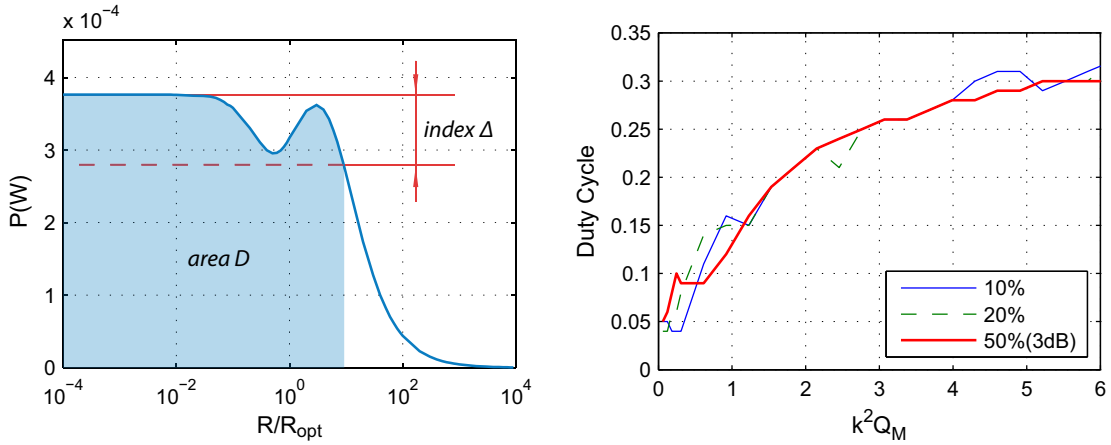

(a) (b)

Figure 4-14. The optimal duty cycle for bandwidth. (a) The difinition of idnex and bandwidth (b) The optimal duty cycle with various indexes.

(high k^2Q_M) in Figure 4-13.b. Both the low (0.01) and high (0.3) duty cycles are considered. The power curve represents the maximum power at each k^2Q_M condition with different duty cycle. When coupling coefficient is weak (k^2Q_M <2), a shorter duty cycle means higher power ratio. The maximum power improvement is more than 2 times like the previous case. When coupling coefficient becomes strong (k^2Q_M >2), the S3H and STD reach at the same power output level. In this case, even the duty cycle 0.01 can maintain high power output at strong coupling condition. However, load-independent property is lost in this configuration, because the optimal load now is out of load-independent region at strong coupling condition (Figure 4-11.c).

As a wide bandwidth technique, another way to assess the global performance comparison is considering both the power output and band width (load) at the same time. Evaluation of the area *D* in Figure 4-14.a is used to estimate the power bandwidth properties. In order to calculate area *D*, an index *Δ* is considered. An index of *Δ*=10% allows to define a band in terms of load in order to ensure that the power remains in the limit of 90% of the maximum harvester power. Area *D* is therefore calculated within this load band. For each k^2Q_M, the optimal duty cycle corresponding to the maximum area *D* is defined. Figure 4-14.b illustrates how this optimal duty cycle increases with the coupling coefficient figure of merit k^2Q_M. The optimal duty cycle is only slightly affected by index Δ. Unlike the previous case, the optimal duty cycle is around 0.3 even at strong k^2Q_M condition.

Figure 4-15 compares the power bandwidth property *D* versus k^2Q_M. The comparison baseline is the standard case (STD) with corresponding index *Δ*. If a narrow index *Δ* is considered (10%), S3H has a much large response. However, all these advantages shrink in

Cette thèse est accessible à l'adresse : http://theses.insa-lyon.fr/publication/2014ISAL0077/these.pdf
© [Y. Li], [2014], INSA de Lyon, tous droits réservés

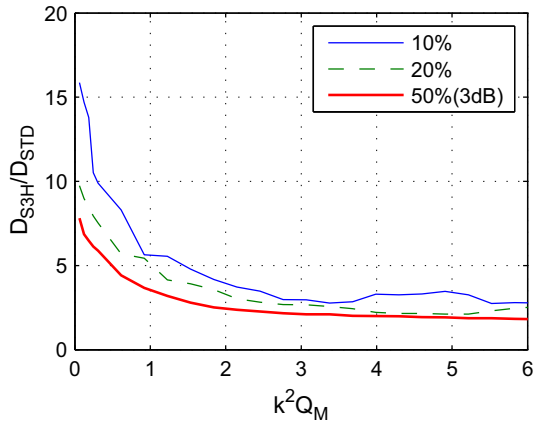

Figure 4-15. The optimal duty cycle vesus coupling coefficient k^2Q_M with various indexes.

strong coupling condition (k^2Q_M >2). It is worthy to point out that, even in high coupling condition, S3H still performs slightly better thanks to its inherent low dependence to the load.

4.4 Experimental validation

4.4.1 Set-up

The experimental set-up is schematically depicted on Figure 4-16. The piezoelectric generator device used for the experimental validation is a cantilever beam clamped on one end on a strong base. Eighteen piezoelectric patches (2cm² and 0.5mm thick) are bonded on the plate close to the clamping edge, nine patches on each face. The beam is excited with an electromagnet driven with a sinusoidal current supplied by an audio power amplifier. A dSPACE DS1104 rapid prototyping board along with the Matlab-Simulink environment is used to set up the various electronic control signals. The input signal of the amplifier is fed either by a function generator or by a dSPACE board real-time output. The switch itself is made with a pair of MOSFET transistors associated in order to build a bidirectional switch. The switch is driven, via an opto-coupler, by an output of the dSPACE board. The diving signal is a square pulse with a controlled duration t_0 synchronized with the beam displacement extremum. The beam displacement is monitored either by one of the piezoelectric patches, or by an eddy current displacement sensor aiming at the plate.

Cette thèse est accessible à l'adresse : http://theses.insa-lyon.fr/publication/2014ISAL0077/these.pdf
© [Y. Li], [2014], INSA de Lyon, tous droits réservés

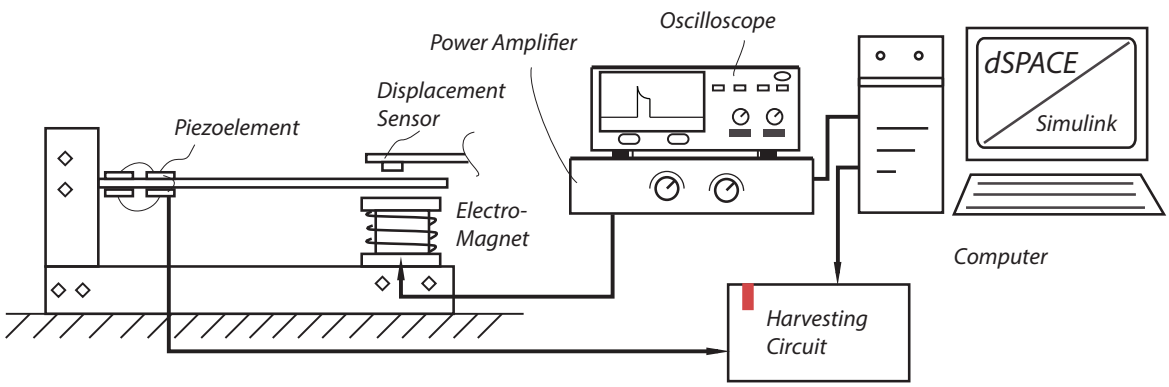

Figure 4-16. Experimental set-up architecture

Close to the first bending mode resonance, the motion and resonant behavior of the experimental structure can be represented by the mass-spring-damper model described on Figure 4-3. The various parameters can be easily identified from simple characterization of the resonance. Table 4-1 and Equation (4.50) summarize the various parameters identified on the considered experimental structure. Note that the open circuit voltage coefficient γ is the piezoelectric device open-circuit voltage to the beam free end displacement ratio.

$$\alpha = \gamma C_0 \qquad k^2 = \frac{f_{oc}^2 - f_{cc}^2}{f_0^2} \qquad M = \frac{\alpha^2}{4\pi^2 f_{oc}^2 k^2 C_0}$$
$$K_E = 4\pi^2 M f_{cc}^2 \qquad Q_M = \frac{f_{oc}}{f_{oc} - f_{cc}} \qquad C = \frac{2\pi M f_{oc}}{Q_M} \tag{4.50}$$

4.4.2 Mono-mode case study

Figure 4-17 illustrates the voltage measured both on the piezoelement and on the resistance load with a sinusoidal excitation close to the resonance. At low load (Figure 4-17.a), the piezoelement voltage is strongly modified by the switching due to the rapid discharge of the blocked capacitance in the load. By contrast, with higher load impedance and the same value of the duty cycle (0.04), the piezoelement voltage is only slightly modified by the switching (Figure 4-17.b).

Cette thèse est accessible à l'adresse : http://theses.insa-lyon.fr/publication/2014ISAL0077/these.pdf
© [Y. Li], [2014], INSA de Lyon, tous droits réservés

Table 4-1. System Identification

Short circuit resonance frequency f_{cc}	56.45 Hz
Open circuit resonance frequency f_{oc}	56.72 Hz
Dynamic mass M	74.1 g
Short-circuit stiffness K_E	9317Nm^{-1}
Force factor α	0.0039 N/V
Mechanical quality factor Q_m	61.12
Electromechanical coupling coefficient k^2	0.0094
Viscous coefficient C	0.4318 Nm^{-1}S^{-1}
Piezoelectric blocked capacitance C_0	170 nF

For constant displacement, the structure is excited at a frequency close to the first bending mode resonance frequency. The input force (electromagnet driving current) is tuned to maintain a constant displacement. RMS Voltage over the resistance load is measured to calculate the output power obtained for each technique. Note that for S3H this measurement is somehow critical when the on-state time is short or when the load is only a small resistance. The RMS values are obtained numerically by monitoring the load voltage on an oscilloscope and then calculating explicitly the root mean square of the recorded voltage. Figure 4-18 shows a comparison of the experimental results and analytical predictions for constant displacement condition obtained with the model described in Section 4.2. For sake of comparison the data are normalized with the maximum theoretical power of the standard (STD) technique and the load is normalized to the optimal load of the standard technique defined by Equation(4.12).

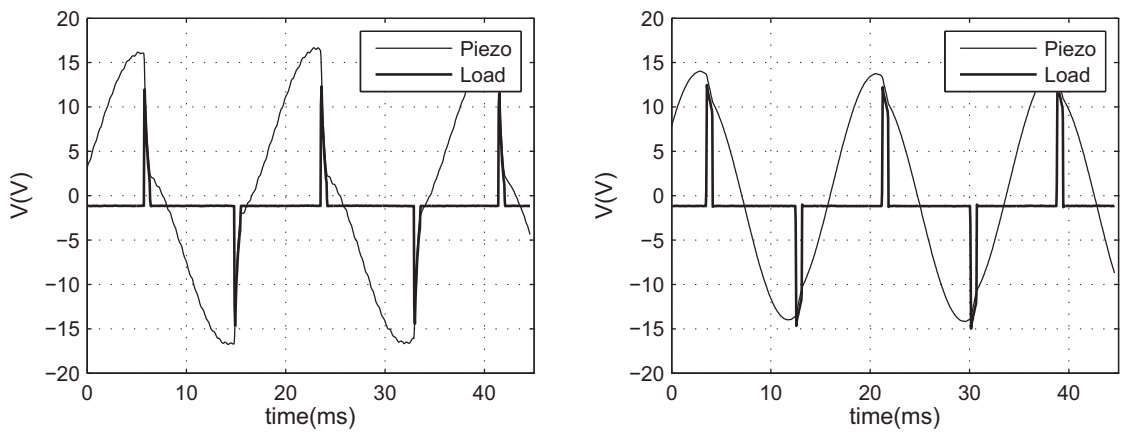

(a) (b)

Figure 4-17. Measured piezoelement and load voltages for a 0.04 duty cycle. –a) load R=2kΩ –b) load R=20kΩ

Cette thèse est accessible à l'adresse : http://theses.insa-lyon.fr/publication/2014ISAL0077/these.pdf
© [Y. Li], [2014], INSA de Lyon, tous droits réservés

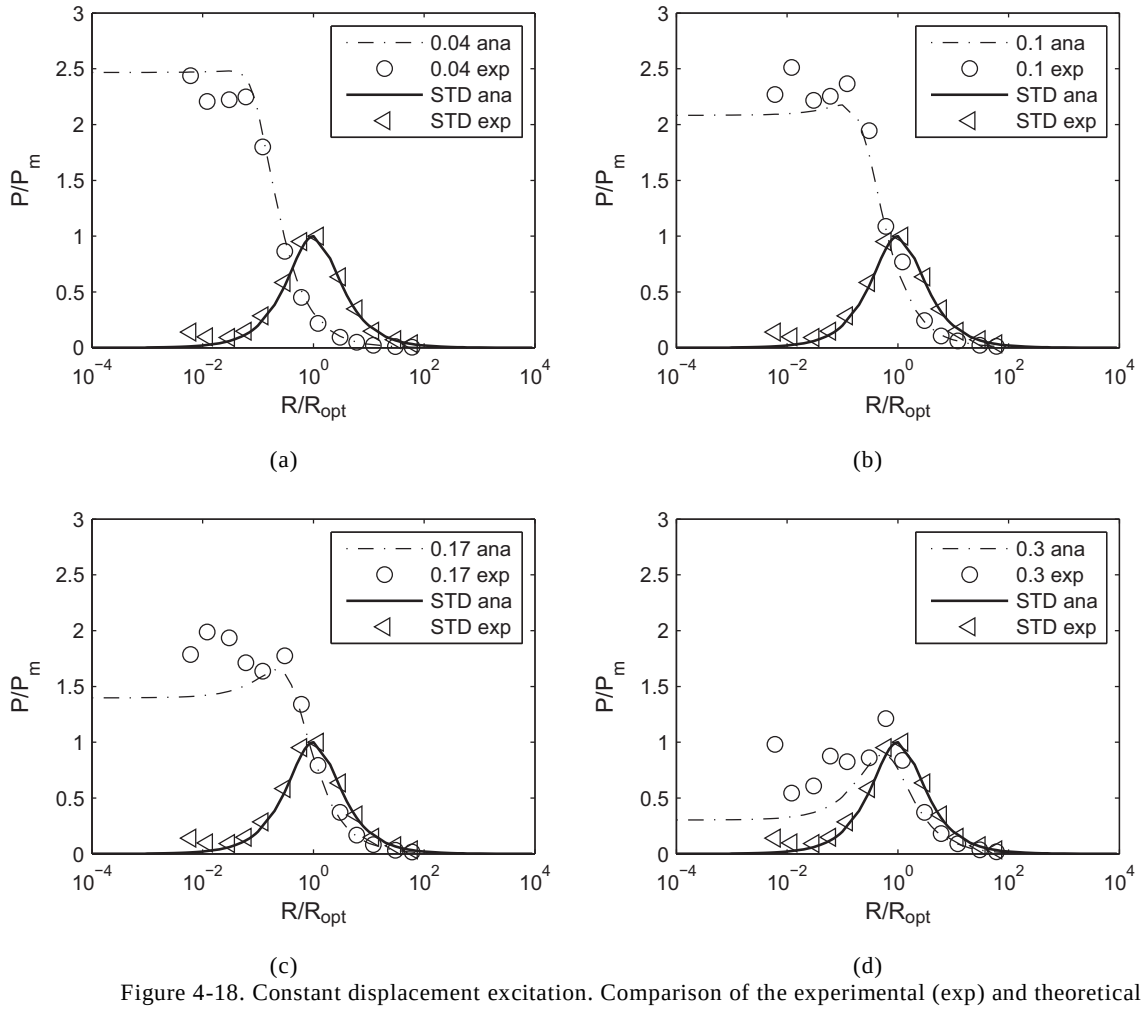

Figure 4-18. Constant displacement excitation. Comparison of the experimental (exp) and theoretical (ana) extracted powers versus the normalized load for S3H at various duty cycles and for the standard techniques. Power is normalized according to the theoretical maximum output power of the standard (STD) technique. Load is normalized to the STD optimal load defined by Equation (4.12).

It is clearly seen that the output power of the S3H technique is decreasing with the increase of the duty cycle (on-state time). For low duty cycles, a 2.5 times gain in power is achieved compared to standard circuit, in excellent agreement with the theoretical prediction. When the duty cycle increases and approaches 0.5, the power curve tends to merge with the standard case measurements. For low duty cycle, the optimal power is nearly independent to resistance load; whereas for high duty cycle, the optimal power is very sensitive to the load and requires impedance matching. It has to be noted that for low impedance, the experimental data has much more variations and imprecision due measurement errors resulting from the pulsed

Cette thèse est accessible à l'adresse : http://theses.insa-lyon.fr/publication/2014ISAL0077/these.pdf
© [Y. Li], [2014], INSA de Lyon, tous droits réservés

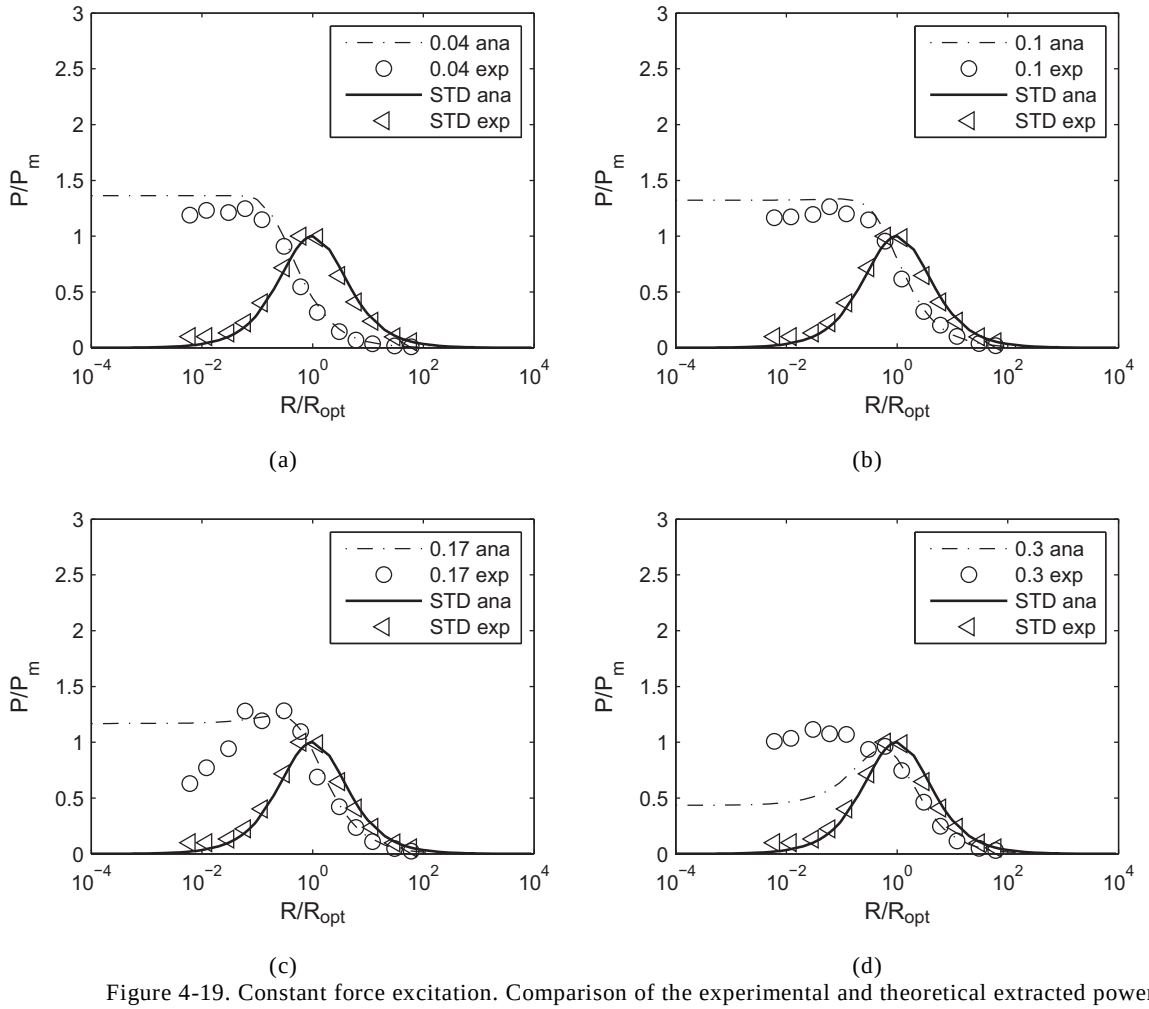

Figure 4-19. Constant force excitation. Comparison of the experimental and theoretical extracted power versus the load for S3H at various duty cycles and the standard techniques. Power is normalized according to the theoretical maximum output power of the standard (STD) technique.

nature of the voltage and non-perfect resistance nature of the load. Nevertheless the experimental results appear to be in overall very good agreement with the theoretical predictions.

For constant force conditions, the piezoelectric device is driven at the mechanical resonance frequency of the structure. The electromagnet current has constant amplitude, thus imposing a constant force on the beam. Figure 4-19 shows a comparison of the experimental output power and of the theoretical predictions for S3H technique at different duty cycles and for the standard (STD) technique. According to the theoretical predictions, the output power gain is smaller in this case due to the damping of the structure, but the independence of the

Cette thèse est accessible à l'adresse : http://theses.insa-lyon.fr/publication/2014ISAL0077/these.pdf
© [Y. Li], [2014], INSA de Lyon, tous droits réservés

output power to the load is still visible for low impedance values. The power gain is directly a consequence of the figure of merit k^2Q_M of the structure (k^2Q_M=0.61 in this experiment). For high figure of merit, no gain can be obtained with S3H, but a large useful impedance load bandwidth is provided. Moreover, there is an optimal on-time that results in the widest load impedance band at constant output power (approximately a 0.17 duty-cycle in this experimental case). Finally, measurement errors are still visible for low impedance values for the previously mentioned reasons.

4.4.3 Multi-mode case study

In the previous sections, the load-independent circuit S3H is validated theoretically and experimentally. For the sake of simplification of the analysis, a very simple harvesting circuit model is used (no bridge). In this subsection, a full energy harvesting circuit (with bridge) for S3H will be deployed. The STD and SECE circuit will be used as the comparison techniques. In the previous validation, only one excitation mode is considered. To have a more practical result, the multi-mode excitation is used to validate such load-independent circuit.

In this study a 4 mode sinusoidal excitation (40 Hz, 70Hz, 90Hz and 180 Hz) is applied to the beam (Figure 4-16). The energy harvesting circuits are STD, S3H and SECE. The AC-DC bridge is included (Figure 4-20). The extracted energy in such complex excitation condition is also considered, in order to emphasize the losses in the bridge and in the power processing (switch, inductor and diode). The piezoelectric voltage was recorded in one whole period. The extracted energy is calculated by,

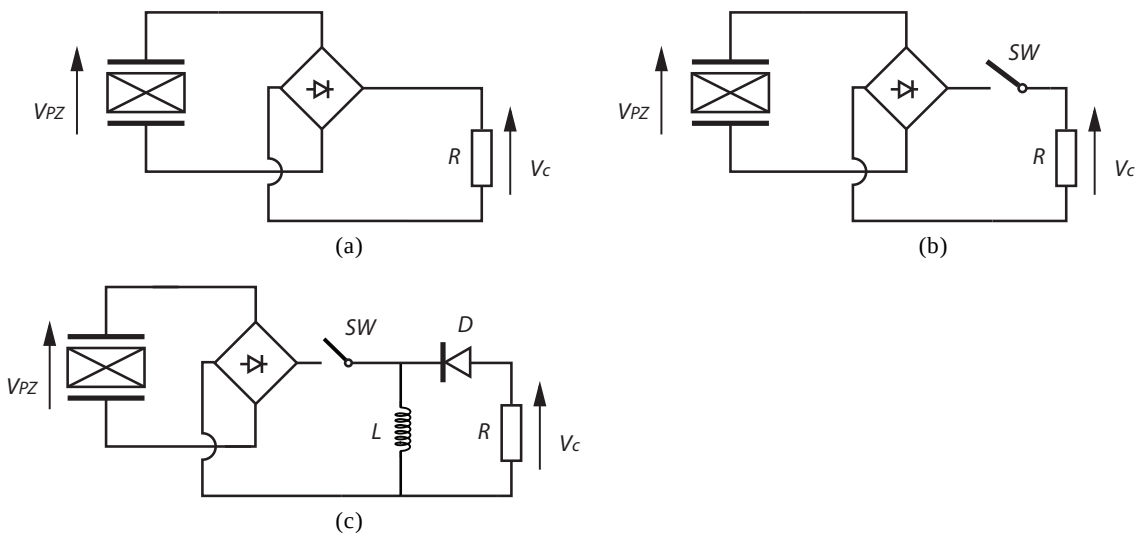

Figure 4-20. The harvesting circuit for multi mode excitation (a) STD (b) S3H (c) SECE

Cette thèse est accessible à l'adresse : http://theses.insa-lyon.fr/publication/2014ISAL0077/these.pdf
© [Y. Li], [2014], INSA de Lyon, tous droits réservés

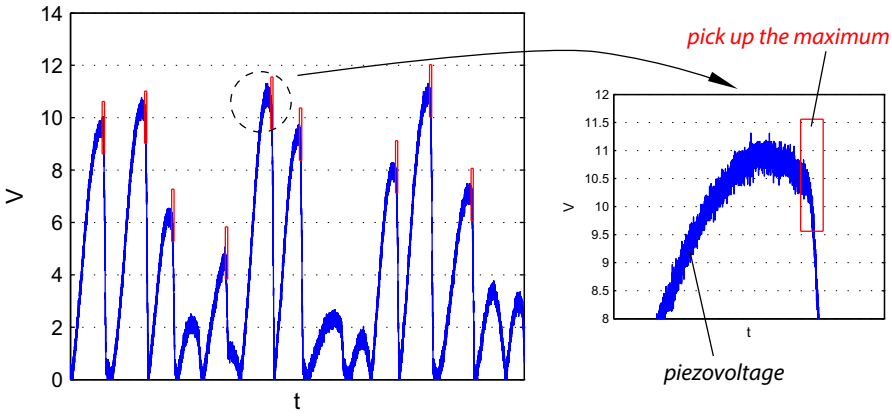

Figure 4-21. The piezovoltage at multimode excitation.

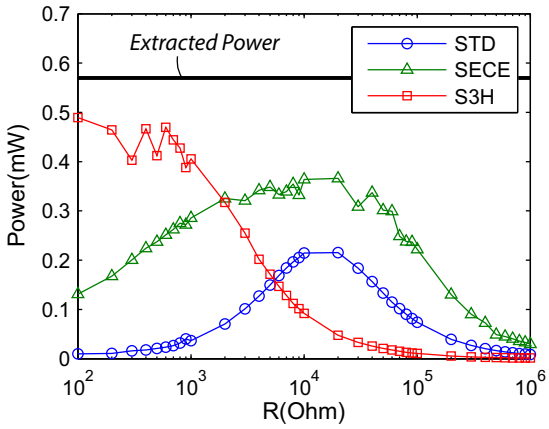

Figure 4-22. Power comparison with multimode excitation

$$E_{extract} = \frac{1}{2}\sum C_0 V_{PZ}^2 \tag{4.51}$$

here, C_0 is the blocked capacitance of piezoelectric element. V_{PZ} is the maximum value of each voltage extremum (Figure 4-21).

The experiments results are illustrated in Figure 4-22. The S3H can harvest more energy than the other two setups. Although the SECE circuit is load-independent, it is affected by the noise at low load region and electrical losses in high load region. Therefore the SECE circuit is load-independent in a restricted region (10^3 to 10^5 Ohm). Theoretically speaking, SECE and S3H have nearly the same power output. However, the S3H performs better thanks to its simple circuit topology and switch strategy as well as the absence of losses in the inductance. The difference between extracted energy and harvested energy is not trivial to predict.

Cette thèse est accessible à l'adresse : http://theses.insa-lyon.fr/publication/2014ISAL0077/these.pdf
© [Y. Li], [2014], INSA de Lyon, tous droits réservés

The experiments results proved that S3H circuit can work well on multi-mode excitation. The performance is better than SECE due to its simple topology.

4.5 S3H working in pulsed mode

Discontinuous signal is one important form of excitation. To investigate S3H technique under discontinuous excitation force, an energy harvesting circuit containing only a storage capacitor is considered. Same as previous, the standard technique is also considered as the comparison baseline (Figure 4-23).

The configuration of this experiment is similar as sinusoidal case, except for the input force. An arbitrary impulse signal is used in this experiment to investigate the feasibility of S3H technique. The response of S3H is illustrated in Figure 4-24.

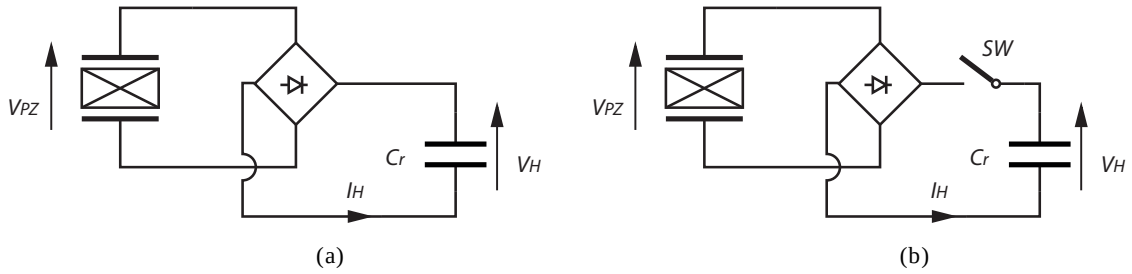

Figure 4-23. Energy harsvting circuit for pulse excitaion (a) STD (b) S3H

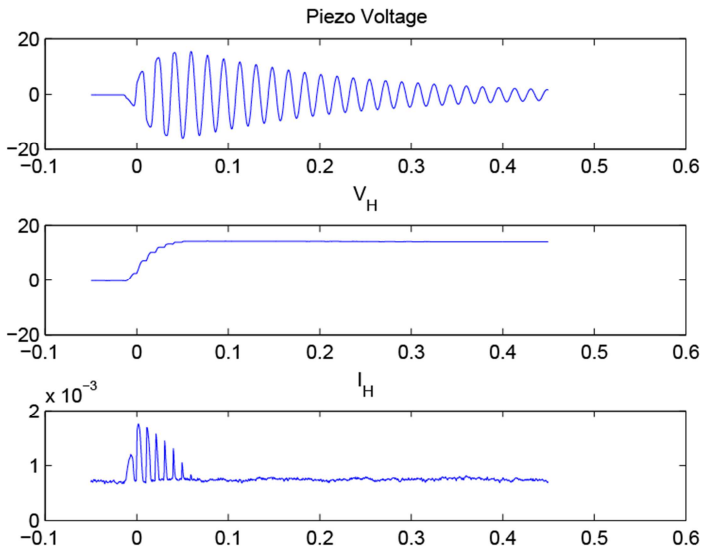

Figure 4-24. The experiment waveform of S3H with pulse excitaion. Piezovoltage, harvested voltage and current.

Cette thèse est accessible à l'adresse : http://theses.insa-lyon.fr/publication/2014ISAL0077/these.pdf
© [Y. Li], [2014], INSA de Lyon, tous droits réservés

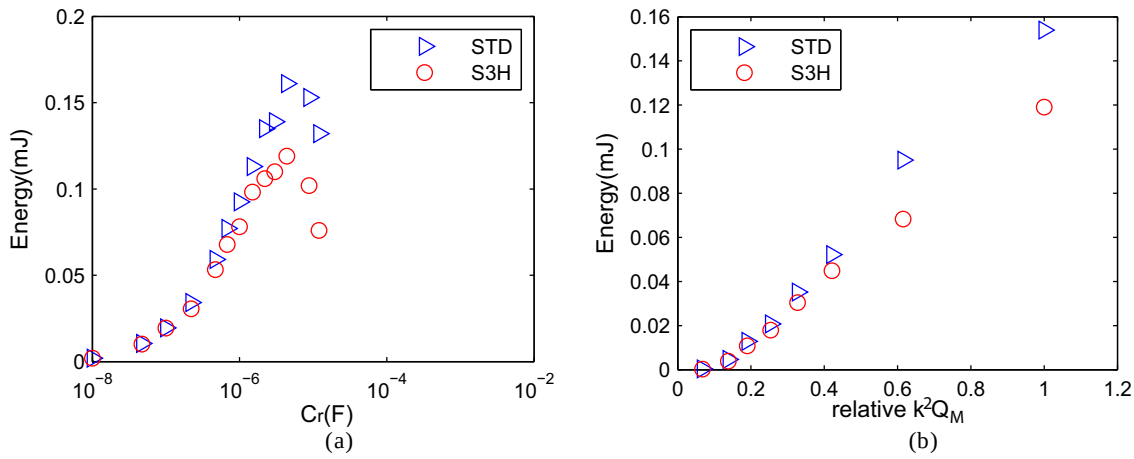

Figure 4-25. The experiment energy comparison of S3H and STD in pulse case. (a) various capacitances (b)various coupling factors

The harvested energy has been evaluated with this setup for various load comparisons and for various couplings of the piezogenerator. The results have been summarized on Figure 4-25. Unfortunately, the advantage of S3H is not so clear in pulse excitation mode. The harvested energy is lower than STD case whether with optimal capacitance (Figure 4-25.a) or with various figure of merit k^2Q_M (Figure 4-25.b). S3H in this condition can be seen as a twofold process. In a first stage, when the switch is open, the piezoelement blocked capacitance is charged due to the motion of the structure. Then, when the voltage reaches an extremum, the switch is closed and a discharge occurs between two capacitors: the charged piezoelement blocked capacitance and the load capacitance. Regrettably, it is well known that this type of process presents a very poor efficiency. Therefore, even if the energy converted is imposed due to the proposed switching process, the efficiency energy harvested on the output capacitance remains comparable or slightly smaller than with a conventional process.

4.6 Combination with Buck-boost circuit

The optimization failure of S3H with capacitance load denotes that S3H is only advantageous for purely resistive load case. To extend the application of S3H, the combination with buck-boost circuit should be considered. Lefeuvre *et al.* [66]have implemented a buck-boost converter in order to adjust the proper matching load of an energy harvester. Following their work, the input impedance of such converter is,

$$R_{in} = \frac{2Lf_{SW2}}{D^2} \tag{4.52}$$

here, D refers to the duty cycle of the converter, f_{SW2} is the switching frequency of the Buck-boost converter, L denotes the inductor. Since S3H contains only one switch, combining the

Cette thèse est accessible à l'adresse : http://theses.insa-lyon.fr/publication/2014ISAL0077/these.pdf
© [Y. Li], [2014], INSA de Lyon, tous droits réservés

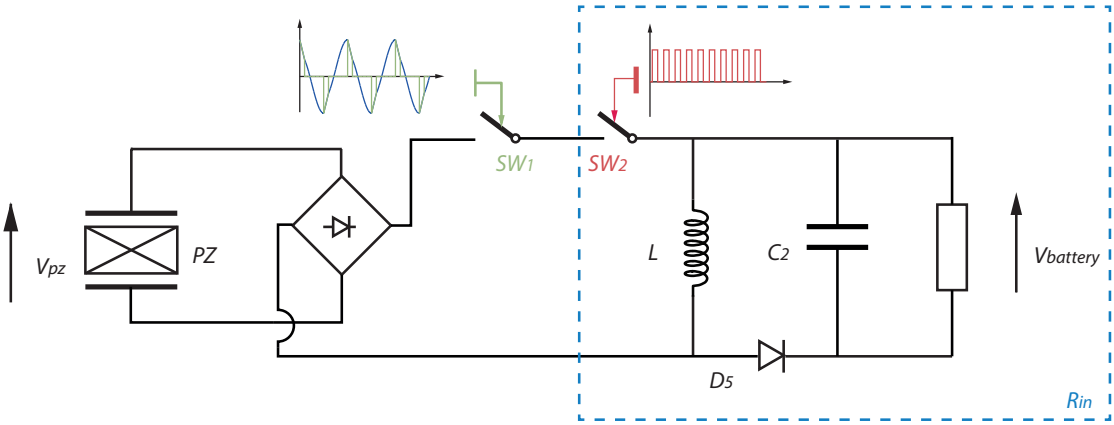

Figure 4-26. The schematic for S3H with buck-boost circuit

two switches together is possible. Figure 4-26 illustrates one possible deployment method for such a combination. The SW_1 and SW_2 can be achieved by one high frequency switch. Such high frequency switch will only be driven during an arbitrary time t_0 when the piezovoltage or displacement reaches its maximum or minimum. The working frequency is designed to make the S3H circuit working in load-independent region.

4.7 Conclusion

A new technique is proposed to optimize the output power of a piezoelectric generator. It consists of a simple switch in series with the piezoelectric element and the load triggered-on synchronously with the piezoelectric voltage or strain extremum. Following this technique called S3H for "Synchronized Serial Switch Harvesting", the switch on-time is arbitrarily fixed. The main advantage of this technique is that for a very large impedance range, the output power is completely independent to the load thus making ideal power generator. Moreover, for constant displacement excitation, corresponding usually to direct energy harvesting, the harvested power is more than twice the power harvested using the standard technique. Indeed the global power performance is similar to the SECE technique but S3H does not require fine tuning of the on-state of the switch such as in SECE, making S3H much easier to implement for energy harvesting on harmonic mechanical vibrations.

Experiments and theoretical predictions presented here are limited to a resistive load in AC mode. However, implementation with a rectifier bridge will not modify the global performance. Finally the resistive load can be replaced by a simple DC-DC buck-boost stage to generate a continuous output power. The load independent character of the power extraction strategy suppresses any need for complex tuning or regulation of the mentioned DC-DC stage allowing very easy and robust implementation.

Further work aims at emphasizing the importance of the piezogenerator figure of merit k^2Q_M on the global performance of S3H, and defining the corresponding optimal on-time.

Cette thèse est accessible à l'adresse : http://theses.insa-lyon.fr/publication/2014ISAL0077/these.pdf
© [Y. Li], [2014], INSA de Lyon, tous droits réservés

Moreover, multimode and pulsed operations were considered to validate the robustness of the proposed technique.

Cette thèse est accessible à l'adresse : http://theses.insa-lyon.fr/publication/2014ISAL0077/these.pdf
© [Y. Li], [2014], INSA de Lyon, tous droits réservés

(this page intentionally left blank)

Cette thèse est accessible à l'adresse : http://theses.insa-lyon.fr/publication/2014ISAL0077/these.pdf
© [Y. Li], [2014], INSA de Lyon, tous droits réservés

CHAPTER 5 Conclusion

Piezoelectric energy harvesting is a promising technique for powering small-scale standalone electronic devices. The work presented in this thesis discussed the development of simple and reliable approaches in order to optimize piezoelectric energy harvesting by focusing on modeling and circuit topology design. The piezoelectric energy harvester discussed in this work is treated as a resonator kind. The developments involved in this work are based on linear assumptions and basic applications. The input force are either purely sinusoidal or purely pulse signal, the load circuit of the harvester is simplified to a resistor or a passive complex load. The resistor is referred as the input impedance of the powered device. This work is fundamental research, which object is inspiring application researchers and industry engineers to optimize the performance of piezoelectric energy harvesting devices.

5.1 Designing the harvesting circuit for piezoelectric energy harvester

Since a resonating piezoelectric energy harvester is a device working around its resonance frequency, it can be treated as a SDOF system. A powerful tool, Mason equivalent circuit, is used to model this SDOF system. Starting from this classical tool, a lightweight equivalent circuit with comprehensive parameter definition is derived. It is the first equivalent circuit model which connects the system parameters, such as damping ratio, electromechanical coupling factor, excitation frequency, with the energy harvesting circuit parameter, such as load voltage , load current and load power in a very synthetic way.

The impedance of piezoelectric generator is easily derived from this lightweight circuit form. In the viewpoint of the harvester, the competition between damping ratio and electromechanical coupling coefficient determine the reactance property of such piezoelectric generator. Generally speaking, the piezoelectric generator is fully capacitive at strong damping condition. Its impedance may vary from capacitive to inductive for large coupling and low mechanical losses. Using the well-known impedance matching theory, the harvester generator can be matched either with a resistive or a complex load.

Resistive load case. Considering that the harvester is excited on a large frequency range, the power extracted from a resonating harvester is always optimized in the frequency range within short circuit and open circuit frequencies. These two frequencies play an important role at strong coupling condition. The optimal power is obtained around both critical frequencies. Graphically, the power versus frequency plot has two peaks as long as the coupling is high and the damping is low. In the opposite case, only one extremum is remaining. For a resistive load for which only the modulus of the impedance can be matched, the optimal power is not constant and reach an optimum wherever the transducer impedance is real which happens only at the resonance and anti-resonance of a highly coupled piezoelectric generator.

Yang LI
École doctorale EEA de Lyon / 2014
Institut national des sciences appliquées de Lyon

Cette thèse est accessible à l'adresse : http://theses.insa-lyon.fr/publication/2014ISAL0077/these.pdf
© [Y. Li], [2014], INSA de Lyon, tous droits réservés

Complex load case. In the case of a complex load type, whatever the coupling and the damping coefficient, optimal load can always be defined thus resulting in a constant optimal extracted power versus the frequency as long as the load is physically feasible. In the case of a highly coupled generator, optimal load impedance is essentially inductive except between short circuit and open circuit frequency where the load should be capacitive.

An electric modelling circuit such as Mason equivalent circuit is very practical to represent physically the electric generator and its impedance. Moreover, following this approach a simple and robust technique for equivalent circuit and impedance identification was presented. Consequent impedance matching with passive component was implemented and appeared to be in very good agreement with the equivalent circuit prediction. It was shown that load matching with a resistor is quite robust. Unlikely, the sensitivity of the matching of a transducer reactance with the reactance of the load is very sensitive making wide frequency load matching practically impossible. Such difficulties in achieving optimization of the output power of any piezoelectric generator justify perfectly the development of alternative non-liner approaches such as SSHI, S3H or SECE developed in these last years that replace the needed phase shift implemented by the reactance of the load by a specific switching of the harvester voltage.

5.2 Employing distributed harvesters

In this study, the feasibility of the association of various energy harvesting piezoelectric elements in order to form a unique source of energy has been demonstrated in the case of a planar structure excited in pulse mode. Five different topologies have been compared in terms of structure damping, harvested voltage and energy. These topologies include non linear parallel SSHI networks in order to optimize the extracted energy. It is shown that associating in parallel or in series different complete harvesting unit, each comprising a piezoelectric element, a parallel SSHI network and the rectifier diode bridge, do not change significantly the harvested power in comparison with the usual separate harvesters. It is however compulsory, in the case of a complex vibration pattern, to add as many SSHI network as piezoelectric elements used. Despite its simplicity, the use of a unique SSHI network in parallel with an association of piezoelectric elements results in degrades strongly the global harvesting capability due to improper definitions of the switching instants. According to the simulations, higher voltage (series) or higher current (parallel) configurations can be equally considered.

The problem of the electric insulation of the elements of the network in the case of a metallic conductive structure has been considered, and especially the influence of the thickness of the insulating bonding layer between the planar piezoelectric element and the structure. This layer is compulsory to ensure a proper energy harvesting, but in the same time, it degrades the piezoelectric element coupling coefficient. A very realistic 10 to 40 µm thick bonding layer is shown as a good trade-off ensuring both electrical integrity of the network and high energy

Cette thèse est accessible à l'adresse : http://theses.insa-lyon.fr/publication/2014ISAL0077/these.pdf
© [Y. Li], [2014], INSA de Lyon, tous droits réservés

extraction level. Both results demonstrate the possibility to build direct piezoelectric energy harvesting networks useful in the case of large bodies or shells where the harvesting piezoelectric elements are distributed all over the structure in the regions of maximum strain.

5.3 Obtaining a robust harvester

For most of the piezoelectric energy harvesters, a constant critical issue is power optimization and load matching. The proper load is determined by the piezoelectric energy harvester inherent impedance which is sensitive to the operation environment influenced by temperature, vibration amplitude, aging of electric components. All these changes could affect severely the output power.

A new technique is proposed to optimize the output power of a piezoelectric generator. It consists of a simple switch in series with the piezoelectric element and the load triggered-on synchronously with the piezoelectric voltage or strain extremum. Following this technique called S3H for “Synchronized Serial Switch Harvesting”, the switch on-time is arbitrarily fixed. The main advantage of this technique is that for a very large impedance range, the output power is completely independent to the load thus making ideal power generator. Moreover, for constant displacement excitation, corresponding usually to direct energy harvesting, the harvested power is more than twice the power harvested using the standard technique. Indeed the global power performance is similar to the SECE technique but S3H does not require fine tuning of the switch on-state time such as for SECE, making S3H much easier to implement for energy harvesting on harmonic mechanical vibrations. Experiments and theoretical development presented in this work are limited to a resistive load in AC mode. However, implementation with a rectifier bridge or with multimodel type of excitation showed experimentally that they do not affect strongly the global performances. Finally the resistive load can be replaced by a simple DC-DC buck-boost stage to generate a continuous output power. The load independent character of the power extraction strategy suppresses any need for complex tuning or regulation of the mentioned DC-DC stage allowing very easy and robust implementation. Further work aims at emphasizing the importance of the piezogenerator figure of merit k^2Q_M on the global performance of S3H, and defining the corresponding optimal on-time. Moreover, multimode or pulsed operation will be considered to demonstrate the robustness of the proposed technique.

5.4 Revisit the energy harvesting system architecture

The power output of piezoelectric energy harvester is coupled with the energy source. The power efficiency can be pulled up by applying power conditioning circuit. In energy harvesting, this power conditioning circuit is called energy harvesting circuit. The lightweight equivalent circuit derived from Mason equivalent circuit gives global view of energy harvesting circuit design. It shows that shunting a reactance component to the harvesting circuit to optimize

Cette thèse est accessible à l'adresse : http://theses.insa-lyon.fr/publication/2014ISAL0077/these.pdf
© [Y. Li], [2014], INSA de Lyon, tous droits réservés

power is difficult but possible. The challenge is the design of a low-consuming robust active component to simulate the required inductance/capacitance. But now the possible solution for wide bandwidth harvesting is placed multi-frequency harvesters. The network topology research has proven that a set of harvesters could be linked with one common storage capacitor without energy loss. Although this validation work is carried with SSHI technique, but it is believed that the results could be extended to SECE and S3H technique too. In practice, if the multi-piezoelectric element is boned on the vibration source directly, the float ground or common ground issues should be taken into account. This is due to the parasitic capacitor generated by the bonding layer. Other practical problems can't considered in energy harvesting circuit is the operation conditions, such as the temperature, working cycle and electronics aging, etc. These factors will change the character of piezoelectric energy harvester resulting in the shift of optimal load matching. In this respect, a tuning-free energy harvesting circuit is required. S3H is one of the solutions. Unfortunately, it is not suitable for charging capacitor directly. Therefore, additional voltage regulated circuit are required, such as buck boost. The extension of S3H could be combination with SSHI circuit, in this way, the harvesting circuit is load-robust and high power efficiency.

Cette thèse est accessible à l'adresse : http://theses.insa-lyon.fr/publication/2014ISAL0077/these.pdf
© [Y. Li], [2014], INSA de Lyon, tous droits réservés

BIBLIOGRAPHY

[1] J. W. Matiko, N. J. Grabham, S. P. Beeby, and M. J. Tudor, "Review of the application of energy harvesting in buildings," *Measurement Science and Technology*, vol. 25, p. 25, 2014.

[2] R. J. M. Vullers, R. van Schaijk, I. Doms, C. Van Hoof, and R. Mertens, "Micropower energy harvesting," *Solid-State Electronics*, vol. 53, pp. 684-693, 2009.

[3] A. Harb, "Energy harvesting: State-of-the-art," *Renewable Energy*, vol. 36, pp. 2641-2654, 2011.

[4] S. R. Anton and H. A. Sodano, "A review of power harvesting using piezoelectric materials (2003-2006)," *Smart Materials and Structures*, vol. 16, 2007.

[5] E. Becquerel, "Mémoire sur les effets électriques produits sous l'influence des rayons solaires," *Comptes Rendus des Séances Hebdomadaires*, vol. 9, pp. 561-567, 1839.

[6] A. Goetzberger, C. Hebling, and H.-W. Schock, "Photovoltaic materials, history, status and outlook," *Materials Science and Engineering: R: Reports*, vol. 40, pp. 1-46, 2003.

[7] European Commission, "PHOTOVOLTAICS," http://ec.europa.eu/research/energy/eu/index_en.cfm?pg=research-photovoltaics.

[8] NREL, "Best Research-cell Efficientcies," 2014, http://www.nrel.gov/ncpv/.

[9] T. Esram and P. L. Chapman, "Comparison of photovoltaic array maximum power point tracking techniques," *IEEE TRANSACTIONS ON ENERGY CONVERSION EC*, vol. 22, p. 439, 2007.

[10] E. Koutroulis, K. Kalaitzakis, and N. C. Voulgaris, "Development of a microcontroller-based, photovoltaic maximum power point tracking control system," *Power Electronics, IEEE Transactions on*, vol. 16, pp. 46-54, 2001.

[11] Y. Qiu, C. Van Liempd, B. Op het Veld, P. G. Blanken, and C. Van Hoof, "5uW-to-10mW input power range inductive boost converter for indoor photovoltaic energy

Cette thèse est accessible à l'adresse : http://theses.insa-lyon.fr/publication/2014ISAL0077/these.pdf
© [Y. Li], [2014], INSA de Lyon, tous droits réservés

harvesting with integrated maximum power point tracking algorithm," in *Solid-State Circuits Conference Digest of Technical Papers (ISSCC), 2011 IEEE International*, 2011, pp. 118-120.

[12] K. Tae-Yeop, A. Ho-Gyun, P. Seung Kyu, and L. Youn-Kyun, "A novel maximum power point tracking control for photovoltaic power system under rapidly changing solar radiation," in *Industrial Electronics, 2001. Proceedings. ISIE 2001. IEEE International Symposium on*, 2001, pp. 1011-1014 vol.2.

[13] T. Hiyama, S. Kouzuma, and T. Imakubo, "Identification of optimal operating point of PV modules using neural network for real time maximum power tracking control," *Energy Conversion, IEEE Transactions on*, vol. 10, pp. 360-367, 1995.

[14] R. Vullers, Z. Wang, M. Renaud, H. Visser, J. Oudenhoven, and V. Pop, "Micropower Generation: Principles and Applications," in *Smart Sensor Systems*: John Wiley & Sons, Ltd, 2014, pp. 237-274.

[15] D. Samson, M. Kluge, T. Becker, and U. Schmid, "Wireless sensor node powered by aircraft specific thermoelectric energy harvesting," *Sensors and Actuators A: Physical*, vol. 172, pp. 240-244, 2011.

[16] L. TECHNOLOGIES, "eTEG Series PG37,72,F2,0203,GG Thin Film Energy Harvester," http://www.lairdtech.com/Products/Power-Products/Power-Generators.

[17] X. Lu and S.-H. Yang, "Thermal energy harvesting for WSNs," in *Systems Man and Cybernetics (SMC), 2010 IEEE International Conference on*, 2010, pp. 3045-3052.

[18] S. J. Kim, J. H. We, and B. J. Cho, "A wearable thermoelectric generator fabricated on a glass fabric," *Energy & Environmental Science*, 2014.

[19] G. Sebald, E. Lefeuvre, and D. Guyomar, "Pyroelectric energy conversion: Optimization principles," *Ultrasonics, Ferroelectrics and Frequency Control, IEEE Transactions on*, vol. 55, pp. 538-551, 2008.

[20] A. Cuadras, M. Gasulla, and V. Ferrari, "Thermal energy harvesting through pyroelectricity," *Sensors and Actuators A: Physical*, vol. 158, pp. 132-139, 2010.

[21] S. W. Lee, Y. Yang, H.-W. Lee, H. Ghasemi, D. Kraemer, G. Chen, and Y. Cui, "An electrochemical system for efficiently harvesting low-grade heat energy," *NATURE COMMUNICATIONS*, vol. 5, 2014.

Cette thèse est accessible à l'adresse : http://theses.insa-lyon.fr/publication/2014ISAL0077/these.pdf
© [Y. Li], [2014], INSA de Lyon, tous droits réservés

[22] "Energy harveter ECO 200," enocean, http://www.enocean.com/en/enocean_modules/eco-200/.

[23] "Autonomous sensors, all-motion harvesters," Gravit innovation, http://www.gravit-innovation.org/projets/enerbee/.

[24] Z. L. Wang and J. Song, "Piezoelectric Nanogenerators Based on Zinc Oxide Nanowire Arrays," *Science*, vol. 312, pp. 242-246, 2006.

[25] S. Xu, Y. Qin, C. Xu, Y. Wei, R. Yang, and Z. L. Wang, "Self-powered nanowire devices," *Nature nanotechnology*, vol. 5, pp. 366-373, 2010.

[26] Y. Hu, C. Xu, Y. Zhang, L. Lin, R. L. Snyder, and Z. L. Wang, "A Nanogenerator for Energy Harvesting from a Rotating Tire and its Application as a Self-Powered Pressure/Speed Sensor," *Advanced Materials*, vol. 23, pp. 4068-4071, 2011.

[27] S. N. Cha, J.-S. Seo, S. M. Kim, H. J. Kim, Y. J. Park, S.-W. Kim, and J. M. Kim, "Sound-Driven Piezoelectric Nanowire-Based Nanogenerators," *Advanced Materials*, vol. 22, pp. 4726-4730, 2010.

[28] S. Lee, S.-H. Bae, L. Lin, Y. Yang, C. Park, S.-W. Kim, S. N. Cha, H. Kim, Y. J. Park, and Z. L. Wang, "Super-Flexible Nanogenerator for Energy Harvesting from Gentle Wind and as an Active Deformation Sensor," *Advanced Functional Materials*, vol. 23, pp. 2445-2449, 2013.

[29] D. Choi, K. Y. Lee, K. H. Lee, E. S. Kim, T. S. Kim, S. Y. Lee, S.-W. Kim, J.-Y. Choi, and J. M. Kim, "Piezoelectric touch-sensitive flexible hybrid energy harvesting nanoarchitectures," *Nanotechnology*, vol. 21, p. 405503, 2010.

[30] Z. Wang, X. Wang, J. Song, J. Liu, and Y. Gao, "Piezoelectric Nanogenerators for Self-Powered Nanodevices," *Pervasive Computing, IEEE*, vol. 7, pp. 49-55, 2008.

[31] X. Wang, J. Song, J. Liu, and Z. L. Wang, "Direct-Current Nanogenerator Driven by Ultrasonic Waves," *Science*, vol. 316, pp. 102-105, 2007.

[32] X. Wang, "Piezoelectric nanogenerators - Harvesting ambient mechanical energy at the nanometer scale," *Nano Energy*, vol. 1, pp. 13-24, 2012.

[33] B. Y. Lee, J. Zhang, C. Zueger, W.-J. Chung, S. Y. Yoo, E. Wang, J. Meyer, R. Ramesh, and S.-W. Lee, "Virus-based piezoelectric energy generation," *Nat Nano*, vol. 7, pp. 351-356, 2012.

Cette thèse est accessible à l'adresse : http://theses.insa-lyon.fr/publication/2014ISAL0077/these.pdf
© [Y. Li], [2014], INSA de Lyon, tous droits réservés

[34] LBNL, "Berkeley Lab Scientists Generate Electricity From Viruses," 2012, http://newscenter.lbl.gov/news-releases/2012/05/13/electricity-from-viruses/.

[35] J. M. Donelan, Q. Li, V. Naing, J. A. Hoffer, D. J. Weber, and A. D. Kuo, "Biomechanical Energy Harvesting: Generating Electricity During Walking with Minimal User Effort," *Science*, vol. 319, pp. 807-810, 2008.

[36] M. Deterre, E. Lefeuvre, and E. Dufour-Gergam, "An active piezoelectric energy extraction method for pressure energy harvesting," *Smart Materials and Structures*, vol. 21, 2012.

[37] C. Dagdeviren, B. D. Yang, Y. Su, P. L. Tran, P. Joe, E. Anderson, J. Xia, V. Doraiswamy, B. Dehdashti, X. Feng, B. Lu, R. Poston, Z. Khalpey, R. Ghaffari, Y. Huang, M. J. Slepian, and J. A. Rogers, "Conformal piezoelectric energy harvesting and storage from motions of the heart, lung, and diaphragm," *Proceedings of the National Academy of Sciences*, 2014.

[38] "PowerWalk M-Series R5 Datasheet," Bionic Power, http://bionic-power.com/downloads/PowerWalkMDatasheet%20V1.1.pdf.

[39] E. Lefeuvre, S. Risquez, M. Woytasik, M. Deterre, B. Boutaud, and R. Dal Molin, "Energy harvesting devices as long lasting power sources for the next generation pacemakers," in *Microelectronics (ICM), 2013 25th International Conference on*, 2013, pp. 1-4.

[40] P. H. de Jong, "Power harvesting using piezoelectric materials: applications in helicopter rotors," Enschede: University of Twente, 2013, p. 164, http://doc.utwente.nl/84388/

[41] S. W. Arms, C. P. Townsend, D. L. Churchill, S. M. Moon, and N. Phan, "Energy harvesting wireless sensors for helicopter damage tracking," in *ANNUAL FORUM PROCEEDINGS-AMERICAN HELICOPTER SOCIETY*, 2006, p. 1336.

[42] P. H. de Jong, R. Loendersloot, A. de Boer, and P. J. M. van der Hoogt, "Power harvesting in a helicopter lag damper," in *SMART'11* Saarbrucken, Germany, 2011, http://doc.utwente.nl/77688/

[43] M. Bryant, A. Fang, and E. Garcia, "Self-powered smart blade: helicopter blade energy harvesting," in *Proc. SPIE 7643, Active and Passive Smart Structures and Integrated Systems 2010*, pp. 764317-10.

[44] S. Dmitry Zakharov and Gor Lebedev and Orphee Cugat and Jerome Delamare and Bernard Viala and Thomas Lafont and Leticia Gimeno and Alexander, "Thermal energy

Cette thèse est accessible à l'adresse : http://theses.insa-lyon.fr/publication/2014ISAL0077/these.pdf
© [Y. Li], [2014], INSA de Lyon, tous droits réservés

conversion by coupled shape memory and piezoelectric effects," *Journal of Micromechanics and Microengineering,* vol. 22, p. 094005, 2012.

[45] C. Xu, X. Wang, and Z. L. Wang, "Nanowire structured hybrid cell for concurrently scavenging solar and mechanical energies," *Journal of the American Chemical Society,* vol. 131, pp. 5866-5872, 2009.

[46] T. Lafont, L. Gimeno, J. Delamare, G. A. Lebedev, D. I. Zakharov, B. Viala, O. Cugat, N. Galopin, L. Garbuio, and O. Geoffroy, "Magnetostrictive–piezoelectric composite structures for energy harvesting," *Journal of Micromechanics and Microengineering,* vol. 22, 2012.

[47] B. J. Hansen, Y. Liu, R. Yang, and Z. L. Wang, "Hybrid nanogenerator for concurrently harvesting biomechanical and biochemical energy," *ACS nano,* vol. 4, pp. 3647-3652, 2010.

[48] W. P. Mason, "Physical Acoustics:Principles and Methods," in *Physical Acoustics*. vol. 1-A: Academic Press, 1964.

[49] "IEEE Standard on Piezoelectricity," *ANSI/IEEE Std 176-1987,* 1988.

[50] A. Badel, D. Guyomar, E. Lefeuvre, and C. Richard, "Efficiency Enhancement of a Piezoelectric Energy Harvesting Device in Pulsed Operation by Synchronous Charge Inversion," *Journal of Intelligent Material Systems and Structures,* vol. 16, pp. 889-901, 2005.

[51] T. Ikeda, *Fundamentals of Piezoelectricity*: Oxford University Press, 1996.

[52] Y. C. Shu, I. C. Lien, and W. J. Wu, "An improved analysis of the SSHI interface in piezoelectric energy harvesting," *Smart Materials and Structures,* vol. 16, p. 2253, 2007.

[53] H. A. C. Tilmans, "Equivalent circuit representation of electromechanical transducers: I. Lumped-parameter systems," *Journal of Micromechanics and Microengineering,* vol. 6, p. 157, 1996.

[54] S. Sherrit, S. P. Leary, B. P. Dolgin, and Y. Bar-Cohen, "Comparison of the Mason and KLM equivalent circuits for piezoelectric resonators in the thickness mode," in *Ultrasonics Symposium, 1999. Proceedings. 1999 IEEE,* 1999, pp. 921-926 vol.2.

[55] A. Ballato, "Equivalent circuits for resonators and transducers driven piezoelectrically," DTIC Document 1990.

Cette thèse est accessible à l'adresse : http://theses.insa-lyon.fr/publication/2014ISAL0077/these.pdf
© [Y. Li], [2014], INSA de Lyon, tous droits réservés

[56] S. Butterworth, "On a Null Method of Testing Vibration Galvanometers," *Proceedings of the Physical Society of London,* vol. 26, p. 264, 1913.

[57] K. S. Van Dyke, "The Piezo-Electric Resonator and Its Equivalent Network," *Radio Engineers, Proceedings of the Institute of,* vol. 16, pp. 742-764, 1928.

[58] A. Erturk and D. J. Inman, "On Mechanical Modeling of Cantilevered Piezoelectric Vibration Energy Harvesters," *Journal of Intelligent Material Systems and Structures,* vol. 19, pp. 1311-1325, 2008.

[59] A. Erturk and D. J. Inman, "A distributed parameter electromechanical model for cantilevered piezoelectric energy harvesters," *Journal of Vibration and Acoustics,* vol. 130, p. 041002, 2008.

[60] A. Erturk and D. J. Inman, "Issues in mathematical modeling of piezoelectric energy harvesters," *Smart Materials and Structures,* vol. 17, p. 065016, 2008.

[61] D. Guyomar, A. Badel, E. Lefeuvre, and C. Richard, "Toward energy harvesting using active materials and conversion improvement by nonlinear processing," *Ultrasonics, Ferroelectrics and Frequency Control, IEEE Transactions on,* vol. 52, pp. 584-595, 2005.

[62] D. Guyomar, G. Sebald, S. Pruvost, M. Lallart, A. Khodayari, and C. Richard, "Energy Harvesting from Ambient Vibrations and Heat," *Journal of Intelligent Material Systems and Structures,* vol. 20, pp. 609-624, 2009.

[63] Y. Li, M. Lallart, and C. Richard, "Piezoelectric energy harvesting using a series synchronized switch technique," in *Proc. SPIE 9057, Active and Passive Smart Structures and Integrated Systems 2014,* San Diego, California, USA, 2014.

[64] G. K. Ottman, H. F. Hofmann, A. C. Bhatt, and G. A. Lesieutre, "Adaptive piezoelectric energy harvesting circuit for wireless remote power supply," *Power Electronics, IEEE Transactions on,* vol. 17, pp. 669-676, 2002.

[65] G. K. Ottman, H. F. Hofmann, and G. A. Lesieutre, "Optimized piezoelectric energy harvesting circuit using step-down converter in discontinuous conduction mode," in *Power Electronics Specialists Conference, 2002. pesc 02. 2002 IEEE 33rd Annual,* 2002, pp. 1988-1994.

[66] E. Lefeuvre, D. Audigier, C. Richard, and D. Guyomar, "Buck-Boost Converter for Sensorless Power Optimization of Piezoelectric Energy Harvester," *Power Electronics, IEEE Transactions on,* vol. 22, pp. 2018-2025, 2007.

Cette thèse est accessible à l'adresse : http://theses.insa-lyon.fr/publication/2014ISAL0077/these.pdf
© [Y. Li], [2014], INSA de Lyon, tous droits réservés

[67] N. Kong, D. S. Ha, A. Erturk, and D. J. Inman, "Resistive Impedance Matching Circuit for Piezoelectric Energy Harvesting," *Journal of Intelligent Material Systems and Structures*, 2010.

[68] M. Guan and W.-H. Liao, "Studies on the circuit models of piezoelectric ceramics," in *Information Acquisition, 2004. Proceedings. International Conference on*, 2004, pp. 26-31.

[69] L. Tang and Y. Yang, "A multiple-degree-of-freedom piezoelectric energy harvesting model," *Journal of Intelligent Material Systems and Structures*, 2012.

[70] C. Richard, D. Guyomar, D. Audigier, and H. Bassaler, "Enhanced semi passive damping using continuous switching of a piezoelectric device on an inductor," in *7th SPIE International Symposium on Smart Materials and Structures* Newsport, 2000.

[71] C. Richard, D. Guyomar, D. Audigier, and G. Ching, "Semi-passive damping using continuous switching of a piezoelectric device," 1999, pp. 104-111.

[72] W. W. Clark, "Vibration Control with State-Switched Piezoelectric Materials," *Journal of Intelligent Material Systems and Structures*, vol. 11, pp. 263-271, 2000.

[73] G. W. Taylor, J. R. Burns, S. A. Kammann, W. B. Powers, and T. R. Welsh, "The Energy Harvesting Eel: a small subsurface ocean/river power generator," *Oceanic Engineering, IEEE Journal of*, vol. 26, pp. 539-547, 2001.

[74] E. Lefeuvre, A. Badel, C. Richard, L. Petit, and D. Guyomar, "A comparison between several vibration-powered piezoelectric generators for standalone systems," *Sensors and Actuators A: Physical*, vol. 126, pp. 405-416, 2006.

[75] I. C. Lien, Y. C. Shu, W. J. Wu, S. M. Shiu, and H. C. Lin, "Revisit of series-SSHI with comparisons to other interfacing circuits in piezoelectric energy harvesting," *Smart Materials and Structures*, vol. 19, p. 125009, 2010.

[76] E. Lefeuvre, A. Badel, C. Richard, and D. Guyomar, "Piezoelectric Energy Harvesting Device Optimization by Synchronous Electric Charge Extraction," *Journal of Intelligent Material Systems and Structures*, vol. 16, pp. 865-876, 2005.

[77] Y. Wu, A. Badel, F. Formosa, W. Liu, and A. E. Agbossou, "Piezoelectric vibration energy harvesting by optimized synchronous electric charge extraction," *Journal of Intelligent Material Systems and Structures*, vol. 24, pp. 1445-1458, 2013.

Cette thèse est accessible à l'adresse : http://theses.insa-lyon.fr/publication/2014ISAL0077/these.pdf
© [Y. Li], [2014], INSA de Lyon, tous droits réservés

[78] M. Lallart, L. Garbuio, L. Petit, C. Richard, and D. Guyomar, "Double synchronized switch harvesting (DSSH): a new energy harvesting scheme for efficient energy extraction," *Ultrasonics, Ferroelectrics and Frequency Control, IEEE Transactions on,* vol. 55, pp. 2119-2130, 2008.

[79] Y. Wu, A. Badel, F. Formosa, W. Liu, and A. Agbossou, "Self-powered optimized synchronous electric charge extraction circuit for piezoelectric energy harvesting," *Journal of Intelligent Material Systems and Structures,* 2014.

[80] R. L. Harne and K. W. Wang, "A review of the recent research on vibration energy harvesting via bistable systems," *Smart materials and structures,* vol. 22, p. 023001, 2013.

[81] F. Cottone, H. Vocca, and L. Gammaitoni, "Nonlinear Energy Harvesting," *Physical Review Letters,* vol. 102, p. 080601, 2009.

[82] W. Q. Liu, A. Badel, F. Formosa, Y. P. Wu, and A. Agbossou, "Novel piezoelectric bistable oscillator architecture for wideband vibration energy harvesting," *Smart Materials and Structures,* vol. 22, p. 035013, 2013.

[83] W. Q. Liu, A. Badel, F. Formosa, Y. P. Wu, and A. Agbossou, "Wideband energy harvesting using a combination of an optimized synchronous electric charge extraction circuit and a bistable harvester," *Smart Materials and Structures,* vol. 22, p. 125038, 2013.

[84] M. Ferrari, V. Ferrari, M. Guizzetti, D. Marioli, and A. Taroni, "Piezoelectric multifrequency energy converter for power harvesting in autonomous microsystems," *Sensors and Actuators A: Physical,* vol. 142, pp. 329-335, 2008.

[85] H. Xue, Y. Hu, and Q.-M. Wang, "Broadband piezoelectric energy harvesting devices using multiple bimorphs with different operating frequencies," *Ultrasonics, Ferroelectrics and Frequency Control, IEEE Transactions on,* vol. 55, pp. 2104-2108, 2008.

[86] I. C. Lien and Y. C. Shu, "Array of piezoelectric energy harvesting by the equivalent impedance approach," *Smart Materials and Structures,* vol. 21, p. 082001, 2012.

[87] M. Lallart, Y.-C. Wu, C. Richard, D. Guyomar, and E. Halvorsen, "Broadband modeling of a nonlinear technique for energy harvesting," *Smart Materials and Structures,* vol. 21, p. 115006, 2012.

Cette thèse est accessible à l'adresse : http://theses.insa-lyon.fr/publication/2014ISAL0077/these.pdf
© [Y. Li], [2014], INSA de Lyon, tous droits réservés

[88] Y. C. Wu, E. Halvorsen, M. Lallart, C. Richard, and D. Guyomar, "Stochastic Modeling in the Frequency Domain for Energy Harvester With Switching Electronic Interface," 2014.

[89] N. W. Hagood and A. von Flotow, "Damping of structural vibrations with piezoelectric materials and passive electrical networks," *Journal of Sound and Vibration,* vol. 146, pp. 243-268, 1991.

[90] S.-y. Wu, "Piezoelectric shunts with a parallel RL circuit for structural damping and vibration control," in *1996 Symposium on Smart Structures and Materials*, 1996, pp. 259-269.

[91] W.-J. Wu, Y.-Y. Chen, B.-S. Lee, J.-J. He, and Y.-T. Peng, "Tunable resonant frequency power harvesting devices," in *Smart Structures and Materials*, 2006, pp. 61690A-61690A-8.

[92] J. M. Renno, M. F. Daqaq, and D. J. Inman, "On the optimal energy harvesting from a vibration source," *Journal of Sound and Vibration,* vol. 320, pp. 386-405, 2009.

[93] Y. Liao and H. A. Sodano, "Optimal parameters and power characteristics of piezoelectric energy harvesters with an RC circuit," *Smart Materials and Structures,* vol. 18, p. 045011, 2009.

[94] G. K. Ottman, H. F. Hofmann, and G. A. Lesieutre, "Optimized piezoelectric energy harvesting circuit using step-down converter in discontinuous conduction mode," *Power Electronics, IEEE Transactions on,* vol. 18, pp. 696-703, 2003.

[95] C. B. Williams and R. B. Yates, "Analysis of a micro-electric generator for microsystems," *Sensors and Actuators A: Physical,* vol. 52, pp. 8-11, 1996.

[96] X. Wang and L. Lin, "Dimensionless optimization of piezoelectric vibration energy harvesters with different interface circuits," *Smart Materials and Structures,* vol. 22, p. 085011, 2013.

[97] W. L. Winston, *Operations Research: Applications and Algorithms*, 4th ed. Pacific Grove, CA: Duxbury Press, 2003.

[98] M. Lallart, D. Guyomar, C. Richard, and L. Petit, "Nonlinear optimization of acoustic energy harvesting using piezoelectric devices," *The Journal of the Acoustical Society of America,* vol. 128, pp. 2739-2748, 2009.

Cette thèse est accessible à l'adresse : http://theses.insa-lyon.fr/publication/2014ISAL0077/these.pdf
© [Y. Li], [2014], INSA de Lyon, tous droits réservés

[99] D. Guyomar, T. Richard, and C. Richard, "Sound wave transmission reduction through a plate using piezoelectric synchronized switch damping technique," *Journal of Intelligent Material Systems and Structures,* vol. 19, pp. 791-803, 2008.

[100] E. F. Crawley and E. H. Anderson, "Detailed Models of Piezoceramic Actuation of Beams," *Journal of Intelligent Material Systems and Structures,* vol. 1, pp. 4-25, 1990.

[101] T. Wu, "Modeling and design of a novel cooling device for microelectronics using piezoelectric resonating beams," 2003.

[102] M. Lallart, S. Harari, L. Petit, D. Guyomar, T. Richard, C. Richard, and L. Gaudiller, "Blind switch damping (BSD): A self-adaptive semi-active damping technique," *Journal of Sound and Vibration,* vol. 328, pp. 29-41, 2009.

[103] W. T. Thomson and M. D. Dahleh, *Theory of Viration with Applications,* 5 ed. Beijing: Tsinghua Univesity Press, 2005.

Cette thèse est accessible à l'adresse : http://theses.insa-lyon.fr/publication/2014ISAL0077/these.pdf
© [Y. Li], [2014], INSA de Lyon, tous droits réservés

LIST OF FIGURES

Figure 1-1. Research cell efficiency records of photovoltaic by NREL [8] 11

Figure 1-2. The operation principle of a thermal energy generator using Seebeck effect 12

Figure 1-3. A werable energy harvseting demonstation.[18]..... 13

Figure 1-4. The battery charging process with thermogalvanic effect[21]..... 14

Figure 1-5. EnOcean Motion Harvester[22] 14

Figure 1-6. The piezoelectric nanowire generator(a) and the voltage and curent(b) generated from the movements of winkling [28]. 15

Figure 1-7. Schematic of piezoelectric M13 phage structure (a) and schematic of piezoelectirc electrical energy generation measurement set-up(b)[33] 16

Figure 1-8. Biomechanical energy harvester by the movements of knee [35] 17

Figure 1-9. The flexible MEH and the experiments comparison [37]..... 17

Figure 1-10. Piezoelectric effects..... 18

Figure 1-11. The piezoelectric element (a) plate in thickness mode (b) rod in 3-3 mode 19

Figure 1-12. The equivalent circuit for piezoelectric element(electrical view) 21

Figure 1-13. The 1-DOF modeling of piezoelectric energy harvester 22

Figure 1-14. Fundamental piezoelectric relation type and electromechanical coupling coefficient corresponding to the choice of independent variable set (from [51])..... 23

Figure 1-15. Stanard energy harvseting circuit..... 25

Figure 1-16. p-SSHI energy harvsting circuit..... 26

Figure 1-17. s-SSHI energy harvesting circuit..... 27

Figure 1-18. SECE energy harvsting circuit..... 28

Cette thèse est accessible à l'adresse : http://theses.insa-lyon.fr/publication/2014ISAL0077/these.pdf
© [Y. Li], [2014], INSA de Lyon, tous droits réservés

Figure 1-19. The OSECE energy harvesting circuit 28

Figure 1-20. DSSH energy harvesting circuit 29

Figure 1-21. Comparison of harveted power(f_{oc}=56.72Hz, α=0.0045 N/V, K^E=10272Nm^{-1},M=0.0818g, C_0=170nF, k^2=0.0113, Q_M=54. Q_I=5.6. γ_c=0.5,γ_0=0.74) 30

Figure 1-22.Three different bistable harvester.(a) Magnetic repulsion type (b) Magnetic attraction type(c) Buckled beam type [80] 31

Figure 1-23. A buckled-spring-mass bistable piezoeelctric enegy harvester [82] 32

Figure 1-24. The structure of piezoelectric energy harvester array [84] 32

Figure 1-25. Power response of harvseter array with different connection topology (a) parallel connection (b) mixed connection [85] 32

Figure 2-1. Mass-spring-damper model of a seismic piezoelectric generator with (a)purely resistive load or (b)inductive load 36

Figure 2-2. Mason Equivalent Circuit for the piezoelectric disk 37

Figure 2-3. Equivalent circuit on the mechanical side of the electromechanical transformer (a)Initial Mason circuit - (b) Simplified electrical equivalent circuit 38

Figure 2-4. Piezogenerator equivalent circuit: (a) open-circuit and (b) with load Z_L 39

Figure 2-5. Piezoelectric harvester equivalent circuit (Piezoelectric generator with load)using Norton (a) or Thevenin (b) representations 40

Figure 2-6. Admittance behaviour of the piezoelectric generator as a function of normalized frequency (ζ=0.04, k_e=0.6). 42

Figure 2-7. The amplitdue and phase of the impedance of piezoelectric generator(k_e=0.6) 42

Figure 2-8. Optimal load R_{opt} for pure resistive load matching with various damping coefficients ζ (k_e=0.6). 45

Figure 2-9. Optimal ouptut power (a) and corresponding proof mass motion amplitude (b) as a function of the normalized frequency obtained for the optimal load resistance depicted in Figure 6. Calculation is done for various loss coefficient ζ, for k_e=0.6 and for a 1g base acceleration. 46

Figure 2-10. Circuit property with optimal load (a) voltage (b)current. k_e=0.6 46

Cette thèse est accessible à l'adresse : http://theses.insa-lyon.fr/publication/2014ISAL0077/these.pdf
© [Y. Li], [2014], INSA de Lyon, tous droits réservés

Figure 2-11. The impedance of complex load (a) modulous (b) phase (c) resistance (d) reactance 51

Figure 2-12. Optimal power harvested (a) and corresponding proof mass motion amplitude (b) as a function of the relative frequency. 52

Figure 2-13. Circuit parameter for complex load case. (a) Voltage (b) Current 52

Figure 2-14. Circuit property for RL parallel case. (a) Voltage (b) Current..... 53

Figure 2-15. RL parallel case : optimal inductor and resistor with various of viscous loss 53

Figure 2-16. Optimal resistor (a) and optimal inductor (b) as a function of the normalized frequency for optimal impedance matching with a resistance in parralel with an inductance (k_e=0.6 and ζ=0.04) 55

Figure 2-17. Optimal ouptut power (b) and corresponding proof mass motion amplitude (a) as a function of the normalized frequency obtained for the optimal impedance defined in Figure 8. Calculation is done for k_e=0.6, for ζ=0.04 and for a 10 m/s² base acceleration. 56

Figure 2-18. The negative inductor by gyrator 56

Figure 2-19. The optimal load for LR parallel case obtained KKT method (a) Optimal inductor with various losses (b) Optimal resistor with various losses 58

Figure 2-20. Piezoelectric generator equivalent impedance near its resonance. 59

Figure 2-21. Experimental device: a) seismic piezoelectric-harvester mounted on the shaker. b) Cross-section of the piezoelectric-harvester made with a commercial piezoelectric buzzer. ... 60

Figure 2-22. Equivalent circuit identification process: a) Real and imaginary parts of the identified piezoelectric harvester admittance. Central frequency is 2335Hz; b) open circuit voltage response comparison. 60

Figure 2-23. The model for LR load..... 62

Figure 2-24. Impedance matching of the experimental harvester structure with a pure resistive load. a) Experimental and theoretical normalized out power, b) Theoretical and experimental optimal resistance..... 63

Figure 2-25. Impedance matching of the experimental harvester structure with a R-L load. a) Experimental and theoretical normalized out power, b) Theoretical and experimental optimal inductance, c) Theoretical and experimental optimal resistance. 64

Cette thèse est accessible à l'adresse : http://theses.insa-lyon.fr/publication/2014ISAL0077/these.pdf
© [Y. Li], [2014], INSA de Lyon, tous droits réservés

Figure 2-26. Sensitivity of the impedance matching to the optimal load for resistive optimal load: a) 30% standard deviation of the optimal resistance load, b) corresponding optimal output power. 65

Figure 2-27. Sensitivity of the impedance matching to the optimal load for parralel R-L load: a) 30% standard deviation of the optimal resistance load, b) 10% standard deviation of the optimal inductance load, c) corresponding output power dispersion and d) zoomed version of the plot shown in c) 66

Figure 2-28. Power sensitivity with 30% error of resistive load. (a) 5% error of inductor and (b)the corresponding power output (c) 1% error of inductor and (d) the corresponding power output. 67

Figure 3-1. The direct energy harvesting (a) and indirect energy harveting (b) 70

Figure 3-2. The metallic plate structure equipped with piezoelectric generators used in this study 71

Figure 3-3. Multimodal mass-spring-damper model of the smart structure with *n* piezoelectric elements 72

Figure 3-4. Basic energy harvesting circuit (a) Standard circuit (b) SSHI circuit 75

Figure 3-5. The SSHI circuit topology in detail 76

Figure 3-6. The inperfect switch and perfect switch in SSHI. (a) Rc=1e^3 Ohm. (b) Rc=1e^5 Ohm 77

Figure 3-7. Different network topologies for distribtued piezoelectric energy harvester: (a) A. Standard Network (b) B. Independent SSHI Network (c) C. SSHI in Parallel Network (d) D. Mono-SSHI Network (e) E. SSHI in Series Network. 79

Figure 3-8. Damping of the structure: (a) The 4 modal displacement waveforms for topology C (b) Decay time comparison. 81

Figure 3-9. Voltage waveform of the 3 harvesting piezoelectric elements. Solid line represents the piezovoltage, dashed line represents the harvested voltage on storage the capacitor 82

Figure 3-10. Harvested energy versus the capacitance C_r, A. Standard Network. B. Independent SSHI Network. C. SSHI Network in Parallel. D. Mono-SSHI Network. E. SSHI Network in Series. 83

Figure 3-11. Mechanical and harvested energy variations during the pulse (the values are normalized according to the initial pulse energy: 0.88 *mJ*: (a) Standard Network (b) SSHI based networks. 84

Cette thèse est accessible à l'adresse : http://theses.insa-lyon.fr/publication/2014ISAL0077/these.pdf
© [Y. Li], [2014], INSA de Lyon, tous droits réservés

Figure 3-12. Total harvested electrical energy versus the square of the coupling multiplication factor. Each simulations are obtained with the optimal output capacitance A. Standard Network. B. Independent SSHI Network. C. SSHI Network in Parallel. D. Mono-SSHI Network. E. SSHI Network in Series: (a) Harvested energy (b) Normalized harvested energy. 85

Figure 3-13. The enhanced storage capacitor for pulse operation (a) the circuit (b) the harvested voltage 87

Figure 3-14. Harvested eenrgy compasition of enhanced storage capacitor and normal storage capacitor. Topolocy C is used, pulse excitaiton. The value of capacitors in enhanced version are identical 88

Figure 3-15. Definition of the insulating bonding layer: (a) schematic of the t_b thick bonding layer; (b) Corresponding electric capacitance C_b. 88

Figure 3-16. Parasitic capacitance effect on the network harvesting performance with perfect coupling: (a) Location of the bonding parasitic capacitances within the E network. (b) Harvested voltage as a function of C_b. 89

Figure 3-17. The thickness affects the bending of piezoelectric element (a) ideal bending (b) bonding layer is too thick..... 90

Figure 3-18. Bonding Layer thickness influence on the harvester performance: (a) The piezoelectric force coefficient vs. the bonding layer thickness (normalized) (b) Overall harvested voltage. 92

Figure 4-1. The shifting of optimal load 96

Figure 4-2. Two energy harvsting circuits (a) Standard circuit (b) S3H circuit..... 96

Figure 4-3 The MDS modeling method 97

Figure 4-4. Standard circuit. (a) Circuit principle (b) Piezoelectric voltage V_{PZ} and displacement U 99

Figure 4-5. S3H circuit. (a) Circuit principle (b) Piezovoltage and load voltage.....100

Figure 4-6. Piezoelectric element voltage for S3H – The thin line (b to c) represents the voltage during the off-state position of the switch (Stage I) and the thick line (a to b) the voltage during the on-state (Stage II). 101

Figure 4-7. The harvested power dependence with the load resistance and duty cycle at constant displacement condition. a) Power variation for duty-cycle varying from 0 to 0.5 – b) harvested power for various duty-cycle and comparison to standard technique – c) 3D plot variation(f_{oc}=56.72Hz, α=0.0039 N/V, K^E=9317Nm-1, M=74.1g, C_0=170nF, k^2=0.0094, Q_M=61.1207.) 108

Cette thèse est accessible à l'adresse : http://theses.insa-lyon.fr/publication/2014ISAL0077/these.pdf
© [Y. Li], [2014], INSA de Lyon, tous droits réservés

Figure 4-8. Energy Cycle (a)STD circuit with various loads (b) S3H circuit with various duty cycle with load case R/R_{opt}=0.1 109

Figure 4-9. Energy Cycle comparison. STD and S3H (with various duty cycle). STD load case R/R_{opt}=1, S3H load case R/R_{opt}=0.1. 109

Figure 4-10. The harvested power dependence with the load resistance and duty cycle at constant force condition. a) power variation for duty-cycle varying from 0 to 0.5 – b) harvested power for various duty-cycle and comparison to standard technique – c) 3D plot variation. (f_{oc}=56.72Hz, α=0.0045 N/V, K^E=10272Nm^{-1},M=0.0818g, C_0=170nF, k^2=0.0113, Q_M=54.) .. 110

Figure 4-11. Power with various k^2Q_M (a) k^2Q_M= 0.61 (b) k^2Q_M= 6.1 (c) k^2Q_M= 61 112

Figure 4-12. Maximum power with various k^2Q_M. The load of S3H is R/R_{opt}=1e^{-4}. The load of STD is R/R_{opt}=1.(a) Relative view (b)Global view 113

Figure 4-13. Maximum power with various k^2Q_M. 113

Figure 4-14. The optimal duty cycle for bandwidth. (a) The difinition of idnex and bandwidth (b) The optimal duty cycle with various indexes. 114

Figure 4-15. The optimal duty cycle vesus coupling coefficient k^2Q_M with various indexes. . 115

Figure 4-16. Experimental set-up architecture 116

Figure 4-17. Measured piezoelement and load voltages for a 0.04 duty cycle. –a) load R=2kΩ – b) load R=20kΩ 117

Figure 4-18. Constant displacement excitation. Comparison of the experimental (exp) and theoretical (ana) extracted powers versus the normalized load for S3H at various duty cycles and for the standard techniques. Power is normalized according to the theoretical maximum output power of the standard (STD) technique. Load is normalized to the STD optimal load defined by Equation (4.12). 118

Figure 4-19. Constant force excitation. Comparison of the experimental and theoretical extracted power versus the load for S3H at various duty cycles and the standard techniques. Power is normalized according to the theoretical maximum output power of the standard (STD) technique. 119

Figure 4-20. The harvesting circuit for multi mode excitation (a) STD (b) S3H (c) SECE 120

Figure 4-21. The piezovoltage at multimode excitation. 121

Figure 4-22. Power comparison with multimode excitation..... 121

Figure 4-23. Energy harsvting circuit for pulse excitaion (a) STD (b) S3H 122

Cette thèse est accessible à l'adresse : http://theses.insa-lyon.fr/publication/2014ISAL0077/these.pdf
© [Y. Li], [2014], INSA de Lyon, tous droits réservés

Figure 4-24. The experiment waveform of S3H with pulse excitaion. Piezovoltage, harvested voltage and current. 122

Figure 4-25. The experiment energy comparison of S3H and STD in pulse case. (a) various capacitances (b)various coupling factors 123

Figure 4-26. The schematic for S3H with buck-boost circuit 124

Cette thèse est accessible à l'adresse : http://theses.insa-lyon.fr/publication/2014ISAL0077/these.pdf
© [Y. Li], [2014], INSA de Lyon, tous droits réservés

(this page intentionally left blank)

Cette thèse est accessible à l'adresse : http://theses.insa-lyon.fr/publication/2014ISAL0077/these.pdf
© [Y. Li], [2014], INSA de Lyon, tous droits réservés

LIST OF TABLES

Table 1-1. Summary of energy sources in residential and commercial buildings[1] 10

Table 1-2. Direct electromechanical analogies for lumped translational systems[53] 23

Table 1-3. Comparison of the principle energy harvesting circuits (the various constants are defined in the text) 30

Table 2-1. Numerical data for seismic piezogenerator [92]..... 37

Table 2-2. The comparison between KKT approach and equivalent circuit approach 58

Table 3-1. Smart structure numerical data used in the simulation..... 74

Table 3-2. Direct piezoelectric harvester deploying parameters 90

Table 4-1. System Identification 117

Cette thèse est accessible à l'adresse : http://theses.insa-lyon.fr/publication/2014ISAL0077/these.pdf
© [Y. Li], [2014], INSA de Lyon, tous droits réservés

(this page intentionally left blank)

Cette thèse est accessible à l'adresse : http://theses.insa-lyon.fr/publication/2014ISAL0077/these.pdf
© [Y. Li], [2014], INSA de Lyon, tous droits réservés

Appendix. A. Piezoelectric generator modeling by Mason Equivalent circuit

The detail derivation process from Mason equivalent circuit is described in this short paper. The basic relationship of various piezoelectric constant is given firstly, and then the simplified approach.

A.1 Piezoelectric constants relationship

In this section, we assume that piezoelectric generator is unidimensional, therefore,

$$\varepsilon_{33}^{T} = \varepsilon_{33}^{S} + \frac{e_{33}^{2}}{c_{33}^{E}} \tag{A.1}$$

$$k_{33}^{2} = \frac{e_{33}^{2}}{\varepsilon_{33}^{T} c_{33}^{E}} \tag{A.2}$$

$$c_{33}^{E} = c_{33}^{D} - \frac{e_{33}^{2}}{\varepsilon_{33}^{S}} \tag{A.3}$$

To have a complete view of such piezoelectric constants relationships, please refer to Figure 1-14 in Chapter 1.

A.1.1 Permittivity

Starting from Equation (A.1), we have,

$$\varepsilon_{33}^{T} = \varepsilon_{33}^{S} + \frac{e_{33}^{2}}{c_{33}^{E}} \Rightarrow \frac{e_{33}^{2}}{c_{33}^{E}} = \varepsilon_{33}^{T} - \varepsilon_{33}^{S} \tag{A.4}$$

Considering Equations(A.2)(A.4), we can find the relationship between two permittivity linked by electromechanical coefficient,

$$k_{33}^{2} = \frac{\varepsilon_{33}^{T} - \varepsilon_{33}^{S}}{\varepsilon_{33}^{T}}$$

$$\Rightarrow \quad k_{33}^{2}\varepsilon_{33}^{T} = \varepsilon_{33}^{T} - \varepsilon_{33}^{S}$$

$$\Rightarrow \quad \varepsilon_{33}^{S} = \varepsilon_{33}^{T} - k_{33}^{2}\varepsilon_{33}^{T}$$

That is

$$\varepsilon_{33}^{S} = \left(1 - k_{33}^{2}\right)\varepsilon_{33}^{T} \tag{A.5}$$

A.1.2 Elastic stiffness coefficient

Starting from Equation (A.3), we have,

Cette thèse est accessible à l'adresse : http://theses.insa-lyon.fr/publication/2014ISAL0077/these.pdf
© [Y. Li], [2014], INSA de Lyon, tous droits réservés

$$\frac{e_{33}^2}{\varepsilon_{33}^S} = c_{33}^D - c_{33}^E \tag{A.6}$$

Substituting Equation (A.5) into (A.6), obtain,

$$\frac{e_{33}^2}{\left(1-k_{33}^2\right)\varepsilon_{33}^T} = c_{33}^D - c_{33}^E \tag{A.7}$$

Then substituting Equation (A.2) into (A.7), obtain,

$$\frac{k_{33}^2 c_{33}^E}{\left(1-k_{33}^2\right)} = c_{33}^D - c_{33}^E \tag{A.8}$$

Then we could derive Equation (A.8) as following,

$$k_{33}^2 c_{33}^E = \left(c_{33}^D - c_{33}^E\right)\left(1-k_{33}^2\right)$$

$$k_{33}^2 c_{33}^E = c_{33}^D\left(1-k_{33}^2\right) - c_{33}^E\left(1-k_{33}^2\right)$$

$$k_{33}^2 c_{33}^E + c_{33}^E\left(1-k_{33}^2\right) = c_{33}^D\left(1-k_{33}^2\right)$$

$$c_{33}^E = c_{33}^D\left(1-k_{33}^2\right)$$

Then we get,

$$c_{33}^D = \frac{1}{\left(1-k_{33}^2\right)} c_{33}^E \tag{A.9}$$

A.1.3 Stiffness and others

The resonance frequency is defined as,

$$\omega_n = \sqrt{\frac{K}{m}} \tag{A.10}$$

We assume that it is a high-stiffness structure, therefore the global stiffness is determined by piezoelectric element's stiffness K_P^E. In this case, Equation (A.10) is rewritten as,

$$\omega_n = \sqrt{\frac{K_P^E}{m}} \tag{A.11}$$

The equivalent mass of the harvester is defined as,

$$m = M + \frac{1}{2} m_p \tag{A.12}$$

With the definition of piezoelectric stiffness,

$$K = K_P^E = \frac{A_p}{t_p} c_{33}^E \tag{A.13}$$

Specifically, the short circuit angular frequency is defined as,

Cette thèse est accessible à l'adresse : http://theses.insa-lyon.fr/publication/2014ISAL0077/these.pdf
© [Y. Li], [2014], INSA de Lyon, tous droits réservés

$$\omega_E = \sqrt{\frac{K_P^E}{m}} \tag{A.14}$$

The open circuit angular frequency is defined as,

$$\omega_D = \sqrt{\frac{K_P^D}{m}} \tag{A.15}$$

Substituting Equation (A.9)(A.13) into (A.14), obtain,

$$\omega_E = \sqrt{\frac{K_P^E}{m}} = \sqrt{\frac{\frac{A_p}{t_p} c_{33}^E}{m}} = \sqrt{\frac{\frac{A_p}{t_p} c_{33}^D \left(1-k_{33}^2\right)}{m}} = \sqrt{\frac{K_P^D}{m}} \sqrt{1-k_{33}^2} \tag{A.16}$$

$$= \omega_D \sqrt{1-k_{33}^2}$$

Starting from Equation (A.11)(A.13), the expression of c_{33}^E is obtained,

$$c_{33}^E = \frac{\omega_n^{\,2} t_p m}{A_p} \tag{A.17}$$

A.2 The simplification of Mason equivalent circuit: Preparation

We will simplify the Mason equivalent circuit (Figure A-1) based on the work of Section A.1. The fundamental relationship is derived firstly, and then the circuit is simplified by KCL/KVL.

A.2.1 Propagation speed

The propagation speed v_b^D is defined as,

$$v_b^D = \sqrt{\frac{1}{\rho s_{33}^D}} = \sqrt{\frac{c_{33}^D}{\rho}} \tag{A.18}$$

Considering the damping effect (the loss angle δ_p), we have,

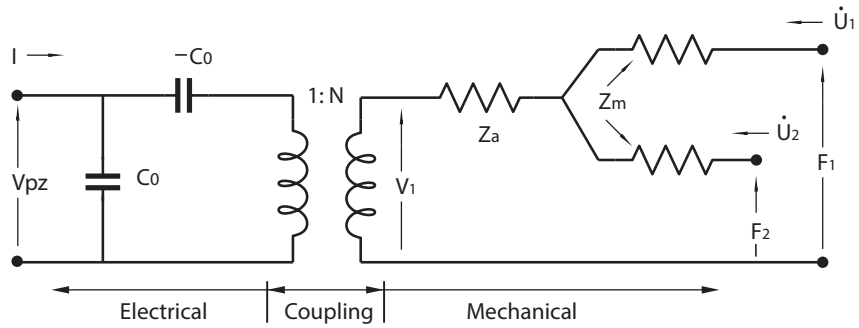

Figure A-1. Mason Equivalent circuit

Cette thèse est accessible à l'adresse : http://theses.insa-lyon.fr/publication/2014ISAL0077/these.pdf
© [Y. Li], [2014], INSA de Lyon, tous droits réservés

$$v_b^D = \sqrt{\frac{c_{33}^D(1+j\tan\delta_p)}{\rho}} \tag{A.19}$$

Substituting Equation (A.17) into (A.9), obtain,

$$c_{33}^D = \frac{1}{1-k_{33}^2}c_{33}^E = \frac{1}{1-k_{33}^2}\frac{\omega_n{}^2 t_p m}{A_p} \tag{A.20}$$

Then substituting (A.20) into (A.19), yield,

$$\left(v_b^D\right)^2 = \frac{1}{1-k_{33}^2}\frac{\omega_n{}^2 t_p m}{A_p\rho}(1+j\tan\delta_p) \tag{A.21}$$

A.2.2 Impedance in mechanical side

In the SDOF modelling method, the signal wavelength is larger than the device size, mathematically, it means,

$$\frac{\omega l}{v_b^D} \longrightarrow 0 \tag{A.22}$$

So we have,

$$\sin\frac{\omega l}{v_b^D} \approx \frac{\omega l}{v_b^D} \tag{A.23}$$

$$\tan\frac{\omega l}{2v_b^D} \approx \frac{\omega l}{2v_b^D} \tag{A.24}$$

Considering the mechanical impedance is defined as,

$$Z_a = \frac{Z_0}{j\sin\frac{\omega l}{v_b^D}}, \qquad Z_m = jZ_0\tan\frac{\omega l}{2v_b^D}, \qquad Z_0 = \rho w t v_b^D. \tag{A.25}$$

Therefore,

$$Z_a = \frac{Z_0}{j\sin\frac{\omega l}{v_b^D}} = \frac{\rho A_p\left(v_b^D\right)^2}{j\omega t_p} \tag{A.26}$$

Substituting Equation (A.21) into (A.26), obtain,

$$\begin{aligned} Z_a &= \frac{\rho A_p\left(v_b^D\right)^2}{j\omega t_p} = \frac{\rho A_p}{j\omega t_p}\frac{1}{1-k_{33}^2}\frac{\omega_n{}^2 t_p m}{A_p\rho}(1+j\tan\delta_P) = \frac{\omega_n{}^2 m}{j\omega\left(1-k_{33}^2\right)}(1+j\tan\delta_P) \\ &= \tan\delta_P \Big/ \frac{\omega\left(1-k_{33}^2\right)}{\omega_n{}^2 m} + 1 \Big/ j\omega\frac{\left(1-k_{33}^2\right)}{\omega_n{}^2 m} \end{aligned} \tag{A.27}$$

Cette thèse est accessible à l'adresse : http://theses.insa-lyon.fr/publication/2014ISAL0077/these.pdf
© [Y. Li], [2014], INSA de Lyon, tous droits réservés

For another equivalent mechanical impedance Z_m, we can find,

$$Z_m = jZ_0 \tan\frac{\omega l}{2v_b^D} = j\rho A_p v_b^D \frac{\omega l}{2v_b^D} = j\frac{\rho A_p t_p}{2}\omega \tag{A.28}$$

A.2.3 Turn ratio (Coupling)

The turn ratio (it stands for the electromechanical coupling, in fact) is defined as,

$$N = \frac{wt}{l}\frac{g_{33}}{s_{33}^E \beta_{33}^T} = \frac{wt}{l}\frac{d_{33}}{s_{33}^E} = \frac{A_p}{t_p}e_{33} \tag{A.29}$$

The constant e_{33} is unknown. However, we can find the proper expression for this unknown constant as following.

Starting from Equation (A.2),

$$k_{33}^2 = \frac{e_{33}^2}{\varepsilon_{33}^T c_{33}^E} \quad \Rightarrow \quad e_{33}^2 = k_{33}^2 \varepsilon_{33}^T c_{33}^E \tag{A.30}$$

Substituting (A.5) into (A.30), we have,

$$e_{33}^2 = k_{33}^2 \frac{1}{1-k_{33}^2}\varepsilon_{33}^S c_{33}^E \tag{A.31}$$

Consideration Equation (A.17), we can find,

$$e_{33}^2 = \frac{k_{33}^2}{1-k_{33}^2}\frac{\omega_n{}^2 t_p m}{A_p}\varepsilon_{33}^S \tag{A.32}$$

Finally, we find,

$$e_{33} = \sqrt{\frac{k_{33}^2}{1-k_{33}^2}\frac{\omega_n{}^2 t_p m}{A_p}\varepsilon_{33}^S} \tag{A.33}$$

Now, we can express the turn ratio N by known constants,

$$N = \frac{A_p}{t_p}\sqrt{\frac{k_{33}^2}{1-k_{33}^2}\frac{\omega_n{}^2 t_p m}{A_p}\varepsilon_{33}^S} = \omega_n\sqrt{\frac{k_{33}^2}{1-k_{33}^2}\frac{A_p m}{t_p}\varepsilon_{33}^S} \tag{A.34}$$

Cette thèse est accessible à l'adresse : http://theses.insa-lyon.fr/publication/2014ISAL0077/these.pdf
© [Y. Li], [2014], INSA de Lyon, tous droits réservés

A.3 The simplification of Mason equivalent circuit

A.3.1 Mechanical side

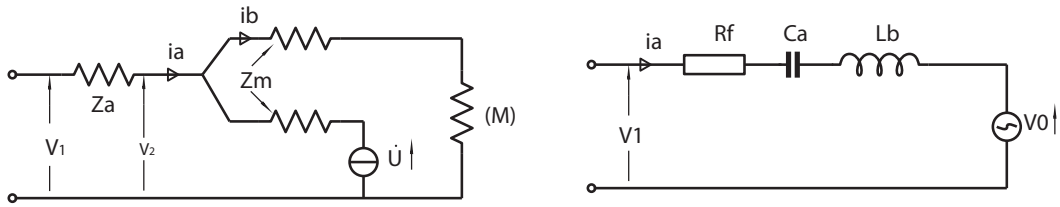

Figure A-2. The equivalent circuit on mechanical side

On the mechanical side, with Kirchhoff's current law, we have,

$$\dot{U} + i_a = i_b \tag{A.35}$$

And notice that,

$$\frac{V_1 - V_2}{Z_a} = i_a \tag{A.36}$$

$$\frac{V_2}{Z_m + M} = i_b \tag{A.37}$$

From Equation (A.37), we could get,

$$V_2 = i_b (Z_m + M) \tag{A.38}$$

Considering Equations (A.35)(A.36)(A.38), we can find,

$$\frac{V_1 - (\dot{U} + i_a)(Z_m + M)}{Z_a} = i_a \tag{A.39}$$

Starting from Equation (A.39),

Cette thèse est accessible à l'adresse : http://theses.insa-lyon.fr/publication/2014ISAL0077/these.pdf
© [Y. Li], [2014], INSA de Lyon, tous droits réservés

$$
\begin{aligned}
V_1 &= i_a Z_a + (\dot{U} + i_a)(Z_m + M) \\
&= i_a \frac{\tan\delta}{\dfrac{\omega\left(1-k_{33}^2\right)}{\omega_n^{\,2} m}} + i_a \frac{1}{j\omega \dfrac{\left(1-k_{33}^2\right)}{\omega_n^{\,2} m}} + (\dot{U} + i_a)\left(j\frac{\rho A_p t_p}{2}\omega + j\omega M \right) \\
&= i_a \frac{\tan\delta}{\dfrac{\omega\left(1-k_{33}^2\right)}{\omega_n^{\,2} m}} + i_a \frac{1}{j\omega \dfrac{\left(1-k_{33}^2\right)}{\omega_n^{\,2} m}} + j\omega(\dot{U} + i_a)\left(M + \frac{M_p}{2} \right) \\
&= i_a \frac{\tan\delta}{\dfrac{\omega\left(1-k_{33}^2\right)}{\omega_n^{\,2} m}} + i_a \frac{1}{j\omega \dfrac{\left(1-k_{33}^2\right)}{\omega_n^{\,2} m}} + j\omega\dot{U}L_b + j\omega i_a L_b \qquad with, \quad L_b = M + \frac{m_p}{2} \\
&= i_a \frac{\tan\delta}{\dfrac{\omega\left(1-k_{33}^2\right)}{\omega_n^{\,2} m}} + i_a \frac{1}{j\omega \dfrac{\left(1-k_{33}^2\right)}{\omega_n^{\,2} m}} + j\omega i_a L_b - \omega^2 U L_b
\end{aligned}
\tag{A.40}
$$

From Equation (A.40), the equivalent circuit for mechanical side is obtained(Figure A-2),

$$
V_1 = R_a i_a + \frac{1}{j\omega C_a} i_a + j\omega L_b i_a + V_0 \tag{A.41}
$$

with,

$$
\begin{aligned}
R_a &= \frac{\tan\delta_p}{\omega} \frac{\omega_n^{\,2} m}{\left(1-k_{33}^2\right)}, \quad C_a = \frac{\left(1-k_{33}^2\right)}{\omega_n^{\,2} m}, \\
L_b &= \frac{m_p}{2} + M, \qquad V_0 = \omega^2 L_b U.
\end{aligned}
\tag{A.42}
$$

Moreover, the piezoelectric loss angle is much smaller than the total harvester loss angle. Therefore an additional resistance R_f, much larger than R_a has to be considered.

$$
R_f = m\omega_n \tan\delta = 2m\omega_n\zeta \tag{A.43}
$$

Therefore the final expression of output voltage of mechanical portion V_1 becomes:

$$
V_1 = R_f i_a + \frac{1}{j\omega C_a} i_a + j\omega L_b i_a + V_0 \tag{A.44}
$$

A.3.2 The combination with electrical side

The mechanical side is transposed to the electrical side by turn ratio N transformer,

Cette thèse est accessible à l'adresse : http://theses.insa-lyon.fr/publication/2014ISAL0077/these.pdf
© [Y. Li], [2014], INSA de Lyon, tous droits réservés

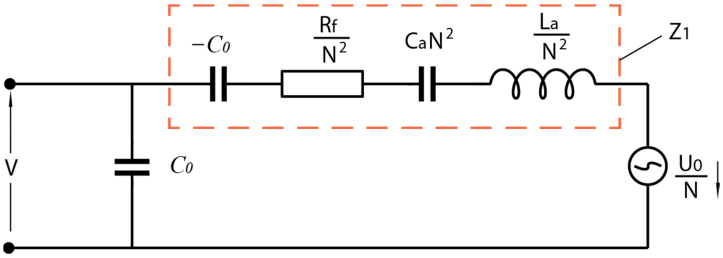

Figure A-3. The combination

$$Z_1 = \frac{R_f}{N^2} + j\omega\frac{L_b}{N^2} + \frac{1}{j\omega C_a N^2} - \frac{1}{j\omega C_0} \tag{A.45}$$

where,

$$\frac{R_a}{N^2} = 2m\omega_n\zeta \Bigg/ \left(\omega_n\sqrt{\frac{k_{33}^2}{1-k_{33}^2}\frac{A_p m}{t_p}\varepsilon_{33}^S}\right)^2 = 2\zeta \Bigg/ \left(\omega_n\frac{k_{33}^2}{1-k_{33}^2}\frac{A_p}{t_p}\varepsilon_{33}^S\right) \tag{A.46}$$

$$\frac{L_b}{N^2} = L_b \Bigg/ \left(\omega_n\sqrt{\frac{k_{33}^2}{1-k_{33}^2}\frac{A_p m}{t_p}\varepsilon_{33}^S}\right)^2 = \frac{1}{\omega_n^2}\frac{\left(1-k_{33}^2\right)}{k_{33}^2}\frac{t_p}{A_p\varepsilon_{33}^S}\frac{L_b}{m} \tag{A.47}$$

$$C_a N^2 = \frac{\left(1-k_{33}^2\right)}{\omega_n^2 m}\cdot\left(\omega_n\sqrt{\frac{k_{33}^2}{1-k_{33}^2}\frac{A_p m}{t_p}\varepsilon_{33}^S}\right)^2 = \frac{\left(1-k_{33}^2\right)}{\omega_n^2 m}\cdot\omega_n^2\frac{k_{33}^2}{1-k_{33}^2}\frac{A_p m}{t_p}\varepsilon_{33}^S = k_{33}^2\frac{A_p\varepsilon_{33}^S}{t_p} \tag{A.48}$$

Substituting Equation (A.46)(A.47)(A.48) into (A.45), we have,

Cette thèse est accessible à l'adresse : http://theses.insa-lyon.fr/publication/2014ISAL0077/these.pdf
© [Y. Li], [2014], INSA de Lyon, tous droits réservés

$$
\begin{aligned}
Z_1 &= \frac{R_f}{N^2} + j\omega\frac{L_b}{N^2} + \frac{1}{j\omega C_a N^2} - \frac{1}{j\omega C_0} \\
&= 2\zeta \Big/ \left(\omega_n \frac{k_{33}^2}{1-k_{33}^2}\frac{A_p}{t_p}\varepsilon_{33}^S \right) + j\omega\frac{1}{\omega_n^{\,2}}\frac{\left(1-k_{33}^2\right)}{k_{33}^2}\frac{t_p}{A_p\varepsilon_{33}^S}\frac{L_b}{m} + \frac{1}{j\omega k_{33}^2\dfrac{A_p\varepsilon_{33}^S}{t_p}} - \frac{1}{j\omega C_0} \\
&= 2\zeta \Big/ \left(\omega_n \frac{k_{33}^2}{1-k_{33}^2}\frac{A_p}{t_p}\varepsilon_{33}^S \right) + j\left[\omega\frac{1}{\omega_n^{\,2}}\frac{\left(1-k_{33}^2\right)}{k_{33}^2}\frac{t_p}{A_p\varepsilon_{33}^S}\frac{L_b}{m} - \frac{1}{\omega k_{33}^2\dfrac{A_p\varepsilon_{33}^S}{t_p}} + \frac{1}{\omega C_0} \right] \\
&= 2\zeta \Big/ \left(\omega_n \frac{k_{33}^2}{1-k_{33}^2}C_0 \right) + j\left[\omega\frac{1}{\omega_n^{\,2}}\frac{\left(1-k_{33}^2\right)}{k_{33}^2}\frac{1}{C_0}\frac{L_b}{m} - \frac{1}{\omega k_{33}^2 C_0} + \frac{1}{\omega C_0} \right] \\
&= 2\zeta \Big/ \left(\omega_n \frac{k_{33}^2}{1-k_{33}^2}C_0 \right) + j\frac{1}{\omega C_0}\left[\Omega^2\frac{\left(1-k_{33}^2\right)}{k_{33}^2}\frac{L_b}{m} - \frac{1}{k_{33}^2} + 1 \right] \\
&= 2\zeta \Big/ \left(\omega_n \frac{k_{33}^2}{1-k_{33}^2}C_0 \right) + j\frac{1}{\omega C_0}\left[\Omega^2\frac{\left(1-k_{33}^2\right)}{k_{33}^2}\frac{L_b}{m} - \frac{1-k_{33}^2}{k_{33}^2} \right] \\
&= 2\zeta \Big/ \left(\omega_n \frac{k_{33}^2}{1-k_{33}^2}C_0 \right) + j\frac{1}{\omega C_0}\frac{\left(1-k_{33}^2\right)}{k_{33}^2}\left(\Omega^2\frac{L_b}{m} - 1 \right)
\end{aligned}
\tag{A.49}
$$

where,

$$
C_0 = \frac{A_p\varepsilon_{33}^S}{t_p} \qquad \Omega = \frac{\omega}{\omega_n} \tag{A.50}
$$

Next, we find the way to replace loss angle by damping ratio,
As we known that,

$$
\zeta = \frac{c}{2m\omega_n} \tag{A.51}
$$

$$
c = \frac{m\omega_n}{Q_m} \tag{A.52}
$$

The relationship between damping ratio and mechanical quality factor is derived,

$$
\zeta = \frac{m\omega_n}{Q_m}\frac{1}{2m\omega_n} = \frac{1}{2Q_m} \tag{A.53}
$$

It is well known that

Cette thèse est accessible à l'adresse : http://theses.insa-lyon.fr/publication/2014ISAL0077/these.pdf
© [Y. Li], [2014], INSA de Lyon, tous droits réservés

$$Q_m = \frac{1}{\tan\delta} \tag{A.54}$$

Considering Equation (A.53)(A.54) , we have,

$$\tan\delta = 2\zeta \tag{A.55}$$

The alternative electromechanical coupling coefficient we have discussed in Chapter 1 is defined as,

$$k_e^2 = \frac{k_{33}^2}{1-k_{33}^2} \tag{A.56}$$

Then, we have,

$$k_{33}^2 = \frac{k_e^2}{1+k_e^2} \tag{A.57}$$

We also should notice that,

$$L_b = m \tag{A.58}$$

Substituting equation(A.55)(A.57)(A.58) into (A.49), the impedance Z_1 can be simplified as,

$$Z_1 = \frac{1}{\omega_n C_0}\frac{1}{\Omega}\alpha + j\frac{1}{\omega_n C_0}\frac{1}{\Omega}\beta \tag{A.59}$$

where,

$$C_0 = \frac{A_p \varepsilon_{33}^S}{t_p} \qquad \Omega = \frac{\omega}{\omega_n} \qquad k_e^2 = \frac{k_{33}^2}{1-k_{33}^2} \qquad \zeta = \frac{\tan\delta}{2}$$
$$\alpha = \Omega\frac{2\zeta}{k_e^2} \qquad \beta = \frac{\Omega^2-1}{k_e^2} \tag{A.60}$$

A.3.3 The impedance of generator

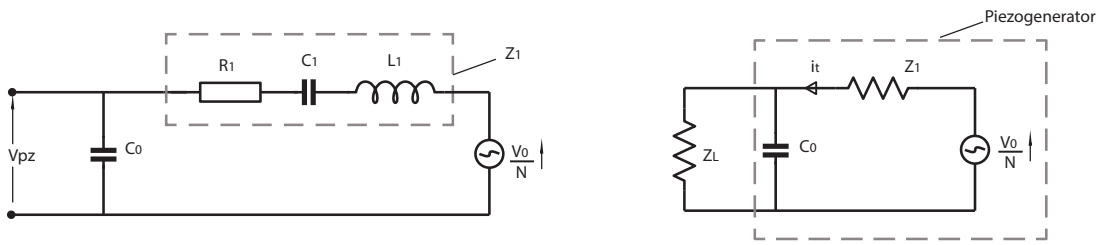

Figure A-4. The impedance of generator

Firstly, let's consider a general case. For a given Z which is defined by,

Cette thèse est accessible à l'adresse : http://theses.insa-lyon.fr/publication/2014ISAL0077/these.pdf
© [Y. Li], [2014], INSA de Lyon, tous droits réservés

$$Z = \frac{1}{\frac{1}{a+jb} + jc} \tag{A.61}$$

is simplified as,

$$\begin{aligned}
Z &= \frac{1}{\frac{1}{a+jb} + jc} = \frac{1}{\frac{a-jb}{a^2+b^2} + jc} = \frac{1}{\frac{a+j\left[c(a^2+b^2)-b\right]}{a^2+b^2}} = \frac{a^2+b^2}{a+j\left[c(a^2+b^2)-b\right]} \\
&= \left(a^2+b^2\right)\frac{a-j\left[c(a^2+b^2)-b\right]}{a^2+\left[c(a^2+b^2)-b\right]^2} = \left(a^2+b^2\right)\frac{a-j\left[c(a^2+b^2)-b\right]}{a^2+\left[c^2(a^2+b^2)^2+b^2-2bc(a^2+b^2)\right]} \\
&= \frac{a-j\left[c(a^2+b^2)-b\right]}{1+c^2(a^2+b^2)-2bc} = \frac{a-j\left[c(a^2+b^2)-b-b+b\right]}{1+c\left[c(a^2+b^2)-2b\right]} = \frac{a-j\left[c(a^2+b^2)-2b+b\right]}{1+c\left[c(a^2+b^2)-2b\right]} \\
&= \frac{a-j\left(A+b\right)}{1+cA} \qquad where \qquad A = c(a^2+b^2)-2b
\end{aligned} \tag{A.62}$$

The impedance of piezoelectric generator is Z_1 and C_0 in parallel, which is given by,

$$Z_T = Z_1 // C_0 = \frac{1}{\frac{1}{Z_1} + \frac{1}{Z_{C0}}} = \frac{1}{\frac{1}{\frac{1}{C_0\omega}(\alpha+j\beta)} + \frac{1}{\frac{1}{jC_0\omega}}} = \frac{1}{C_0\omega}\frac{1}{\frac{1}{\alpha+j\beta}+j} \tag{A.63}$$

Using the results showed in Equation (A.62), the impedance of generator is,

$$\begin{aligned}
Z_T &= \frac{1}{C_0\omega}\frac{1}{\frac{1}{\alpha+j\beta}+j} = \frac{1}{C_0\omega}\frac{\alpha-j(A+\beta)}{1+A} \\
&= \frac{1}{C_0\omega}\left(\frac{\alpha}{1+A} - j\frac{A+\beta}{1+A}\right) \qquad where, \qquad A = \alpha^2+\beta^2-2\beta \\
&= \frac{1}{C_0\omega_n}\frac{1}{\Omega}\left(\frac{\alpha}{1+A} - j\frac{A+\beta}{1+A}\right)
\end{aligned} \tag{A.64}$$

Cette thèse est accessible à l'adresse : http://theses.insa-lyon.fr/publication/2014ISAL0077/these.pdf
© [Y. Li], [2014], INSA de Lyon, tous droits réservés

Appendix. B. The power optimization for piezoelectric energy harvester

B.1 Purely resistive case

To maximum the power output, the load R is defined by,

$$R = |Z_T| = \frac{1}{C_0\omega_n\Omega}\frac{1}{1+x}|\alpha - j(x+\beta)| = \frac{1}{C_0\omega_n\Omega}\sqrt{\frac{\alpha^2+\beta^2}{1+x}} \tag{B.1}$$

We could get the Voltage V_L over the load R and the current I_L through load R,

$$V_L = \frac{I_s}{1/R + 1/Z_0} \qquad I_L = \frac{V_L}{R} \tag{B.2}$$

The power is calculated by,

$$P = \frac{V_L I_L^*}{R} \tag{B.3}$$

More, V_L could be expressed as,

$$\begin{aligned} V_L &= \frac{I_s}{1/R + 1/Z_0} \\ &= \frac{U_0}{N}\frac{1}{Z_1/R + Z_1/Z_0} \\ &= \frac{U_0}{N}\frac{1}{\dfrac{\alpha+j\beta}{C_0\omega_n\Omega R} + (1+x)\dfrac{\alpha+j\beta}{\alpha - j(x+\beta)}} \\ &= \frac{U_0}{N}\frac{1}{\left(\dfrac{\alpha}{R_x} + 1 - \beta\right) + j\left(\dfrac{\beta}{R_x} + \alpha\right)} \qquad with, \quad R_x = \sqrt{\frac{\alpha^2+\beta^2}{1+x}} \end{aligned} \tag{B.4}$$

Here, let's consider a general case. If Z is defined by,

$$Z = \frac{1}{a+jb}$$

We could get,

Cette thèse est accessible à l'adresse : http://theses.insa-lyon.fr/publication/2014ISAL0077/these.pdf
© [Y. Li], [2014], INSA de Lyon, tous droits réservés

$$|Z| = \frac{1}{\sqrt{a^2+b^2}}$$
$$Z \cdot Z^* = |Z|^2 = \frac{1}{a^2+b^2} \tag{B.5}$$

With Equation (B.1) (B.2), (B.4) and (B.5), the power (B.3) could be expressed as,

$$\begin{aligned} P &= V_L I_L^* = \frac{V_L V_L^*}{R} \\ &= \left(\frac{U_0}{N}\right)^2 \frac{1}{\left[\left(\frac{\alpha}{R_x}+1-\beta\right)^2+\left(\frac{\beta}{R_x}+\alpha\right)^2\right]R} \\ &= \left(\frac{U_0}{N}\right)^2 \frac{C_0\omega_n}{\left[\left(\frac{\alpha}{R_x}+1-\beta\right)^2+\left(\frac{\beta}{R_x}+\alpha\right)^2\right]R_x\frac{1}{\Omega}} \end{aligned} \tag{B.6}$$

Using Equation (B.6), it is possible to plot the power versus normalized frequency Ω under different conditions (Figure B-1), for instance, damping ratio ζ. Now the problem to find the extreme value of P is equal to find the extreme value of following expression,

$$\begin{aligned} y &= \left[\left(\frac{\alpha}{R_x}+1-\beta\right)^2+\left(\frac{\beta}{R_x}+\alpha\right)^2\right]R_x\frac{1}{\Omega} \\ &= \frac{2}{\Omega}\left(\sqrt{\left(\alpha^2+\beta^2\right)\left(\alpha^2+\beta^2-2\beta+1\right)}+\alpha\right) \end{aligned} \tag{B.7}$$

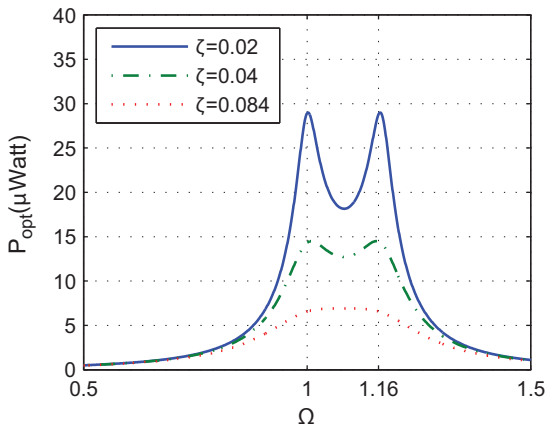

Figure B-1. The power versus normalized frequency with various damping ratios

Cette thèse est accessible à l'adresse : http://theses.insa-lyon.fr/publication/2014ISAL0077/these.pdf
© [Y. Li], [2014], INSA de Lyon, tous droits réservés

B.1.1 Low loss (low coupling) condition

(A) Stationary points

If the loss factor ζ becomes zero, according to the definition of alpha, alpha becomes zero, Equation (B.7) is simplified to,

$$y_1 = \pm 2(\beta - 1)\beta \frac{1}{\Omega} \tag{B.8}$$

Noticing, if $\beta = 0$ or $\beta = 1$, $y_1 \equiv 0$, That means y_1 is always at its extreme value as $\beta = 0$ or $\beta = -1$. This gives the four roots of normalized frequency Ω,

$$\begin{aligned} \frac{\Omega^2 - 1}{\kappa^2} = 0 \quad &\Rightarrow \quad \Omega_{1,2} = \pm 1 \\ \frac{\Omega^2 - 1}{\kappa^2} = 1 \quad &\Rightarrow \quad \Omega_{3,4} = \pm\sqrt{\kappa^2 + 1} \end{aligned} \tag{B.9}$$

Considering normalized frequency Ω is real and positive,

$$\Omega_{extreme1} = 1 \qquad \Omega_{extreme2} = \sqrt{\kappa^2 + 1} \tag{B.10}$$

If $1 - \beta \neq 0$ and $\beta \neq 0$,

$$y_1 = \pm 2(\beta - 1)\beta \frac{1}{\Omega} = \pm\left(2\beta^2 \frac{1}{\Omega} - 2\beta \frac{1}{\Omega}\right) \tag{B.11}$$

Differentiate y_1 with respect to normalized frequency Ω,

$$y_1' = \pm\left(4\beta\beta' \frac{1}{\Omega} - 2\beta^2 \frac{1}{\Omega^2} - 2\beta' \frac{1}{\Omega} + 2\beta \frac{1}{\Omega^2}\right) \tag{B.12}$$

Substituting β into (B.12),

$$\begin{aligned} y_1' &= \pm\left(4\frac{\Omega^2 - 1}{\kappa^2}\frac{2\Omega}{\kappa^2}\frac{1}{\Omega} - 2\left(\frac{\Omega^2 - 1}{\kappa^2}\right)^2 \frac{1}{\Omega^2} - 2\frac{2\Omega}{\kappa^2}\frac{1}{\Omega} + 2\frac{\Omega^2 - 1}{\kappa^2}\frac{1}{\Omega^2}\right) \\ &= \pm\left(8\frac{\Omega^2 - 1}{\kappa^2}\frac{1}{\kappa^2} - 2\left(\frac{\Omega^2 - 1}{\kappa^2}\right)^2 \frac{1}{\Omega^2} - \frac{4}{\kappa^2} + 2\frac{\Omega^2 - 1}{\kappa^2}\frac{1}{\Omega^2}\right), \quad with \quad \Omega \neq 0 \end{aligned} \tag{B.13}$$

Here, set a new variable,

$$A = \Omega^2 - 1 \tag{B.14}$$

Then the initial problem could be changed to find the solution of $g=0$, which is given by,

$$g(A) = \pm\left(8\frac{A}{\kappa^2}\frac{1}{\kappa^2} - 2\frac{A^2}{\kappa^4}\frac{1}{A+1} - \frac{4}{\kappa^2} + 2\frac{A}{\kappa^2}\frac{1}{A+1}\right) \tag{B.15}$$

Solve the g=0,

Cette thèse est accessible à l'adresse : http://theses.insa-lyon.fr/publication/2014ISAL0077/these.pdf
© [Y. Li], [2014], INSA de Lyon, tous droits réservés

$$8\frac{A}{\kappa^2}\frac{1}{\kappa^2}-2\frac{A^2}{\kappa^4}\frac{1}{A+1}-\frac{4}{\kappa^2}+2\frac{A}{\kappa^2}\frac{1}{A+1}=0 \tag{B.16}$$

If $\kappa^4(A+1)\neq 0$,

$$\begin{aligned} 8A(A+1)-2A^2-4\kappa^2(A+1)+2\kappa^2 A=0 \\ 6A^2+\left(8-2\kappa^2\right)A-4\kappa^2=0 \end{aligned} \tag{B.17}$$

With the discriminant,

$$\Delta=b^2-4ac=\left(8-2\kappa^2\right)^2+96\kappa^2=4\kappa^4+64\kappa^2+64>0 \tag{B.18}$$

So target function *g(A)* has two different real roots, given by,

$$A_{1,2}=\frac{2\kappa^2-8\pm\sqrt{4\kappa^4+64\kappa^2+64}}{12}=\frac{\kappa^2-4\pm\sqrt{\kappa^4+16\kappa^2+16}}{6} \tag{B.19}$$

Substituting Equation (B.14) into (B.19), normalized frequency Ω is solved,

$$\Omega_{5,6,7,8}=\pm\sqrt{\frac{\kappa^2-4\pm\sqrt{\kappa^4+16\kappa^2+16}}{6}+1}=\pm\frac{1}{\sqrt{6}}\sqrt{\kappa^2+2\pm\sqrt{\kappa^4+16\kappa^2+16}} \tag{B.20}$$

$$\begin{aligned} &\Omega_5=\frac{1}{\sqrt{6}}\sqrt{\kappa^2+2+\sqrt{\kappa^4+16\kappa^2+16}},\quad \Omega_6=-\frac{1}{\sqrt{6}}\sqrt{\kappa^2+2+\sqrt{\kappa^4+16\kappa^2+16}}, \\ &\Omega_7=\frac{1}{\sqrt{6}}\sqrt{\kappa^2+2-\sqrt{\kappa^4+16\kappa^2+16}},\quad \Omega_8=-\frac{1}{\sqrt{6}}\sqrt{\kappa^2+2-\sqrt{\kappa^4+16\kappa^2+16}}. \end{aligned} \tag{B.21}$$

Noticing that,

$$\begin{aligned} &\frac{\left(\kappa^2+2\right)^2}{\kappa^4+16\kappa^2+16}=\frac{\left(\kappa^2+2\right)^2}{\left(\kappa^2+2\right)^2+12\kappa^2+12}<1 \\ &\Rightarrow\sqrt{\frac{\left(\kappa^2+2\right)^2}{\kappa^4+16\kappa^2+16}}=\frac{\kappa^2+2}{\sqrt{\kappa^4+16\kappa^2+16}}<1 \\ &\Rightarrow\kappa^2+2-\sqrt{\kappa^4+16\kappa^2+16}<0 \end{aligned} \tag{B.22}$$

The real and positive value among the four roots is Ω_5, this gives the third root for extreme value of power,

$$\Omega_{extreme3}=\frac{1}{\sqrt{6}}\sqrt{\kappa^2+2+\sqrt{\kappa^4+16\kappa^2+16}} \tag{B.23}$$

Finally, for the case small damping (ζ = 0), the power's extreme values (stationary points in plot) are given by,

Cette thèse est accessible à l'adresse : http://theses.insa-lyon.fr/publication/2014ISAL0077/these.pdf
© [Y. Li], [2014], INSA de Lyon, tous droits réservés

$$\begin{cases} \Omega_{extreme1} = 1 \\ \Omega_{extreme2} = \sqrt{\kappa^2 + 1} \\ \Omega_{extreme3} = \dfrac{1}{\sqrt{6}}\sqrt{\kappa^2 + 2 + \sqrt{\kappa^4 + 16\kappa^2 + 16}} \end{cases} \tag{B.24}$$

(B) When Ω=1

In this condition, we have,

$$\beta = 0 \qquad R_x = \sqrt{\frac{\alpha^2 + \beta^2}{1 + x}} = \sqrt{\frac{\alpha^2}{1 + \alpha^2}} = \frac{\alpha}{\sqrt{1 + \alpha^2}} \tag{B.25}$$

Then the power is expressed as,

$$\begin{aligned} P &= \left(\frac{V_0}{N}\right)^2 \frac{C_0\omega_n}{\left[\left(\frac{\alpha}{R_x} + 1 - \beta\right)^2 + \left(\frac{\beta}{R_x} + \alpha\right)^2\right] R_x \frac{1}{\Omega}} = \left(\frac{V_0}{N}\right)^2 \frac{C_0\omega_n}{\left[\left(\frac{\alpha}{R_x}\right)^2 + 1 + \frac{2\alpha}{R_x} + \alpha^2\right] R_x \frac{1}{\Omega}} \\ &= \left(\frac{V_0}{N}\right)^2 \frac{C_0\omega_n}{\left(1 + \alpha^2 + 1 + 2\sqrt{1 + \alpha^2} + \alpha^2\right)\frac{\alpha}{\sqrt{1 + \alpha^2}}\frac{1}{\Omega}} = \left(\frac{V_0}{N}\right)^2 \frac{C_0\omega_n}{2\alpha\left(1 + \sqrt{1 + \alpha^2}\right)\frac{1}{\Omega}} \end{aligned} \tag{B.26}$$

Comparing the Equation (A.45) and (A.59), we can find that,

$$\alpha = C_0\omega_n\Omega\frac{R_f}{N^2} \tag{B.27}$$

Substituting it into Equation (B.26), the power is simplified as ,

$$\begin{aligned} P &= \left(\frac{V_0}{N}\right)^2 \frac{C_0\omega_n}{2\alpha\left(1 + \sqrt{1 + \alpha^2}\right)\frac{1}{\Omega}} = \left(\frac{V_0}{N}\right)^2 \frac{C_0\omega_n}{2C_0\omega_n\Omega\frac{R_a}{N^2}\left(1 + \sqrt{1 + \left(C_0\omega_n\Omega\frac{R_a}{N^2}\right)^2}\right)\frac{1}{\Omega}} \\ &= \frac{V_0^{\,2}}{2R_a}\frac{1}{1 + \sqrt{1 + \left(C_0\omega_n\Omega\frac{R_a}{N^2}\right)^2}} \end{aligned} \tag{B.28}$$

From the derivation process in Appendix A, it is easy to find that,

$$R_a = 2\zeta\omega_n m \tag{B.29}$$

$$N = \omega_n\sqrt{\kappa^2 C_0 m} \tag{B.30}$$

Substituting them into power expression (B.28), we have,

Cette thèse est accessible à l'adresse : http://theses.insa-lyon.fr/publication/2014ISAL0077/these.pdf
© [Y. Li], [2014], INSA de Lyon, tous droits réservés

$$P=\frac{V_0^{\ 2}}{2R_a}\frac{1}{1+\sqrt{1+\left(C_0\omega_n\Omega\frac{R_a}{N^2}\right)^2}}=\frac{V_0^{\ 2}}{4\zeta\omega_n m}\frac{1}{1+\sqrt{1+\left(C_0\omega_n\Omega\frac{2\zeta\omega_n m}{\omega_n^{\ 2}\kappa^2 C_0 m}\right)^2}}$$
$$=\frac{V_0^{\ 2}}{4\zeta\omega_n m}\frac{1}{1+\sqrt{1+\left(\frac{2\zeta}{\kappa^2}\right)^2}} \tag{B.31}$$

assuming $\frac{\zeta}{\kappa^2}\ll 1$, Power could be simplified to

$$P=\frac{V_0^{\ 2}}{4\zeta\omega_n m}\frac{1}{1+\sqrt{1+\left(\frac{2\zeta}{\kappa^2}\right)^2}}=\frac{V_0^{\ 2}}{8\zeta\omega_n m}=\left(U^2\omega_n^2\right)^2\frac{K}{8\zeta\omega_n^3} \tag{B.32}$$

(C) When $\Omega=\sqrt{1+\kappa^2}$

At this condition, we have,

$$\beta=1 \qquad R_x=\sqrt{\frac{\alpha^2+1}{1+x}}=\sqrt{\frac{\alpha^2+1}{\alpha^2}}=\frac{\sqrt{1+\alpha^2}}{\alpha} \tag{B.33}$$

The Equation (B.6) is simplified to

$$P=\left(\frac{V_0}{N}\right)^2\frac{C_0\omega_n}{\left[\left(\frac{\alpha}{R_x}+1-\beta\right)^2+\left(\frac{\beta}{R_x}+\alpha\right)^2\right]R_x\frac{1}{\Omega}}$$
$$=\left(\frac{V_0}{N}\right)^2\frac{C_0\omega_n}{\left[\left(\frac{\alpha^2}{\sqrt{1+\alpha^2}}\right)^2+\left(\frac{\alpha}{\sqrt{1+\alpha^2}}+\alpha\right)^2\right]\frac{\sqrt{1+\alpha^2}}{\alpha}\frac{1}{\Omega}} \tag{B.34}$$
$$=\left(\frac{V_0}{N}\right)^2\frac{C_0\omega_n}{\left(\frac{\alpha^4}{1+\alpha^2}+\frac{\alpha^2}{1+\alpha^2}+\alpha^2+\frac{2\alpha^2}{\sqrt{1+\alpha^2}}\right)\frac{\sqrt{1+\alpha^2}}{\alpha}\frac{1}{\Omega}}$$
$$=\left(\frac{V_0}{N}\right)^2\frac{C_0\omega_n}{2\alpha\left(\sqrt{1+\alpha^2}+1\right)\frac{1}{\Omega}}$$

Substituting (B.27) into Equation (B.34), the power expression is simplified as,

Cette thèse est accessible à l'adresse : http://theses.insa-lyon.fr/publication/2014ISAL0077/these.pdf
© [Y. Li], [2014], INSA de Lyon, tous droits réservés

$$P=\left(\frac{V_0}{N}\right)^2\frac{C_0\omega_n}{2\alpha\left(1+\sqrt{1+\alpha^2}\right)}=\left(\frac{V_0}{N}\right)^2\frac{C_0\omega_n}{2C_0\omega_n\Omega\frac{R_f}{N^2}\left(1+\sqrt{1+\left(C_0\omega_n\Omega\frac{R_f}{N^2}\right)^2}\right)}$$
$$=\frac{V_0^{\,2}}{2R_a}\frac{1}{1+\sqrt{1+\left(C_0\omega_n\Omega\frac{R_f}{N^2}\right)^2}} \tag{B.35}$$

Considering Equations(B.29)(B.30), the power expression (B.35) is simplified as,

$$P=\frac{V_0^{\,2}}{2R_f}\frac{1}{1+\sqrt{1+\left(C_0\omega_n\Omega\frac{R_f}{N^2}\right)^2}}=\frac{V_0^{\,2}}{4\zeta\omega_n m}\frac{1}{1+\sqrt{1+\left(C_0\omega_n\Omega\frac{2\zeta\omega_n m}{\omega_n^{\,2}\kappa^2 C_0 m}\right)^2}}$$
$$=\frac{V_0^{\,2}}{4\zeta\omega_n m}\frac{1}{1+\sqrt{1+\left(1+\kappa^2\right)\left(\frac{2\zeta}{\kappa^2}\right)^2}} \tag{B.36}$$

Same as before, assuming $\frac{\zeta}{\kappa^2}\ll 1$, Power could be simplified to,

$$P=\frac{V_0^{\,2}}{4\zeta\omega_n m}\frac{1}{1+\sqrt{1+\left(1+\kappa^2\right)\left(\frac{2\zeta}{\kappa^2}\right)^2}}=\frac{V_0^{\,2}}{8\zeta\omega_n m}=\left(U\omega_n^2\right)^2\frac{K}{8\zeta\omega_n^3} \tag{B.37}$$

B.1.2 General case

In general, neglecting the damping effect is not practical, in this subsection the full analytical solution is given for general case.

Our task is finding the stationary points for Equation (B.7),

$$y=\frac{2}{\Omega}\left(\sqrt{\left(\alpha^2+\beta^2\right)\left(\alpha^2+\beta^2-2\beta+1\right)}+\alpha\right)$$

Firstly, introducing a new target function g_2

$$g_2=\frac{u}{v} \tag{B.38}$$

with,

$$u=\left(\alpha^2+\beta^2\right)\left(\alpha^2+\beta^2-2\beta+1\right) \tag{B.39}$$

$$v=\Omega^2 \tag{B.40}$$

Cette thèse est accessible à l'adresse : http://theses.insa-lyon.fr/publication/2014ISAL0077/these.pdf
© [Y. Li], [2014], INSA de Lyon, tous droits réservés

Noticing that, finding the stationary points of function g_2 is equal to finding the stationary points of function y.

Differentiate g_2 with respect to Ω,

$$g_2' = \frac{u'v - v'u}{v^2}$$
$$g_2' = \frac{u'\Omega^2 - 2\Omega u}{\Omega^4} \tag{B.41}$$

It is known that Ω is not zero, the solution of g_3 is the solution for y, which is given by,

$$g_3 = u'\Omega - 2u = 0 \tag{B.42}$$

Solve it as follows,

$$u = \left(\alpha^2 + \beta^2\right)\left(\alpha^2 + \beta^2 - 2\beta + 1\right) = \alpha^4 + \beta^4 + 2\alpha^2\beta^2 + \alpha^2 + \beta^2 - 2\alpha^2\beta - 2\beta^3$$
$$= \frac{16\zeta^4\Omega^4}{\kappa^8} + \frac{\left(\Omega^2 - 1\right)^4}{\kappa^8} + 8\frac{\zeta^2\left(\Omega^2 - 1\right)^2\Omega^2}{\kappa^8} + \frac{4\zeta^2\Omega^2}{\kappa^4} + \frac{\left(\Omega^2 - 1\right)^2}{\kappa^4} - \frac{8\zeta^2\left(\Omega^2 - 1\right)\Omega^2}{\kappa^6} - 2\frac{\left(\Omega^2 - 1\right)^3}{\kappa^6} \tag{B.43}$$

$$u' = \left(\alpha^4 + \beta^4 + 2\alpha^2\beta^2 + \alpha^2 + \beta^2 - 2\alpha^2\beta - 2\beta^3\right)'$$
$$= 4\alpha^3\alpha' + 4\beta^3\beta' + 4\alpha\alpha'\beta^2 + 4\beta\beta'\alpha^2 + 2\alpha\alpha' + 2\beta\beta' - 4\alpha\alpha'\beta - 2\beta'\alpha^2 - 6\beta^2\beta'$$
$$= 4\left(\Omega\frac{2\zeta}{\kappa^2}\right)^3\frac{2\zeta}{\kappa^2} + 4\left(\frac{\Omega^2 - 1}{\kappa^2}\right)^3\frac{2\Omega}{\kappa^2} + 4\Omega\frac{2\zeta}{\kappa^2}\frac{2\zeta}{\kappa^2}\left(\frac{\Omega^2 - 1}{\kappa^2}\right)^2 + 4\frac{\Omega^2 - 1}{\kappa^2}\frac{2\Omega}{\kappa^2}\left(\Omega\frac{2\zeta}{\kappa^2}\right)^2 \tag{B.44}$$
$$+2\Omega\frac{2\zeta}{\kappa^2}\frac{2\zeta}{\kappa^2} + 2\frac{\Omega^2 - 1}{\kappa^2}\frac{2\Omega}{\kappa^2} - 4\Omega\frac{2\zeta}{\kappa^2}\frac{2\zeta}{\kappa^2}\frac{\Omega^2 - 1}{\kappa^2} - 2\frac{2\Omega}{\kappa^2}\left(\Omega\frac{2\zeta}{\kappa^2}\right)^2 - 6\left(\frac{\Omega^2 - 1}{\kappa^2}\right)^2\frac{2\Omega}{\kappa^2}$$

Substituting the (B.43)(B.44) into (B.42), and using the relationship given in (B.14), g_3 is simplified as,

$$\begin{aligned} &3A^4 + (16\zeta^2 - 4\kappa^2 + 4)A^3 \\ &+\left(16\zeta^4 + 32\zeta^2 + \kappa^4 - 8\zeta^2\kappa^2 - 6\kappa^2\right)A^2 \\ &+\left(32\zeta^4 + 16\zeta^2 + 2\kappa^4 - 16\zeta^2\kappa^2\right)A \\ &+16\zeta^4 - 8\zeta^2\kappa^2 = 0 \end{aligned} \tag{B.45}$$

Factoring Equation (B.45), obtain,

$$\begin{aligned} &\left(A^2 + \left(4\zeta^2 - \kappa^2\right)A + 4\zeta^2\right)\cdot \\ &\left(3A^2 + \left(4\zeta^2 - \kappa^2 + 4\right)A + 4\zeta^2 - 2\kappa^2\right) = 0 \end{aligned} \tag{B.46}$$

Equation (B.46) is composed of two quadratic equations; therefore the solutions of Equation (B.46) are the solutions of its member equations.

The solution for $A^2 + \left(4\zeta^2 - \kappa^2\right)A + 4\zeta^2 = 0$ is,

Cette thèse est accessible à l'adresse : http://theses.insa-lyon.fr/publication/2014ISAL0077/these.pdf
© [Y. Li], [2014], INSA de Lyon, tous droits réservés

$$A_{1,2}=\frac{\kappa^2-4\zeta^2\pm\sqrt{\left(4\zeta^2-\kappa^2\right)^2-16\zeta^2}}{2} \tag{B.47}$$

The solution for $3A^2+\left(4\zeta^2-\kappa^2+4\right)A+4\zeta^2-2\kappa^2=0$ is,

$$A_{3,4}=\frac{\kappa^2-4\zeta^2-4\pm\sqrt{\left(4\zeta^2-\kappa^2+4\right)^2-24\left(2\zeta^2-\kappa^2\right)}}{6} \tag{B.48}$$

In this way, all the roots of target function g_3 are obtained. Therefore, all the corresponding roots for normalized frequency Ω are,

$$\begin{aligned}\Omega_{1,2,3,4}&=\pm\sqrt{\frac{\kappa^2-4\zeta^2+2\pm\sqrt{\left(4\zeta^2-\kappa^2\right)^2-16\zeta^2}}{2}}\\ \Omega_{5,6,7,8}&=\pm\sqrt{\frac{\kappa^2-4\zeta^2+2\pm\sqrt{\left(4\zeta^2-\kappa^2+4\right)^2-24\left(2\zeta^2-\kappa^2\right)}}{6}}\\ &=\pm\sqrt{\frac{\kappa^2-4\zeta^2+2\pm\sqrt{\left(4\zeta^2-\kappa^2\right)^2-16\zeta^2+16(1+\kappa^2)}}{6}}\end{aligned} \tag{B.49}$$

If $\left(4\zeta^2-\kappa^2\right)^2-16\zeta^2<0$, $\Omega_{1,2}$ are not the real roots, which is defined by,

$$\zeta_b=\frac{1}{2}\left(\sqrt{1+\kappa^2}-1\right) \tag{B.50}$$

We should notice that, when $\left(4\zeta^2-\kappa^2\right)^2-16\zeta^2>0$, the condition (B.51) is satisfied.

$$\kappa^2-4\zeta^2+2\pm\sqrt{\left(4\zeta^2-\kappa^2\right)^2-16\zeta^2}>0 \tag{B.51}$$

Finally, we get the three real positive roots for normalized frequency Ω,

$$\begin{aligned}\Omega_{ext1}&=\sqrt{\frac{\kappa^2-4\zeta^2+2-\sqrt{\left(4\zeta^2-\kappa^2\right)^2-16\zeta^2}}{2}}\\ \Omega_{ext2}&=\sqrt{\frac{\kappa^2-4\zeta^2+2+\sqrt{\left(4\zeta^2-\kappa^2\right)^2-16\zeta^2}}{2}}\\ \Omega_{ext3}&=\sqrt{\frac{\kappa^2-4\zeta^2+2+\sqrt{\left(4\zeta^2-\kappa^2\right)^2-16\zeta^2+16(1+\kappa^2)}}{6}}\end{aligned} \tag{B.52}$$

Cette thèse est accessible à l'adresse : http://theses.insa-lyon.fr/publication/2014ISAL0077/these.pdf
© [Y. Li], [2014], INSA de Lyon, tous droits réservés

B.2 Complex load case

In this case, the optimal load impedance is the conjunctive of source impedance,

$$Z_L = Z_T^{\ *} = \frac{1}{C_0\omega_n}\frac{1}{\Omega}\left(\frac{\alpha}{1+x} + j\frac{x+\beta}{1+x}\right) \tag{B.53}$$

Assuming harvester is a voltage source with impedance in series (Figure 1-5.b), the current I_L through the load Z_L is,

$$I_L = \frac{V_S}{Z_T + Z_L} \tag{B.54}$$

Substituting Equations (A.64)and (B.53) into (B.54), yields,

$$\begin{aligned} I_L &= \frac{V_S}{Z_T + Z_L} = \frac{V_0}{N}\frac{\frac{1}{jC_0\omega}}{Z_1 + \frac{1}{jC_0\omega}}\frac{1}{\frac{1}{\frac{1}{Z_1} + jC_0\omega} + Z_L} = \frac{V_0}{N}\frac{1}{jC_0\omega Z_1 + 1}\frac{1}{\frac{1}{\frac{1}{Z_1} + jC_0\omega} + Z_L} \\ &= \frac{V_0}{N}\frac{1}{\frac{jC_0\omega Z_1 + 1}{\frac{1}{Z_1} + jC_0\omega} + Z_L\left(jC_0\omega Z_1 + 1\right)} = \frac{V_0}{N}\frac{1}{\frac{\left(jC_0\omega Z_1 + 1\right)Z_1}{1 + jC_0\omega Z_1} + Z_L\left(jC_0\omega Z_1 + 1\right)} \\ &= \frac{V_0}{N}\frac{1}{Z_1 + Z_L + jC_0\omega Z_1 Z_L} \end{aligned} \tag{B.55}$$

Substituting (A.59) and (B.53) in (B.55), yields,

$$\begin{aligned} I_L &= \frac{V_0}{N}\frac{1}{Z_1 + Z_L + jC_0\omega Z_1 Z_L} \\ &= \frac{V_0}{N}\frac{1}{\frac{1}{C_0\omega_n}\frac{1}{\Omega}\left(\alpha + j\beta\right) + \frac{1}{C_0\omega_n}\frac{1}{\Omega}\left(\frac{\alpha}{1+x} + j\frac{x+\beta}{1+x}\right) + jC_0\omega\frac{1}{C_0\omega_n}\frac{1}{\Omega}\left(\alpha + j\beta\right)\frac{1}{C_0\omega_n}\frac{1}{\Omega}\left(\frac{\alpha}{1+x} + j\frac{x+\beta}{1+x}\right)} \\ &= \frac{V_0}{N}C_0\omega_n\Omega\left(1+x\right)\frac{1}{B}, \end{aligned} \tag{B.56}$$

with,

$$B = \left(1+x\right)\left(\alpha + j\beta\right) + \alpha + j\left(x+\beta\right) + j\left(\alpha + j\beta\right)\left[\alpha + j\left(x+\beta\right)\right] \tag{B.57}$$

B could be solved as,

Cette thèse est accessible à l'adresse : http://theses.insa-lyon.fr/publication/2014ISAL0077/these.pdf
© [Y. Li], [2014], INSA de Lyon, tous droits réservés

$$\begin{aligned}
B &= (1+x)(\alpha+j\beta)+\alpha+j(x+\beta)+j(\alpha+j\beta)\left[\alpha+j(x+\beta)\right] \\
&= \alpha(1+x)+j\beta(1+x)+\alpha+j(x+\beta)+j\alpha^2-\alpha(x+\beta)-\alpha\beta-j\beta(x+\beta) \\
&= \alpha(1+x)+\alpha-\alpha(x+\beta)-\alpha\beta+j\left[\beta(1+x)+(x+\beta)+\alpha^2-\beta(x+\beta)\right] \\
&= 2\alpha-2\alpha\beta+j2\alpha^2
\end{aligned} \tag{B.58}$$

Substituting (B.58) into (B.56), yields,

$$\begin{aligned}
I_L &= \frac{V_0}{N}C_0\omega_n\Omega(1+x)\frac{1}{2\alpha-2\alpha\beta+j2\alpha^2} \\
&= \frac{V_0}{N}C_0\omega_n\Omega\frac{(1+x)}{2\alpha}\frac{1-\beta-j\alpha}{(1-\beta)^2+\alpha^2} \\
&= \frac{V_0}{N}C_0\omega_n\Omega\frac{1}{2\alpha}(1-\beta-j\alpha)
\end{aligned} \tag{B.59}$$

Then, the voltage over load Z_L is,

$$V_L = I_L Z_L \tag{B.60}$$

Substituting (B.59) and (B.60) into(B.3), the power is,

$$\begin{aligned}
P &= real(V_L I_L^*) \\
&= real(I_L I_L^* Z_L) \\
&= real(|I_L|^2 Z_L)
\end{aligned} \tag{B.61}$$

Notice that,

$$\begin{aligned}
|I_L|^2 &= \frac{V_0}{N}C_0\omega_n\Omega\frac{1}{2\alpha}(1-\beta-j\alpha)\frac{V_0}{N}C_0\omega_n\Omega\frac{1}{2\alpha}(1-\beta+j\alpha) \\
&= \left(\frac{V_0}{N}C_0\omega_n\Omega\right)^2\frac{1}{4\alpha^2}\left[(1-\beta)^2+\alpha^2\right]
\end{aligned} \tag{B.62}$$

Substituting (B.62) and (B.53) into(B.61), yields,

$$\begin{aligned}
P &= real(|I_L|^2 Z_L) \\
&= real\left(\left(\frac{V_0}{N}C_0\omega_n\Omega\right)^2\frac{1}{4\alpha^2}\left[(1-\beta)^2+\alpha^2\right]\frac{1}{C_0\omega_n}\frac{1}{\Omega}\left(\frac{\alpha}{1+x}+j\frac{x+\beta}{1+x}\right)\right) \\
&= real\left(\left(\frac{V_0}{N}\right)^2 C_0\omega_n\Omega\frac{\alpha+j(x+\beta)}{4\alpha^2}\right) \\
&= \left(\frac{V_0}{N}\right)^2 C_0\omega_n\Omega\frac{1}{4\alpha}
\end{aligned} \tag{B.63}$$

Substituting Equation (B.27) into (B.63), yields,

Cette thèse est accessible à l'adresse : http://theses.insa-lyon.fr/publication/2014ISAL0077/these.pdf
© [Y. Li], [2014], INSA de Lyon, tous droits réservés

$$P = (V)^2 C_0 \omega_n \Omega \frac{1}{4\alpha} = \left(\frac{V_0}{N}\right)^2 C_0 \omega_n \Omega \frac{1}{4C_0 \omega_n \Omega \frac{R_f}{N^2}} = \frac{V_0^2}{4R_f} \tag{B.64}$$

With some known relationship,

$$R_f = \omega_n m \tan \delta_f \tag{B.65}$$

$$V_0 = \omega^2 L_b U \tag{B.66}$$

$$L_b = m \tag{B.67}$$

Power (B.64) is simplified to,

$$\begin{aligned} P &= \frac{V_0^2}{4R_f} = \frac{\left(L_b \omega^2 U\right)^2}{4\omega_n m \tan \delta_f} = \left(\omega^2 U\right)^2 \frac{L_b^2}{8\omega_n m \zeta} \\ &= \left(\omega^2 U\right)^2 \frac{K^E}{8\zeta \omega_n^3} \end{aligned} \tag{B.68}$$

Cette thèse est accessible à l'adresse : http://theses.insa-lyon.fr/publication/2014ISAL0077/these.pdf
© [Y. Li], [2014], INSA de Lyon, tous droits réservés

Appendix. C. Simulink Simscape model for network SSHI harvester

The modelling method of piezoelectric energy harvester by Simulink Simscape is introduced in this short paper. The description is based on a 4 modal vibration system, but it can be derived from SDOF system or other multi modal system.

C.1 Method

The whole harvester is modeled by State-space method (Figure C-1). The State-space equation is solved by Simulink **State-Space block**. The input variable is

$$U = \begin{bmatrix} F & V_1 & V_2 & V_3 & V_4 \end{bmatrix}^T \tag{C.1}$$

In Simulink Simscape model, the force F is provided by **Pulse Generator Block**. The voltage vector is the feedback of piezoelectric element output voltage.Considering the state-space equation we used in Chapter 2, the output variable is the cluster of displacement and corresponding velocity.

$$Y = \begin{bmatrix} u_1 & u_2 & u_3 & u_4 & \dot{u}_1 & \dot{u}_2 & \dot{u}_3 & \dot{u}_4 \end{bmatrix}^T \tag{C.2}$$

As we introduced in Chapter 1, the electrical part of harvester is modelled by a **Controlled Current Source** shunted by a **Capacitor** block. The capacitor is the blocked capacitor of piezoelectric element.

For instance, the 4 modes displacement is used to control the current output of PZT patch 1 by a **Gain** block **Matrix(K*u)** , where the gain **K** is **alphas(:,1)'**. The piezoelectric element is connected to the **Storage Device** subsystem (a customized subsystem) directly. The storage device could be the standard energy harvesting circuit, the SSHI energy harvesting circuit, S3H energy harvesting circuit, etc. The outgoing voltage of piezoelectric element is measured by **Voltage Sensor** block. All the four piezoelectric element output voltages are grouped to a vector by **Mux** block.

C.2 Simulation environment

To have a precise but swift simulation results, especially for the switch action in SSHI, the Simulink diagram solver is **ode4(Runge-Kutta)** with **Fixed-step** Type. The Fixed-step size is determined by variable **simu_step**, which will be discussed later.

For such physical environment (Simscape), a local solver should be connected to the circuit model. In general, **Trapezoidal Rule** solver type with Sample time **simu_step** is enough for precise simulation. The Consistency tolerance shall be **simu_step*0.01**.

For a normal SSHI simulation, the most sensitive parameter is the switch on time, which is 1.4e-4 typically. Therefore, 2 orders magnitudes higher **simu_step** is suitable for

Cette thèse est accessible à l'adresse : http://theses.insa-lyon.fr/publication/2014ISAL0077/these.pdf
© [Y. Li], [2014], INSA de Lyon, tous droits réservés

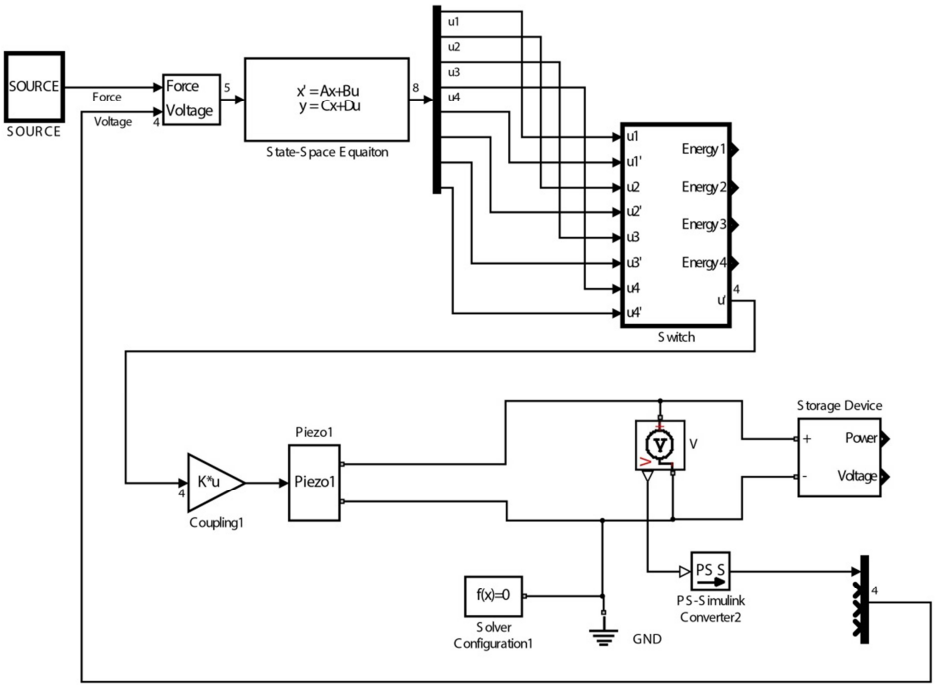

Figure C-1. The overview of Simulink model (simplified)

simulation, such as 1e-6. Although the 1e-6 **simu_step** is suitable for most of the cases, smaller simulation step should be considered when oscillation phenomenon is obviously in circuit.

C.3 An example: SSHI circuit

Figure C-2 shows the diagram of SSHI circuit in Simulink Simscape. The state-space section is not included in this drawing. The piezo is connected directly to the full-wave bridge, a switchable inductor is shunted with piezo unit, the storage device unit is connected with the end port of bridge circuit unit. The switch is controlled by a unit named Check the peak. The function of this Check the peak is detecting the maximum/minimum value of piezoelectric output voltage and operating the switch for a time t_0. The principle and implementation method is described in Appendix D.

Cette thèse est accessible à l'adresse : http://theses.insa-lyon.fr/publication/2014ISAL0077/these.pdf
© [Y. Li], [2014], INSA de Lyon, tous droits réservés

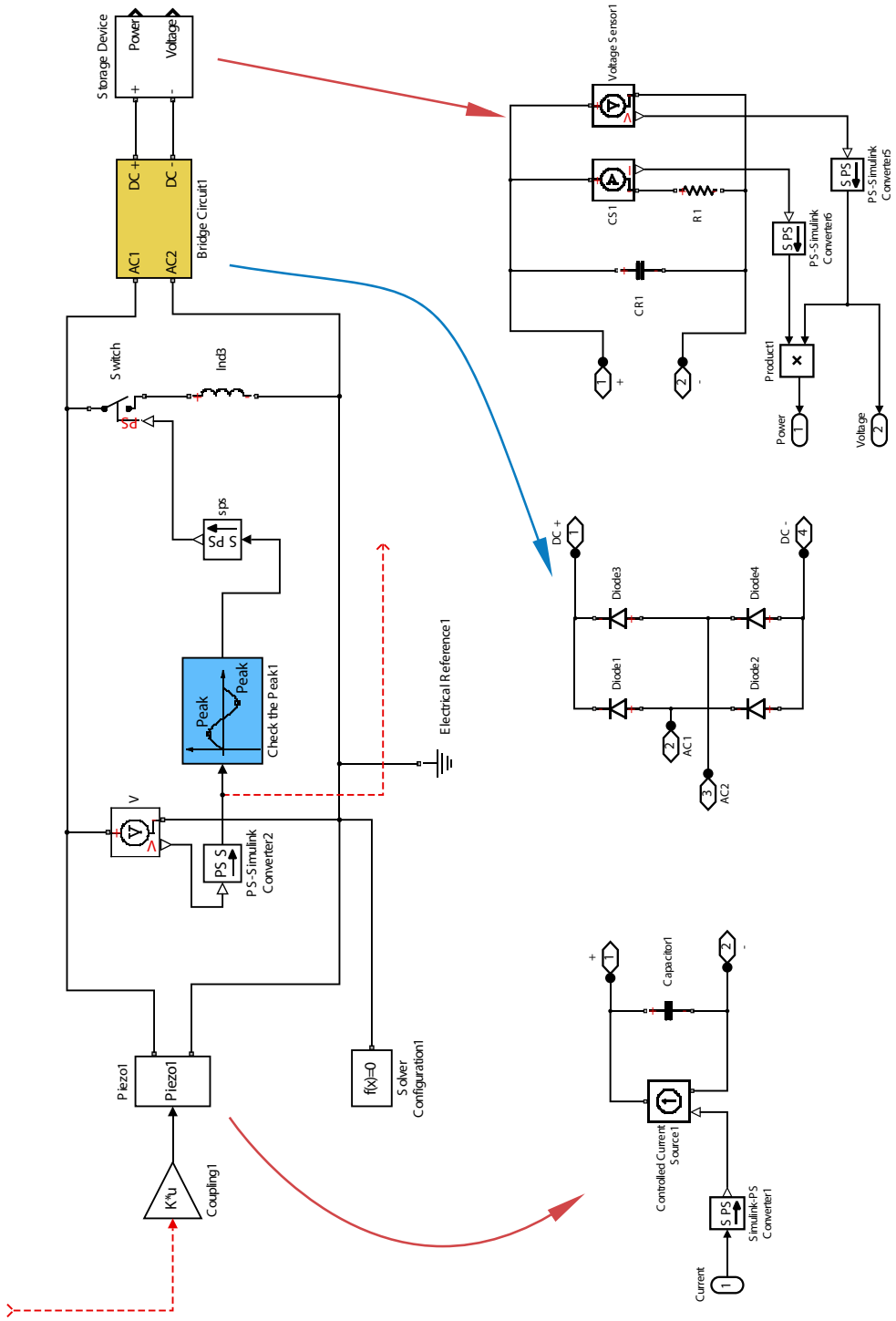

Figure C-2. The diagram of SSHI technique

Cette thèse est accessible à l'adresse : http://theses.insa-lyon.fr/publication/2014ISAL0077/these.pdf
© [Y. Li], [2014], INSA de Lyon, tous droits réservés

Appendix. D. Simulink Simscape model for peak-detecting switch

In this short article, the principle and implementation method by Simulink Simscape of Check the peak unit is described. Check the peak unit is used to detect the maximum/minimum of input signal then generate a pulse control signal. The width of this pulse control is determined by the parameter Δt.

D.1 Peak detecting

We divide the input signal into 2 branches. The second branch is picked up and delayed for a time t, and then compared with the first branch. It is obviously that, in some region, the first signal is larger than the second, in the other region, the second is larger. Graphically, there is a watershed point for this comparison. If the delay time t is shorter enough, this watershed point is equal to the maximum/minimum point of original signal. Details is showed in Figure D-1.a.

D.2 Generate the switch on pulse

In peak detecting operation, a transient signal is generated by **Detect Change** block. Then it is transformed by a specified transfer function transmitted a comparator block. The comparator will create a logic signal and then transform to pulse signal. Details is showed in Figure D-1.b. Starting from this stable pulse signal, the desired width pulse Δt. signal is created by a series of logic operations (Figure D-1.c).

D.3 Generate the dead zone pulse

Once the main circuit is switched, parasitic maximum/minimum peak may be detected. In fact, this peak value is useless, and should be avoided. Therefore, we introduced the Dead zone mechanism to prevent the unwanted peak detection. The dead zone time could be 2 times of the switch time. The generating method for dead zone signal is similar with the switch on pulse generation method, except the output signal. The output for a dead zone signal is logic False.

D.4 Control signal (output)

The dead zone signal is used to control the Simulink **Switch** block (Figure D-1.d, Figure D-2). Two input signal of this Switch block is logic False and switch on signal. When dead zone is active (logic False), the logic False is selected and output to the out port. When the dead zone is inactive (logic True), the switch on pulse is selected and output to the out port.

Cette thèse est accessible à l'adresse : http://theses.insa-lyon.fr/publication/2014ISAL0077/these.pdf
© [Y. Li], [2014], INSA de Lyon, tous droits réservés

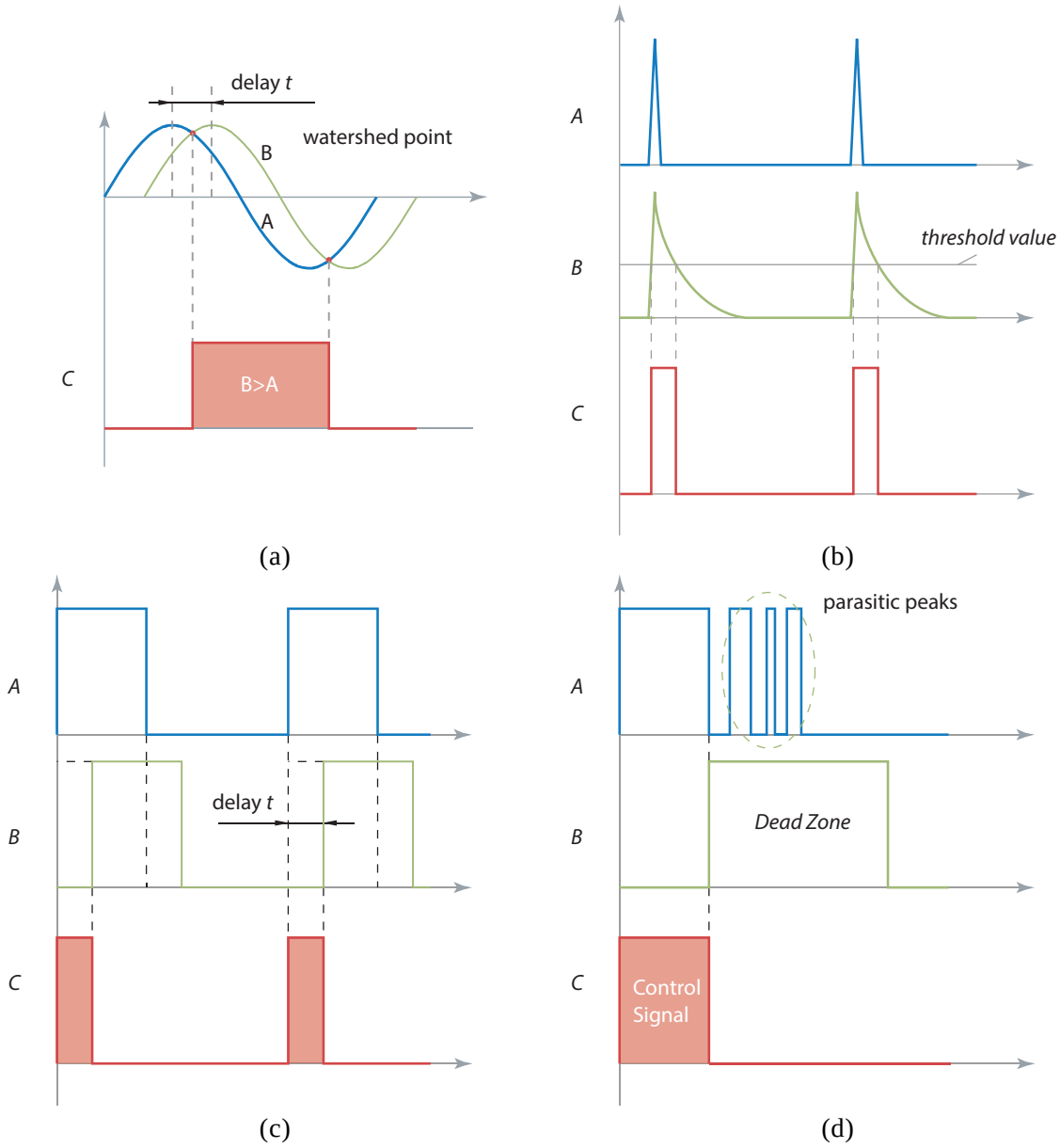

Figure D-1. The logic for Check the peak

Interpretation of Figure D-1.c

Waveform A is the raw signal,

Waveform B is identical to Waveform A, but is delayed for arbitrary time *t*

Waveform C is based on Waveform A and B, has *C= (A **XOR** B) **AND** A*

Cette thèse est accessible à l'adresse : http://theses.insa-lyon.fr/publication/2014ISAL0077/these.pdf
© [Y. Li], [2014], INSA de Lyon, tous droits réservés

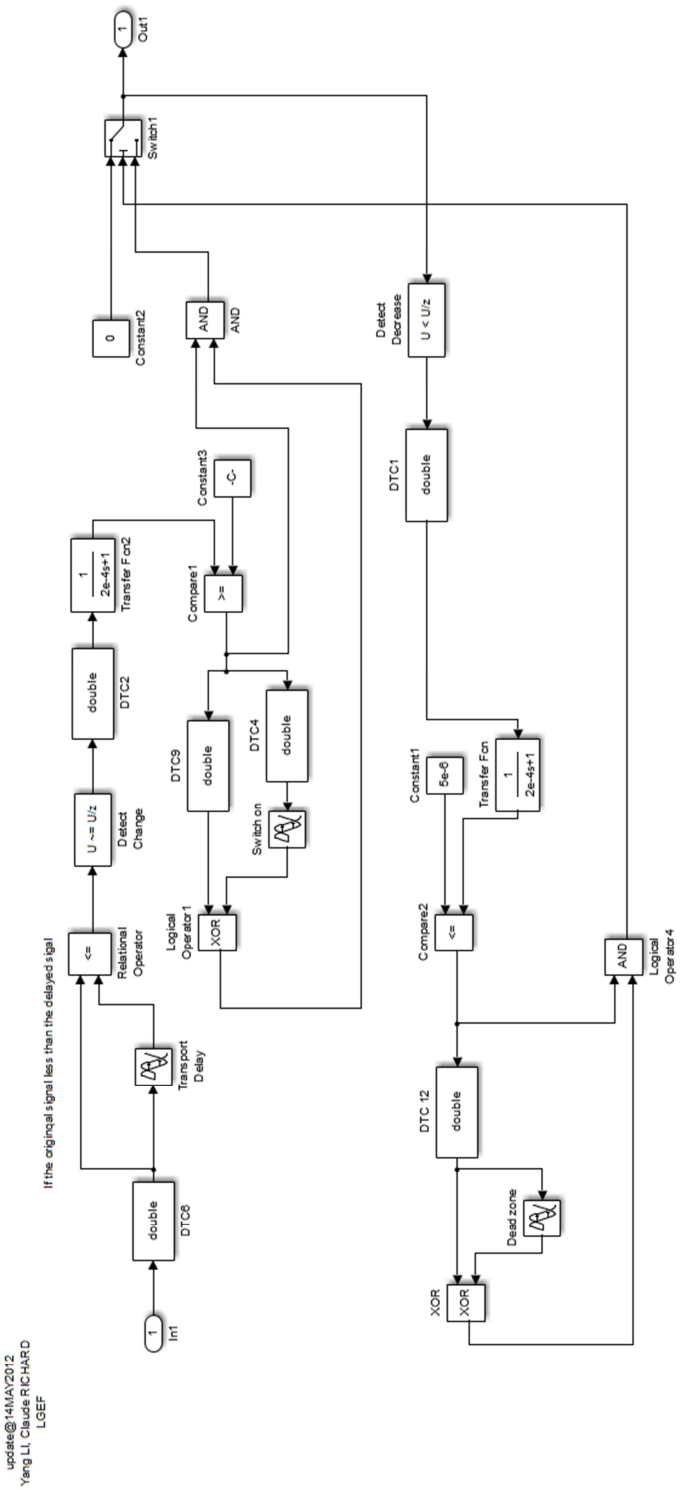

Figure D-2. The diagram of check the peak unit

Cette thèse est accessible à l'adresse : http://theses.insa-lyon.fr/publication/2014ISAL0077/these.pdf
© [Y. Li], [2014], INSA de Lyon, tous droits réservés

Appendix. E. The optimization for STD

In steady state, the voltage on load (piezovoltage) is expressed as,

$$y(t)=\frac{\alpha U_m}{C_0}\frac{R^2C_0^2\omega^2}{1+R^2C_0^2\omega^2}\left(\cos\omega t-\frac{1}{RC_0\omega}\sin\omega t\right) \tag{E.1}$$

Using first harmonic analysis method, we have,

$$\tilde{V}_1=\frac{1}{T}\int V(t)e^{-j\omega t}dt=\tilde{B}U_m \quad\Rightarrow\quad \tilde{V}_1=\tilde{B}\tilde{U} \tag{E.2}$$

Considering U_m as unity, we have,

$$B=\int y(t)e^{-j\omega t}dt=\int y(t)e^{-j\omega t}dt=\frac{2}{T}\int_0^T y(t)(\cos\omega t-j\sin\omega t)dt$$

$$=\frac{2}{T}\int_0^T y(t)\cos\omega t dt-\frac{2}{T}j\int_0^T y(t)\sin\omega t dt dt$$

$$=\frac{\alpha U_m}{C_0}\frac{R^2C_0^2\omega^2}{1+R^2C_0^2\omega^2}\frac{2}{T}\left\{\int_0^T\left(\cos\omega t-\frac{1}{RC_0\omega}\sin\omega t\right)\cos\omega t dt-j\int_0^T\left(\cos\omega t-\frac{1}{RC_0\omega}\sin\omega t\right)\sin\omega t dt dt\right\}$$

$$=\frac{\alpha U_m}{C_0}\frac{R^2C_0^2\omega^2}{1+R^2C_0^2\omega^2}\frac{2}{T}\left\{\begin{array}{l}\left[\frac{1}{\omega}\left(\frac{\omega t}{2}+\frac{1}{4}\sin 2\omega t\right)-\frac{1}{RC_0\omega}\frac{1}{2\omega}\sin^2\omega t\right]_0^T\\ -j\left[\frac{1}{2\omega}\sin^2\omega t-\frac{1}{RC_0\omega}\frac{1}{\omega}\left(\frac{\omega t}{2}-\frac{1}{4}\sin 2\omega t\right)\right]_0^T\end{array}\right\}$$

$$=\frac{\alpha U_m}{C_0}\frac{R^2C_0^2\omega^2}{1+R^2C_0^2\omega^2}\left(1+j\frac{1}{RC_0\omega}\right)=\frac{\alpha}{C_0}\frac{R^2C_0^2\omega^2}{1+R^2C_0^2\omega^2}\left(1+j\frac{1}{RC_0\omega}\right)$$

(E.3)

The amplitude and phase are,

$$\begin{cases}B_m=\dfrac{\alpha}{C_0}\sqrt{\dfrac{R^2C_0^2\omega^2}{1+R^2C_0^2\omega^2}}\\ \theta_B=\arctan\dfrac{1}{RC_0\omega}\end{cases} \tag{E.4}$$

From Chapter 4 Section 4.2.3, we have known that,

$$\tilde{U}=\frac{\tilde{F}}{K^E+\alpha\tilde{B}-M\omega^2+j\omega C}=\mathcal{F}(\tilde{F},\tilde{B}) \tag{E.5}$$

Substituting Equation (E.3) into (E.5),

Cette thèse est accessible à l'adresse : http://theses.insa-lyon.fr/publication/2014ISAL0077/these.pdf
© [Y. Li], [2014], INSA de Lyon, tous droits réservés

$$\tilde{U}=\frac{\tilde{F}}{K_E+\alpha\left(\frac{\alpha}{C_0}\frac{R^2C_0^2\omega^2}{1+R^2C_0^2\omega^2}\left(1+j\frac{1}{RC_0\omega}\right)\right)-M\omega^2+j\omega C}$$

$$=\frac{1}{K_E+\alpha\left(\frac{\alpha}{C_0}\frac{R^2C_0^2\omega^2}{1+R^2C_0^2\omega^2}\left(1+j\frac{1}{RC_0\omega}\right)\right)-M\omega^2+j\omega C} \tag{E.6}$$

$$=\frac{1}{K_E+\frac{\alpha^2}{C_0}\frac{R^2C_0^2\omega^2}{1+R^2C_0^2\omega^2}-M\omega^2+j\left(\omega C+\frac{\alpha^2}{C_0}\frac{RC_0\omega}{1+R^2C_0^2\omega^2}\right)}$$

the corresponding amplitude and phase are,

$$U_m=\left[\left(K_E+\frac{\alpha^2}{C_0}\frac{R^2C_0^2\omega^2}{1+R^2C_0^2\omega^2}-M\omega^2\right)^2+\left(\omega C+\frac{\alpha^2}{C_0}\frac{RC_0\omega}{1+R^2C_0^2\omega^2}\right)^2\right]^{-\frac{1}{2}} \tag{E.7}$$

$$\theta_U=-\arctan\frac{\omega C+\frac{\alpha^2}{C_0}\frac{RC_0\omega}{1+R^2C_0^2\omega^2}}{K_E+\frac{\alpha^2}{C_0}\frac{R^2C_0^2\omega^2}{1+R^2C_0^2\omega^2}-M\omega^2} \tag{E.8}$$

In constant displacement analysis (Chapter 4, Section 4.2.2.A), we have known that, the power harvested by load R is,

$$P=\frac{\alpha^2U_m^2\omega}{2C_0}\left(\frac{RC_0\omega}{1+R^2C_0^2\omega^2}\right) \tag{E.9}$$

Substituting (E.7) into(E.9),

$$P=\frac{\alpha^2F_m^2\omega}{2C_0}\cdot\frac{\frac{RC_0\omega}{1+R^2C_0^2\omega^2}}{\left(K_E+\frac{\alpha^2}{C_0}\frac{R^2C_0^2\omega^2}{1+R^2C_0^2\omega^2}-M\omega^2\right)^2+\left(\omega C+\frac{\alpha^2}{C_0}\frac{RC_0\omega}{1+R^2C_0^2\omega^2}\right)^2} \tag{E.10}$$

Our object here is finding the maximum power output for STD case. As we have analysed in Chapter 2, at strong coupling condition, the piezoelectric harvester has its maximum power output around open circuit frequency and close circuit frequency. Therefore, we use condition as following,

$$\omega=\omega_D=\sqrt{\frac{K^D}{M}} \tag{E.11}$$

Then the power expression is simplified as,

Cette thèse est accessible à l'adresse : http://theses.insa-lyon.fr/publication/2014ISAL0077/these.pdf
© [Y. Li], [2014], INSA de Lyon, tous droits réservés

$$P=\frac{\alpha^2F_m^2\pi f}{C_0}\cdot\frac{\dfrac{RC_0\omega}{1+R^2C_0^2\omega^2}}{\left(K_E+\dfrac{\alpha^2}{C_0}\dfrac{R^2C_0^2\omega^2}{1+R^2C_0^2\omega^2}-M\omega^2\right)^2+\left(\omega C+\dfrac{\alpha^2}{C_0}\dfrac{RC_0\omega}{1+R^2C_0^2\omega^2}\right)^2}$$

$$=F_m^2\frac{\omega_D}{2}\frac{C_0}{\alpha^2}\frac{RC_0\omega_D}{\left(\dfrac{\omega_DCC_0}{\alpha^2}RC_0\omega_D+1\right)^2+\left(\dfrac{\omega_DCC_0}{\alpha^2}\right)^2} \tag{E.12}$$

$$=\frac{F_m^2}{2C}\cdot\frac{\dfrac{\omega_DCC_0}{\alpha^2}RC_0\omega_D}{\left(\dfrac{\omega_DCC_0}{\alpha^2}RC_0\omega_D+1\right)^2+\left(\dfrac{\omega_DCC_0}{\alpha^2}\right)^2}$$

Next,

$$P=\frac{F_m^2}{2C}\cdot\frac{\dfrac{\omega_DCC_0}{\alpha^2}RC_0\omega_D}{\left(\dfrac{\omega_DCC_0}{\alpha^2}RC_0\omega_D+1\right)^2+\left(\dfrac{\omega_DCC_0}{\alpha^2}\right)^2}$$

$$=\frac{F_m^2}{2C}\cdot\frac{\mathcal{BR}}{(\mathcal{BR}+1)^2+(\mathcal{B})^2} \tag{E.13}$$

$$=\frac{F_m^2}{2C}\cdot\frac{\mathcal{B}}{y}$$

where,

$$y=\frac{\mathcal{B}^2\mathcal{R}^2+1+2\mathcal{BR}+\mathcal{B}^2}{\mathcal{R}} \tag{E.14}$$

$$\mathcal{B}=\frac{\omega_DCC_0}{\alpha^2},\qquad \mathcal{R}=RC_0\omega_D \tag{E.15}$$

Finding the maximum of P is equal to finding the minimum value of function y.

$$y=\frac{\mathcal{B}^2\mathcal{R}^2+1+2\mathcal{BR}+\mathcal{B}^2}{\mathcal{R}}$$

$$=\mathcal{B}^2\mathcal{R}+\frac{\mathcal{B}^2+1}{\mathcal{R}}+2\mathcal{B} \tag{E.16}$$

$$\geq 2\sqrt{\mathcal{B}^2\mathcal{R}\frac{\mathcal{B}^2+1}{\mathcal{R}}}+2\mathcal{B}$$

Then the minimum value of function y is given as,

Cette thèse est accessible à l'adresse : http://theses.insa-lyon.fr/publication/2014ISAL0077/these.pdf
© [Y. Li], [2014], INSA de Lyon, tous droits réservés

$$y_{\min} = 2\sqrt{\mathcal{B}^2 \mathcal{R} \frac{\mathcal{B}^2+1}{\mathcal{R}}} + 2\mathcal{B}$$
$$= 2\mathcal{B}\left(\sqrt{\mathcal{B}^2+1}+1\right) \tag{E.17}$$

Now, the maximum of function P is given as,

$$P = \frac{F_m^2}{2C} \cdot \frac{\mathcal{B}}{y_{\min}}$$
$$= \frac{F_m^2}{2C} \cdot \frac{\mathcal{B}}{2\mathcal{B}\left(\sqrt{\mathcal{B}^2+1}+1\right)} \tag{E.18}$$
$$= \frac{F_m^2}{4C} \cdot \frac{1}{\left(\sqrt{\mathcal{B}^2+1}+1\right)}$$

We can find that, when $\mathcal{B} \to 0$, the power has its maximum,

$$P = \frac{F_m^2}{4C} \cdot \frac{1}{\left(\sqrt{0+1}+1\right)} = \frac{F_m^2}{8C} \tag{E.19}$$

In fact, we should notice that,

$$k^2 = \frac{\alpha^2}{K_D C_0} \tag{E.20}$$

$$Q_m = \frac{m\omega_n}{C} \tag{E.21}$$

yield,

$$\mathcal{B} = \omega_d C C_0 \big/ \alpha^2 = \frac{1}{k^2 Q_m} \tag{E.22}$$

In other words, at strong coupling condition $k^2 Q_m \gg 1$, the power reaches it maximum value, the value is given by Equation (E.19).

Cette thèse est accessible à l'adresse : http://theses.insa-lyon.fr/publication/2014ISAL0077/these.pdf
© [Y. Li], [2014], INSA de Lyon, tous droits réservés

Appendix. F. The optimization for S3H

F.1 Power of S3H at constant displacement condition

The RMS value of voltage is defined by,

$$V_{rms} = \sqrt{\frac{1}{T}\int_0^T \left[V(t)\right]^2 dt} \tag{F.1}$$

Considering the voltage on load R is given as,

$$V(t) = \begin{cases} V_{II}(t) & , \quad 0 < t \le t_0 \\ 0 & , \quad t_0 < t \le \frac{T}{2} \\ -V_{II}(t - \frac{T}{2}) & , \quad \frac{T}{2} < t \le \frac{T}{2} + t_0 \\ 0 & , \quad \frac{T}{2} + t_0 < t \le T \end{cases} \tag{F.2}$$

During switch action, the voltage of V_{II} is given by,

$$V_{II}(t) = e^{-\frac{t}{RC_0}} \frac{1}{e^{-t_0/RC_0} + 1} \frac{\alpha U_m}{C_0}\left(1 + \cos\omega t_0 - A(t_0)\right) + \frac{\alpha U_m}{C_0} A(t) \tag{F.3}$$

with

$$A(t) = \frac{R^2 C_0^2 \omega^2}{1 + R^2 C_0^2 \omega^2}\left(\cos\omega t - \frac{1}{RC_0\omega}\sin\omega t - e^{-\frac{t}{RC_0}}\right) \tag{F.4}$$

$$A(t_0) = \frac{R^2 C_0^2 \omega^2}{1 + R^2 C_0^2 \omega^2}\left(\cos\omega t_0 - \frac{1}{RC_0\omega}\sin\omega t_0 - e^{-\frac{t_0}{RC_0}}\right) \tag{F.5}$$

Rewrite it by formal format,

$$V_{II}(t) = \mathcal{A}\cos\omega t + \mathcal{B}\sin\omega t + \mathcal{C} e^{-t/\tau} \tag{F.6}$$

where

$$\begin{aligned} &\mathcal{A} = \frac{\alpha U_m}{C_0}\frac{\tau^2\omega^2}{1+\tau^2\omega^2}, \quad \mathcal{B} = -\frac{\alpha U_m}{C_0}\frac{\tau^2\omega^2}{1+\tau^2\omega^2}\frac{1}{\tau\omega}, \\ &\mathcal{C} = \frac{\alpha U_m}{C_0}\left(\frac{g(t_0)}{2} - \frac{\tau^2\omega^2}{1+\tau^2\omega^2}\right), \quad \tau = RC_0 \end{aligned} \tag{F.7}$$

Then the square of voltage RMS value is obtained,

Cette thèse est accessible à l'adresse : http://theses.insa-lyon.fr/publication/2014ISAL0077/these.pdf
© [Y. Li], [2014], INSA de Lyon, tous droits réservés

$$V_{rms}^2 = \frac{1}{T}\int_0^{t_0}\left(\mathcal{A}\cos\omega t + \mathcal{B}\sin\omega t + Ce^{-t/\tau}\right)^2 dt$$

$$= \frac{1}{T}\left\{\begin{array}{l} -\frac{\tau}{2}C^2 e^{-2t/\tau}\Big|_0^{t_0} + \frac{1}{\omega}\left[\mathcal{A}^2\left(\frac{\omega t}{2}+\frac{1}{4}\sin 2\omega t\right)+\mathcal{B}^2\left(\frac{\omega t}{2}-\frac{1}{4}\sin 2\omega t\right)+\mathcal{AB}\sin^2\omega t\right]_0^{t_0} \\ +2e^{-t/\tau}\frac{C\tau^2}{1+\tau^2\omega^2}\left[\mathcal{A}\left(\omega\sin\omega t-\frac{1}{\tau}\cos\omega t\right)-\mathcal{B}\left(\frac{1}{\tau}\sin\omega t+\omega\cos\omega t\right)\right]_0^{t_0} \end{array}\right\}$$

$$= \frac{1}{T}\left\{\begin{array}{l} \frac{\tau}{2}C^2\left(1-e^{-2t_0/\tau}\right)+\frac{1}{\omega}\left[\mathcal{A}^2\left(\frac{\omega t_0}{2}+\frac{1}{4}\sin 2\omega t_0\right)+\mathcal{B}^2\left(\frac{\omega t_0}{2}-\frac{1}{4}\sin 2\omega t_0\right)+AB\sin^2\omega t_0\right] \\ +2e^{-t_0/\tau}\frac{C\tau^2}{1+\tau^2\omega^2}\left[\mathcal{A}\left(\omega\sin\omega t_0-\frac{1}{\tau}\cos\omega t_0\right)-\mathcal{B}\left(\frac{1}{\tau}\sin\omega t_0+\omega\cos\omega t_0\right)\right]+2\frac{C\tau^2}{1+\tau^2\omega^2}\left(\frac{\mathcal{A}}{\tau}+\mathcal{B}\omega\right) \end{array}\right\}$$

(F.8)

From Equation (F.7), we can find that,

$$\mathcal{B} = -\frac{\mathcal{A}}{\tau\omega} \tag{F.9}$$

Then Equation (F.8) is simplified to,

$$V_{rms}^2 = \frac{1}{T}\left\{\begin{array}{l} \frac{\tau}{2}C^2\left(1-e^{-2t_0/\tau}\right)+\frac{1}{\omega}\frac{1}{\tau^2\omega^2}\mathcal{A}^2\left[\frac{1}{4}\left(\tau^2\omega^2-1\right)\sin 2\omega t_0-\tau\omega\sin^2\omega t_0+\frac{\omega t_0}{2}\left(\tau^2\omega^2+1\right)\right] \\ +2e^{-t_0/\tau}\mathcal{A}C\frac{1}{\omega}\sin\omega t_0 \end{array}\right\} \tag{F.10}$$

Substituting Equation (F.7) into (F.10), we get the squared RMS voltage,

$$V_{rms}^2 = \frac{1}{T}\left\{\begin{array}{l} \frac{\tau}{2}\frac{\alpha U_m}{C_0}\left(\frac{\cos\omega t_0+1-A(t_0)}{e^{-t_0/\tau}+1}-\frac{\tau^2\omega^2}{1+\tau^2\omega^2}\right)\left(1-e^{-2t_0/\tau}\right) \\ +\frac{1}{\omega}\frac{1}{\tau^2\omega^2}\left(\frac{\alpha U_m}{C_0}\frac{\tau^2\omega^2}{1+\tau^2\omega^2}\right)^2\left[\frac{1}{4}\left(\tau^2\omega^2-1\right)\sin 2\omega t_0-\tau\omega\sin^2\omega t_0+\frac{\omega t_0}{2}\left(\tau^2\omega^2+1\right)\right] \\ +2e^{-t_0/\tau}\left(\frac{\alpha U_m}{C_0}\right)^2\frac{\tau^2\omega^2}{1+\tau^2\omega^2}\left(\frac{\cos\omega t_0+1-A(t_0)}{e^{-t_0/\tau}+1}-\frac{\tau^2\omega^2}{1+\tau^2\omega^2}\right)\frac{1}{\omega}\sin\omega t_0 \end{array}\right\} \tag{F.11}$$

Then the RMS voltage can be calculated as,

$$V_{RMS} = \sqrt{\frac{1}{T}\int_0^T\left[V(t)\right]^2 dt} = \sqrt{\frac{1}{T}A} \tag{F.12}$$

Cette thèse est accessible à l'adresse : http://theses.insa-lyon.fr/publication/2014ISAL0077/these.pdf
© [Y. Li], [2014], INSA de Lyon, tous droits réservés

The average power is defined as,

$$P=\frac{1}{T}\int_0^T P(t)dt=\frac{1}{T}\int_0^T \frac{V(t)^2}{R}dt \tag{F.13}$$

Substituting Equation (F.11)(F.12) into Equation (F.13), the average power on load R is yielded(whole period),

$$P=2\frac{V_{RMS}{}^2}{R}=\frac{\omega}{\pi}\frac{\alpha^2U_m^2}{C_0}\left\{\begin{array}{l}\frac{1}{2}\left(\frac{\cos\omega t_0+1-A(t_0)}{e^{-t_0/\tau}+1}-\frac{\tau^2\omega^2}{1+\tau^2\omega^2}\right)^2\left(1-e^{-2t_0/\tau}\right)\\+\frac{\tau\omega}{1+\tau^2\omega^2}\left[\frac{1}{4}\left(\tau^2\omega^2-1\right)\sin 2\omega t_0-\tau\omega\sin^2\omega t_0+\frac{\omega t_0}{2}\left(\tau^2\omega^2+1\right)\right]\\+2e^{-t_0/\tau}\frac{\tau\omega}{1+\tau^2\omega^2}\left(\frac{\cos\omega t_0+1-A(t_0)}{e^{-t_0/\tau}+1}-\frac{\tau^2\omega^2}{1+\tau^2\omega^2}\right)\sin\omega t_0\end{array}\right\} \tag{F.14}$$

When the switch on-time is very small($t_0 \approx 0$), the power expression is simplified to,

$$\lim_{t_0\to 0}P=\frac{1}{\pi}\frac{\alpha^2U_m^2\omega}{C_0}\left\{\frac{1}{2}\left(\frac{2-A(t_0)}{e^{-t_0/\tau}+1}-\frac{\tau^2\omega^2}{1+\tau^2\omega^2}\right)^2\left(1-e^{-2t_0/\tau}\right)\right\} \tag{F.15}$$

Then consider load R is chosen a relative low value ($\tau << t_0$),

$$\begin{array}{l}e^{-t_0/\tau}\to 0\\ \frac{\tau^2\omega^2}{1+\tau^2\omega^2}\to 0\\ A(t_0)\to 0\end{array} \tag{F.16}$$

Power reaches its maximum value,

$$P=\frac{1}{\pi}\frac{\alpha^2U_m^2\omega}{C_0}\left\{\frac{1}{2}\left(\frac{2-0}{0+1}-0\right)^2(1-0)\right\}=\frac{2}{\pi}\frac{\alpha^2U_m^2\omega}{C_0} \tag{F.17}$$

F.2 S3H for constant force

The piezovoltage is given as,

Cette thèse est accessible à l'adresse : http://theses.insa-lyon.fr/publication/2014ISAL0077/these.pdf
© [Y. Li], [2014], INSA de Lyon, tous droits réservés

$$V(t)=\begin{cases} V_{II}(t) & , \quad 0<t\le t_0 \\ V_I(t) & , \quad t_0<t\le \dfrac{T}{2} \\ -V_{II}(t-\dfrac{T}{2}) & , \quad \dfrac{T}{2}<t\le \dfrac{T}{2}+t_0 \\ -V_I(t-\dfrac{T}{2}) & , \quad \dfrac{T}{2}+t_0<t\le T \end{cases} \tag{F.18}$$

Then the factor ***B*** can be calculated as,

$$\begin{aligned} B &= \int V(t)e^{-j\omega t}dt \\ &= \frac{2}{T}\int_0^{t_0} V(t)e^{-j\omega t}dt + \frac{2}{T}\int_{t_0}^{\frac{T}{2}} V(t)e^{-j\omega t}dt + \frac{2}{T}\int_{\frac{T}{2}}^{t_0+\frac{T}{2}} V(t)e^{-j\omega t}dt + \frac{2}{T}\int_{t_0+\frac{T}{2}}^{T} V(t)e^{-j\omega t}dt \\ &= B_1+B_2+B_3+B_4 \\ &= 2\left(B_1+B_2\right) \end{aligned} \tag{F.19}$$

When $0<t\le t_0$,

$$\begin{aligned} B_1 &= \frac{2}{T}\int_0^{t_0}\left(\frac{\alpha U_m}{C_0}\frac{R^2C_0^2\omega_0^2}{1+R^2C_0^2\omega_0^2}\left(\cos\omega t-\frac{1}{RC_0\omega_0}\sin\omega t\right)+e^{-\frac{t}{RC_0}}\frac{\alpha U_m}{C_0}\left(\frac{1}{2}g(t_0)-\frac{R^2C_0^2\omega_0^2}{1+R^2C_0^2\omega_0^2}\right)\right)e^{-j\omega t}dt \\ &= \frac{2}{T}\left\{\frac{A_{II}}{\omega}\left(\frac{\omega t_0}{2}+\frac{1}{4}\sin 2\omega t_0\right)+\frac{B_{II}}{2\omega}\sin^2\omega t_0+\frac{C_{II}}{\alpha_{II}^2+\omega^2}\left[e^{\alpha_{II}t_0}\left(\omega\sin\omega t_0+\alpha_{II}\cos\omega t_0\right)-\alpha_{II}\right]\right\} \\ &-j\frac{2}{T}\left\{\frac{A_{II}}{2\omega}\sin^2\omega t_0+\frac{B_{II}}{\omega}\left(\frac{\omega t_0}{2}-\frac{1}{4}\sin 2\omega t_0\right)+\frac{C_{II}}{\alpha_{II}^2+\omega^2}\left[e^{\alpha_{II}t_0}\left(\alpha_{II}\sin\omega t_0-\omega\cos\omega t_0\right)+\omega\right]\right\} \end{aligned} \tag{F.20}$$

Where,

$$\begin{aligned} A_{II} &= \frac{\alpha}{C_0}\frac{R^2C_0^2\omega_0^2}{1+R^2C_0^2\omega_0^2} & B_{II} &= -\frac{\alpha}{C_0}\frac{1}{RC_0\omega_0}\frac{R^2C_0^2\omega_0^2}{1+R^2C_0^2\omega_0^2} \\ C_{II} &= \frac{\alpha}{C_0}\left(\frac{1}{2}g(t_0)-\frac{R^2C_0^2\omega_0^2}{1+R^2C_0^2\omega_0^2}\right) & \alpha_{II} &= -\frac{1}{RC_0} \end{aligned} \tag{F.21}$$

When $t_0<t\le\dfrac{T}{2}$,

Cette thèse est accessible à l'adresse : http://theses.insa-lyon.fr/publication/2014ISAL0077/these.pdf
© [Y. Li], [2014], INSA de Lyon, tous droits réservés

$$B_2 = \frac{2}{T}\int_{t_0}^{\frac{T}{2}}\left(\frac{\alpha U_m}{C_0}\cos\omega t + \frac{\alpha U_m}{C_0}\left(1-\frac{g(t_0)}{2}\right)\right)e^{-j\omega t}dt$$

$$= \frac{2}{T}\left\{\frac{A_I}{\omega}\left(\frac{\omega\left(\frac{T}{2}-t_0\right)}{2}-\frac{1}{4}\sin 2\omega t_0\right)-\frac{C_I}{\omega}\sin\omega t_0\right\} - j\frac{2}{T}\left\{-\frac{A_I}{2\omega}\sin^2\omega t_0 + \frac{C_I}{\omega}\left(1+\cos\omega t_0\right)\right\} \quad \text{(F.22)}$$

Where,

$$A_I = \frac{\alpha}{C_0} \quad C_I = \frac{\alpha}{C_0}\left(1-\frac{g(t_0)}{2}\right) \quad \text{(F.23)}$$

Then B is expressed as,

$$\tilde{B} = \frac{4}{T}\left\{\frac{A_{II}}{\omega}\left(\frac{\omega t_0}{2}+\frac{1}{4}\sin 2\omega t_0\right)+\frac{B_{II}}{2\omega}\sin^2\omega t_0 + \frac{C_{II}}{\alpha_{II}^2+\omega^2}\left[e^{\alpha_{II}t_0}\left(\omega\sin\omega t_0+\alpha_{II}\cos\omega t_0\right)-\alpha_{II}\right]\right\}$$

$$-j\frac{4}{T}\left\{\frac{A_{II}}{2\omega}\sin^2\omega t_0 + \frac{B_{II}}{\omega}\left(\frac{\omega t_0}{2}-\frac{1}{4}\sin 2\omega t_0\right)+\frac{C_{II}}{\alpha_{II}^2+\omega^2}\left[e^{\alpha_{II}t_0}\left(\alpha_{II}\sin\omega t_0-\omega\cos\omega t_0\right)+\omega\right]\right\} \quad \text{(F.24)}$$

$$+\frac{4}{T}\left\{\frac{A_I}{\omega}\left(\frac{\omega\left(\frac{T}{2}-t_0\right)}{2}-\frac{1}{4}\sin 2\omega t_0\right)-\frac{C_I}{\omega}\sin\omega t_0\right\} - j\frac{4}{T}\left\{-\frac{A_I}{2\omega}\sin^2\omega t_0 + \frac{C_I}{\omega}\left(1+\cos\omega t_0\right)\right\}$$

Cette thèse est accessible à l'adresse : http://theses.insa-lyon.fr/publication/2014ISAL0077/these.pdf
© [Y. Li], [2014], INSA de Lyon, tous droits réservés

PUBLICATIONS

Journal papers

[1] D. Guyomar, **Y. Li**, G. Sebald, P.-J. Cottinet, B. Ducharne, and J.-F. Capsal, "Elastocaloric modelling of natural rubber," *Applied Thermal Engineering,* vol. 57, pp. 33-38, 2013.

[2] M. Lallart, C. Richard, **Y. Li**, Y.-C. Wu, and D. Guyomar, "Load-tolerant, high efficiency self-powered energy harvesting scheme using a nonlinear approach," *IEEE Transactions on Ultrasonics Ferroelectrics and Frequency Control*. (submitted)

Conference papers

[3] **Y. Li**, D. Guyomar, and C. Richard, "Influence of the topology for a networked SSHI piezoelectric harvesting configuration," in *Proc. SPIE 8688, Active and Passive Smart Structures and Integrated Systems 2013*, San Diego, California, USA, 2013. *oral presentation*

[4] **Y. Li**, M. Lallart, and C. Richard, "Piezoelectric energy harvesting using a series synchronized switch technique," in *Proc. SPIE 9057, Active and Passive Smart Structures and Integrated Systems 2014*, San Diego, California, USA, 2014. *poster presentation*

[5] **Y. Li** and C. Richard, "Piezogenerator impedance matching using Mason equivalent circuit for harvester identification," in *Proc. SPIE 9057, Active and Passive Smart Structures and Integrated Systems 2014*, San Diego, California, USA, 2014. *oral presentation*

[6] **Y. Li**, M. Lallart, and C. Richard, "Load-independent piezoelectric energy harvseting by a simple switch," in *JNRSE2014*, Annecy le Vieux, France, 2014. *oral presentation*

Cette thèse est accessible à l'adresse : http://theses.insa-lyon.fr/publication/2014ISAL0077/these.pdf
© [Y. Li], [2014], INSA de Lyon, tous droits réservés

(this page intentionally left blank)

Cette thèse est accessible à l'adresse : http://theses.insa-lyon.fr/publication/2014ISAL0077/these.pdf
© [Y. Li], [2014], INSA de Lyon, tous droits réservés

FOLIO ADMINISTRATIF

THESE SOUTENUE DEVANT L'INSTITUT NATIONAL DES SCIENCES APPLIQUEES DE LYON

NOM : LI
(avec précision du nom de jeune fille, le cas échéant)

DATE de SOUTENANCE : 03 Septembre 2014

Prénoms : Yang

TITRE :
Approches simplifiées pour l'optimisation de systèmes piézoélectriques de récupération d'énergie ;
Simple techniques for piezoelectric energy harvesting optimization

NATURE : Doctorat

Numéro d'ordre : 2014ISAL0077

Ecole doctorale : Électronique , Électrotechnique, Automatique de Lyon

Spécialité : Énergie et Systèmes

RESUME :
La récupération d'énergie par élément piézoélectrique est une technique prometteuse pour les futurs systèmes électroniques nomades autoalimentés. L'objet de ce travail est d'analyser des approches simples et agiles d'optimisation de la puissance produite par un générateur piézoélectrique.

D'abord le problème de l'optimisation de l'impédance de charge d'un générateur piézoélectrique sismique est posé. Une analyse du schéma équivalent global de ce générateur a été menée sur la base du schéma de Mason. Il est démontré que la puissance extraite avec une charge complexe adaptée puisse être constante quelle que soit la fréquence et que de plus elle est égale à la puissance extraite avec la charge résistive adaptée du même système sans pertes. Il est montré toutefois que la sensibilité de cette adaptation à la valeur de la réactance de la charge la rend difficilement réaliste pour une application pratique.

Une autre solution pour améliorer l'énergie extraite est de considérer un réseau de générateurs positionnés en différents endroits d'une structure. Des simulations sont proposées dans une configuration de récupération d'énergie de type directe sur une plaque encastrée. Les générateurs piézoélectriques, associés à la technique SSHI, ont été reliés selon différentes configurations. Les résultats attestent que l'énergie produite ne dépend pas de façon critique de la manière dont sont connectés les éléments. Toutefois l'utilisation d'un seul circuit SSHI pour l'ensemble du réseau dégrade l'énergie extraite du fait des interactions entre les trop nombreuses commutations.

Enfin une nouvelle approche non-linéaire est étudiée qui permet l'optimisation de l'énergie extraite tout en gardant une grande simplicité et des possibilités d'auto alimentation. Cette technique appelée S3H pour « Synchronized Serial Switch Harvesting » n'utilise pas d'inductance et consiste en un simple interrupteur en série avec l'élément piézoélectrique. La puissance récupérée est le double de celle extraite par les méthodes conventionnelles et reste totalement invariante sur une large gamme de résistances de charge.

MOTS-CLES : Récupération d'énergie ; Piézoélectricité ; Schéma équivalent de Mason ; Traitement non-linéaire ; Réseau de générateurs piézoélectriques

Laboratoire (s) de recherche : Laboratoire de Génie Électrique et Ferroélectricité (LGEF) de l'INSA de Lyon

Directeur de thèse: Pr. Daniel GUYOMAR; Pr. Claude RICHARD

Président de jury :

Composition du jury :

Dr. David AUDIGIER; Pr. Philippe COMBETTE; Dr. Jean-Louis COMPEAU; Pr. Elie LEFEUVRE;

Pr. Paul MURALT; Pr. Lionel PETIT; Pr. Claude RICHARD

Cette thèse est accessible à l'adresse : http://theses.insa-lyon.fr/publication/2014ISAL0077/these.pdf
© [Y. Li], [2014], INSA de Lyon, tous droits réservés